MODELING BIOGEOCHEMISTRY AND FLOW WITHIN HETEROGENEOUS FORMATIONS IN VARIABLY-SATURATED MEDIA

A Dissertation

by

BHAVNA ARORA

Submitted to the Office of Graduate Studies of
Texas A&M University
in partial fulfillment of the requirements for the degree of

DOCTOR OF PHILOSOPHY

August 2012

Major Subject: Water Management and Hydrological Science

MODELING BIOGEOCHEMISTRY AND FLOW WITHIN HETEROGENEOUS FORMATIONS IN VARIABLY-SATURATED MEDIA

A Dissertation

by

BHAVNA ARORA

Submitted to the Office of Graduate Studies of
Texas A&M University
in partial fulfillment of the requirements for the degree of

DOCTOR OF PHILOSOPHY

Approved by:

Co-Chairs of Committee,	Binayak P. Mohanty
	Jennifer T. McGuire
Committee Members,	Kung-Hui Chu
	Yalchin Efendiev
	Hongbin Zhan
Intercollegiate Faculty Chair,	Ronald Kaiser

August 2012

Major Subject: Water Management and Hydrological Science

ABSTRACT

Modeling Biogeochemistry and Flow within Heterogeneous Formations in Variably-Saturated Media. (August 2012)

Bhavna Arora, B.Tech., Indian Institute of Technology Kharagpur, India;

M.Tech., Indian Institute of Technology Kharagpur, India

Co-Chairs of Advisory Committee: Dr. Binayak P. Mohanty
Dr. Jennifer T. McGuire

This dissertation focuses on understanding the complex interactions between hydrological and geochemical processes, and specifically how these interactions are affected by subsurface heterogeneity across scales. Heterogeneity in the form of macropores and fractures provide preferential flowpaths and affect contaminant transport. Biogeochemical processes are also strongly affected by such heterogeneities. Any lithological layering or interface (e.g. plume fringe, wetland-aquifer boundary, etc.) increases biogeochemical activity around that interface. Hydrologic conditions, rainfall events, drainage patterns, and pH variations are also dominant controls on redox processes and thereby affect contaminant distribution and migration. An inherent limitation of modeling fate and transport of contaminants in the subsurface is that the interactions among biogeochemical processes are complex and non-linear. Therefore, this research investigates the effect of hydrological variations and physical heterogeneity on coupled biogeochemical processes across column and landfill scales.

Structural heterogeneity in the form of macropore distributions (no macropore, single macropore, and multiple macropores) in experimental soil columns is investigated to accurately model preferential flow and tracer transport. This research is crucial to agricultural systems where soil and crop management practices modify soil structure and alter macropore densities. The comparison between deterministic and stochastic approaches for simulating preferential flow improved the characterization of interface parameters of the dual permeability model, and outlined the need for efficient sampling algorithms or additional datasets to yield unique (equifinal) soil hydraulic parameters.

To evaluate the effect of heterogeneity on redox processes, repacked soil columns with homogeneous and heterogeneous (layered) profiles from soil cores collected at the Norman Landfill site, Oklahoma, USA were employed. Results indicate that heterogeneity in the form of textural layering is paramount in controlling redox processes in the layered column.

To evaluate the effect of hydrologic conditions on redox processes, temporal data at the Norman landfill site was used. Results indicate that seasonal hydrologic variations exert dominant control over redox-sensitive concentrations.

An integrated MCMC algorithm was devised to upscale linked biogeochemical processes from the column to the field scale. Results indicate that heterogeneity and hydrologic processes are paramount in controlling effective redox concentrations at the Norman landfill site.

DEDICATION

This dissertation is dedicated to my parents for their love and support.

ACKNOWLEDGEMENTS

The realization of this dissertation would not have been possible without the help and support of several people. I owe this gratitude to my family, advisors, teachers and friends who have truly enhanced my graduate experience.

I would like to acknowledge my committee chair, Dr. Binayak P. Mohanty, for his passionate guidance, constant encouragement, and invaluable advice. I have been fortunate to have an advisor who gave me the liberty to explore ideas and work on them. Thank you for providing me the challenges and opportunities in reaching this stage of my academic career and preparing me for a successful future. I am especially grateful to my committee co-chair, Dr. Jennifer T. McGuire, for introducing me to the intricacies and exciting prospects of the field of geochemistry. I am thankful for her patient guidance and significant contribution in this endeavor. Her endless support and trust in my work have been an inspiration for me. I would also like to thank my doctoral committee members Dr. Yalchin Efendiev, Dr. Kung-Hui Chu, and Dr. Hongbin Zhan for their advice, comments, and support during my research work.

I would also like to thank Dr. Isabella M. Cozzarelli for sharing her field data for my research work. A special mention goes to Dr. David Hansen for his experimental datasets and advice. I acknowledge the financial support of NSF Hydrological Sciences grant (EAR-0635961) and Texas Water Resources Institute.

I am also grateful to many former and current colleagues, especially Dipankar, Sayena, Raghu, Yongchul, Zhenlei, and Tara for their unselfish assistance and

suggestions. Also, Rosario, Malixole, Adam, Clint, Raka, Abhishek, and many others deserve a mention for my cherishable graduate experience.

Last, but definitely not the least, gratitude goes to my parents for their unwavering love and patience. Heartfelt thanks goes to my sister for her enthusiastic support of all my endeavors.

TABLE OF CONTENTS

Page

CHAPTER Page

CHAPTER Page

CHAPTER Page

LIST OF FIGURES

Page

Page

Page

Page

Page

Page

Page

Page

Page

Page

LIST OF TABLES

Page

Page

CHAPTER I

GENERAL INTRODUCTION

1.1 Problem statement

Contamination of subsurface systems is a significant environmental concern. Contaminant distribution and migration is affected considerably by changes in the reduction-oxidation (redox) potential of the vadose zone. Other biogeochemical processes in the vadose zone (e.g. precipitation-dissolution, sorption-desorption, microbial biodegradation, biotransformation) can also change the reactivity and transport of contaminants before they reach groundwater. These processes have complex non-linear linkages that are difficult to determine and are strongly affected by structural heterogeneities. The presence of certain heterogeneities such as macropores and fractures can itself increase groundwater vulnerability to potential contamination from harmful chemicals. Hence, to improve the predictions of the fate and transport of contaminants in water, an understanding of the coupled hydrological, geochemical, and microbiological processes occurring in the subsurface under homogeneous and heterogeneous conditions is desired.

This dissertation follows the style of *Water Resources Research*.

1.2 Motivation

Understanding relationships between hydrological (e.g. initial and boundary conditions, hydraulic conductivity ratio, soil layering), geochemical (e.g. mineralogy, redox potential, organic matter content) and microbiological factors (e.g. changes in microbial community type and structure) that alter biogeochemical processes is an inherent requirement of modeling contaminant fate and transport in subsurface environments. The uncertainty associated with these predictions is further magnified due to variable flow dynamics and transient redox states as a result of structural heterogeneity. While it is known that the biogeochemical processes are influenced by subsurface heterogeneity, the exact nature of these linkages and transition across scales is generally unknown.

1.3 Research objectives

The main aim of this research was to bring together physical, geochemical, mathematical, and modeling perspectives to improve the understanding of coupled processes and enable better prediction of fate and transport of chemicals in subsurface systems. The role of subsurface heterogeneity on transport processes using different modeling techniques at appropriate spatial scales was also explored.

The primary objectives of this research were:

- To *examine the effect of heterogeneity* in the form of macropore distributions, layers and lenses on contaminant flow and transport at the column scale.
- To *examine the effect of hydrologic variations* such as hydrologic boundary conditions, seasonal variability, rainfall intensity on redox processes at both column and landfill scales.

- To *develop suitable mathematical schemes* which describe linkages and transitions between biogeochemical processes from column to the landfill scale.

In Chapters I – III, structural heterogeneity in the form of macropore distributions and layering is evaluated at the column scale. In Chapter I, the effect of different macropore densities (no macropore, single macropore, and multiple macropores) and the degree of model complexity on preferential flow and tracer transport through experimental soil columns is evaluated. Chapter II builds upon this work and quantifies uncertainty in parameters and outputs obtained from experiments of single and multiple macropore soil columns.

In Chapter III, the effect of heterogeneity on redox processes is investigated by comparing a layered soil column with two texturally homogeneous soil columns. These repacked soil columns are obtained from soil cores collected at the Norman Landfill research site, Norman, Oklahoma, USA. The Norman landfill site is a closed municipal landfill with prevalent organic contamination. Chapter III also contains the analysis of hydrologic perturbations on dominant biogeochemical processes within these soil columns.

In Chapter IV, the effects of different hydrologic interactions and seasonal water table variability on conservative and redox-sensitive concentrations at three well locations at the Norman landfill site are investigated. Wavelet analysis techniques are used to extract the dominant processes affecting geochemical concentrations at the temporal scale.

In Chapter V, a new upscaling methodology is developed that derives upscaling coefficients for hydrologic and redox parameters from the column to the field scale. This upscaling algorithm tests for redox variations across heterogeneous systems (layers, lenses) and interaction of hydrologic flow processes across spatial scales.

CHAPTER II

INVERSE ESTIMATION OF PARAMETERS FOR MULTIDOMAIN FLOW MODELS IN SOIL COLUMNS WITH DIFFERENT MACROPORE DENSITIES*

2.1 Synopsis

Macropores and fractures provide preferential flow paths and faster pathways for contaminants to reach groundwater. Heterogeneity related to the density, connectivity, and geometry of pores changes preferential flow and transport characteristics of structured soils. Soil and crop management practices (e.g. tillage operations, multiple cropping, etc.) have been found to modify soil structure and alter macropore densities. An ability to accurately determine soil hydraulic parameters and their variation with changes in macropore density is crucial for assessing groundwater vulnerability to potential contamination from agricultural chemicals. This study investigates the consequences of using consistent matrix and macropore parameters in simulating preferential flow and bromide transport in soil columns with different macropore densities (no macropore, single macropore and multiple macropores). As used herein, the term 'macropore density' is intended to refer to the number of macropores per unit area. A comparison between continuum-scale models including single porosity (SPM),

---

*Reprinted with permission from "Inverse estimation of parameters for multidomain flow models in soil columns with different macropore densities" by Arora, B., B. P. Mohanty, and J. T. McGuire (2011), *Water Resour. Res.*, *47*, W04512, doi: 1029/2010WR009451, Copyright 2011 American Geophysical Union.

mobile immobile (MIM), and dual permeability model (DPM) with first and second-order between-domain water transfer functions that employed these matrix and macropore parameters is also conducted.

Results indicate that consistent matrix and macropore parameters are successful in describing preferential flow but not tracer transport in both types of multiple macropore columns. We believe that lateral exchange between matrix and macropore domains needs better accounting to efficiently simulate preferential transport in case of dense, closely-spaced macropores. Model comparison showed that increasing model complexity from SPM, MIM, to DPM improved the description of preferential flow and bromide transport in the multiple macropore columns but not in the single macropore column. This suggests that the use of a more complex model is recommended with an increase in macropore density to generate forecasts with higher accuracy.

2.2 Introduction

Containment of contaminants in the vadose zone is a viable option to prevent groundwater pollution from landfill and waste sites (Halton Waste Management site, Canada; Yucca Mountain, Nevada; etc.). The feasibility of this option is generally hampered by the presence of macropores and fractures in the soil that can cause preferential transport of contaminants to groundwater [*National Research Council*, 1994; *Kladivko et al.*, 2001; *Böhlke*, 2002*; Jamieson et al.*, 2002]. Preferential flow modeling using classical area-averaged Richards' equation is not enough to account for bypass flow through the macropores [*Beven and Germann*, 1982; *van Genuchten et al.*, 1990]. Additionally, early breakthrough and tailing due to preferential solute transport discredit

the use of classical convection dispersion equation (CDE) [*Biggar and Nielsen*, 1962; *Liu et al.*, 1991; *Jury and Flühler*, 1992]. For a model to sufficiently reproduce characteristic features of preferential flow and transport, all sources of non-equilibrium should be effectively addressed [*Brusseau and Rao*, 1990]. For physical non-equilibrium processes, a common approach has been the use of continuum-scale models like dual porosity, dual permeability, multiple porosity/permeability, etc. [*Gee et al.*, 1991; *Feyen et al.*, 1998; *Hendrickx and Flury*, 2001; *Šimůnek et al.*, 2003].

The Single Porosity Model (SPM), the simplest conceptualization of the porous media, depends on a single-domain representation of the soil pore system. An equilibrium approach using SPM describes variably-saturated water flow and solute transport through Richards' and convection dispersion equations, respectively. It has been used extensively in experimental studies to simulate transient conditions of porous media [e.g., *Šimůnek et al.*, 1999; *Jansson et al.*, 2005; *Köhne et al.*, 2006b]. Alternatively, two-domain conceptualization considers two interacting regions, one associated with the less permeable intra-aggregate pore region, or the rock matrix, and the other associated with the more permeable inter-aggregate, macropore or fracture system. In this regard, mobile immobile models (MIMs) consider water to be stagnant in the immobile domain [*van Genuchten and Wierenga*, 1976]. A widespread use of MIM has been reported by *Köhne et al.* [2009] especially for simulating preferential flow at column and plot scales [cf. *Larsson et al.*, 1999; *Miller et al.*, 1999; *Abbasi et al.*, 2003; *Šimůnek et al.*, 2003]. Dual permeability models (DPMs) assume both matrix and fracture continua to conduct fluids and solute [*Gerke and van Genuchten*, 1993a; *Jarvis*,

1994]. Analogous to dual porosity models, a number of approaches are available for DPMs which differ in the description of flow and solute transport in the preferential flow domain [*Germann*, 1985; *Ahuja and Hebson*, 1992; *Chen and Wagenet*, 1992] and of between-domain mass transfer [*Novák et al.*, 2000; *Köhne et al.*, 2004]. DPM has been applied at column, plot, and field scales [*Villholth and Jensen*, 1998; *Köhne and Mohanty*, 2005; *Dousset et al.*, 2007; *Köhne et al.*, 2009].

A complete explicit representation of structural geometry and macroporosity in terms of well-defined physical parameters is usually not feasible with these continuum-scale models [*Vogel et al.*, 2000; *Gerke*, 2006]. In addition, farming practices and climatic patterns modify soil structure and change macropore density. Mechanized agricultural practices, rooting characteristics, biological activity, multiple cropping, etc. tend to disrupt the physical structure and cause changes to macroporosity at different times during a season [*Franzluebbers et al.*, 1995; *Schäffer et al.*, 2008]. Differences in macropore density are of particular concern for agricultural soils as leaching of chemicals through macropores can contribute to pollution from agricultural lands. Many investigators have shown that variation in pore size and connectivity, as a result of soil and crop management practices, affects the rate, flow, and retention of water [*Jarvis*, 2007]. Changes to model parameters reflecting an increase in the number or density of pores and its impact on preferential flow movement has not been addressed to date. The use of continuum-scale models to predict soil hydraulic properties and water movement requires adjustments to effective parameters to develop better agreement between observations and predictions. Previous studies have shown that soil hydraulic parameters

need to be altered at both spatial and temporal scales to accurately reproduce preferential flow occurring through the macropores [*Logsdon and Jaynes*, 1996; *Dasgupta et al.*, 2006]. The focus of the present study is to test whether transport through macropores is a function of its density, and if consistency in soil hydraulic parameters can be maintained while accounting for changes in macropore density.

A problem of increasing model complexity (from SPM, MIM to DPM) is the task of understanding how these models compare under different scenarios. Continuum-scale models have resulted in different best-model-performances in the past based on field/experimental settings being explored. For example, *Köhne et al.* [2006a] found a triple-porosity model (DPM in conjunction with MIM) to yield better results for tracer transport (Br^-) while dual permeability model performed better for adsorptive solutes (isoproturon and terbuthylazine) in a macroporous (aggregated) column. Nonetheless, both models behaved in a similar manner for an aggregated soil column with time-variant sorption. Evaluation and intercomparison of models can provide meaningful insights on the suitability of these models under different conditions (e.g. initial and boundary conditions, prominence vs. lack of preferential flow, etc.). This study evaluates the performance of SPM, MIM, and DPM using designed soil column experiments with artificial macropores under conditions of different macropore densities and distributions (e.g., single (central) macropore, low density (3 macropores), and high density (19 macropores) columns). Model comparison, especially in multiple macropore columns, offers a closer representation of the agricultural field. The specific objectives of this study are: i) to find the degree of model complexity (SPM, MIM, or DPM) that can

adequately describe preferential flow in the single (central) as well as in low and high density multiple macropore columns, and ii) to evaluate if domain-specific parameters obtained from inverse modeling of homogeneous and single (central) macropore columns can consistently represent those individual domains in both low and high density multiple macropore columns during transient flow and transport conditions. In summary, the evaluation of continuum-scale models and consideration of changes in macropore density are beneficial for quantifying contaminant transport particularly through agricultural soils.

2.3 Continuum scale models for flow and transport in macroporous soil

Figure 2.1 depicts the characteristic features of continuum models (SPM, MIM and DPM) for a hypothetical infiltration scenario of a central macropore column. In this study, matrix domain is chosen as the sole porous medium for flow in conceptualizing the single porosity model. A unimodal pore size distribution is sufficient in describing the closed form expressions for the hydraulic conductivity functions for the equilibrium SPM. The MIM approach represents the flow field through the macropore (mobile) domain and allows for water and solute transfer between the mobile and immobile regions. As opposed to SPM, mobile immobile model describes soil hydraulic functions using the macropore (mobile) domain parameters, and utilizes information on matrix (immobile) domain for quantifying the inter-domain mass transfer. The DPM approach uses two different hydraulic functions, one for each domain, for describing flow through the column. The DPM approach uses two different hydraulic functions, one for each domain, for describing flow through the column. Exchange between the matrix and

macropore domains is established through a first- or second- order coupling term. A summarized description of the continuum scale flow and transport models is given below.

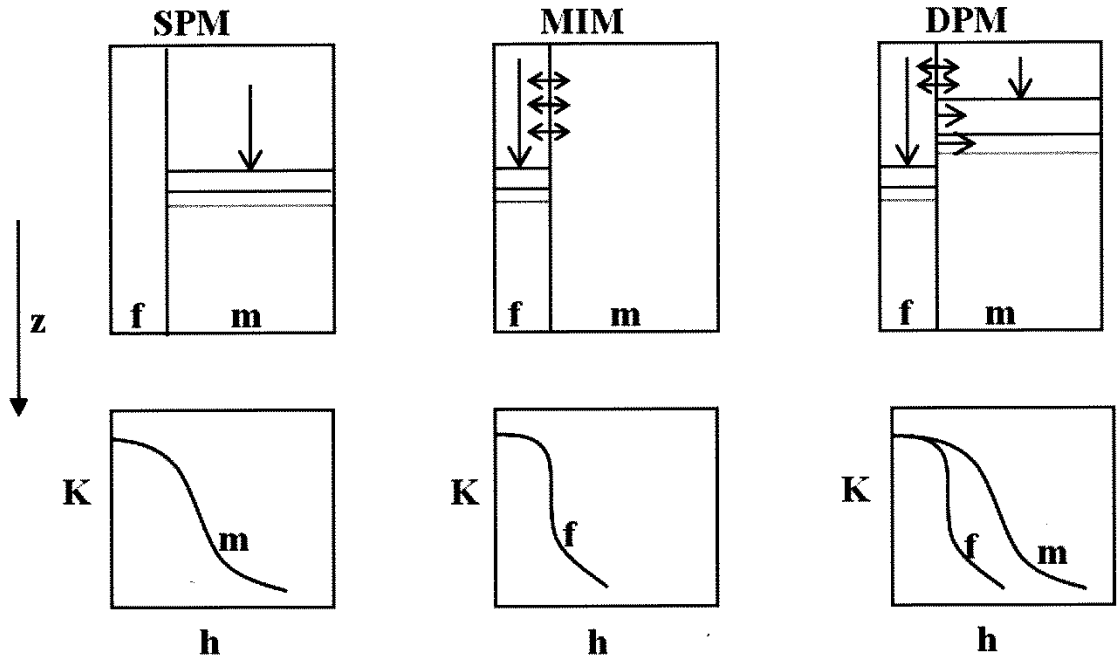

Figure 2.1: Schematic representation of the single-porosity model (SPM), mobile immobile model (MIM), and dual permeability model (DPM) along with their corresponding water retention characteristic curves. Symbols: *z*, depth coordinate; *f*, fracture/macropore or mobile domain; *m*, matrix or immobile domain; *K*, hydraulic conductivity; *h*, pressure head.

2.3.1 Single porosity model, SPM

In the one-dimensional single porosity model, Richards' equation (2.1) is used for describing variably-saturated flow and CDE (2.2) for modeling solute transport:

$$\frac{\partial \theta}{\partial t} = \frac{\partial}{\partial z}\left[K(h)\left(\frac{\partial h}{\partial z} + 1 \right) \right] - S \tag{2.1}$$

$$\frac{\partial \theta c}{\partial t} + \frac{\partial \rho s}{\partial t} = \frac{\partial}{\partial z}\left(\theta D \frac{\partial c}{\partial z} \right) - \frac{\partial qc}{\partial z} - \mu(\theta c + \rho s) + \gamma\theta + \gamma\rho \tag{2.2}$$

where t is time [T], z is the vertical coordinate positive upwards [L], θ is the water content [L^3L^{-3}], h is the pressure head [L], K is the unsaturated hydraulic conductivity [LT^{-1}], S is a sink term, c and s are solute concentrations in the liquid [ML^{-3}] and solid phases [MM^{-1}], respectively, ρ is the soil bulk density [ML^{-3}], q is the volumetric flux density [LT^{-1}], μ is a first-order rate constant [T^{-1}], γ is a zero-order rate constant [$ML^{-3}T^{-1}$], and D is the dispersion coefficient [L^2T^{-1}]. This formulation allows single porosity model to describe flow and transport that is uniform and at local equilibrium [*Šimůnek et al.*, 2003; *Köhne et al.*, 2009].

2.3.2 Mobile immobile model, MIM

Richards' equation is used to simulate mobile water, and a source/sink term is used to account for water exchange with the soil matrix (immobile region) [*Šimůnek et al.*, 2001; *Köhne et al.*, 2006a]:

$$\frac{\partial \theta_m}{\partial t} = \frac{\partial}{\partial z}\left[K(h_m)\left(\frac{\partial h_m}{\partial z} + 1 \right) \right] - \Gamma_w^{MIM} \tag{2.3}$$

$$\frac{\partial \theta_{im}}{\partial t} = \Gamma_w^{MIM} = w\left[Se^m - Se^{im} \right] \tag{2.4}$$

where Γ_w^{MIM} is the water transfer rate from mobile to immobile region [T^{-1}], w is a first-order rate coefficient [T^{-1}], and Se^m and Se^{im} are effective fluid saturations in the mobile and immobile regions, respectively. Convective-dispersive solute transport is assumed for the mobile region and analogous to water flow, first-order solute exchange process is employed between the two regions [*Šimůnek et al.*, 2003]:

$$\frac{\partial \theta_m c_m}{\partial t} + \frac{\partial \rho_m s_m}{\partial t} = \frac{\partial}{\partial z}\left(\theta_m D_m \frac{\partial c_m}{\partial z} \right) - \frac{\partial q_m c_m}{\partial z} - \mu \theta_m c_m - \Gamma_s^{MIM} \tag{2.5}$$

$$\frac{\partial \theta_{im} c_{im}}{\partial t} + \frac{\partial \rho_{im} s_{im}}{\partial t} = -\mu \theta_{im} c_{im} + \Gamma_s^{MIM} \tag{2.6}$$

$$\Gamma_s^{MIM} = w_s (c_m - c_{im}) + \Gamma_w^{MIM} c^* \tag{2.7}$$

where Γ_s^{MIM} is the solute transfer rate between the two regions [$ML^{-3}T^{-1}$], w_s is the constant first-order diffusive solute mass transfer coefficient [T^{-1}], and c^* is equal to c_m for $\Gamma_w^{MIM} > 0$ and c_{im} for $\Gamma_w^{MIM} < 0$.

2.3.3 Dual permeability model, DPM

In the dual permeability model, water flow in both macropore (subscript *f*) and matrix (subscript *m*) domains is described by two coupled Richards' equations [*Gerke and van Genuchten*, 1993a]:

$$\frac{\partial \theta_f}{\partial t} = \frac{\partial}{\partial z}\left[K_f(h_f)\left(\frac{\partial h_f}{\partial z} + 1 \right) \right] - \frac{\Gamma_w}{w_f} \tag{2.8}$$

$$\frac{\partial \theta_m}{\partial t} = \frac{\partial}{\partial z}\left[K_m(h_m)\left(\frac{\partial h_m}{\partial z} + 1 \right) \right] + \frac{\Gamma_w}{1 - w_f} \tag{2.9}$$

where w_f is the dimensionless volume factor defined as the ratio of the macropore domain volume (V_f) relative to the total soil volume (V_t):

$$w_f = \frac{V_f}{V_t} \tag{2.10}$$

Γ_w is the rate of water exchange between the two domains [T^{-1}] described with first-order mass transfer for DPM1 as:

$$\Gamma_w^{DPM1} = \alpha_w \left(h_f - h_m\right) \tag{2.11}$$

in which α_w is a first-order mass transfer coefficient for water [$L^{-1}T^{-1}$] given by:

$$\alpha_w = \frac{\beta}{a^2} K_a \gamma_w \tag{2.12}$$

where β is a dimensionless geometry-dependent shape factor, a is the characteristic length of the aggregate (L) (i.e., radius of the cylindrical aggregate for the single macropore column, and half-width diffusion length between the macropores and the soil matrix for the multiple macropore columns), K_a is the hydraulic conductivity of the fracture/matrix interface region [LT^{-1}], and γ_w is a dimensionless scaling factor. Since fracture coatings were absent for artificial macropores in this study, K_a was evaluated as follows:

$$K_a = 0.5\left(K_f(h_f) + K_m(h_m)\right) \tag{2.13}$$

DPM with a second order term (DPM2) for inter-domain mass transfer of water was also considered [*Köhne et al.*, 2004]:

$$\Gamma_w^{DPM2} = \frac{\beta K_a}{2a^2} \frac{\left(h_f - h_m\right)\left[\left|h_m - h_i\right| - \left|h_f - h_i\right|\right]}{\left|h_m - h_i\right|} \tag{2.14}$$

where h_i is the initial pressure head assumed to be equal for matrix and macropore [L]. For DPM2, K_a is evaluated as:

$$K_a = \frac{pK_m(h_m) + K_m(h_f)}{p+1} \tag{2.15}$$

where p is a weighting factor for which an average value of 17 was found to be suitable for a range of hydraulic properties and initial conditions [*Köhne et al.*, 2004]. For both DPM1 and DPM2, geometrical parameters can be derived according to *Gerke and van Genuchten* [1996] as:

$$\beta = \frac{1}{[0.19\ln(16\varsigma)]^2} \qquad 1<\varsigma<100 \tag{2.16}$$

$$\text{with } \varsigma = \frac{a+b}{b} \tag{2.17}$$

where b is the radius of the cylindrical macropore [L].

Transport of non-reactive solutes in DPM is described by two coupled convection-dispersion equations:

$$\frac{\partial}{\partial t}(\theta_f c_f) = \frac{\partial}{\partial z}\left(\theta_f D_f \frac{\partial c_f}{\partial z} - q_f c_f\right) + \frac{\Gamma_s^{DPM}}{w_f} \tag{2.18}$$

$$\frac{\partial}{\partial t}(\theta_m c_m) = \frac{\partial}{\partial z}\left(\theta_m D_m \frac{\partial c_m}{\partial z} - q_m c_m\right) + \frac{\Gamma_s^{DPM}}{1-w_f} \tag{2.19}$$

where Γ_s^{DPM} is the solute mass transfer term [T^{-1}] given by:

$$\Gamma_s^{DPM} = \alpha(1-w_f)(c_f - c_m) + \begin{cases} \Gamma_w^{DPM} c_f, \Gamma_w^{DPM} \geq 0 \\ \Gamma_w^{DPM} c_m, \Gamma_w^{DPM} < 0 \end{cases} \tag{2.20}$$

in which α is a first-order solute transfer coefficient of the form

$$\alpha_s = \frac{\beta}{a^2} D_a(\theta) \tag{2.21}$$

in which D_a is an effective diffusion coefficient [L^2T^{-1}] that is obtained analogous to K_a (equation 2.13).

2.4 Experimental setup

2.4.1 Multiple macropore columns

Soil column setup used in this study has been described in detail elsewhere [*Castiglione et al.*, 2003]. Only salient features of the setup are mentioned here. Two soil columns 75 cm long and 24 cm wide were constructed with 3 and 19 vertical macropores in one-half of the column cross-section and soil matrix in the other half (Figure 2.2). Soil used in the experimental setups was sandy loam (Typic Haploxeralf) with a 6% clay fraction (mostly Kaolinite). Soil packing was done using a piston compactor to attain a dry bulk density of 1.56 g/cm^3. Hollow stainless steel tubes of 1 mm diameter were used to create the macropores in one-half of the column cross-section. Designed pores with cylindrical diameter of 1 mm were characterized as macropores [*Jarvis*, 2007]. Polyacrylamide, a water soluble polymer, was used along the macropore walls to help stabilize the artificially-created pores. At the bottom of the column, 15-cm high vertical dividers were installed to form six pie-shaped chambers (Figure 2.2). These were useful in maintaining separate outflow measurements from the two-halves with and without macropores, and also for regulating bottom boundary conditions of pressure head.

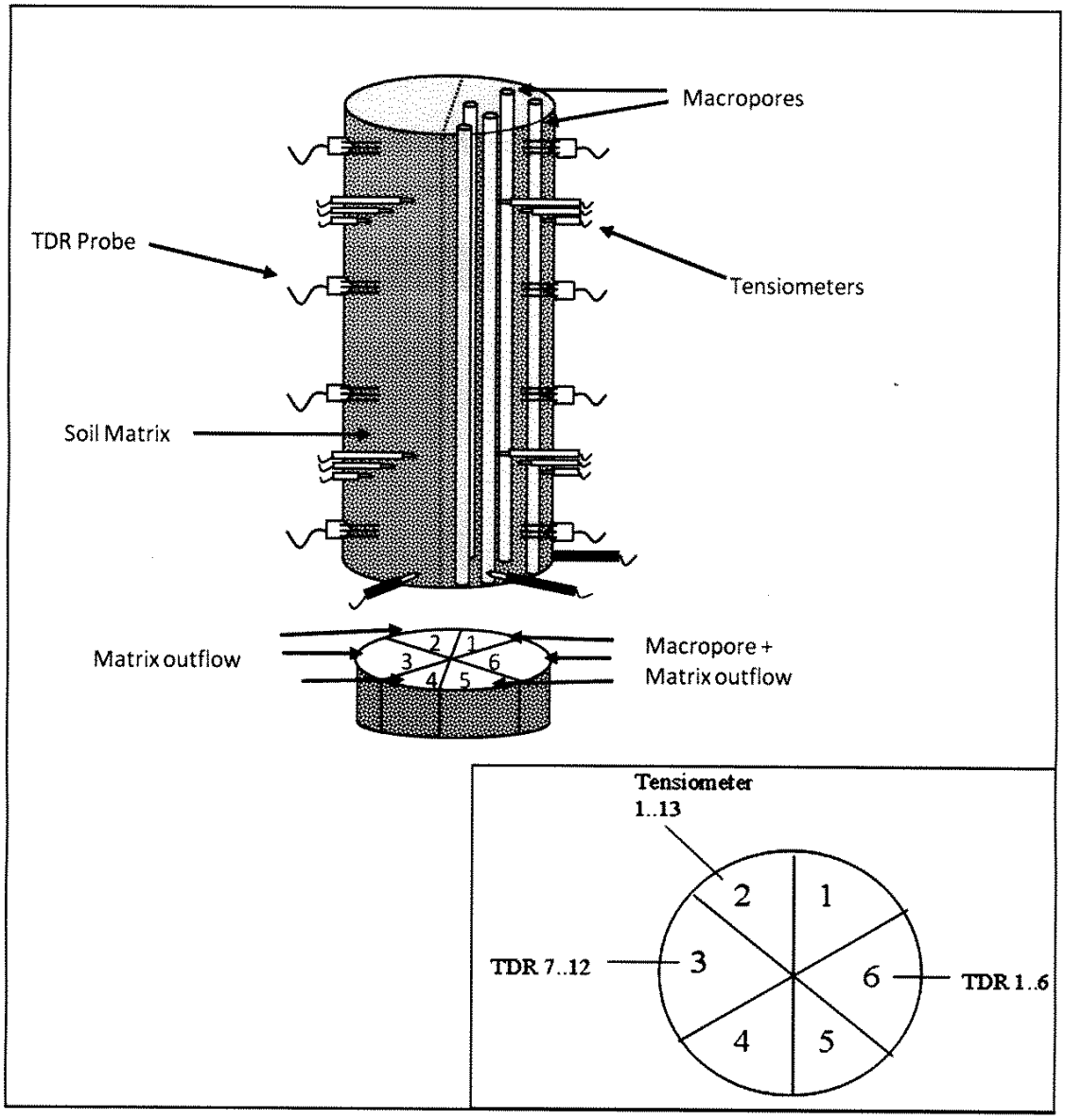

Figure 2.2: Schematic of the soil column with placement of TDRs and tensiometers in particular chambers.

Water and bromide concentrations were monitored using twelve TDR probes installed at 5, 15, 25, 35, 45 and 55 cm depths from the top of the column in both halves of the column cross-section (Figure 2.2). Mini-tensiometers were used to register matric potential in the matrix domain. Tensiometers were placed 5 cm apart in the soil matrix, with the first tensiometer close to the top of the column (Figure 2.2). Horizontal heterogeneity in pressure potential was captured by two sets of (six) tensiometers placed around the circumference of the soil column at the depths of 50 and 75 cms. These were useful in comparing pressure head profiles of the chambers with and without macropores. Analogous to these circumferential tensiometers, outflow rates and flux-averaged Br^- concentrations were measured separately for the six effluent chambers. A fraction collector was used intermittently to collect outflow from the bottom at small time intervals (5 min).

Boundary conditions (pressure heads) at the top of the soil column were maintained using a tension infiltrometer with a matching diameter disc (24 cm). Bottom boundary conditions were suction pressure heads varying between 0 and 30kPa.

2.4.2 Homogeneous and central macropore columns

Two laboratory soil columns were filled with the same sandy loam soil to create a homogeneous column and another column with a central macropore (Figure 2.3). The central macropore column was provided with a single macropore of 1 mm diameter. A hollow stainless steel tube of equivalent diameter (1 mm) was used for this purpose. Soil packing, installation of TDRs and tensiometers, and boundary condition monitoring were very similar to the multiple macropore columns.

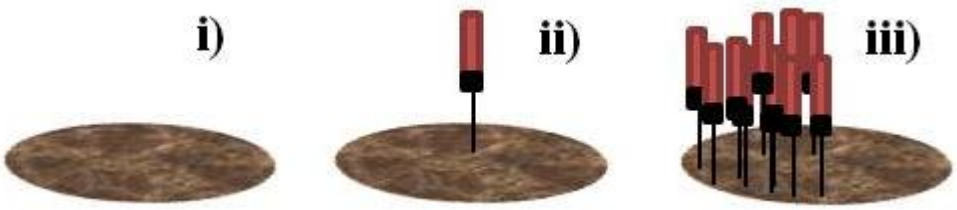

Figure 2.3: Experimental designs: (i) homogeneous soil, (ii) central macropore, and (iii) multiple macropore columns.

2.4.3 Flow and transport experiments

Infiltration and drainage experiments were performed on all four experimental columns, the homogeneous soil, central macropore, and low (3) and high (19) density multiple macropore columns. For all infiltration experiments, variability in pressure head profiles was approximately between -210 cm at the top to -42 cm at the bottom of the column at the start of the experiment (Table 2.1). Observations at all 13 tensiometer locations in the soil were used to describe initial conditions at depth layers of 0-5, 5-10, 10-15, 15-20, 20-25, 25-30, 30-35, 35-40, 40-45, 45-50, 50-55, 55-60 and 60-75 cms in the soil column. Drainage experiments were conducted by initially saturating the columns from the bottom. Upper and lower boundary conditions for infiltration and drainage experiments were set according to the transient flow conditions of the experiments (Table 2.1). Tracer transport studies using potassium bromide solution were conducted only on the high density macropore column with 19 macropores, while initial bromide concentration in the column was considered to be zero.

Table 2.1: Initial and boundary conditions as specified at the soil surface ($z=L$) and bottom of the soil profile ($z=0$) for different experiments of the soil columns*.

Columns	Experiment	Initial Condition**	Upper BC	Lower BC
Homogeneous soil column	Infiltration	h(L, 0) = -119 cm h(d, 0) = h_0(d) h(0, 0) = -42 cm	h(L, t) = 0	q(0, t) = 0, if h(0, t) < 0 h(0, t) = 0, else#.
	Infiltration	h(L, 0) = -155 cm h(d, 0) = h_0(d) h(0, 0) = -139 cm	h(L, t) = 6.5cm	q(0, t) = 0, if h(0, t) < 0 h(0, t) = 0, else#.
	Drainage	h(L, 0) = 0.9 cm h(d, 0) = h_0(d) h(0, 0) = 68.6 cm	q(L, t) = 0	q(0, t) = 0, if h(0, t) < 0 h(0, t) = 0, else#.
Central Macropore column	Infiltration	h(L, 0) = -186 cm h(d, 0) = h_0(d) h(0, 0) = -133 cm	h(L,0) < h(L, t_r) < h(L, T)## h(L, t_r) = -186 cm,..,2 cm	h(0,0) < h(0, t_r) < h(0, T) h(0, t_r) = -133 cm,…,-49 cm
Low density macropore column	Infiltration	h(L, 0) = -209 cm h(d, 0) = h_0(d) h(0, 0) = -168 cm	h(L,0) < h(L, t_r) < h(L, T)## h(L, t_r) = -209 cm,..,7 cm	h(0,0) < h(0, t_r) < h(0, T) h(0, t_r) = -168 cm,…,-1 cm
High density macropore column	Infiltration	h(L, 0) = -114 cm h(d, 0) = h_0(d) h(0, 0) = -45 cm	h(L,0) < h(L, t_r) < h(L, T)## h(L, t_r) = -114 cm,..,-17 cm	h(0,0) < h(0, t_r) < h(0, T) h(0, t_r) = -45 cm,…,23.5 cm
	Drainage	h(L, 0) = -9 cm h(d, 0) = h_0(d) h(0, 0) = 51 cm	h(L,0) < h(L, t_r) < h(L, T)## h(L, t_r) = -9 cm,..,-195 cm	h(0,0) < h(0, t_r) < h(0, T) h(0, t_r) = 51 cm,…,-185 cm

* Symbols: *h*, pressure head; *q*, flux; *z*, vertical coordinate positive upwards; *L*, column length; *t*, time; *T*, duration of the experiment.

** Equilibrium profile with *h* values linearly interpolated for depths between 0 and *d*, where *d* represents the tensiometer location.

These conditions represent a seepage face boundary condition [*Šimůnek et al.*, 1998].

Variable boundary condition with h values linearly interpolated for time between 0 and t_r, where t_r represents the time of tensiometer reading.

2.5 Modeling framework

2.5.1 Simulation models

Hydrus-1D [*Šimůnek et al.*, 2001, 2003] was used for all simulations. Single porosity model (SPM), mobile-immobile model (MIM) and dual-permeability model with first (DPM1) and second (DPM2) order water transfer functions were used to simulate flow and tracer transport experiments of the central and multiple macropore columns. Among these, infiltration and drainage experiments were described by fitting the numerical solution of Richards' equation. The hydraulic conductivity function $K(h)$, which is required to solve the Richards equation, is described using a set of closed-form equations [*Mualem*, 1976; *van Genuchten*, 1980]:

$$K_d(h) = Ks_d \left(\frac{\theta(h) - \theta r_d}{\theta s_d - \theta r_d} \right) \left\{ 1 - \left[1 - \left(\frac{\theta(h) - \theta r_d}{\theta s_d - \theta r_d} \right)^{\frac{1}{m_d}} \right]^{m_d} \right\}^2 \tag{2.22}$$

$$\theta_d(h) = \theta r + \frac{\theta s_d - \theta r_d}{\left[1 + \left| \alpha_d h \right|^{n_d} \right]^{m_d}} \tag{2.23}$$

$$m_d = 1 - \frac{1}{n_d} \tag{2.24}$$

where d represents the matrix (m) or fracture (f) domains, $\theta(h)$ is the measured volumetric water content [L^3L^{-3}] at the suction h [L] that is taken positive for increasing suctions. The parameters θr and θs are the residual and saturated water contents [L^3L^{-3}], respectively, Ks is the saturated hydraulic conductivity [LT^{-1}], α [L^{-1}], n [-], m [-], and l [-] are empirical parameters determining the shape of the hydraulic conductivity

functions. In particular, α [L^{-1}] is related to the inverse of the air entry suction, n [-] is a measure of the pore-size distribution, and l [-] reflects pore discontinuity and tortuosity of the flow path.

Tracer transport was described using CDE in the dominant pore regions as realized in Hydrus-1D for the specific conceptual model. For tracer transport simulations, bromide concentrations at all depths were normalized with respect to initially applied concentrations.

2.5.2 Model parameterization

To reduce the number of fitting parameters, some parameter values were fixed. Matrix and macropore tortuosity parameters were fixed at 0.5 [*Mualem*, 1976; *van Genuchten*, 1980; *Köhne et al.*, 2002]. Some of the matrix-macropore interface parameters (w_f, β, and a) for the central and multiple macropore columns were based on their geometry (e.g. for the high density macropore column, a = 1.89 cm, b = 0.05 cm, ς = 38.8, β = 0.67, w_f = 3.3 x 10^{-4} based on equations 2.10, 2.16 and 2.17). The γ_w value was fixed at 0.001 on the basis of soil mantle radii and estimated saturated hydraulic conductivity for the macropore domain [*Castiglione et al.*, 2003]. Bromide diffusion coefficient was calculated as 1.797 cm^2/d [*Atkins*, 1990]. The rest of the model parameters were inversely estimated.

Observations of matrix pressure head at 3 tensiometer locations, and water content in both matrix and macropore domains at 2 TDR depths were the minimum data used for inverse analysis of water flow experiments. Bromide transport experiment of the 19 (high density) macropore column utilized additional information on Br^-

concentrations at a minimum of 3 depths for inverse modeling. A spatial discretization of 0.5 cm was adopted for all flow and transport modeling. An initial time-step of 10^{-5} h, and minimum and maximum time steps of 10^{-6} and 0.24 h were employed for both one- and two- domain model simulations.

The inverse parameter estimation was performed by Levenberg-Marquardt minimization of the objective function φ [*Šimůnek et al.*, 1999]:

$$\phi(b) = \sum_{j=1}^{m} v_j \sum_{i=1}^{n} w_{i,j} \left[O_j(x,t_i) - E_j(x,t_i,b) \right]^2 \qquad (2.25)$$

where m is the total number of measurements, n is the number of observations in a particular measurement set, $O_j(x, t_i)$ is the observation at time i for the j^{th} measurement set at location x, $E_j(x, t_i, \boldsymbol{b})$ are the corresponding estimated space-time variables for the vector $\boldsymbol{b}$ of optimized van Genuchten (1980) parameters, and v_j and $w_{i,j}$ are weighting factors associated with a particular measurement set or point, respectively. In this study, $w_{i,j}$ are set equal to one assuming similar error variances within a particular measurement set. Only data that are measured at larger time intervals and are under-represented with respect to more frequent measurements require larger weights $w_{i,j}$. v_j is calculated for each simulation as [*Clausnitzer and Hopmans*, 1995]:

$$v_j = \frac{1}{n_j \sigma_j^2} \qquad (2.26)$$

which assumes that v_j is inversely related to the variance σ_j^2 within the j^{th} measurement set and to the number of measurements n_j within the set.

2.5.3 Modeling strategy

Comparison of continuum-scale models and evaluation of inversely modeled parameters was done in the following manner. Inverse simulations were first performed with the homogeneous soil column to extract matrix-specific parameters. Then, keeping the matrix parameters fixed, macropore parameters were derived through inverse analysis of the experimental data of the central macropore column. To evaluate the suitability of these domain-specific parameters, forward simulations were performed with variably-saturated flow and transport experiments of the low and high density multiple macropore columns. Dual permeability framework was used for inverse estimation of effective parameters from central macropore column and evaluation of multiple macropore columns.

For comparison among continuum-scale models (SPM, MIM, DPM1, DPM2), inversely-estimated soil hydraulic parameters were employed. Separate adjustments of parameters for each model were not done to prevent bias in comparison as fine-tuning of parameters would have enhanced agreement between predictions and observations.

2.5.4 Goodness-of-fit criteria

Apart from graphical analysis, two statistical parameters were used for direct comparison between models and for evaluating best fit of parameters in inverse analysis. Modified coefficient of efficiency (E) and the mean absolute error (MAE) were used to obtain relative and absolute error estimates, respectively:

$$E = 1.0 - \frac{\sum_{i=1}^{N}\left[\left|O_j(x,t_i) - E_j(x,t_i,b)\right|\right]}{\sum_{i=1}^{N}\left[\left|O_j(x,t_i) - \overline{O}\right|\right]} \tag{2.27}$$

$$MAE = \frac{\sum_{i=1}^{N}\left[\left|O_j(x,t_i) - E_j(x,t_i,b)\right|\right]}{N} \tag{2.28}$$

where N is the total number of time-steps, and E is a normalized measure varying between minus infinity to 1.0. An E value = 1.0 indicates perfect agreement between model and data, an E value = 0 indicates that the model is statistically as good as the observation mean in predicting the data, and an E value <0.0 indicates an altogether questionable choice of model. E is a more conservative and reliable statistical measure and is less sensitive to extreme values as compared to commonly used goodness-of-fit measures such as the coefficient of determination (R^2) [*Legates and McCabe*, 1999]. In addition, an absolute error measure like the *MAE* carries the same units as the observations and is able to better assess the magnitude of deviation. A lower *MAE* and E>0.5 typically signify better agreement between modeled and observed values.

2.6 Results and discussion

2.6.1 Inverse estimation of matrix and macropore parameters

Experimental observations and predictions of inverse modeling on flow experiments of the homogeneous soil column are documented briefly (Figure 2.4). Figure 2.4 illustrates simulated and observed pressure head and water content profiles of the soil column for the respective duration of the experiments.

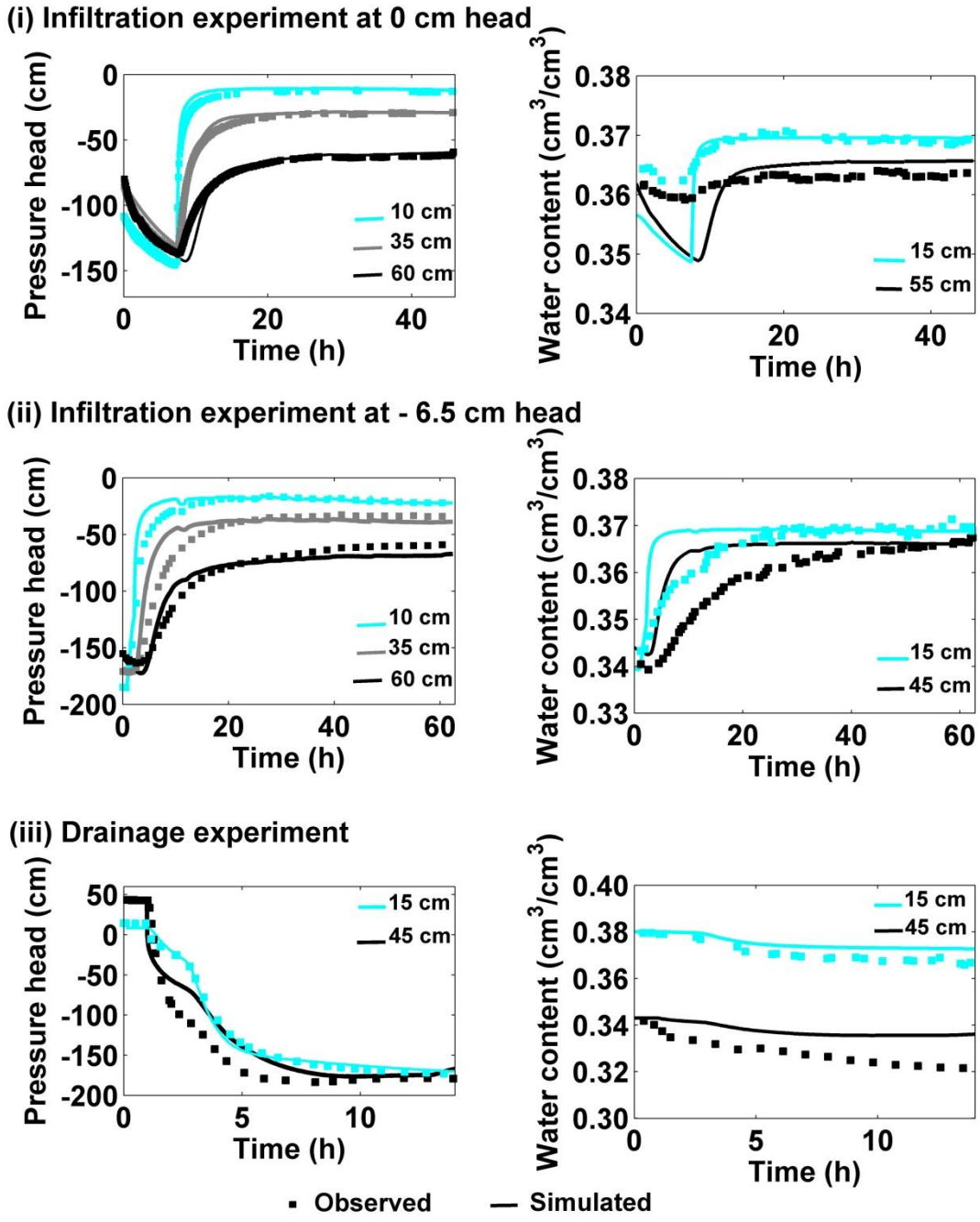

Figure 2.4: Simulated and observed pressure head and water content profiles for one drainage and two different infiltration experiments of the homogeneous soil column.

Table 2.2: Effective soil hydraulic parameters and corresponding (±) 95% confidence limits for low and high density macropore columns obtained from inverse modeling of homogeneous and single macropore soil columns.

Column type			**3 macropore Low density**	**19 macropore High density**	**95% confidence limits**
Soil		Units			
Matrix parameters (Obtained from homogeneous soil column)	θr_m	-	0.2	0.2	± 0.029
	θs_m	-	0.38	0.38	± 0.005
	α_m	cm^{-1}	0.004	0.004	± 0.003
	n_m	-	1.8	1.8	± 0.326
	Ks_m	$cm.h^{-1}$	0.13	0.13	± 1.998
	l_m	-	0.5	0.5	-
Macropore parameters (Obtained from single macropore column)	θr_m	-	0.078	0.078	± 0.066
	θs_m	-	0.39	0.39	± 0.001
	α_m	cm^{-1}	0.01	0.01	± 0.001
	n_m	-	2	2	± 0.354
	Ks_m	$cm.h^{-1}$	8.265	8.265	± 0.001
	l_m	-	0.5	0.5	-
Interface parameters (Obtained from geometry)	w_f	-	5.2×10^{-5}	3.3×10^{-4}	-
	β	-	0.54	0.67	-
	γ_w	-	0.001	0.001	-
	a	cm	4.85	1.89	-
Interface parameters (Obtained from single macropore column)	K_a	$cm.h^{-1}$	4.174 (0.26*)	4.174 (0.26*)	± 0.052

* Separately optimized value using higher weights for outflow measurements of the single macropore column.

Table 2.3: Goodness-of-fit criteria for inverse estimation of parameters from homogeneous soil and single macropore columns.

Soil column type	**Experiment**	**Modified coefficient of efficiency, *E***	**Mean absolute error, *MAE****
Homogeneous soil column	Infiltration (0 cm head)	0.765	9.050 (0.011)
	Infiltration (-6.5 cm head)	0.625	39.48 (0.227)
	Drainage	0.761	12.205 (0.022)
Single macropore column	Infiltration	0.588	14.649 (0.038)

* MAE is reported with respect to pressure head, cm.h-1 (water content, $cm^3.cm^{-3}.h^{-1}$) measurements.

One drainage and two infiltration experiments under transient flow conditions were used to infer soil hydraulic parameters of the matrix domain i.e. θr_m, θs_m, α_m, n_m, and Ks_m (Table 2.2). The estimated soil hydraulic parameters for the matrix domain were able to reproduce sufficient details of the illustrated results. For example, the two humps in the pressure head curve (0-3.5 h and 3.5-12 h) of the drainage experiment caused by pressure-controlled bottom boundary condition were sufficiently captured by the inversely-estimated parameters. Moreover, the timing of rise (or fall) of soil matric potential was adequately captured by Hydrus-1D simulations for all three experiments. Simulated water content profiles showed considerable agreement with the measured values considering the fact that TDR measurements had a large variance and received lower weight in the objective function.

Separate adjustments of parameters for simulating the wetting and drying cycles (i.e., hysteresis) in the infiltration and drainage experiments were not done in order to obtain a single set of effective matrix parameters. Moreover, parameter estimation from the three experiments qualified the judging criteria of E>0.5 and low mean absolute error (*MAE*) for both pressure head and water content measurements (Table 2.3).

These estimated matrix parameters were then fixed to determine saturated hydraulic conductivity of the matrix-macropore interface (K_a) and macropore domain parameters (θr_f, θs_f, α_f, n_f, and Ks_f) from inverse simulations of the central macropore column experiments (Table 2.2).

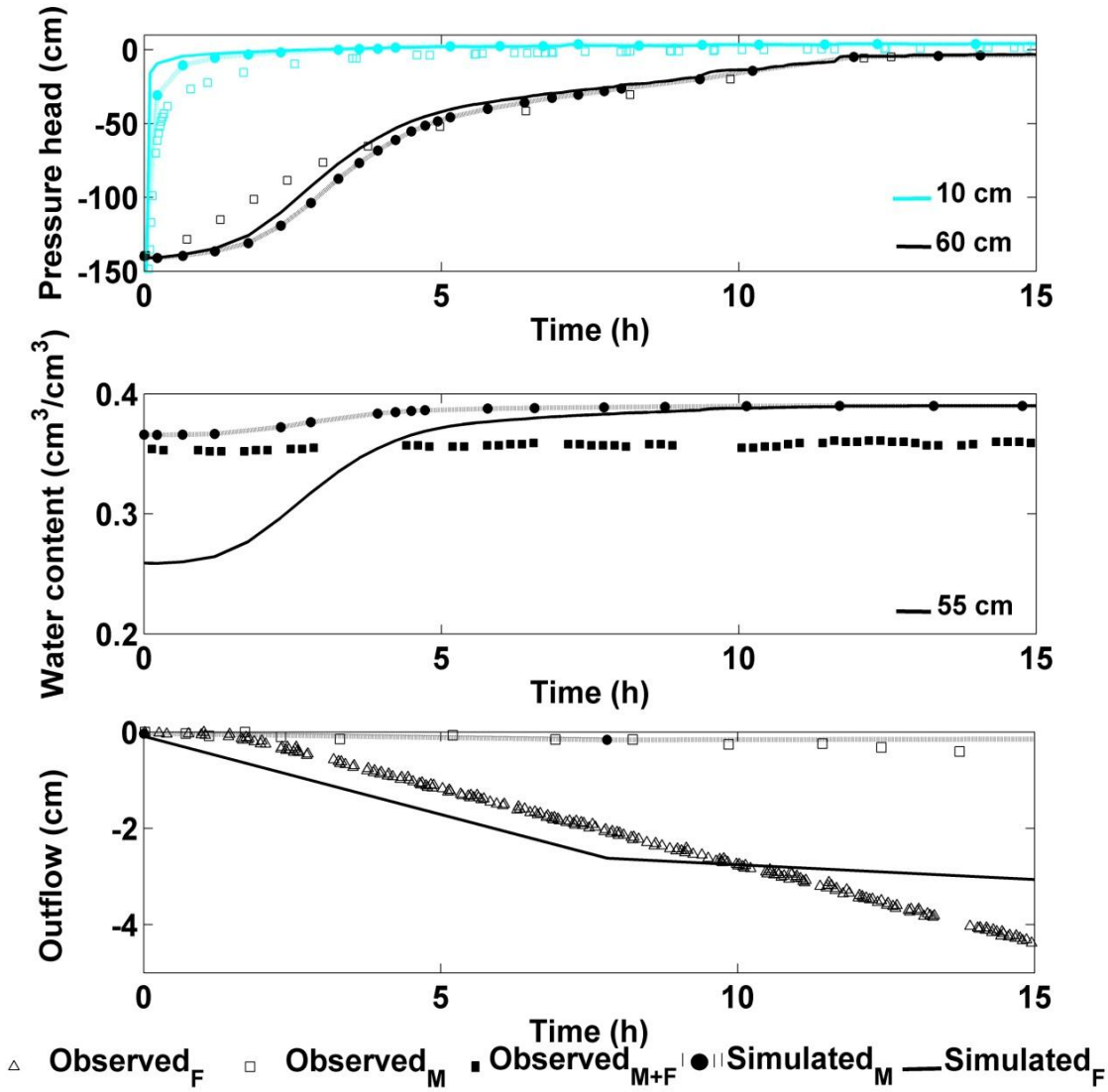

Figure 2.5: Simulated and observed pressure head, water content and outflow profiles for a transient infiltration experiment of the central macropore column. Symbols: M, matrix domain; F, fracture or macropore domain; M+F, combined matrix and macropore domains.

Figure 2.5 shows good conformity between simulated and measured pressure head, average water content, and matrix outflow profiles for a transient infiltration experiment of the central macropore column. It is worthwhile to mention that experimental observations correspond to pressure head values in the soil matrix domain, average water content values of matrix and macropore domains, and domain-specific outflow measurements. The conformity with macropore outflow is low as simulations suggest an immediate outflow while observations suggest the onset of outflow at 1.9 hours, which is reasonable considering the height of the soil column (75 cm) and the fact that the soil was initially quite dry (Table 2.1). The dual permeability model simulates flow from the macropore domain not only as a function of the flow capacity of the macropore but also as its exchange with the matrix domain. This interaction between the matrix and macropore domains is complex and influenced by soil moisture retention characteristics of the unsaturated soil matrix, initial moisture conditions in both domains, geometry of macropores, and the conducting surface area of the interface region [*Weiler*, 2005]. The effect of this exchange is also visible as the predicted decrease in macropore flow at 8 hrs when predictions for matrix outflow begin (Figure 2.5). The rapid exchange predicted between the matrix and macropore domains and lack of outflow measurements in the objective function result in this non-conformity with macropore outflow. The inverse modeling exercise was repeated again with K_a as the only fitting parameter and inclusion of outflow measurements in the objective function. A decrease in K_a from 4.17 to 0.26 $cm.h^{-1}$ produced satisfactory results for all three observations (E=0.588, MAE=14.649 $cm.h^{-1}$ for pressure head, 0.0379 $cm^3.cm\text{-}^3.h^{-1}$ for water content, and 0.465

cm.h^{-1} for outflow measurements). Note that water content in the macropore domain is predicted to be lower than in the matrix domain. This was observed for all soil depths and for other transient flow experiments as well. The reasons for this will be discussed in the next section.

The small differences observed between matrix and macropore domain results (pressure head and water content profiles) indicate that only mild physical non-equilibrium existed for the single macropore column. The derived macropore-domain and interface parameters were able to satisfactorily describe all flow experiments of the single (central) macropore column as per the goodness-of-fit criteria (Table 2.3).

2.6.2 Evaluation of inversely estimated soil hydraulic parameters

Multiple macropore columns with 3 and 19 macropores were used to evaluate the accuracy of the derived domain-specific (matrix and macropore) and interface (K_a) parameters. As per Table 2.2, interface parameters based on macropore geometry (w_f, β, and a) were the only three variables different for the two multiple macropore (high density and low density) columns. The rest of the parameters were based on consistent values for matrix (θr_m, θs_m, α_m, n_m, and Ks_m), macropore (θr_f, θs_f, α_f, n_f, and Ks_f) and interface (K_a = 0.26 cm.h^{-1}) regions obtained from inverse modeling of the homogeneous and single macropore columns, as described above. Forward modeling using modified Hydrus-1D was done for a transient infiltration experiment of the low density macropore column. Matrix outflow and average water content measurements of the matrix and macropore domains for the simulated experiment agree well with the corresponding observations (Figure 2.6). Again, conformity with macropore outflow observations was

found to be low and could be improved by separately fitting K_a (3.91 ± 1.001) and including outflow measurements in the objective function. Instead of separate adjustments to this parameter, the simultaneously fitted value of 4.17 cm.h^{-1} from the single macropore column was adopted to maintain consistency in our inverse estimation procedure (Table 2.3).

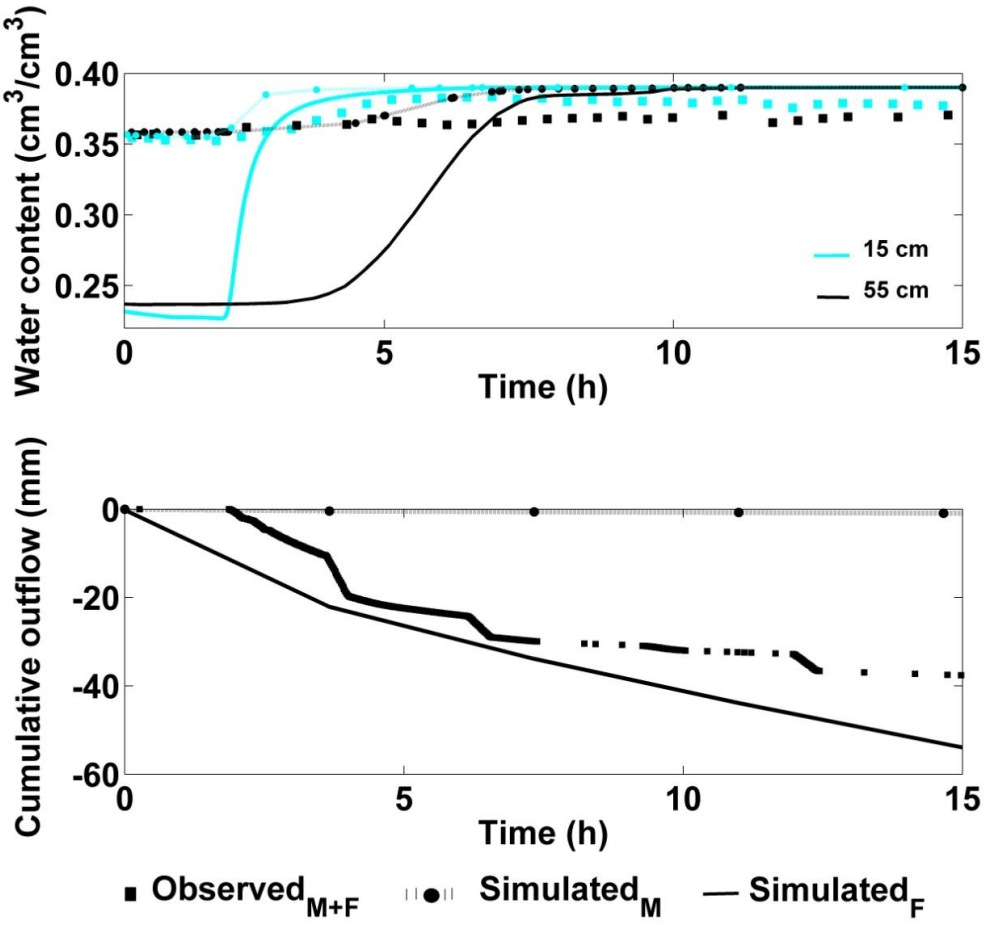

Figure 2.6: Simulated and observed water content at 15 and 55 cm depths and cumulative outflow of the low density macropore column. Symbols: M, matrix domain; F, fracture or macropore domain; M+F, combined matrix and macropore domains.

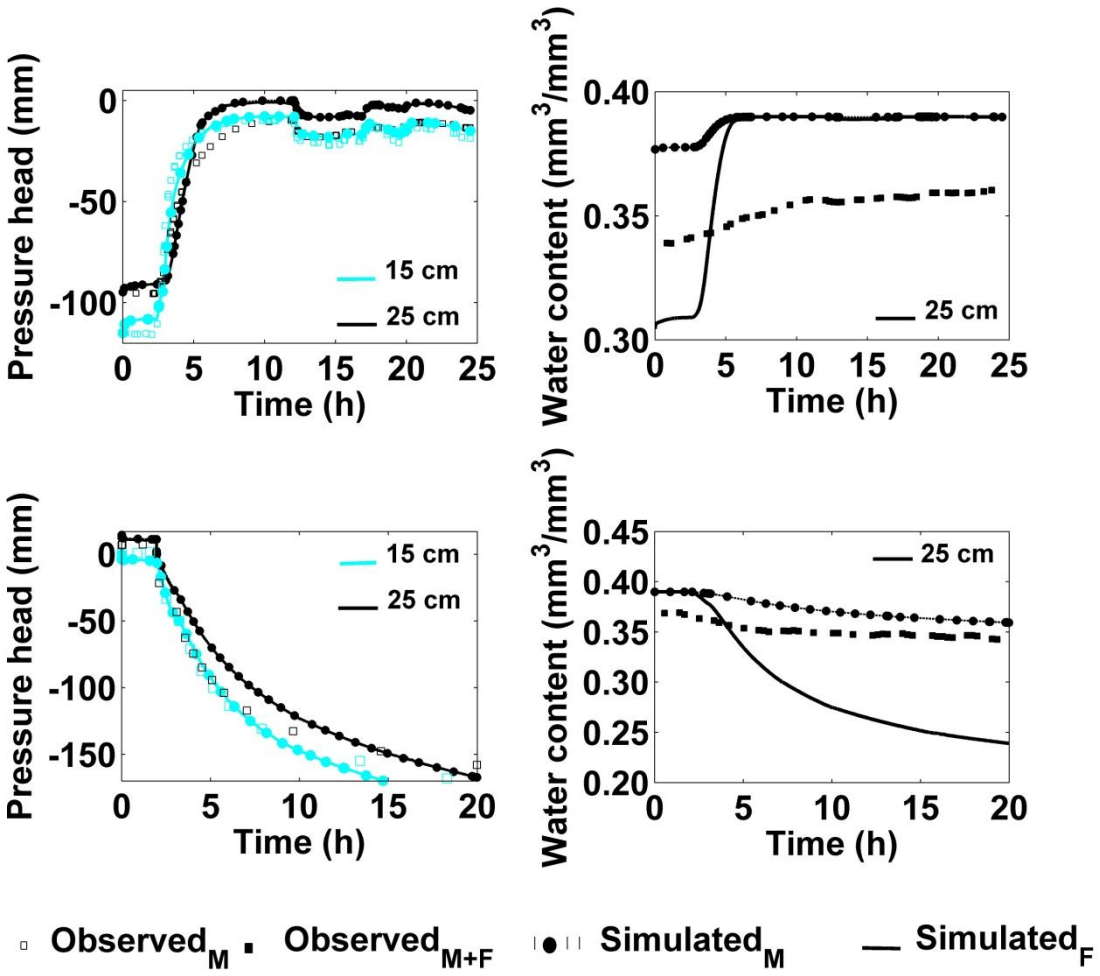

Figure 2.7: Simulated and observed pressure head and water content values for infiltration and drainage of the high density macropore column. Symbols: M, matrix domain; F, fracture or macropore domain; M+F, combined matrix and macropore domains.

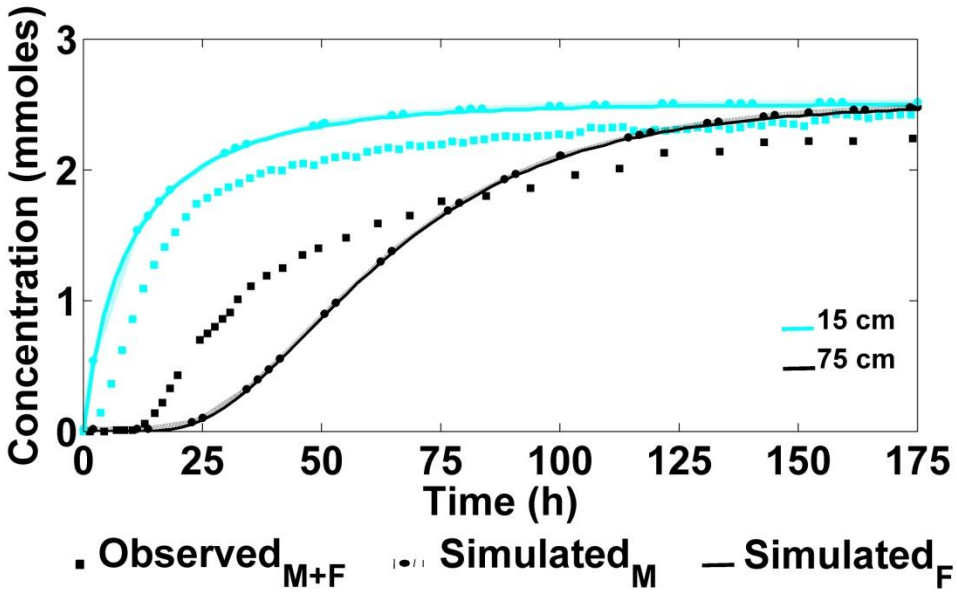

Figure 2.8: Simulated and observed bromide concentration values for a solute transport experiment of the high density macropore column. Symbols: M, matrix domain; F, fracture or macropore domain; M+F, combined matrix and macropore domains.

For the high density macropore column, infiltration, drainage and bromide tracer experiments were conducted to test the performance of the estimated set of domain-specific (matrix and macropore) and interface (K_a= 4.17 cm.h^{-1}) parameters (Figures 2.7 and 2.8). The agreement between pressure head profiles decreased with depth for both infiltration and drainage experiments. It is possible that in the multiple macropore column the lateral water transfer rate needs to be adjusted to better explain the mismatch between higher predictions and lower observations of pressure head in the lower depths of the soil column. Incorrect quantification of lateral water transfer is also the reason for lower water content predictions in the macropore domain as compared to the soil matrix. Observations of lower water transfers (e.g. due to clogging of pores, soil aggregate coatings, etc.) between the fracture and matrix domains have been reported in various

experimental settings [*Gerke and Köhne*, 2004; *Kodešová et al.*, 2008]. This could be a result of clogging of pores as observed in certain experiments of the single macropore column [*Castiglione et al.*, 2003] or simply for maintaining the continuity of pressure potential across the large number of laterally distributed macropores of the multiple macropore columns. Nevertheless, the domain-specific parameters were able to effectively capture the trend in pressure head profiles at all depths during forward simulations of the two transient flow experiments (Figure 2.7). Unlike pressure head profiles, the rise in bromide concentrations was not suitably captured even at shallow depths (Figure 2.8). The matching criteria attributed good performance to inversely-estimated parameters for flow in both the low and high density multiple macropore columns but not to bromide transport (E=-16.777) in the high density macropore column (Table 2.4). Separate adjustments to K_a produced unsatisfactory match to tracer concentration data. It is noteworthy, however, that bromide transport experiment was well explained with changes in only the saturated hydraulic conductivity of the matrix domain (Ks_m) (i.e., from 0.13 to 0.40 cm/h). The increment in Ks is well explained by *Freeze* [1975] who reports that saturated hydraulic conductivity is likely a function of the boundary conditions and soil structure and macropore geometry in case of statistically heterogeneous soils. In our study, structural heterogeneity arises from the use of domain-specific parameters of the homogeneous and single macropore columns on multiple macropore columns with different densities and distributions of macropore. It should be stated up front that we do not consider the changes in Ks_m as calibration of the model based on observed data, but rather as an evaluation of desired variability in

parameters in order to account for increase in macropore density. Since saturated hydraulic conductivity produces the most sensitivity to preferential flow results and has an important bearing on contaminant transport [*Zhang et al.*, 2006], it is feasible that only this parameter required evaluation through inverse modeling.

Table 2.4: Goodness-of-fit criteria for estimated parameters of the multiple macropore columns.

Soil column type	**Experiment**	**Modified coefficient of efficiency, *E***	**Mean absolute error, *MAE****
Low density macropore column	Infiltration	0.686	24.327 (12.029)
High density macropore column	Infiltration	0.899	7.236 (0.039)
	Drainage	0.806	7.019 (0.044)
	Bromide transport (before inverse solution)	-16.777	8.968[#]
	Bromide transport (after inverse solution)	0. 662	0.164[#]

* MAE is reported with respect to pressure head, cm.h-1 (water content, $cm^3.cm^{-3}.h^{-1}$) measurements.
[#] MAE corresponds to bromide concentration, $mmoles.h^{-1}$.

Table 2.5: Correlation between inversely-estimated soil hydraulic parameters*.

Soil column	Experiment	Soil hydraulic parameters						
			θr	θs	α	n	Ks	K_a
Homogeneous soil column	Infiltration† (0 cm head)	θr_m	1					
		θs_m	0.0	1				
		α_m	0.0	0.0	1			
		n_m	0.0	0.0	0.0	1		
		Ks_m	0.0	0.0	0.0	0.0	1	
	Infiltration (6.5 cm head)	θr_m	1					
		θs_m	-0.060	1				
		α_m	0.324	-0.031	1			
		n_m	-0.568	-0.022	<u>0.948</u>	1		
		Ks_m	-0.722	0.057	0.668	0.716	1	
	Drainage	θr_m	1					
		θs_m	-0.383	1				
		α_m	0.382	<u>-0.995</u>	1			
		n_m	-0.016	-0.101	0.101	1		
		Ks_m	-0.489	0.386	-0.384	0.002	1	
Single macropore column#	Infiltration	θr_f	1					
		θs_f	-0.275	1				
		α_f	0.498	-0.293	1			
		n_f	0.406	-0.362	<u>0.925</u>	1		
		Ks_f	-0.235	0.267	-0.272	-0.571	1	
		K_a	0.345	-0.042	-0.255	-0.028	-0.295	1

* Underline indicates high correlation with $|r|>0.75$.

† The correlations for this experiment were of the order of 10^{-15}.

The soil hydraulic parameters for this column represent the macropore domain.

2.6.3 Parameter identification and uniqueness

Problems of non-uniqueness, identifiability, and ill-posedness are often encountered when dealing with simultaneous estimation of soil hydraulic parameters using inverse modeling. To test the uniqueness of the inverse method, i) examination of parameter correlations was conducted, ii) confidence intervals were evaluated for each parameter, and iii) parameter estimation was done using combinations of different starting values for all soil hydraulic parameters.

For the homogeneous soil column, one transient infiltration experiment revealed high correlation ($|r|>0.75$) between α_m and n_m, and the other no correlation, while the drainage experiment revealed high correlation between α_m and θs_m parameters (Table 2.5). Since α_m was the common parameter and had low confidence interval (Table 2.2), all three simulations were repeated with this parameter initialized at ±30% of its originally optimized value. Several combinations of α_m (±30%) with θs_m and n_m fixed at originally optimized values and at different starting values were carried out. The final optimized parameters were either the same or within the confidence intervals of their original values (Table 2.2). As an example, with lower α_m (-30%) values, the final optimized parameters (the original values are given in parentheses) are given as: θr_m = 0.2 (0.2), θs_m = 0.4 (0.38)**,** α_m = 0.003 (0.004), n_m = 1.8 (1.8), and Ks_m = 0.10 (0.13). Table 2.5 further suggests a high correlation between α_f and n_f parameters using inverse modeling of the single macropore column indicating that their simultaneous estimation did not yield unique results. Independent estimation of these parameters would yield lower uncertainty and better results. We fixed α_f at 0.33 based on capillary bundle theory

for a single macropore of 1 mm which did not produce satisfactory match of the data (E = -1.007, MAE = 104.968 cm.h^{-1} for pressure head and 0.348 cm^3.cm-^{3}.h^{-1} for water content measurements). Mild non-equilibrium conditions observed in the single macropore column could have resulted in the existence of highly-correlated macropore domain parameters (α_f and n_f) [*Zurmuhl and Durner*, 1998]. Since all experiments produced mild non-equilibrium differences for this column, α_f and n_f were treated as fitting parameters of the van Genuchten-Mualem model and varied at ±30% of their original values. Again, the final optimized parameter values were within ±10% of their original values.

Table 2.2 suggests small confidence intervals for all soil hydraulic parameters of the matrix domain except Ks_m. One reason for high uncertainty in saturated hydraulic conductivity parameter (Ks_m) stems from establishing a best-compromise parameter set to satisfy observations of different types of experiments. The effects of hysteresis were ignored to arrive at this best set of optimized soil hydraulic parameters since both infiltration and drainage experiments were used for inverse estimation. In this regard, confidence intervals for the macropore (θr_f, θs_f, α_f, n_f, and Ks_f) and interface region (K_a) parameters were generally small, which were derived from a single infiltration experiment. Note that n_f has moderate uncertainty due to its correlation with α_f.

As suggested earlier, all inverse modeling simulations were repeated with different initial parameter values, and resulted in final values within ±10% of the original optimized values. As an example, with higher n_m (+30%) values, the final optimized parameters (the original values are given in parentheses) are given as: θr_m =

0.212 (0.2), θs_m = 0.365 (0.38)**,** α_m = 0.0044 (0.004), n_m = 1.88 (1.8), and Ks_m = 0.136 (0.13), while lower θs_f gave the following results: θr_f = 0.053 (0.08), θs_f = 0.36 (0.39)**,** α_f = 0.009 (0.01), n_f = 1.8 (2), Ks_f = 8 (8.27) , and K_a = 0.27 (0.26).

Overall, the inverse modeling approach produces acceptable representation of the data, and is suitable for estimation of most of the soil hydraulic parameters. We do believe that independent estimation of soil hydraulic parameters and adding data of the same or different types of measurement can improve inverse estimation. Note that we defined the objective function using two different sets of measurements: pressure head response and water content profiles (also bromide concentration, wherever appropriate) at different depths of the experimental soil columns. We found that addition of outflow measurements improved inverse estimation in both homogeneous soil and single macropore columns. Our analysis indicates that inverse optimization runs with simultaneous optimization of parameters consistently converged to similar parameter values, indicating uniqueness of the inverse problem. However, uncertainty in soil hydraulic parameters needs to be further evaluated to better account for preferential flow processes and lateral exchange between the two domains. This is the subject of a parallel study which compares conventional and adaptive Metropolis-Hastings algorithm in simulating correlated soil hydraulic parameters of the matrix and macropore domains and evaluates the output uncertainty associated with them.

Table 2.6: Soil hydraulic parameters of the single and multiple macropore columns used for different conceptual models (SPM, MIM and DPM).

Soil Columns	Soil hydraulic parameters	Matrix or immobile region*					Macropore or mobile region*					Inter-domain transfer				
	Model	θr	θs	α	n	Ks	θr	θs	α	n	Ks	w_f	β	γ_w	a	K_a
Single Macropore column	SPM	0.2	0.38	0.004	1.8	0.13										
	MIM	0.2	0.38				0.08	0.39	0.01	2	8.27	$1.7\text{x}10^{-5}$				
	DPM	0.2	0.38	0.004	1.8	0.13	0.08	0.39	0.01	2	8.27	$1.7\text{x}10^{-5}$	0.45	0.001	11.95	0.26
Low density macropore column	SPM	0.2	0.38	0.004	1.8	0.13										
	MIM	0.2	0.38				0.08	0.39	0.01	2	8.27	$5.2\text{x}10^{-5}$				
	DPM	0.2	0.38	0.004	1.8	0.13	0.08	0.39	0.01	2	8.27	$5.2\text{x}10^{-5}$	0.54	0.001	4.85	4.17
High density macropore column	SPM	0.2	0.38	0.004	1.8	0.13*										
	MIM	0.2	0.38				0.08	0.39	0.01	2	8.27	$3.3\text{x}10^{-4}$				
	DPM	0.2	0.38	0.004	1.8	0.13*	0.08	0.39	0.01	2	8.27	$3.3\text{x}10^{-4}$	0.67	0.001	1.89	4.17

* Tortuosity parameter l for both matrix and macropore domains is considered to be 0.5.

2.6.4 Comparison of models

The inversely-estimated parameters derived using dual permeability formulation were subsequently used for comparison between single porosity (SPM), mobile-immobile (MIM) and dual-permeability models (DPM) for simulating preferential flow and transport through the single and multiple macropore columns (Table 2.6). Note that single and higher density macropore columns differ only in the parameterization of the interface region including the fitted K_a. DPM1 and DPM2 were evaluated with similar parameters because they differ in their treatment of water transfer functions only (equations 2.12 and 2.15). Accuracy of model predictions could have been enhanced with separate parameter adjustments for each model but the aim of this analysis is to evaluate best model performances under conditions of different macropore distributions. Therefore, consistency in parameter values was maintained across different conceptual models.

2.6.5 Single macropore column

Results for experiments other than those used for inverse analysis are shown below. Figure 2.9 illustrates simulations of continuum scale models (SPM, MIM and DPM1) and observations of pressure head and water content profiles at 25 cm depth of the single macropore column for a transient infiltration experiment. Mobile immobile model (MIM) is found to overestimate both pressure head and water content profiles at the given depth as it incorporates flow through the higher-flowing domain i.e. macropore (mobile) region. Single porosity model (SPM) and matrix domain of the dual permeability model (DPM_M) give comparable results because SPM works with matrix

domain as the sole flow medium in this study. Dual permeability predictions for the matrix (DPM_M) and macropore (DPM_F) domains showed minute variations in their results given the mild non-equilibrium conditions observed in the central macropore column.

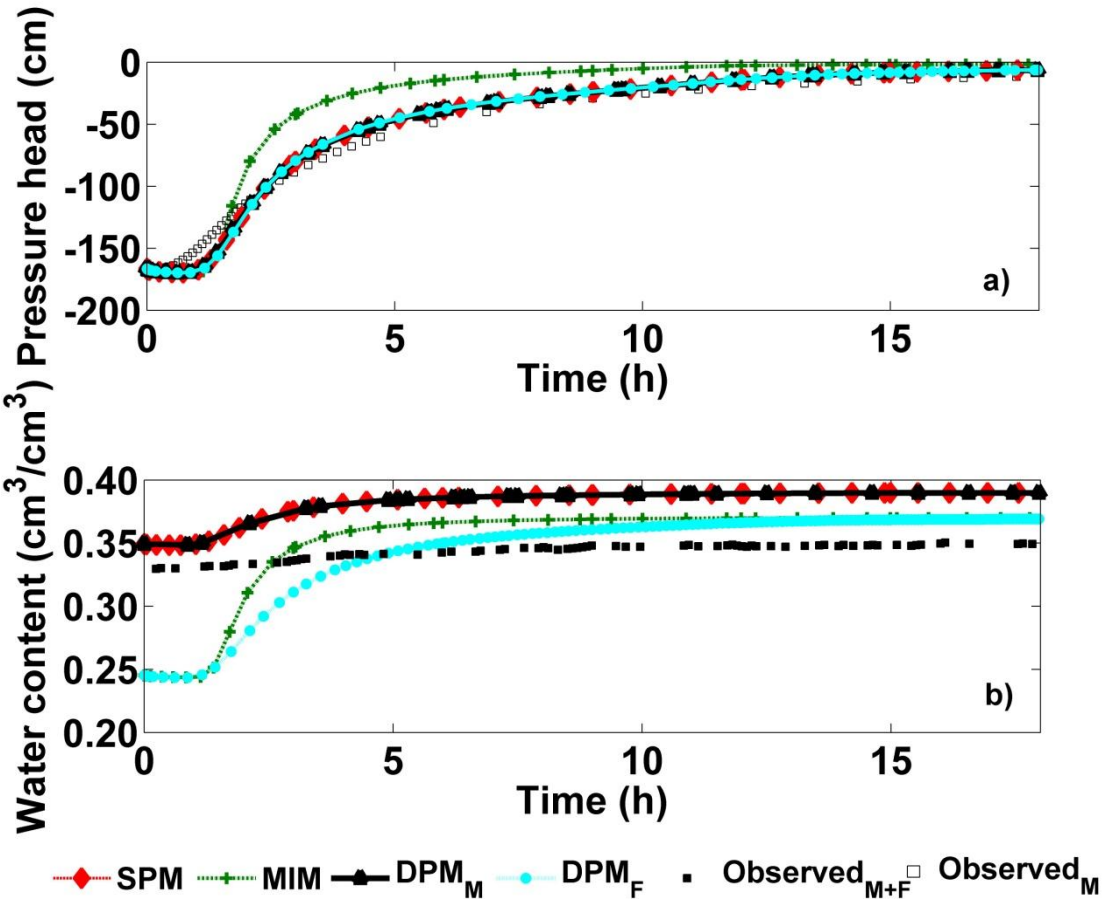

Figure 2.9: Observed and simulated results for infiltration experiment of the central macropore column: (a) pressure head and (b) water content at 25 cm depth. Symbols: M, matrix domain; F, fracture or macropore domain; M+F, combined matrix and macropore domains.

Table 2.7: Goodness-of-fit criteria for comparison of models.

Soil column		SPM		MIM		DPM	
	Experiment	*E*	*MAE* *	*E*	*MAE* *	*E*	*MAE* *
Single macropore	Infiltration	0.517	9.104 (0.036)	0.102	16.628 (0.335)	0.598	9.387 (0.028)
	Drainage	0.852	5.450 (0.017)	0.939	1.927 (0.320)	0.852	5.465 (0.017)
Low density macropore	Infiltration	0.637	24.741 (14.666)	-0.071	50.861 (0.399)	0.686	24.327 (12.029)
High density macropore	Infiltration	0.804	7.337 (0.031)	0.739	6.107 (0.373)	0.899	7.236 (0.039)
	Drainage	0.802	7.103 (0.070)	0.730	5.939 (0.306)	0.806	7.019 (0.044)
	Bromide transport#	-1.294	1.279	-2.881	1.963	0. 662	0.164

* MAE is reported with respect to pressure head, $cm.h^{-1}$ (water content, $cm^3.cm^{-3}.h^{-1}$) measurements.
# The MAE corresponds to bromide concentration, $mmoles.h^{-1}$.

Both SPM and DPM satisfied the goodness-of-fit criteria in simulating preferential flow experiments of the single macropore column (Table 2.7). The choice of MIM to simulate the infiltration experiment is questionable with our criteria of E<0.5. It seems that MIM overestimates flow from soil matrix (immobile) to the macropore (mobile) as it quantifies exchange between the two regions based on relative saturation differences (equation 2.5). According to the capillary bundle theory, flow from matrix to a macropore of size 1 mm is justified when water-entry pressure is close to -1.48 cm, which implies that the surrounding soil matrix should be close to saturation. Our initial conditions indicate that the soil matrix is quite dry (Table 2.1) when MIM predicts this exchange and this is an inherent limitation of the exchange term used in this model.

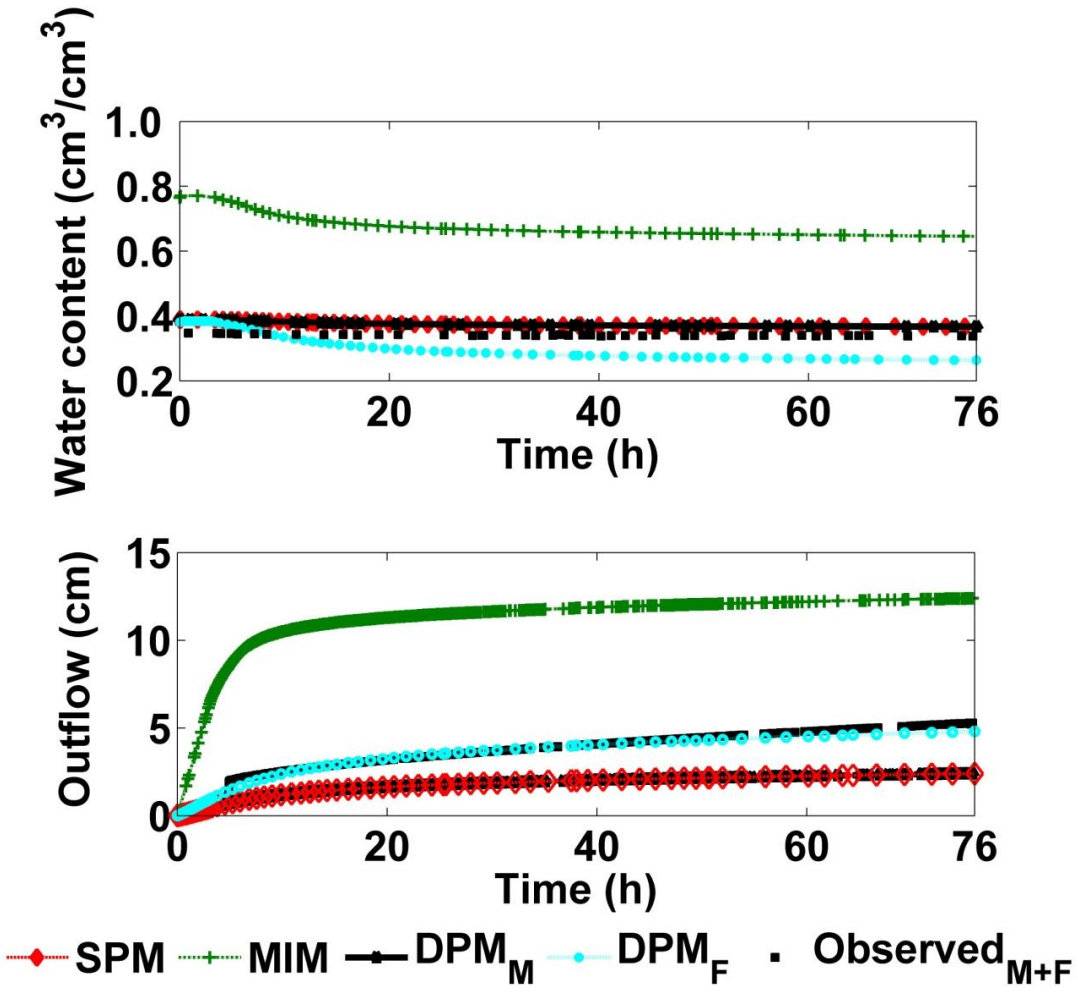

Figure 2.10: Observed and simulated results for drainage experiment of the central macropore column: a) water content at 55 cm depth, and b) outflow at 75 cm. Symbols: M, matrix domain; F, fracture or macropore domain; M+F, combined matrix and macropore domains.

On the other hand, MIM statistically outperforms SPM and DPM in simulating the drainage experiment which is reasonable as drainage occurs through the largest pore first. However, graphical interpretation suggests that average outflow measurements for the drainage experiment were described appropriately by DPM only (Figure 2.10). MIM overestimated and SPM underestimated outflow from the bottom of the soil column. DPM also gave a better match to observations of average water content profiles of the two domains for both experiments (Figures 2.9 and 2.10).

2.6.6 Multiple macropore columns

Figure 2.11 depicts pressure head results for a transient infiltration experiment of the high density multiple macropore column. The pressure head profiles at 10, 20 and 30 cms showcase equivalent results for all models. However, the trend of the pressure head profile is best captured by the dual permeability model (DPM) at all depths (see Figure 2.11 inset). Similarly, observations of average water content at all depths and outflow for a transient drainage experiment are well-described by DPM whereas mobile immobile model (MIM) over-predicts and single porosity model (SPM) under-predicts both types of observations (Figure 2.12). It is apparent that SPM and MIM act according to their parameterization of the low (matrix) and high (macropore) flowing domains, respectively while the dual permeability formulation is able to capture the trend of the pressure head, water content and outflow profiles appropriately.

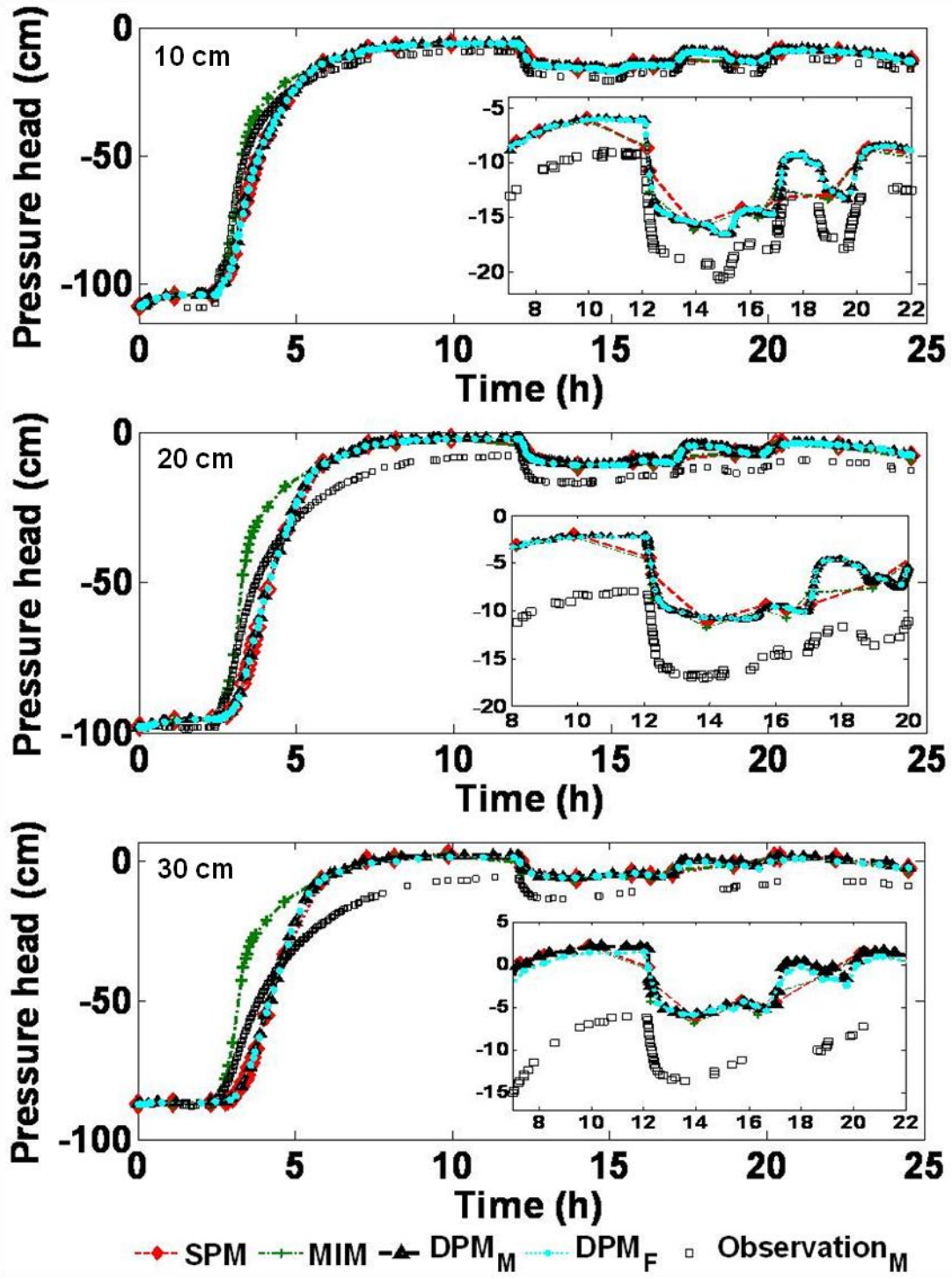

Figure 2.11: Simulated and observed pressure head profiles at 10, 20 and 30 cms for an infiltration experiment of the high density multiple macropore column. Symbols: M, matrix domain; F, fracture or macropore domain.

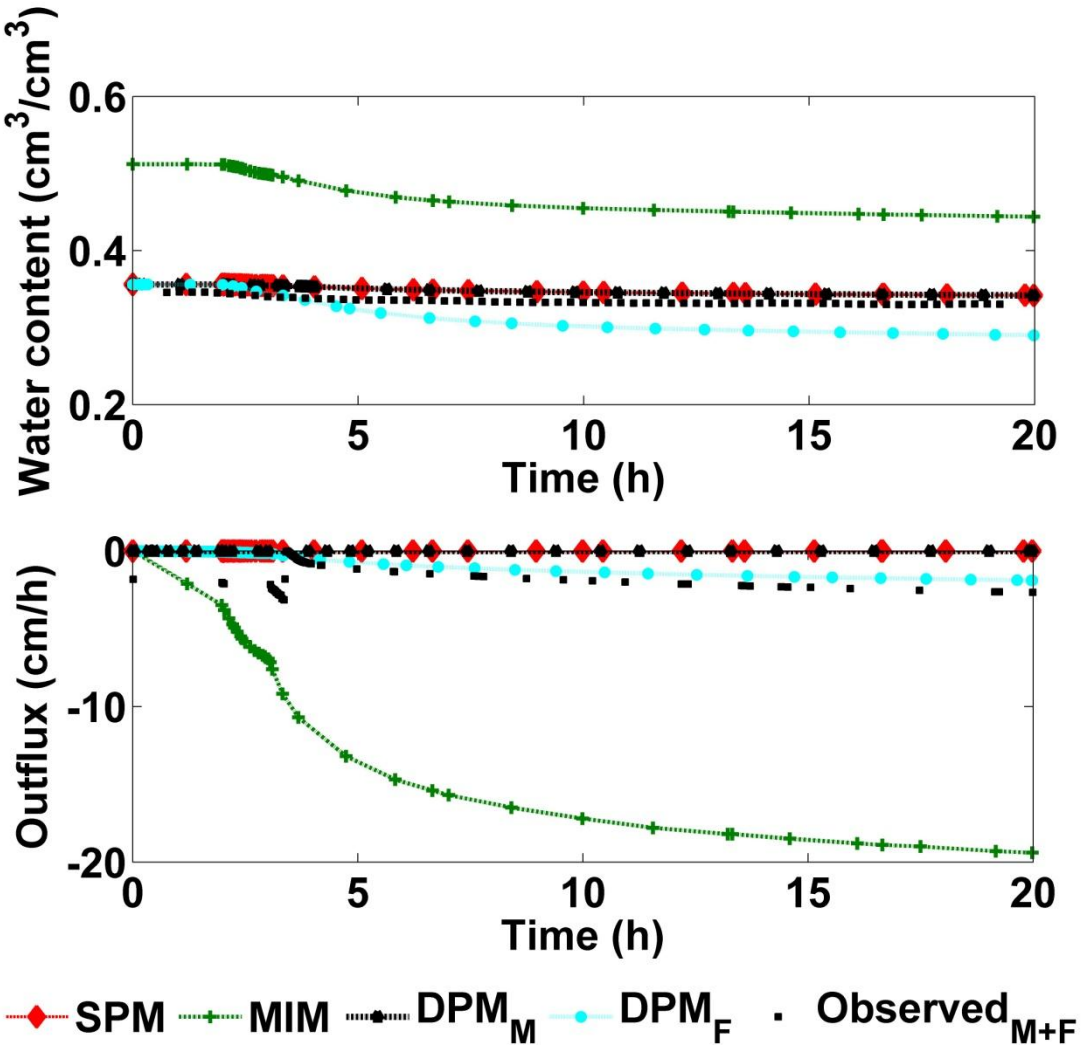

Figure 2.12: Simulated and observed water content at 5 cm and outflow for a drainage experiment of the high density multiple macropore column. Symbols: M, matrix domain; F, fracture or macropore domain; M+F, combined matrix and macropore domains.

Bromide transport experiment also validates the appropriateness of DPM in simulating preferential transport in the multiple macropore columns. Figure 2.13 shows concentration profiles at 25 and 35 cm simulated using different models with the adjusted Ks_m parameter (0.4 cm/h) instead of the effective value (0.13 cm/h). Since the adjusted Ks_m value is kept constant for all conceptual models, it does not affect our comparison of model performances. In Figure 2.13, SPM produced results close to $DPM_{M,}$ yet the rising limb of the solute concentration graph was captured by DPM only (see Figure 2.13 inset). This is important from contaminant transport perspective as knowledge about initial breakthrough is crucial in assessing groundwater vulnerability to potential contamination. SPM and MIM failed to satisfy the goodness-of-fit criteria for this experiment with E<0.0(Table 2.7).

Similar to results of the high density (19) macropore column, DPM gave better results for the experiments of the low density (3) macropore column and surpassed SPM and MIM in model performance criteria (Table 2.7). Unlike results for the single macropore column, DPM consistently performed better for all types of experiments of the multiple macropore columns (Table 2.7). Statistically, the model performance was unacceptable for MIM for the transient infiltration experiment of the low density macropore column.

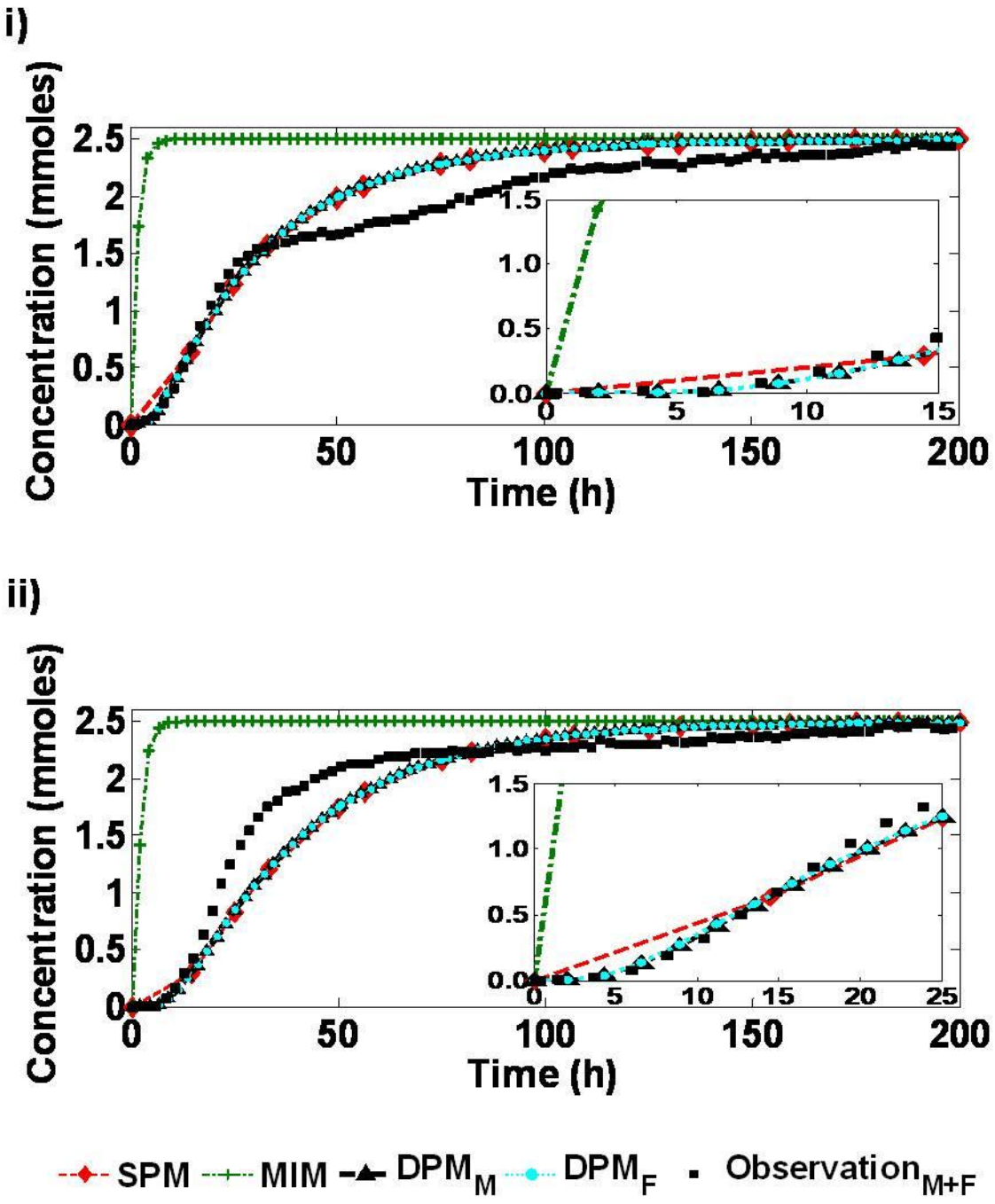

Figure 2.13: Simulated and observed bromide concentration profiles at 25 and 35 cms for a tracer transport experiment of the multiple macropore column with 19 macropores. Symbols: M, matrix domain; F, fracture or macropore domain. Symbols: M, matrix domain; F, fracture or macropore domain; M+F, combined matrix and macropore domains.

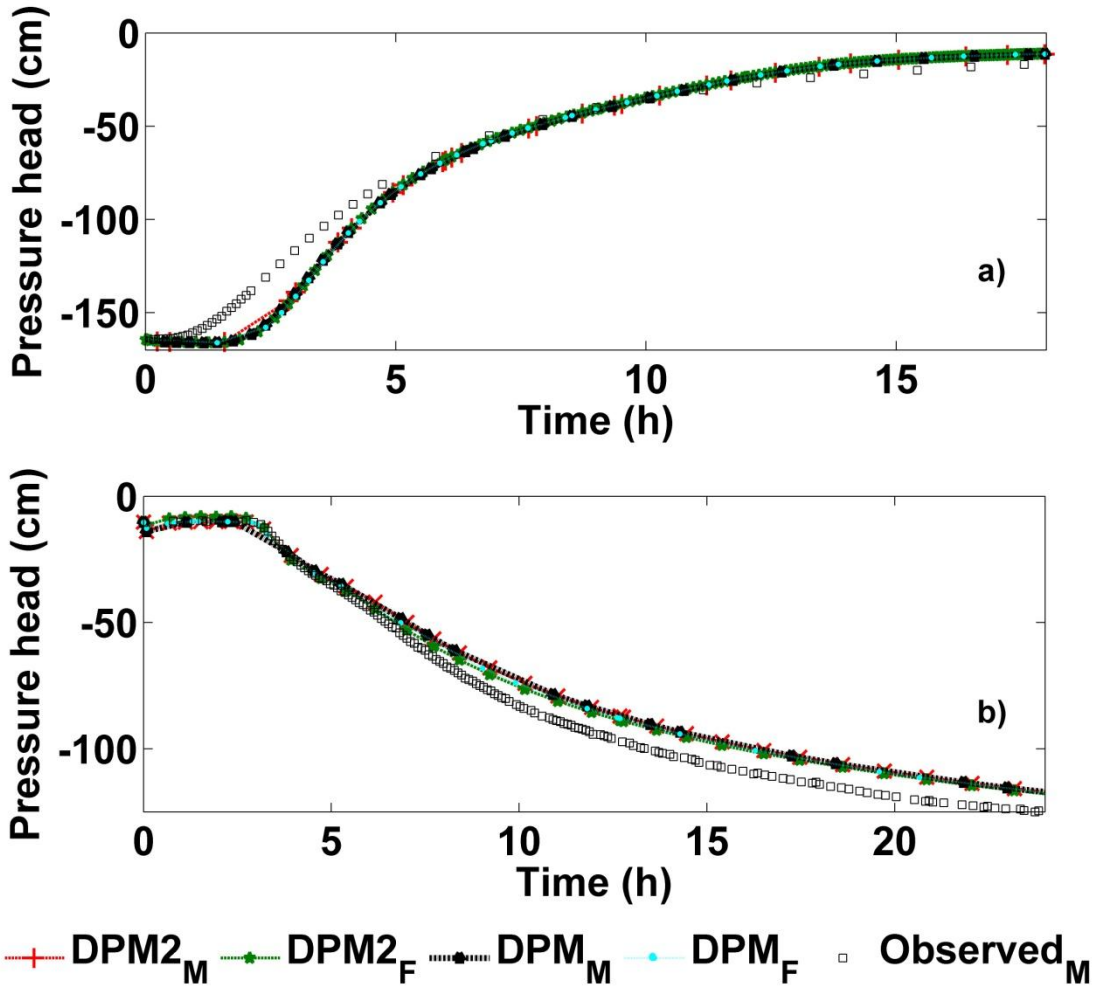

Figure 2.14: Simulated and observed pressure head profiles at 35 cm depth for a) infiltration and b) drainage experiments of the central macropore column. Symbols: M, matrix domain; F, fracture or macropore domain.

2.6.7 DPM1 versus DPM2

Comparison of DPM1 and DPM2 showed only slight variation in simulating infiltration and drainage experiments of the single and multiple macropore columns (Figures 2.14 and 2.15). According to the performance criteria, DPM1 is found to perform slightly better than DPM2 in experiments of the multiple macropore columns. It is possible that the choice of a single domain representation for 19 (3) macropores causes the models to neglect lateral transfers between individual macropores and focus more on the vertical flow through them. This error in analysis (ϵ_a) is more for DPM2 due to the second-order characteristic of the water transfer function:

$$\varepsilon_a = \Gamma_{act} - \Gamma_{sim} \tag{2.29}$$

where Γ_{act} and Γ_{sim} are the actual and simulated transfer rates [T^{-1}], respectively. The corresponding errors for DPM1 and DPM2 can be obtained from equations 2.12, 2.13 and 2.15 as:

$$\varepsilon_a^{DPM1} = \Gamma_{act} - \Gamma_{sim}^{DPM1} = \Gamma_{act} - \frac{\beta K_a \gamma_w}{a^2}\left(h_f - h_m\right) \tag{2.30}$$

$$\varepsilon_a^{DPM2} = \Gamma_{act} - \Gamma_{sim}^{DPM2} = \Gamma_{act} - \frac{\beta K_a}{a^2}\frac{\left(h_f - h_m\right)\left[\left|h_m - h_i\right| - \left|h_f - h_i\right|\right]}{\left|h_m - h_i\right|} \tag{2.31}$$

Considering the entirely similar effective parameter set for DPM1 and DPM2, and the use of lumped observations of the macropore domain, the order of the error is reduced to:

$$\varepsilon_a^{DPM1} = \varepsilon\left(h_f - h_m\right) \cong O(1) \tag{2.32}$$

$$\varepsilon_a^{DPM\,2} = \varepsilon\left(\left(h_f - h_m\right)\frac{\left[\left|h_m - h_i\right| - \left|h_f - h_i\right|\right]}{\left|h_m - h_i\right|}\right) \cong O(2) \tag{2.33}$$

The difference in performance of DPM2 is trivial when lumped datasets are used as the disparity between DPM1 and DPM2 was small to begin with (Figure 2.15). However, this substantiates the significance of using domain-specific measurements to reduce errors while using numerically efficient models and to improve predictions of preferential flow and transport.

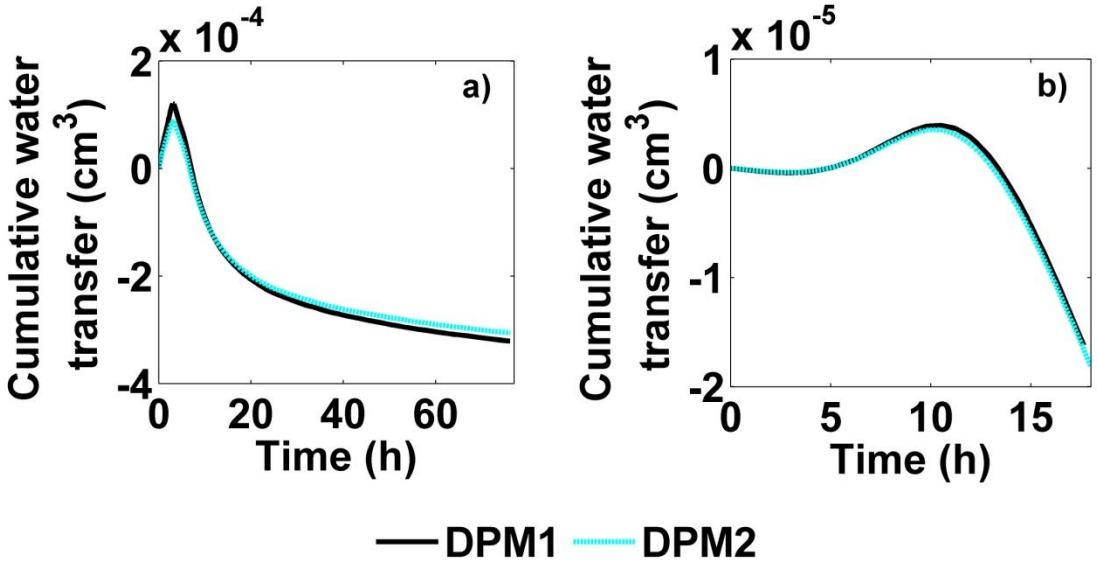

Figure 2.15: Cumulative water transfer for a) infiltration and b) drainage experiments of the high density multiple macropore column.

2.6.8 Best model performance

Proper evaluation of continuum-scale models in predicting contaminant transport under different macropore densities is important for quantifying agricultural pollution via preferential flow paths. The use of consistent matrix and macropore values instead of fitted parameters across the different conceptual models heightens the problem of choosing a superior model. For the case of single (central) macropore column, the choice of a better model between DPM and SPM for simulating infiltration and between DPM and MIM for simulating drainage remains open primarily because of the mild non-equilibrium conditions observed in this column. Judging from statistical criteria, DPM has a consistently better fit in both the low and high density multiple macropore columns than in case of the single macropore column (Table 2.7). This is especially true for the bromide transport experiment where SPM and MIM failed to satisfy the goodness-of-fit criteria. The predictive performance of DPM is reflected in its superiority in simulating average water content profiles at different depths, outflow from the bottom, and in reproducing temporal patterns of pressure head and bromide breakthrough from the high density multiple macropore column. This suggests that the density of the macropore is important in determining the complexity of the model employed. As we move from the central macropore column with a single macropore (1 mm diameter) to the multiple macropore columns with 3 (low density) and 19 (high density) macropores of similar size, a continuum-scale model with higher complexity is essential in accurately predicting preferential water and bromide transport.

2.7 Limitations of the study

Despite the comprehensive dataset and advanced conceptual models used in this study, it is limited in the sense that this study does not evaluate the effect of using objective functions with different formulations and weightings on parameterizing the conceptual models or in quantifying preferential flow from the experimental data. Several studies have shown that the choice of objective functions can alter parameter estimates, parameter uncertainty bounds, and predictive capabilities of the model [*Vrugt et al.*, 2003; *Schoups and Vrugt*, 2010]. Our results containing objective functions with and without outflow measurements also suggest that different combinations of objective functions could lead to improvement in hydrologic predictions. We believe that evaluating uncertainty and assessing its effect on parameters and predictions will improve the scope of the current study. These concerns are addressed in the next chapter.

2.8 Conclusions

This study evaluates whether transport behavior of the macropores is a function of its density, and examines the variability required (if any) in soil hydraulic parameters to account for changes in macropore density. This has serious implications for agricultural soils where crop and management activities such as mechanized farming, irrigation scheduling, crop rooting characteristics, earthworm activity, etc. change macropore density at various times during a season and affect leaching of agrochemicals via preferential flow paths. For this study, domain-specific soil hydraulic parameters were inversely estimated from designed soil columns of representative flow domains (homogeneous and central macropore) and were used for predicting preferential flow

under different macropore distributions (single, low and high density macropore columns) and transient flow conditions. Results indicate that inversely estimated parameters are successful in describing preferential flow but not tracer transport in both types (low and high density) of multiple macropore columns. Preferential bromide transport for the high density macropore column could be predicted with adjustments in saturated hydraulic conductivity of the matrix domain (Ks_m) only. Saturated hydraulic conductivity is likely a function of the boundary conditions and soil geometry in case of statistically heterogeneous soils [*Freeze*, 1975]. In this study, structural heterogeneity stems from the use of consistent domain-specific parameters of the homogeneous and central macropore columns on low and high density multiple macropore columns. The variation in one soil hydraulic parameter (Ks_m) is expected on account of increase in macropore density from single macropore column to multiple macropore columns. Other studies have indicated lower saturated hydraulic conductivities and mismatch with predictions due to the presence of a large number of closely-spaced macropores [*Ahuja et al.*, 1995; *Kramers et al.*, 2005]. We believe that this refinement in inversely estimated Ks_m is required to account for lateral exchange between matrix and macropore domains as a result of high density of macropores and to accurately quantify preferential transport in such soils. Also, proper description of this lateral exchange process using soil hydraulic parameters was found to be crucial in correctly representing outflow from the macropore domain for all macropore columns. Future studies are needed to evaluate the specific contribution and sensitivity of the different soil hydraulic parameters to this interaction.

A performance evaluation of continuum-scale models including single porosity (SPM), mobile immobile (MIM), and dual permeability model (DPM) with first and second-order between-domain water transfer functions that employed these inversely estimated matrix and macropore parameters is also conducted. Judging from statistical criteria, dual permeability model was able to successfully reproduce the preferential flow characteristics of the single and multiple macropore columns in a deterministic framework. Further evaluation suggests that it was able to predict the initial rise (or fall) of pressure head and bromide concentration for the different experiments of the columns which bears significance in early predictions of contaminant transport and prevention of potential contamination. Intercomparison of models indicates that increasing model complexity from SPM, MIM, to DPM improves the description of preferential flow phenomenon in the multiple macropore columns but not in the central macropore column. This suggests that the use of a more complex model is recommended with increase in macropore density to accurately capture all the dynamics of the system including depth profiles, temporal trends and breakthrough curves.

Including lumped observations of pressure head, water content, cumulative outflow and effluent concentration for the matrix and macropore domains into the objective function of DPM2 enhanced errors in model parameters due to the second-order characteristic of the water transfer function. This suggests that domain-specific measurements should be used and macropore density should be accounted for to reduce errors when using numerically efficient models.

CHAPTER III

UNCERTAINTY IN DUAL PERMEABILITY MODEL PARAMETERS FOR STRUCTURED SOILS*

3.1 Synopsis

The difficulty in unique identification of parameters for the additional macropore and matrix-macropore interface regions, and knowledge about requisite experimental data for DPM has not been resolved to date. Therefore, this study quantifies uncertainty in dual permeability model parameters of experimental soil columns with different macropore distributions (single macropore, and low- and high-density multiple macropores). Uncertainty evaluation is conducted using adaptive Markov Chain Monte Carlo (AMCMC) and conventional Metropolis-Hastings (MH) algorithms while assuming 10 out of 17 parameters to be uncertain or random. Results indicate that AMCMC resolves parameter correlations and exhibits fast convergence for all DPM parameters while MH displays large posterior correlations for various parameters. This study demonstrates that the choice of parameter sampling algorithms is paramount in obtaining unique DPM parameters when information on covariance structure is lacking, or else additional information on parameter correlations must be supplied to resolve the problem of equifinality of DPM parameters.

---

*Reprinted with permission from "Uncertainty in dual permeability model parameters for structured soils" by Arora, B., B. P. Mohanty, and J. T. McGuire (2012), *Water Resour. Res.*, *48*, W01524, doi: 1029/2011WR010500, Copyright 2012 American Geophysical Union.

This study also highlights the placement and significance of matrix-macropore interface in flow experiments of soil columns with different macropore densities. Histograms for certain soil hydraulic parameters display tri-modal characteristics implying that macropores are drained first followed by the interface region and then by pores of the matrix domain in drainage experiments. Results indicate that hydraulic properties and behavior of the matrix-macropore interface is not only a function of saturated hydraulic conductivity of the macropore-matrix interface (K_a) and macropore tortuosity (l_f) but also of other parameters of the matrix and macropore domains

3.2 Introduction

Reliable predictions of flow and transport in the vadose zone are important to address the issue of potential contamination of groundwater and deterioration of water quality. Various studies have reported faster transport of fertilizers, pesticides, industrial chemicals, and pathogens to groundwater through fractures and preferential flow paths [*National Research Council*, 1994; *Mohanty et al.*, 1997, 1998; *Kladivko et al.*, 2001; *Böhlke*, 2002; *Jamieson et al.*, 2002]. Preferential flow phenomenon can be described using a variety of single, dual or multiple porosity/permeability models [*Gwo et al.*, 1995; *Šimůnek and van Genuchten*, 2008]. The classical dual permeability approach assumes the soil to be containing two interacting domains, one associated with the fast flowing fracture or macropore domain and the other with the less permeable soil matrix domain [*van Genuchten and Wierenga*, 1976; *Gerke and van Genuchten*, 1993a, 1993b]. Dual permeability model formulations differ in their description of flow through the macropore domain and in their characterization of exchange between the two regions

[*Jarvis*, 1994; *Šimůnek et al.*, 2003; *Köhne et al.*, 2004]. Both types of dual permeability models (DPM) are widely applied at column, plot and field scales [*Larsbo et al.*, 2005; *Köhne and Mohanty*, 2005; *Köhne et al.*, 2009]. The main disadvantage of DPM is the requirement of a large number of input parameters. Parameters associated with additional pore regions and matrix-macropore interface cannot be directly estimated by independent measurements or by expert judgment [e.g., *Gwo et al.*, 1995; *Schwartz et al.*, 2000; *Roulier and Jarvis*, 2003]. Since direct estimation is not feasible, an inverse procedure is applied wherein observed data are used to obtain an optimal set of model parameters [*Zachman et al.*, 1981; *Kool and Parker*, 1988]. Inverse parameter estimation is challenging with respect to obtaining a unique parameter set, non-identifiability of the solution set, and ill-posedness of the inverse problem [*Carrera and Neumann*, 1986]. This problem is significant for the case of structured soils where interdependence and multicolinearity between dual permeability model parameters increase the risk of reaching local minima in the parameter set [*Ginn and Cushman*, 1990]. Identification of parameters is also hindered by poor measurement quality, non-optimal experimental design, and parsimonious datasets such as omitting the near-saturated stage of an outflow experiment [*Durner et al.*, 1999; *Dubus et al.*, 2002].

One response to counter the problem of parameter identification is to adopt a Bayesian viewpoint which evaluates the distribution of parameters instead of a single "best" estimate [*Vrugt et al.*, 2008]. The Bayesian approach quantifies uncertainty bands around parameter mean values and incorporates the associated uncertainty to generate better forecasts, especially for complex non-linear systems [*Wu et al.*, 2010; *Jana and*

Mohanty, 2011]. Consider a radioactive waste disposal facility, for instance, where combining single "best" estimates for the uncertain inputs will not necessarily produce the "most probable" output estimate. Most importantly, Bayesian probabilistic modeling can prove useful in identifying additional parameters of the dual permeability model, analyzing the relationship among parameters of significant domains, and quantifying uncertainty in flow and transport predictions using the dual permeability framework.

Use of Bayesian techniques in the field of preferential flow and transport is generally limited to conventional Markov Chain Monte Carlo algorithms such as Metropolis-Hastings and Gibbs sampling [*Gelman et al.*, 1995; *Cowles and Carlin*, 1996; *Marshall et al.*, 2004; *Reis and Stedinger*, 2005]. The computational efficiency of sampling the parameter space can be improved by employing an adaptive Markov Chain Monte Carlo (AMCMC) scheme that can cater to model parameters having a high degree of correlation and interdependence as is the case with the dual permeability framework [*Haario et al.*, 2001; *Atchadé and Rosenthal*, 2005]. The AMCMC scheme is compared to a conventional Metropolis-Hastings (MH) algorithm that uses a random walk in the parameter space while describing uncertainty based on preexisting (or prior) knowledge and experimental observations [*Metropolis et al.*, 1953; *Hastings*, 1970]. The algorithms differ in their updating mechanisms, the conventional MH algorithm uses a single-site (one parameter at a time) updating while the AMCMC approach uses the history of the process to 'tune' the proposal distribution and update the parameter covariance structure [*Marshall et al.*, 2004; *Peters et al.*, 2009]. The algorithms will be compared for their predictive performance in quantifying parameter and output uncertainty.

In summary, dual permeability models are paramount in predicting reliable estimates of preferential flow and contaminant transport in structured soil systems but their application is hindered by difficulties in estimating the large number of input parameters [*Simunek et al.*, 2001; *Jarvis et al.*, 2007]. The focus of this study is to estimate uncertainty in dual permeability model parameters and to investigate the stability of preferential flow estimates from experimental soil columns, especially when a large number of dual permeability parameters are considered unknown or random. The research is motivated by a realization that correlation and interdependence among parameters of the dual permeability framework cannot be described explicitly for any study for one of the following reasons: it may be unknown, known but extremely complex, or it may even be non-existent, and difficult to investigate through controlled experiments alone. This leads by default to a replacement of the uncertain parameters and unknown covariance structure with probabilistic assumptions which are compatible with Bayesian statistics. Therefore, primary objectives of this study are: i) to quantify uncertainty in dual permeability model parameters obtained from experiments of single and multiple (low- and high-density) macropore soil columns, and ii) to compare the conventional Metropolis-Hastings and adaptive Markov Chain Monte Carlo algorithms in terms of convergence rate and for quantifying uncertainty in simulating preferential flow from the experimental soil columns.

3.3 Theoretical considerations

3.3.1 Dual permeability model formulation

The dual-permeability model of *Gerke and van Genuchten* [1993a, 1993b] is used in this study. Conceptually, the model assumes the porous medium to be divided into two pore regions, with relatively fast water flow in one region (often called the inter-aggregate, macropore, or fracture domain) when close to full saturation, and slow in the other region (often referred to as the intra-aggregate, micropore, or matrix domain) [*Šimůnek and van Genuchten*, 2008]. Flow in both macropore (subscript *f*) and matrix (subscript *m*) domains is described using two Richards' equations primarily with different sets of water retention and hydraulic conductivity functions:

$$\frac{\partial \theta_f}{\partial t} = \frac{\partial}{\partial z}\left(K_f \frac{\partial h_f}{\partial z} + K_f \right) - \frac{\Gamma_w}{w_f} \tag{3.1}$$

$$\frac{\partial \theta_m}{\partial t} = \frac{\partial}{\partial z}\left(K_m \frac{\partial h_m}{\partial z} + K_m \right) - \frac{\Gamma_w}{1 - w_f} \tag{3.2}$$

where z is the vertical coordinate positive upwards [L], t is time [T], h is the pressure head [L], θ is the water content [L^3L^{-3}], K is the unsaturated hydraulic conductivity [LT^{-1}], w_f is the ratio of the volumes of the macropore domain and the total soil system [dimensionless], and Γ_w is the rate of water exchange between the two domains [T^{-1}]. A detailed description of the w_f and Γ_w formulation is given in the previous chapter (§ 2.3.3). Hence, it is not repeated here.

The soil water retention and hydraulic conductivity functions can be described using the equations [*Mualem*, 1976; *van Genuchten*, 1980]:

$$\theta_d(h) = \theta r_d + (\theta s_d - \theta r_d)\left[1 + (\alpha_d h)^{n_d}\right]^{-m_d} \tag{3.3}$$

$$K_d(h) = Ks_d \frac{\left\{1 - (\alpha_d h)^{m_d n_d}\left[1 + (\alpha_d h)^{n_d}\right]^{-m_d}\right\}^2}{\left[1 + \{\alpha_d h\}^{n_d}\right]^{l_d m_d}} \tag{3.4}$$

$$m_d = 1 - \frac{1}{n_d} \tag{3.5}$$

where subscript d represents the matrix (m) or fracture (f) domains, θr and θs are the residual and saturated water contents [L^3L^{-3}], respectively, Ks is the saturated hydraulic conductivity [LT^{-1}], α [L^{-1}], n [-], m [-], and l [-] are empirical parameters determining the shape of the hydraulic conductivity functions.

3.3.2 Description of Bayesian methods

Bayesian methods provide a statistical framework for obtaining an improved estimate of parameter distributions by mathematically combining specific prior knowledge with what is known about those parameters through observations. To facilitate the description of the Bayesian analysis, we represent the soil hydrologic system in a Bayes' framework:

$$p(\boldsymbol{\Theta} \mid \mathbf{D}) = \frac{f(\mathbf{D} \mid \boldsymbol{\Theta})\pi(\boldsymbol{\Theta})}{\pi(\mathbf{D})} \tag{3.6}$$

where $\mathbf{D}$ is the observed data, $p(\boldsymbol{\Theta}|\mathbf{D})$ is the conditional posterior probability of the soil hydraulic parameters given the data, $f(\mathbf{D}|\boldsymbol{\Theta})$ is the likelihood function summarizing the model for the data given the parameters, $\pi(\mathbf{D})$ is a normalizing constant, $\pi(\boldsymbol{\Theta})$ is the prior joint probability for the soil hydraulic parameters, and $\boldsymbol{\Theta}$ is the vector of van Genuchten soil hydraulic parameters given by:

$$\boldsymbol{\Theta} = \left\{\left(\theta r_d, \theta s_d, \alpha_d, n_d, Ks_d, l_d\right); \left(w_f, \beta, \gamma_w, a, K_a\right)\right\}, \text{ d} = \boldsymbol{m} \text{ or } \boldsymbol{f} \tag{3.7}$$

where subscripts *m* and *f* represent the matrix and macropore domain parameters, respectively, and (w_f, β, γ_w, a, K_a) constitute the interface region (*int*) parameters. The prior joint probability can be further broken down as the joint probability for the matrix, macropore and interface components of the dual permeability model:

$$\pi(\boldsymbol{\Theta}) = \Pi_{npar_m} \boldsymbol{\varphi}_m \times \Pi_{npar_f} \boldsymbol{\varphi}_f \times \Pi_{npar_{\text{int}}} \boldsymbol{\varphi}_{\text{int}} \tag{3.8}$$

where *npar* is the number of parameters of a particular region that are considered random, $\boldsymbol{\varphi}$ is the set containing the random soil hydraulic parameters for that particular region. Once the conditional posterior probability is known, the marginal posterior distribution $p(.|\mathbf{D})$ that retains the dependence on one parameter exclusively (e.g. residual soil water content for the matrix domain, θr_m) is given by:

$$p(\theta r_m \mid \mathbf{D}) = \frac{\int\int\int_{\theta_2,\ldots\theta_{tot}} f(\mathbf{D} \mid \boldsymbol{\Theta}) \times \pi(\boldsymbol{\Theta}) d\theta_2 .. d\theta_{tot}}{\pi(\mathbf{D})} \tag{3.9}$$

where $\theta_2, \theta_3, \ldots, \theta_{tot}$ represent the soil hydraulic parameters contained in the set $\boldsymbol{\Theta}$ apart from θ_1 (= θr_m). The main complication is the intractability of the multi-dimensional integration of the target density including the computation of the normalizing constant $\pi(\mathbf{D})$. A possible solution is to use any MCMC algorithm that ignores $\pi(\mathbf{D})$ and generates a sequence of parameter sets, $\{\boldsymbol{\Theta}(0), \boldsymbol{\Theta}(1), .., \boldsymbol{\Theta}(t)\}$ that converge to the stationary proposal distribution $p(\boldsymbol{\Theta}|\mathbf{D})$ for large number of iterations *t* [*Gelman et al.*, 1995]. Diagnostic measures of central tendency and dispersion can then be calculated from the mean and variance of the large sample generated using MCMC simulations. The MCMC algorithms used in this study are described below.

3.3.3 Metropolis-Hastings algorithm

One of the widely used MCMC techniques is the Metropolis-Hastings algorithm proposed by *Hastings* [1970]. It samples the posterior distribution of the parameters as described below:

1. Choose a starting point randomly within the feasible parameter space, $\boldsymbol{\Theta}(i) = \boldsymbol{\Theta}(0)$ with a covariance matrix $\sum_0$.
2. Draw a candidate vector $\boldsymbol{\Theta}(i+1)$ from the previous vector $\boldsymbol{\Theta}(i)$ using a proposal distribution $q(\boldsymbol{\Theta}(i+1)|\ \boldsymbol{\Theta}(i)) \sim N(\boldsymbol{\Theta}(i),\sum_0)$, where $\boldsymbol{\Theta}(i)$ is the current state of the chain, and the proposal density is a normal distribution (for this study).
3. Compute the odds ratio: $r = q(\boldsymbol{\Theta}(i+1))/q(\boldsymbol{\Theta}(i))$.
4. If $r \geq 1$, accept the new candidate vector $\boldsymbol{\Theta}(i+1)$ as it leads to a higher value of the proposal distribution.
5. If $r<1$, draw a number at random from a uniform distribution U[0,1]. If the random number is less than r, accept '$\boldsymbol{\Theta}(i+1)$' else remain at the current position '$\boldsymbol{\Theta}(i)$'.
6. Repeat steps 2-5 for the given number of iterations (t).

A single parameter updating is usually done in this algorithm which may be problematic with high-dimensional $\boldsymbol{\Theta}$. If two or more parameters are highly-correlated, a larger number of simulations are required and block or simultaneous updating is necessitated for correlated parameters [*Marshall et al.*, 2004].

3.3.4 Adaptive Metropolis algorithm

We employ the AMCMC scheme of *Harrio et al.* [2001] which corresponds to our need for resolving a large number of dual permeability parameters and

understanding correlation among these parameters. *Harrio et al.* [2001] chose a multivariate normal distribution as the proposal density which is centered on the current state and obtains empirical covariance from a fixed number of previous states. A fixed value of the covariance matrix $\sum$ is employed for a finite number of initial iterations (t_0) after which it is updated as a function of all the previous iterations:

$$\Sigma_i = \begin{cases} \Sigma_0, i \le t_0 \\ s_d \mathrm{Cov}(\boldsymbol{\Theta}_1, \boldsymbol{\Theta}_2, ..., \boldsymbol{\Theta}_{iter-1}) + s_d \varepsilon \boldsymbol{I}_d, i > t_0 \end{cases} \tag{3.10}$$

where $\sum_{\boldsymbol{0}}$ is the initial covariance based on prior knowledge, d is the dimension of $\boldsymbol{\Theta}$, ϵ is a small parameter chosen to ensure $\sum_{\boldsymbol{i}}$ does not become singular, $\boldsymbol{I_d}$ is the d-dimensional identity matrix, and s_d is a scaling parameter that depends only on d. A basic choice for the scaling parameter can be $s_d = (2.4)^2/d$ for Gaussian targets and Gaussian proposals [*Gelman et al.*, 1995]. The covariance at iteration (i+1) can be obtained without much computational cost using the recursive formula:

$$\Sigma_{i+1} = \frac{i-1}{i}\Sigma_i + \frac{s_d}{i}\left(i\overline{\boldsymbol{\Theta}}_{i-1}\overline{\boldsymbol{\Theta}}_i^T - (i+1)\overline{\boldsymbol{\Theta}}_i\overline{\boldsymbol{\Theta}}_i^T + \varepsilon \boldsymbol{I}_d\right) \tag{3.11}$$

The important steps of the AMCMC algorithm can be described as follows:

1. Choose a starting point randomly within the feasible parameter space, $\boldsymbol{\Theta}(i) = \boldsymbol{\Theta}(0)$ with a covariance matrix $\sum_i = \sum_0$.
2. Draw a candidate vector $\boldsymbol{\Theta}(i+1)$ from the previous vector $\boldsymbol{\Theta}(i)$ using a proposal distribution $q(\boldsymbol{\Theta}(i+1)|\boldsymbol{\Theta}(i)) \sim \mathrm{N}(\boldsymbol{\Theta}(i),\sum_i)$, where $\boldsymbol{\Theta}(i)$ and $\sum_i$ define the current state of the chain, and the proposal density is a normal distribution (for this study). $\sum_i$ depends on the iteration number i according to equation 3.10.
3. Compute the odds ratio: $r = q(\boldsymbol{\Theta}(i+1))/q(\boldsymbol{\Theta}(i))$

4. If $r \geq 1$, accept the new candidate vector $\boldsymbol{\Theta}(i+1)$ as it leads to a higher value of the proposal distribution.
5. If $r<1$, draw a number at random from a uniform distribution U[0,1]. If the random number is less than r, accept '$\boldsymbol{\Theta}(i+1)$' else remain at the current position '$\boldsymbol{\Theta}(i)$'.
6. Repeat steps 2-5 for the given number of iterations (t).

The distinguishing feature of adaptive MCMC algorithms, compared to the MH algorithm, is that it updates all elements of $\boldsymbol{\Theta}$ simultaneously due to the description of the covariance structure. This also helps in adapting the simulation at an early stage and reducing computation time. Both adaptive MCMC and AMCMC terms are used interchangeably throughout the paper.

3.4 Case study

3.4.1 Soil column data

This work uses soil column experiments with well-defined boundary conditions to fully understand the prospects and limitations of employing adaptive MCMC versus the conventional MH algorithm to quantify uncertainty in 10 of 17 dual permeability model parameters. Three large acrylic cylinders (75 cm long and 24 cm wide) were packed with sandy loam soil to a dry bulk density of 1.56 g/cm^3. The central macropore column was provided with a single macropore of 1 mm diameter all along the vertical axis of the column, open to both the soil surface and to the bottom outflow plate. In the low- and high-density multiple macropore columns, 3 and 19 artificial holes (1 mm diameter each) were created with a stainless steel rod in one half of the column cross-

section, respectively (Figure 3.1). Basic outflow curves from the three columns are also displayed in Figure 3.1.

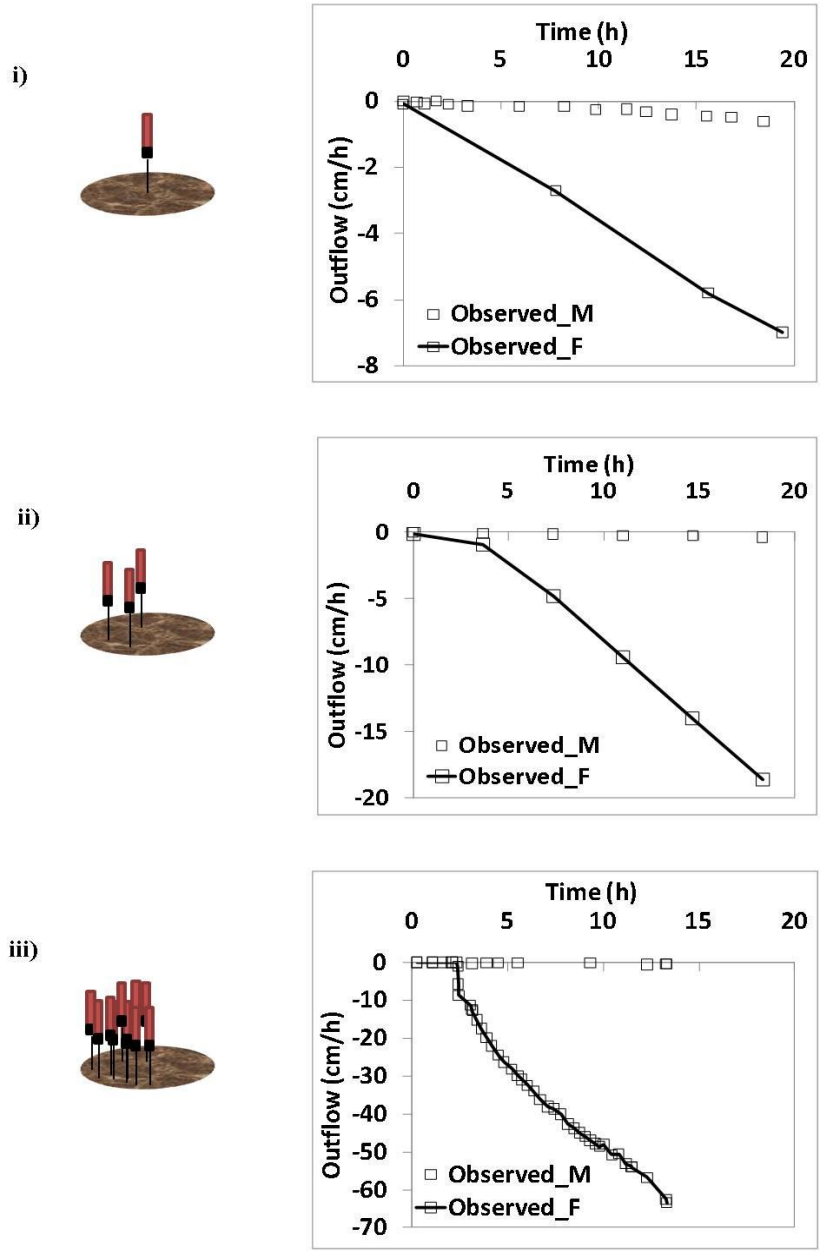

Figure 3.1: Experimental design and outflow from infiltration experiments of the i) single macropore, ii) low density, and iii) high density multiple macropore columns. Symbol *M* represents soil matrix and *F* represents fracture or macropore domain.

Tensiometers and TDR probes were installed at various depths in both macropore and non-macropore halves of the soil columns to monitor pressure head profiles and water/tracer concentrations, respectively (Figure 3.2). In particular, tensiometers were employed at an increment of every 5 cm and TDRs at an increment of 10 cm to obtain a complete representation of the soil profile. At the bottom of the column, outflow rates and flux-averaged bromide (Br^-) concentrations were measured separately in 6 effluent chambers; 3 for each soil region with and without macropores. The top boundary condition was maintained using a tension infiltrometer and the bottom boundary was open to the atmosphere with provision for pressure control. A fraction collector was used intermittently to obtain the outflow from the columns. A detailed description of the soil columns and collection of data are provided in the previous chapter (§ 2.4).

3.4.2 Model parameters, initial and boundary conditions

We present results for infiltration and drainage experiments performed on the single, low- and high-density multiple macropore columns. Simulations of the experimental soil columns are implemented using the HYDRUS-1D software package [*Šimůnek et al.*, 2001, 2003].

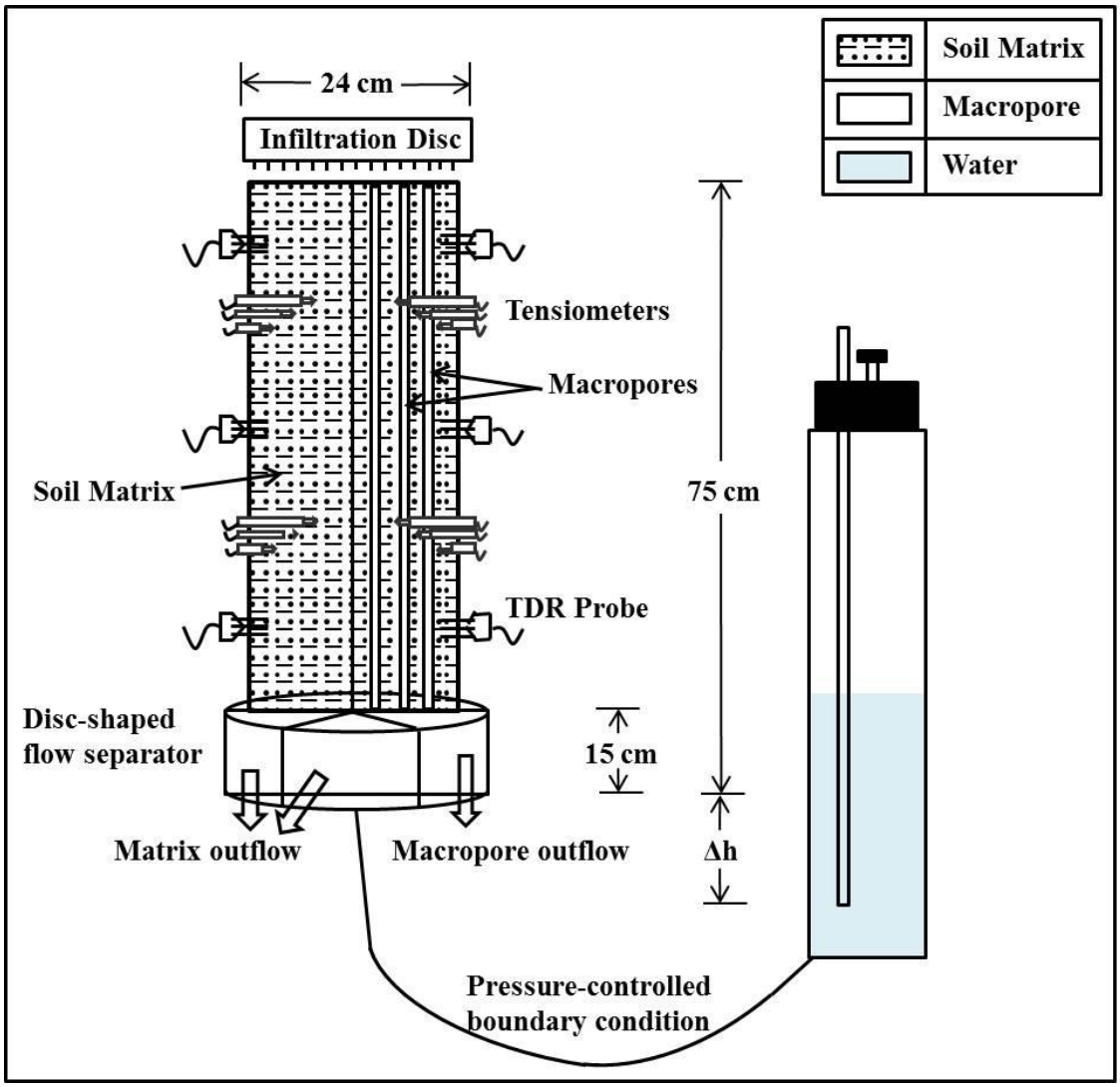

Figure 3.2: Schematic of the soil column with instrumentation.

Initial conditions for the simulations are described in terms of vertical pressure head distribution using tensiometric data at different depths of the soil column (5 cm intervals from the top). Upper and lower boundary conditions are derived from observed tensiometric data at the top (close to 0 cm) and bottom (close to 75 cm) of the soil profile, respectively. A spatial discretization (Δz = 0.5 cm) uniformly distributed over the length of the column is used for all experiments. The initial time step is $\Delta t = 10^{-5}$ h, and minimum and maximum time steps are $\Delta t_{min} = 10^{-6}$ h and $\Delta t_{max} = 10^{-1}$ h, respectively. Space and time discretization are kept identical for all soil columns. Simulation periods for the different experiments vary according to the respective duration of each experiment.

In the dual permeability framework, any water flow simulation requires the following 17 parameters: van Genuchten-Mualem parameters (θr, θs, α, n, Ks, and l) for both matrix and macropore domains, and interface parameters (w_f, β, γ_w, a, and K_a). The parameters of the matrix-macropore interface except K_a are either based on their geometry (w_f, β, and a) or obtained by empirical estimation (γ_w) for the single and multiple macropore columns as shown in the previous chapter [*Castiglione et al.*, 2003]. As these parameters are kept as constants, one may argue that α_w is a function of K_a only (equations 2.11 and 2.12), which is regarded as a calibration parameter in HYDRUS. This suggests that there are only 13 independent parameters based on degrees of freedom. These constant interface parameters along with l_m, θr_m and θr_f are not included in the uncertainty analysis because they are not considered to be sensitive (see § 3.6.1). However, correlations with respect to θr_m and θr_f are taken into account.

3.4.3 Markov chain Monte Carlo sampling

The MCMC algorithms are applied to the experimental soil columns to investigate the effect of parameter correlations and uncertain model parameters on model outputs. The first step is to establish prior density and parameter uncertainty limits for each of the random parameters. As discussed in § 3.4.2, the 10 dual permeability parameters that will be analyzed using MCMC algorithms are $\boldsymbol{\varphi}_m = \{\theta s_m, \alpha_m, n_m,$ and $Ks_m\}$; $\boldsymbol{\varphi}_f = \{\theta s_f, \alpha_f, n_f, Ks_f,$ and $l_f\}$; $\boldsymbol{\varphi}_{int} = \{K_a\}$. A log- transformation is used for the saturated hydraulic conductivity parameter (Ks) of matrix, macropore, and interface regions as suggested by *de Rooij et al.* [2004]. A uniform distribution is assigned to parameters whose literature references are unavailable except for their ranges. Therefore, the prior for l_f is U[0,1]. A normal distribution is assigned as a prior to the rest of the soil hydraulic parameters for both matrix and macropore domains e.g. $\theta s_m \sim N(\mu_{\theta sm}, \sigma_{\theta sm})$. Non-normal priors can be used as well but they will increase the computational complexity considering the number of parameters involved in this problem. The means of the prior densities for the matrix and macropore domains are set at the optimized values obtained using inverse modeling of the various flow experiments as they reflect the least-square estimate from HYDRUS. Table 3.1 summarizes inverse modeling technique used in this study and further details are given in the previous chapter. The variances for the normal densities are obtained from *Vrugt et al.* [2003] using the van Genuchten model for the loam and coarse sand textures reflecting parameters of the matrix and macropore domains, respectively. The uncertainty limits for these parameters are based on ranges obtained from the UNSODA database [*Nemes et al.*, 1999, 2001]

again using the loam and sand textures. To avoid MCMC algorithms from progressively sampling outside realistic parameter ranges, the variances and applicable uncertainty limits are further refined by prior experiences with the model. Table 3.2 enlists the optimized parameter values used as means for the prior density and the uncertainty bounds approximately reflect the values at ± 3σ (standard deviation) for parameters with normal priors.

Table 3.1: Experimental observations used for parameter estimation and likelihood calculations.

Group of observations	**Method**	**Resolution for data collection**	**Minimum resolution for likelihood calculation**
Pressure head, cm	13 Tensiometers	5-cm depth intervals starting from top till bottom of the soil column	3 depths
Soil water content, $cm^3\ cm^{-3}$	12 TDR probes	10-cm depth intervals starting from 5 cm till 55 cm on both matrix and macropore halves of the columns	2 depths in both matrix and macropore halves
Outflow, cm	Six pie-shaped chambers; intermittent use of fraction collector	75 cm depth	1 depth in both matrix and macropore halves

Table 3.2: Initial uncertainty range and optimal parameter values obtained from HYDRUS for MCMC simulations.

Dual permeability parameters		Initial uncertainty range	Parameter value for best HYDRUS simulation		
			Single Macropore column	Low density Macropore column	High density Macropore column
Matrix or immobile region	θr_m (-)	Fixed	0.2	0.2	0.2
	θs_m (-)	0.35-0.41	0.38	0.38	0.38
	α_m (cm^{-1})	0-0.14	0.004	0.004	0.004
	n_m (-)	1.38-2.22	1.8	1.8	1.8
	Ks_m ($cm.h^{-1}$)	0.003-5.53	0.13	0.13	0.13
	l_m (-)	Fixed	0.5	0.5	0.5
Macropore or mobile region	θr_f (-)	Fixed	0.08	0.08	0.08
	θs_f (-)	0.36-0.42	0.39	0.39	0.39
	α_f (cm^{-1})	0-0.14	0.01	0.01	0.01
	n_f (-)	1.1-2.9	2	2	2
	Ks_f ($cm.h^{-1}$)	1.85-37	8.27	8.27	8.27
	l_f (-)	0-1	0.5	0.5	0.5
Interface region	w_f (-)	Fixed	1.7×10^{-5}	5.2×10^{-5}	3.3×10^{-4}
	β (-)	Fixed	0.45	0.54	0.67
	γ_w (-)	Fixed	0.001	0.001	0.001
	a (cm)	Fixed	11.95	4.85	1.89
	K_a ($cm.h^{-1}$)	0.07-4.15* 0.25-13.87**	0.26	4.17	4.17

* value is best suited for the single macropore column.
** value is best suited for the multiple macropore columns.

The second step is to consider an appropriate likelihood function and create a proposal distribution that is close to the posterior target distribution. Sampling from proposal distributions should be consistent with expected model responses to changes in parameter values [*Larsbo et al.*, 2005]. Therefore, the proposal distribution is taken to be a multivariate normal distribution for each region/domain, and a Gaussian jump function is used to move around the parameter space. HYDRUS-1D is run for each 'new' vector in the dual-permeability framework and the likelihood is based on the weighted least squares estimate between observed (D) and predicted values (E) [*Šimůnek et al.*, 2001, 2003]:

$$f\left(\mathbf{D} \mid \boldsymbol{\Theta}_r, \sigma_r\right) \propto \sigma_r^{-N} \exp\left(-\frac{1}{2\sigma_r^2} \sum_{i=1}^{N} w_i \left[r\left(\boldsymbol{\Theta}\right) \right]^2 \right) \tag{3.12}$$

$$r\left(\boldsymbol{\Theta}\right) = \mathrm{D}\left(x,t\right) - \mathrm{E}\left(x,t,\boldsymbol{\Theta}\right) \tag{3.13}$$

where N is the number of observations, w_i are weights associated with a particular observation, $r(\boldsymbol{\Theta})$ are model residuals calculated using the observation data $D(x, t)$ at time t and location x (cf. Table 3.1) and the corresponding model predictions $E(x, t, \boldsymbol{\Theta})$ for the vector $\boldsymbol{\Theta}$ of dual permeability model parameters. We assumed w_i's to be equal to one for this study to represent similar error variances for all observations. A problem with equation 3.12 is that the standard deviation of model residuals (σ_r), which is not known apriori, is also included in the likelihood function. Typically, σ_r can be integrated out of the equation using a Jeffreys prior, and the likelihood therefore becomes [*Scharnagl et al.*, 2011]:

$$f\left(\mathbf{D} \mid \boldsymbol{\Theta}_r\right) \propto \left(\sum_{i=1}^{N} w_i \left[r\left(\boldsymbol{\Theta}\right) \right]^2 \right)^{-N/2} \tag{3.14}$$

The Bayesian technique can thus produce full probability distributions for each parameter that is obtained after integrating all possible combinations of the dual permeability parameters using equation 3.9. This multi-dimensional integration is performed using the MH and AMCMC algorithms which differ primarily in their dealings with the covariance matrix.

3.5 Implementation of the MCMC algorithms

3.5.1 Convergence criteria

A variety of graphical techniques such as trace plots, running mean plots, posterior means, variances and standard errors are used to assess convergence of MCMC chains. Apart from these, convergence diagnostics of MCMC are also based on the Geweke test statistic [*Geweke*, 1992]. The Geweke test splits the MCMC chain into two "windows": the first window containing the beginning 20% of the chain, and the second usually containing the last 50% of the chain. If the samples are drawn from the stationary distribution of the chain, the mean of the two windows are equal. A Z-test of the hypothesis of equality of these two means is carried out and the chi-squared marginal significance is reported. A value of less than 0.01 for the chi-squared estimate indicates that the mean of the series is still drifting.

3.5.2 Number of simulations

Raftery and Lewis's [1992] method is intended to detect convergence to the stationary distribution as well as to provide the total number of iterations required to estimate quantiles of any MCMC output with desired accuracy. The estimation of quantiles is very useful as they provide robust estimates of the mean and variability of

the parameter. If the number of iterations is insufficient, the diagnostic process can be repeated to verify the minimum number of samples (N_{min}) that should be run. One can determine the increment required in the number of simulations due to dependence (I) in the sequence:

$$I = \frac{B+T}{N_{\min}} \tag{3.15}$$

where B is the number of initial iterations to be discarded and commonly referred to as the burn-in length, and T is the total number of simulations. Values of I larger than 5 indicate strong autocorrelation which may be due to a poor choice of starting value, high posterior correlations or stickiness of the MCMC algorithm.

3.6 Results

3.6.1 Sensitivity analysis

The objective of sensitivity analysis is to evaluate appropriate range of parameters and identify critical values that may lead to sub-optimal or local solutions. In this study, sensitivity analysis is carried out by individually varying each parameter by ±30% and keeping the rest of the parameters constant at their inversely estimated values. Table 3.3 lists the top three parameters that produced the most sensitivity to modeled preferential flow results when compared with the optimal HYDRUS simulation. This ranking suggests that variations in matrix parameters cause larger sensitivity than macropore parameters for preferential flow through experimental soil columns. Tortuosity of the matrix domain (l_m), and residual water content (θr) for the matrix and macropore domains are not considered sensitive parameters as they result in small

changes to the optimal HYDRUS simulation. Therefore, these parameters are disregarded for uncertainty evaluation using MCMC simulations essentially to curtail the dimensionality of the problem.

Table 3.3: Sensitive parameters for different types of experiments of the single and multiple macropore columns.

Soil column	Type of experiment	Sensitive parameters		
Single Macropore Column	Infiltration (0 cm head)	θs_m	α_m	n_m
	Drainage	θs_m	α_m	n_m
Low-density Multiple Macropore Column	Infiltration (6 cm head)	θs_m	n_m	-
	Drainage	n_f	θs_m	-
High-density Multiple Macropore Column	Infiltration (0 cm head)	θs_m	α_m	
	Infiltration (4 cm head)	θs_m	n_f	n_m
	Drainage	θs_m	n_m	-

3.6.2 Comparison of adaptive and conventional MH algorithms

MCMC iterations are run for developing an initial covariance structure among the soil hydraulic parameters for the experimental soil columns. Although more than 50% acceptance ratio is observed for all experiments, the initial 4000 MCMC samples do not show convergence for certain parameters. Specifically, pore size distribution index for the matrix domain (n_m), saturated water content for the matrix (θs_m) and fracture (θs_f) domains do not converge for any of the soil columns. Among these, θs_m and n_m are found to be sensitive parameters for most of the experiments (Table 3.3). However, another common sensitive parameter α_m seems to converge efficiently. We argue that it is not the information in the measurements that is lacking but in extracting information about the interactions of the parameters which restricts us from obtaining a unique parameter set. By simultaneously using a number of correlated parameters, identification of unique dual permeability parameters is at stake. This result is confirmed by posterior cross-correlation plots which show high correlation between parameters such as θs_m-n_m, θs_m-α_m, and θs_f-n_f for different experiments of the soil columns. Correlation among soil hydraulic parameters is not uncommon, however, prior information about correlation between the soil properties is non-existent for most soils [*Vrugt et al.*, 2003; *Pollacco et al.*, 2008]. Therefore, the initial covariance structure ($\sum_0$) of the parameters for both MCMC techniques is obtained from the initial 4000 MCMC simulations for all types of flow experiments as follows:

$$\boldsymbol{\Sigma}_0\left(\boldsymbol{\Theta}_m^a\right) = E\left(\left(\boldsymbol{\Theta}_m^a - E\left(\boldsymbol{\Theta}_m^a\right)\right)^T\left(\boldsymbol{\Theta}_m^a - E\left(\boldsymbol{\Theta}_m^a\right)\right)\right),\ \boldsymbol{\Theta}_m^a = \left\{\left(\theta r_m^a, \theta s_m^a, \alpha_m^a, n_m^a, Ks_m^a\right)\right\} \quad (3.16)$$

$$\boldsymbol{\Sigma}_0\left(\boldsymbol{\Theta}_f^a\right) = E\left(\left(\boldsymbol{\Theta}_f^a - E\left(\boldsymbol{\Theta}_f^a\right)\right)^T\left(\boldsymbol{\Theta}_f^a - E\left(\boldsymbol{\Theta}_f^a\right)\right)\right), \boldsymbol{\Theta}_f^a = \left\{\left(\theta r_f^a, \theta s_f^a, \alpha_f^a, n_f^a, Ks_f^a, l_f^a\right)\right\} \quad (3.17)$$

where E is the mathematical expectation, a is the number of accepted samples from the initial 4000 MCMC simulations after 10% burn-in and thinning, and $\boldsymbol{\Theta}_m^a$ ($\boldsymbol{\Theta}_f^a$) is the set of random matrix (macropore) parameters as well as θr_m (θr_f) as suggested in § 3.4.2. The covariance with respect to interface parameters is limited to the variance of K_a as the rest of the parameters are constant (§ 3.4.2). Our goal here is to compare the traditional Metropolis-Hastings (MH) and the adaptive (AMCMC) techniques in estimating soil hydraulic parameters and in producing meaningful outputs that mimic the properties of our preferential flow system.

After initializing the covariance structure, the MH and AMCMC techniques were used to determine uncertainty in the random parameter set $\{\boldsymbol{\varphi}_m, \boldsymbol{\varphi}_f, \boldsymbol{\varphi}_i\}$ for an infiltration experiment of the single macropore column. Although both algorithms share the HYDRUS-optimized starting values and parameter priors, Raftery and Lewis's diagnostic indicates 3295 additional iterations for the MH algorithm as opposed to 235 additional iterations for AMCMC to estimate 0.975 quantile of the parameters to the specified accuracy (=0.02). Figure 3.3 presents contrasting posterior parameter distributions for the two algorithms. Since the truth about parameter distributions is unknown, there is no way to ascertain which algorithm predicts the correct posterior.

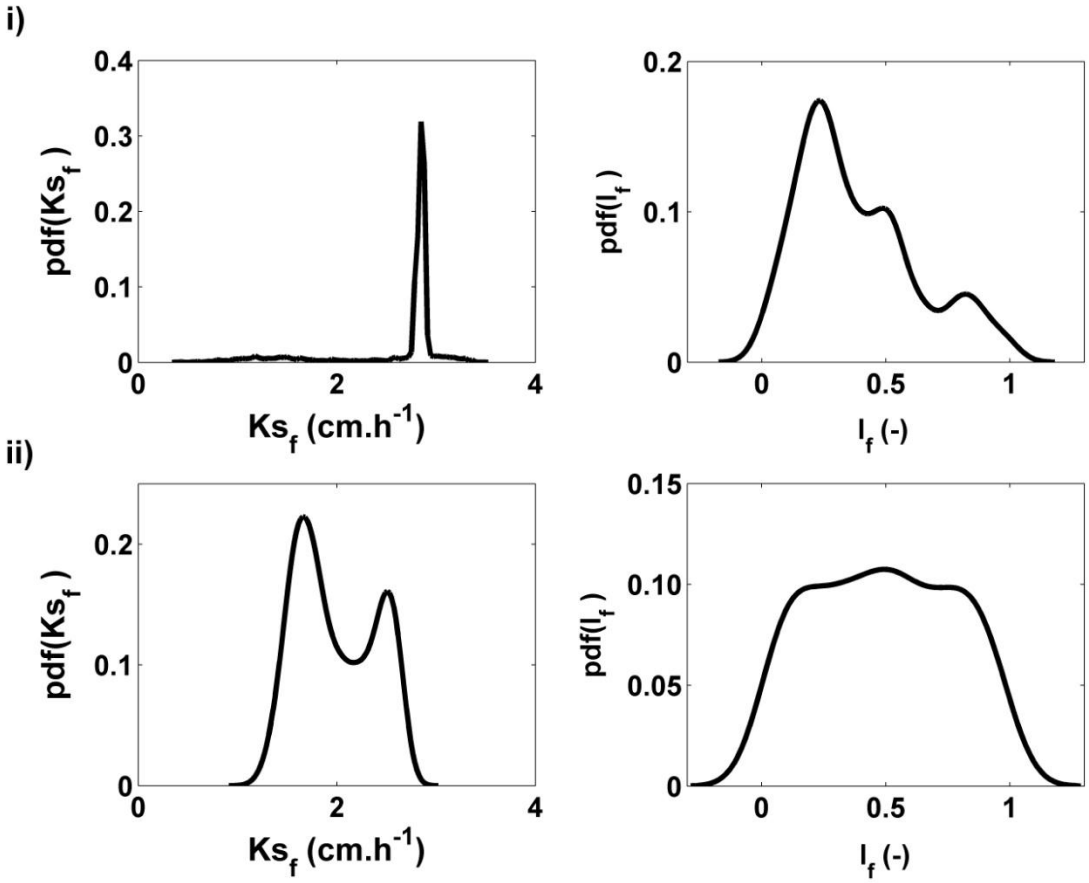

Figure 3.3: Posterior distributions of Ks_f and l_f using i) MH and ii) AMCMC algorithms for an infiltration experiment of the single macropore column.

However, the prediction of a unimodal distribution for Ks_f by the Metropolis-Hastings algorithm implies that the chain takes a long time to move away from a local mode because of the single update mechanism of the MH algorithm. On the other hand, the identification of a multimodal distribution for Ks_f and l_f in the vicinity of local maxima is suggestive of desirable convergence and mixing characteristics of the adaptive MCMC algorithm. The mean acceptance rate of the AMCMC technique (34%) as compared to the traditional Metropolis-Hastings (MH) algorithm (43%) is also suggestive of the comparatively slow convergence of the MH algorithm.

The Markov chain Monte Carlo procedure is also carried out for infiltration experiments with constant pressure head boundary conditions for the low- and high-density multiple macropore columns. Parameter trace plots for 5000 and 3000 simulations for these experimental soil columns are shown in Figures 3.4 and 3.5, respectively.

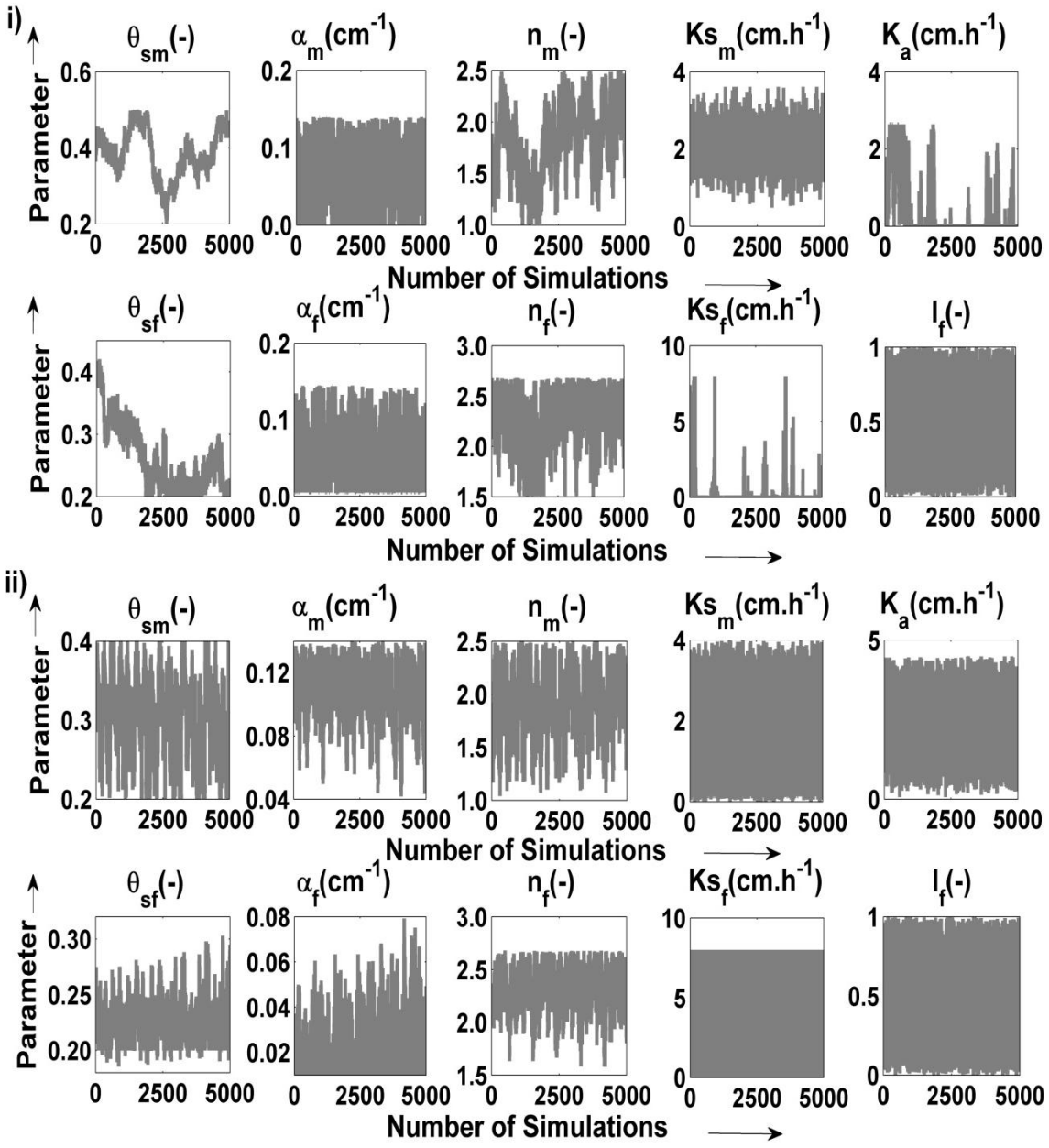

Figure 3.4: Parameter trace plots using i) MH and ii) AMCMC algorithms for an infiltration experiment (6 cm head) of the low density multiple macropore column.

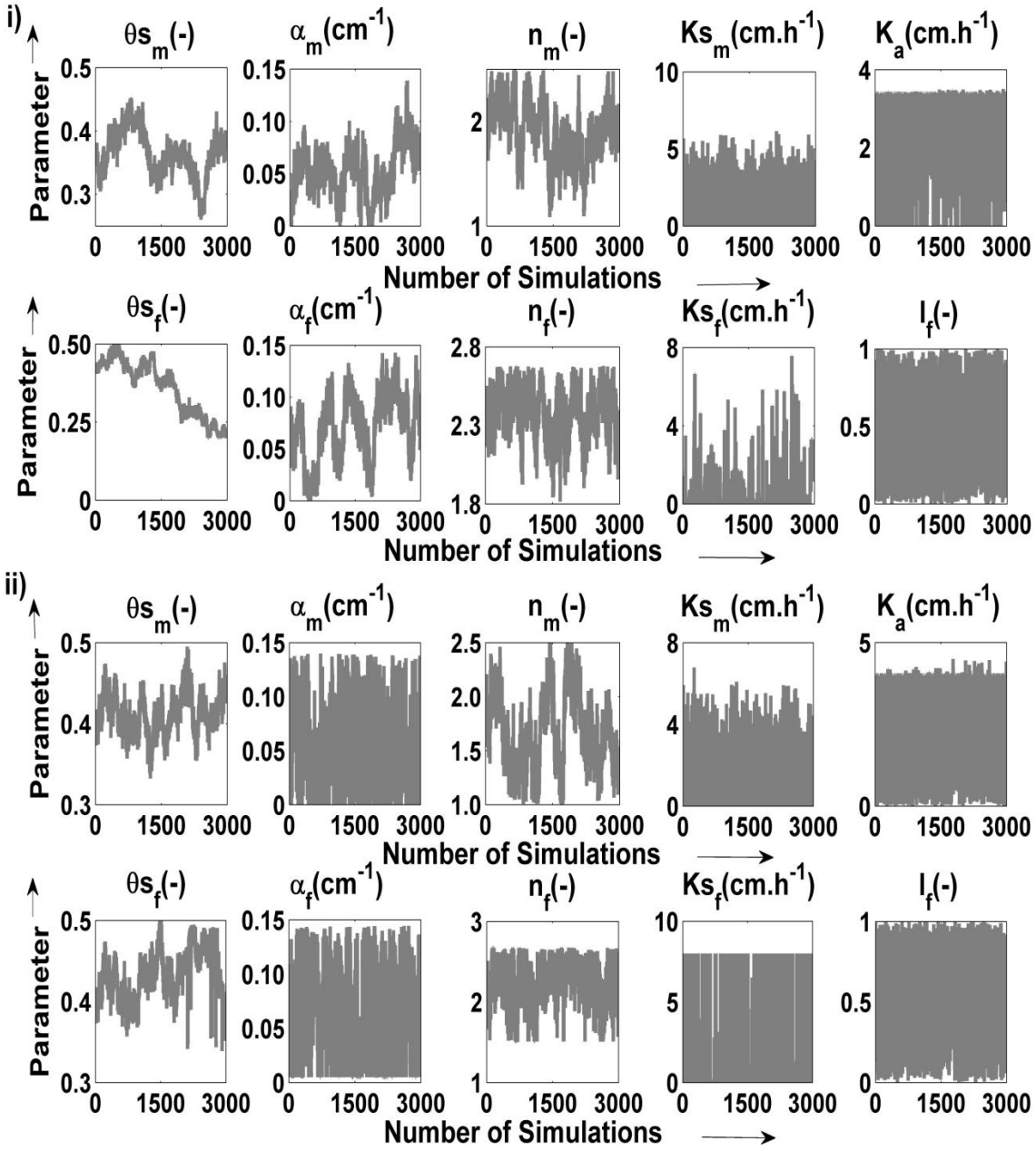

Figure 3.5: Parameter trace plots using i) MH and ii) AMCMC algorithms for an infiltration experiment (4 cm head) of the high density multiple macropore column.

Figure 3.4 indicates that the sequence of draws converged quickly, within 5000 iterations, using the AMCMC technique. The performance of both algorithms is similar except for parameters like θs_m, n_m, θs_f, Ks_f, and K_a. Many more iterations are required to obtain convergence and/or better mixing with the MH approach. Since smoothness of the running mean plots is an indicator of good mixing of the MCMC chain, Figure 3.6 compares the running mean plots of n_m and n_f parameters of the low density macropore column for the two algorithms. This plot suggests slow mixing of the MH chain as compared to the AMCMC chain for both the parameters. Geweke's diagnostic is also used to assess chain convergence and rejects convergence of θs_f and K_a at 90% level of significance using the MH algorithm (column 5 of Table 3.4). On the other hand, Geweke's statistic indicates satisfactory convergence (chi-squared probability > 0.01) for all dual permeability parameters using the AMCMC algorithm (column 6 of Table 3.4). The higher acceptance rate of 33% for the MH algorithm again confirms the slow mixing and convergence characteristics of this algorithm as compared to the lower mean acceptance (26%) of the AMCMC technique.

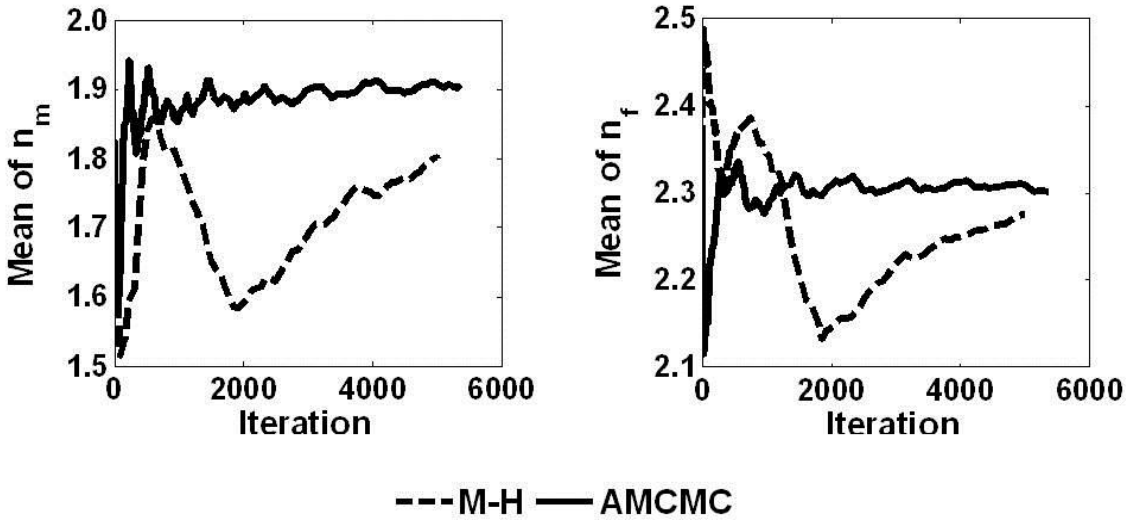

Figure 3.6: Moving average plots for n_m (-) and n_f (-) for an infiltration experiment of the low density multiple macropore column.

Table 3.4: Geweke convergence diagnostics following 10% burn-in for dual permeability parameters of single and multiple macropore columns.

Dual permeability parameters		Chi-squared probability*					
		Single Macropore column		Low density Macropore column		High density Macropore column	
		MH	AMCMC	MH	AMCMC	MH	AMCMC
Matrix or immobile region	θs_m (-)	0.003	0.728	0.963	0.330	0.807	0.992
	α_m (cm^{-1})	0.610	0.164	0.355	0.205	0.060	0.127
	n_m (-)	0.960	0.180	0.057	0.934	0.001	0.147
	Ks_m (cm.h^{-1})	0.632	0.209	0.190	0.809	0.157	0.163
Macropore or mobile region	θs_f (-)	0.898	0.246	0.001	0.161	0.001	0.182
	α_f (cm^{-1})	0.363	0.507	0.155	0.155	0.023	0.870
	n_f (-)	0.234	0.260	0.147	0.579	0.758	0.698
	Ks_f (cm.h^{-1})	0.001	0.448	0.056	0.294	0.268	0.134
	l_f (-)	0.413	0.944	0.798	0.691	0.105	0.680
Interface region	K_a (cm.h^{-1})	0.008	0.336	0.001	0.439	0.342	0.777

* Underline indicates chi-squared probability <0.01

Consistent with findings from the single macropore and low density multiple macropore columns, the AMCMC algorithm provides better mixing and convergence with 36% acceptance rate for the dual permeability parameters of the high density macropore column (Figure 3.5). This time series plot shows poor mixing (θs_m) and trends in data (α_m, n_m, θs_f, and α_f) at 45% acceptance rate for the conventional MH algorithm. The results of the Geweke test confirm the lack of convergence for some of these dual permeability parameters (n_m and θs_f) using the MH algorithm (last two columns of Table 3.4).

Raftery and Lewis convergence diagnostic also indicates high autocorrelation, which is indicated by I>5 in Table 3.5, for all parameters except Ks_m and l_f for the MH algorithm and in θs_m and n_m for the AMCMC algorithm for the high density macropore column. Since the statistic is calculated before thinning of the chains, autocorrelation observed in θs_m and n_m using the adaptive (AMCMC) technique, and n_f, Ks_f, and K_a using the traditional Metropolis-Hastings (MH) algorithm is expected as the chain is not independent and identically distributed (i.i.d.) as yet.

Table 3.5: Evaluation of the Raftery-Lewis statistic for dual permeability parameters of the high density multiple macropore column.

Parameters	MH		AMCMC	
	I	B	I	B
θs_m (-)	34.54	138	10.17	41
α_m (cm^{-1})	17.83	99	1.81	4
n_m (-)	10.36	42	11.62	49
Ks_m ($cm.h^{-1}$)	0.96	2	0.96	2
θs_f (-)	67.71	195	3.82	20
α_f (cm^{-1})	8.29	46	2.63	5
n_f (-)	18.78	78	3.32	12
Ks_f ($cm.h^{-1}$)	6.03	21	2.42	5
l_f (-)	0.71	3	0.71	3
K_a ($cm.h^{-1}$)	38.69	103	5.89	21

The burn-in length (B) and additional number of samples obtained from the Raftery-Lewis statistic are not unreasonable even for the MH algorithm, however, this problem may worsen with addition of parameters, changes to correlation structure, and increment in desired accuracy.

The non-convergent parameters across the different experiments using the conventional Metropolis-Hastings algorithm do not have a direct relationship with the listed sensitive parameters for the different soil columns (Table 3.3). We argue that the MH algorithm was analyzing the tradeoffs in the fitting of these highly correlated parameters due to its one-parameter-at-a-time updating approach. This argument is further strengthened by investigations into posterior cross-correlations among the simulated matrix and macropore domain parameters.

Figures 3.7 and 3.8 present a scatter plot of parameters generated by the MH and AMCMC algorithms after convergence has been achieved for infiltration experiments of

the low- and high-density multiple macropore columns, respectively. Specifically parameter correlations ($|r|>0.5$) are evident for θs_m with α_m and n_m for the low density macropore column, and θs_f with α_f for the high density macropore column using the MH algorithm. For the high density macropore column, the scatter plots developed using the AMCMC algorithm are patchy only at the ends with respect to the saturated hydraulic conductivity parameter of the macropore domain (Ks_f) while the MH algorithm produces scatter plots that are patchy within the parameter space for almost all macropore parameters. This suggests that the MH algorithm has been unable to cover the entire parameter space and explore the full posterior distribution of the parameters in the given number of iterations due to evident correlations between the parameters. On the other hand, the simultaneous updating of the parameters within the AMCMC algorithm enables it to provide better posterior estimates in lesser iterations. We conclude that carefully formulated AMCMC yields sufficient information to estimate parameter uncertainty with faster convergence rate when a large number of parameters (as in dual permeability model) are considered random and prior information with respect to their interdependence and correlation is lacking.

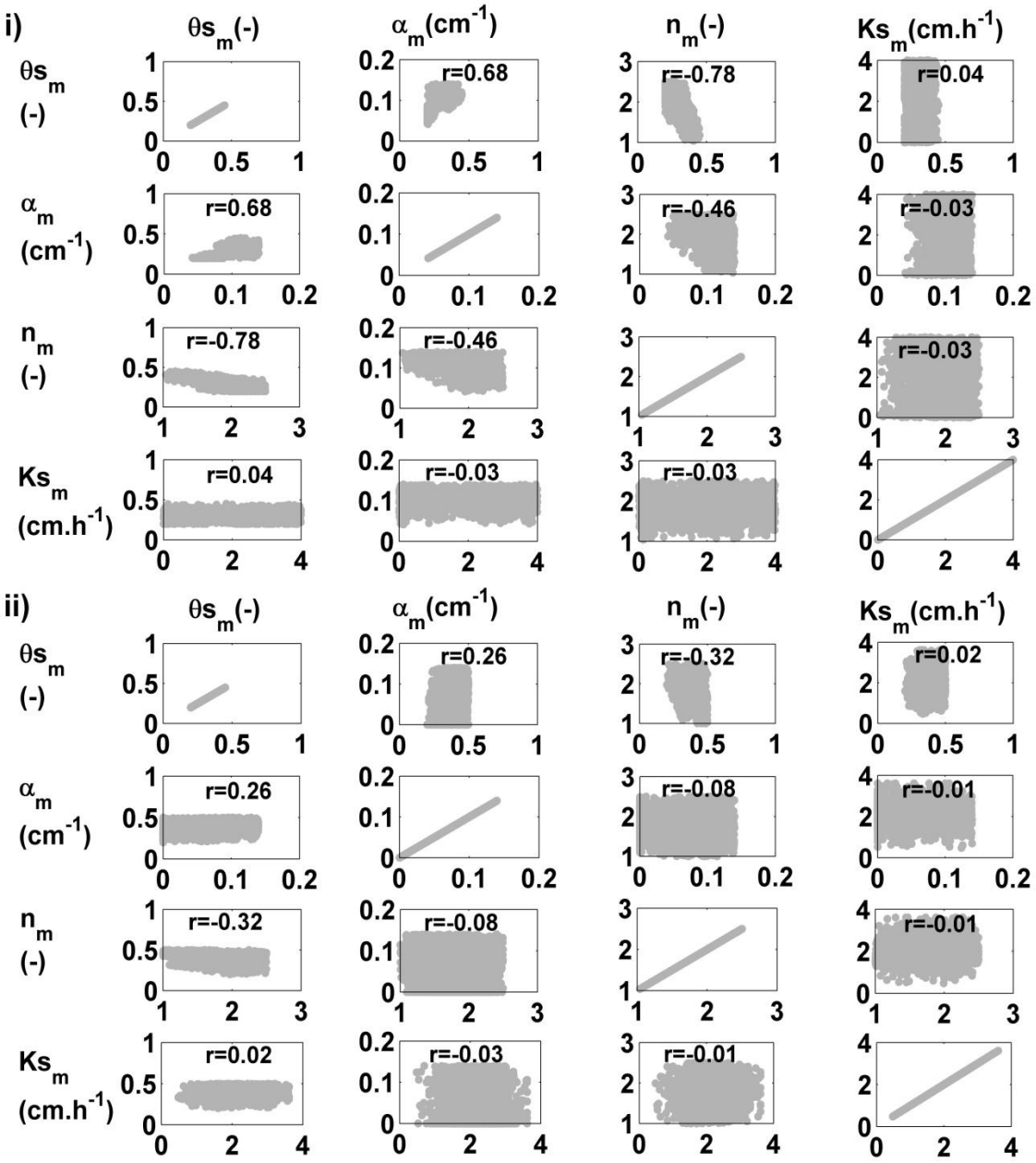

Figure 3.7: Scatter plots of 5000 combinations of different matrix parameters for the low density macropore column using i) MH and ii) AMCMC algorithms.

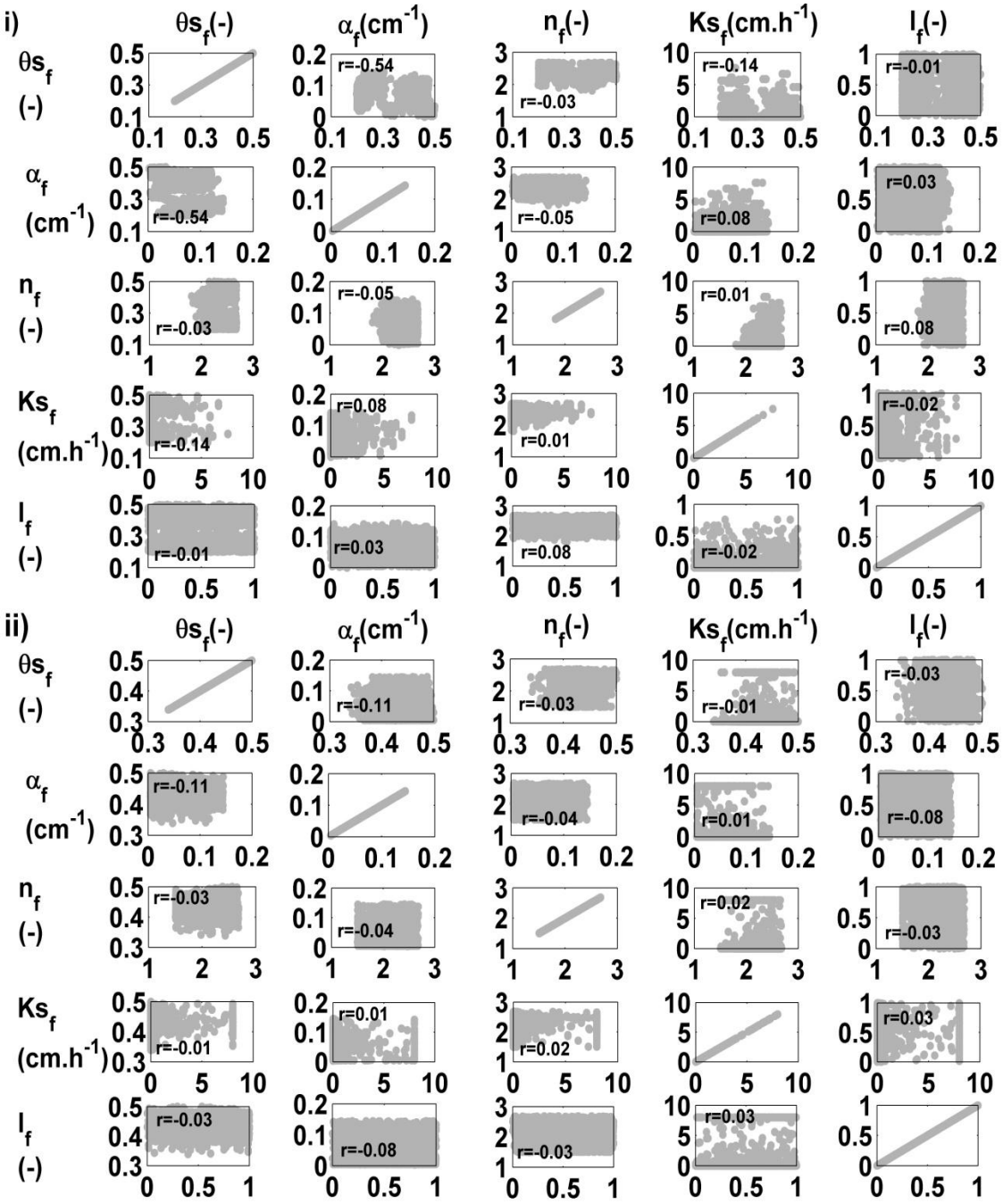

Figure 3.8: Scatter plots of 3000 combinations of different macropore parameters for the high density macropore column using i) MH and ii) AMCMC algorithms.

3.6.3 Output uncertainty

To verify whether improved predictions of preferential flow can be made by either algorithm, we compare AMCMC and MH simulation results for a constant head (0 cm) infiltration experiment of the high density multiple macropore column. Figure 3.9 illustrates pressure head profiles at 10 cm depth and soil water retention curves for the matrix domain for the two algorithms. The MH algorithm displays a wider range of uncertainty in predicting the entire pressure head profile as compared to the AMCMC algorithm. This is also true for other water content profiles at different depths and for experiments of the different soil columns. This can be explained with the reasoning that the AMCMC algorithm has a narrow range of the highest posterior density region in the physically plausible space for each of the dual permeability parameters. The AMCMC algorithm is able to resolve parameter correlations and consequently, has a lower uncertainty associated with the dual permeability parameters. On the other hand, the MH algorithm relies on the inverse procedure, which minimizes the squared residuals between model predictions and measurements, and fails to provide a single, relatively unique set of hydraulic parameters from experimental observations. This is also reflected in the 99% prediction uncertainty bounds where the most optimal hydraulic properties, obtained from the inverse procedure and indicated with the dotted line, are at the center of the bounds for the pressure head curve. On the contrary, the observations, indicated with squares, are at the center of the prediction bounds for the AMCMC algorithm especially during perturbations of the pressure head potential between 12 and 18 hrs.

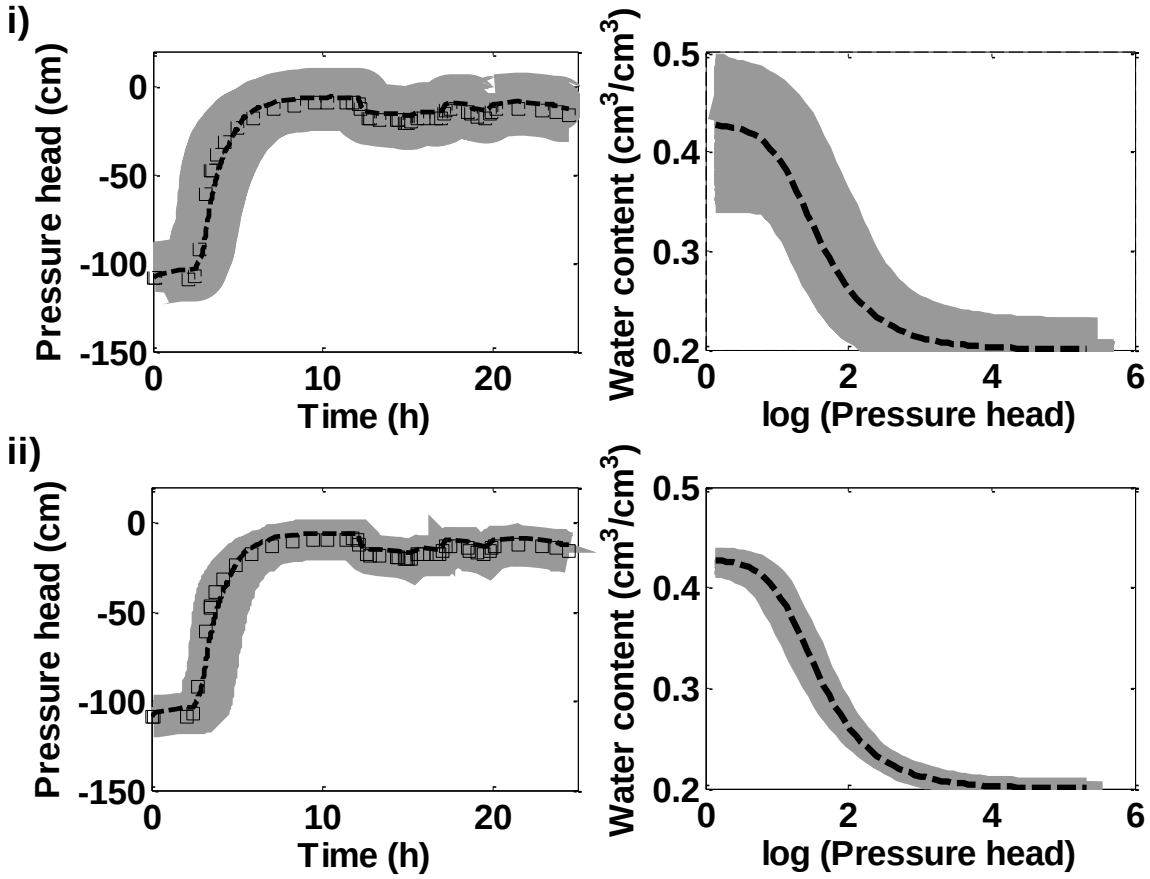

Figure 3.9: Uncertainty in hydrologic output profiles of the high density multiple macropore column for an infiltration experiment using i) MH and ii) AMCMC algorithms. The dashed lines define the HYDRUS simulation for the most likely parameter set, the grey shaded area denotes the 99% prediction uncertainty range, and the squares correspond to experimental observations at 10 cm depth.

There is also considerable uncertainty associated with the MH algorithm where the soil moisture potential is at saturation. This is in agreement with θs_m being highly correlated with other parameters (Figure 3.7) and the high sensitivity of preferential flow output associated with θs_m for all experiments (Table 3.3). It is important to note that AMCMC is not deemed better due to the smaller uncertainty range in output predictions as true uncertainty bounds are unknown for the experimental soil columns. However, we believe that significant uncertainly associated with the fitted soil water retention functions is due to unresolved parameter correlations using the MH algorithm. It is therefore recommended that additional water content measurements at lower pressure potential be included to condense parameter correlations and reduce uncertainty associated with such parameter sampling algorithms. For the dual permeability modeling framework, the comparison between MH and AMCMC algorithms clearly demonstrates that correlation between dual permeability parameters exists, and the output uncertainty range suggests that this correlation must be accounted for by the parameter sampling algorithms (either by including additional information on the correlation structure or through an efficient sampling scheme).

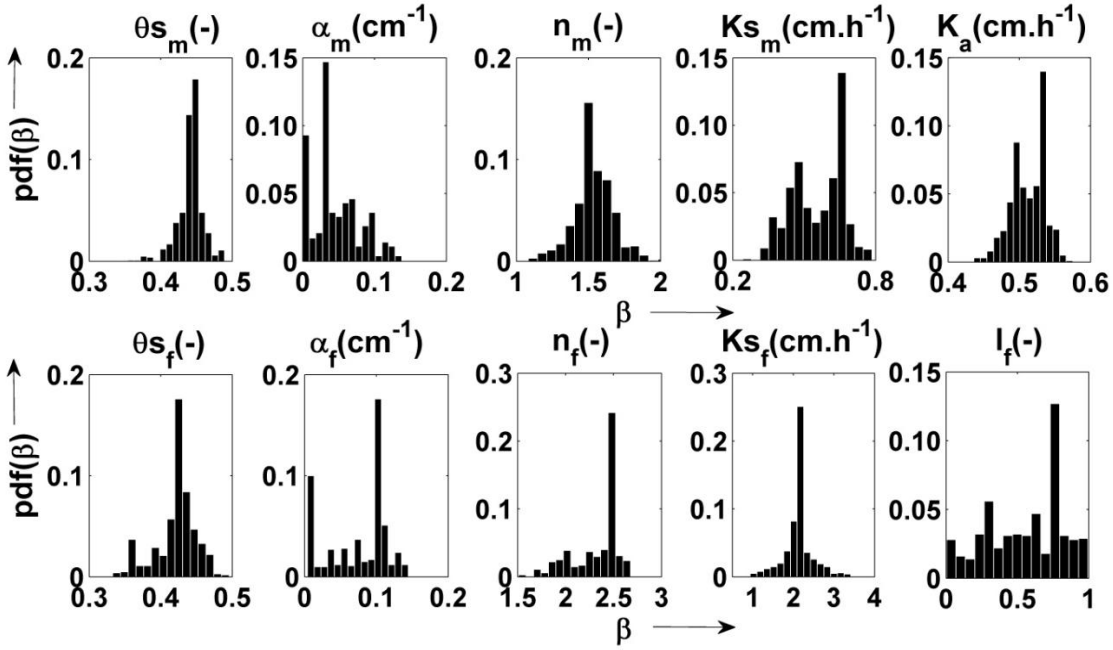

Figure 3.10: Posterior probability distributions of the parameters using observed data for drainage experiment of the single macropore column.

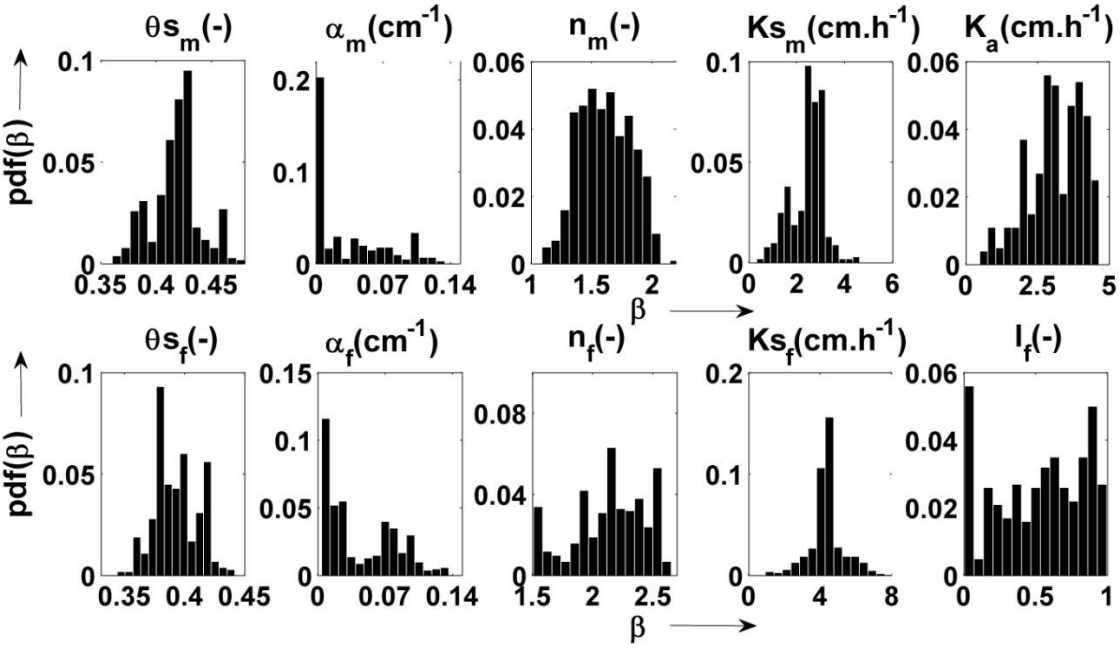

Figure 3.11: Posterior probability distributions of the parameters using observed data for drainage experiment of the high density multiple macropore column.

3.6.4 Uncertainty in soil hydraulic parameters

The estimation of marginal posterior distribution is obtained assuming homoscedatic, uncorrelated error terms using the adaptive MCMC technique. Histograms of the dual permeability parameters generated after convergence to the stationary posterior distribution for drainage experiments of the single and high density multiple macropore columns are shown in Figures 3.10 and 3.11, respectively. The posterior distributions show evidence of bi- and multi- modal nature for certain soil hydraulic parameters. An explanation for the occurrence of multiple modes in the posterior is the inherent structure of the prior distribution. Multivariate normal priors can result in multimodal or student-t type of posterior distributions [*Escobar and West*, 1995].

For the soil column data, the different modes suggest that the experimental data are coming from two (or three) sets of population, which represent the different retention and hydraulic conductivity functions. *de Rooij et al.* [2004] obtained different modes with the same parametric distribution for soil hydraulic parameters of the plough layer and the subsoil thereby reflecting different soil depths and different retention functions. This result can be transferred here to suggest that these modes are related to the different domains of the dual-permeability system. The relative dominance of the matrix, macropore, and interface regions is easy to discern in the histograms. Specifically, in the drainage experiments of the single and high density multiple macropore columns, the macropores are drained first followed by the matrix-macropore interface and then by pores of the matrix domain. Therefore, the existence of three modes in Ks_m, K_a, θs_f, and l_f

for the single macropore column, and in K_a, θs_m, θs_f, n_f, and l_f for the high density multiple macropore column suggest the participation of these parameters in controlling flow processes through the matrix, macropore and interface regions. Note that the parameters showing bimodality such as α_m, α_f, and n_f for the single macropore column, and Ks_m and α_f for the high density multiple macropore column belong to matrix and macropore domains only. This suggests that apart from the conductivity parameter of the matrix-macropore interface (K_a) and the tortuosity of the macropores (l_f), soil hydraulic parameters of matrix and macropore domains also play an important role in regulating the flow through the interface region.

Table 3.6: Summary of posterior distributions for the soil hydraulic parameters using the AMCMC algorithm.

Dual permeability parameters		Single Macropore column		Low density Macropore column		High density Macropore column	
		Mean	Variance	Mean	Variance	Mean	Variance
Matrix or immobile region	θs_m (-)	0.457	0.024	0.304	0.054	0.413	0.024
	α_m (cm^{-1})	0.070	0.027	0.107	0.020	0.060	0.026
	n_m (-)	1.725	0.323	1.904	0.320	1.663	0.342
	Ks_m ($cm.h^{-1}$)	0.434	0.091	2.097	1.002	2.603	1.020
Macropore or mobile region	θs_f (-)	0.256	0.046	0.226	0.020	0.433	0.029
	α_f (cm^{-1})	0.058	0.026	0.021	0.015	0.061	0.034
	n_f (-)	2.220	0.237	2.302	0.223	2.258	0.285
	Ks_f ($cm.h^{-1}$)	2.518	1.092	3.871	1.518	3.530	1.326
	l_f (-)	0.494	0.028	0.530	0.029	0.510	0.028
Interface region	K_a ($cm.h^{-1}$)	0.524	0.034	2.508	1.029	2.311	1.001

Table 3.6 summarizes the posterior mean and variance of the various dual permeability parameters for drainage experiments of the single and multiple macropore

columns using the AMCMC algorithm. Since MH algorithm produces incorrect posterior means and large variances for certain highly-correlated variables, these results are not presented here. It is important to note that same initial parameters were employed for all soil columns and the only difference between them was in the number of macropores and therefore, in geometry-based interface parameters (Table 3.2). The results presented in Table 3.6 illustrate that we end up with different parameter means for the different experimental columns. Most importantly, the posterior means of *Ks* parameter for the matrix, macropore and interface regions show similarity between the low- and high-density macropore columns, and are consistently lower for the single macropore column. Also, saturated hydraulic conductivity for the macropore domain (Ks_f) is found to have the highest posterior variance for all soil columns. This suggests that saturated hydraulic conductivity parameter is influenced by macropore density. Mild non-equilibrium conditions observed in single macropore column are reflected through low posterior mean of *Ks* parameters for all three regions. Results from the previous chapter also indicate the need to adjust saturated hydraulic conductivity parameter (Ks_m) to account for an increase in macropore density and to correctly predict flow through the structured soil system.

3.6.5 Comparison with deterministic approach

For the sake of comparison with the stochastic/Bayesian approach, a deterministic framework is applied using a similar weighted least squares approach as described in equation 3.12:

$$\psi(\boldsymbol{\Theta}) = \sum_{j=1}^{m} v_j \sum_{i=1}^{n_j} w_{i,j} \left[r(\boldsymbol{\Theta}) \right]^2 \tag{3.18}$$

where w_{ij}'s are equal to one (as in the stochastic approach), m is the number of different sets of measurements, n_j is the number of observations in a particular measurement set such that the total number of observations N (in equation 3.12) is a summation of n_j (for j=1,2,…,m). An additional set of weights (v_j) associated with each measurement set is used in the deterministic approach. The weighting elements v_j are inversely related to measurement variances (σ_j^2) and number of data (n_j) [*Clausnitzer and Hopmans*, 1995]:

$$v_j = \frac{1}{n_j \sigma_j^2} \tag{3.19}$$

An advantage of the Bayesian approach is that it integrates out the error related to measurement variances (equation 3.14). As mentioned in § 3.6.4, the deterministic approach resulted in similar parameters for all soil columns except the interface parameters (Table 3.2) and suggested changes to Ks_m for incorporating the effect of macropore density (as also indicated in the previous chapter). On the other hand, the Bayesian framework resulted in consistently lower posterior means for *Ks* parameters for all regions of the single macropore column as compared to the multiple macropore columns. Thus, AMCMC suggests that the impact of macropore density be incorporated by calibrating saturated hydraulic conductivity parameters for all three regions. Another difference between the two approaches is highlighted through hydrologic outputs from the soil columns. The Bayesian framework provides a comprehensive evaluation of multiple realizations of preferential flow output from the columns using uncertain parameters while the deterministic approach provides a single realization of the output (Figure 3.9). This single realization does not even lie at the center of the 99% uncertainty

bounds obtained through AMCMC because the deterministic approach also analyzes parameter tradeoffs due to correlation among DPM parameters. We must mention that the Bayesian technique does not consider error related to the model structure. The use of a probabilistic framework in this study was solely to emphasize the correlation structure of DPM parameters and its effect on posterior parameter values, uncertainty limits, and hydrological output.

3.7 Summary and conclusions

The applicability of dual permeability models for structured soils is hindered by the large number of input parameters, some of which cannot be measured directly [*Šimůnek et al.*, 2003]. This study depicts the usefulness of Bayesian methods in evaluating parameter uncertainty and its effect on model predictions in a preferential flow system that considers 10 out of 17 (or 13 based on degrees of freedom) DPM parameters to be random. Bayesian modeling framework is applied using an adaptive MCMC scheme and the conventional Metropolis-Hastings algorithm on experimental soil columns with different macropore distributions (single macropore, low- and high-density multiple macropores). The distinguishing feature of the AMCMC algorithm is its simultaneous parameter update due to the description of the parameter covariance matrix as opposed to the single site update of the MH algorithm. Results indicate that AMCMC accelerates convergence of the multi-dimensional dual permeability model for all experimental soil columns and identifies marginal posterior distributions even in the vicinity of local maxima due to its online updating mechanism. On the other hand, the MH algorithm reveals high posterior correlations obtained with respect to θs_m with n_m

and α_m, and θs_f with α_f for different experiments of the soil columns. In terms of predicting preferential flow, this study shows that the MH algorithm produces larger uncertainties than AMCMC in pressure head and water content profiles at different depths of the soil columns. The larger variability near the saturation end of the water retention curve using the MH algorithm is related to high correlations with θs_f and high sensitivity of preferential flow estimates to the saturated water content parameter (θs_m). It seems that the MH algorithm requires additional experimental datasets or supplemental information on parameter covariance structure to resolve these correlations efficiently while AMCMC has faster convergence in estimating unique parameters using just the information contained in experimental observations. For the dual permeability framework, the comparison between the two algorithms highlights the existence of a correlation structure among DPM parameters and indicates that the selection of parameter sampling algorithms, whether deterministic or stochastic, is paramount in obtaining unique DPM parameters. When correlation structure of dual permeability parameters is unknown or complex, the parameter sampling schemes should either have efficient update mechanisms (e.g. AMCMC) or be supplied with supplemental information (e.g. MH) to improve identification of DPM parameters. Other studies have also reported that prior knowledge about correlation structure significantly improves equifinality of parameter estimates [*Flores et al.*, 2010; *Scharnagl et al.*, 2011].

In terms of parameter uncertainty, both order and value of parameters are well-estimated and within credible limits according to the UNSODA database using the AMCMC algorithm [*Nemes et al.*, 1999, 2001]. The effect of macropore density is

evident in saturated hydraulic conductivity parameter for matrix (Ks_m), macropore (Ks_f) and interface regions (K_a) as their posterior means are consistently lower for the single macropore column as compared to the multiple macropore columns. A high posterior variance found in K_{sf} also reflects higher uncertainty in the consistency of this parameter across soil columns with changing macropore density. Our previous chapter also emphasizes the need to account for changes in macropore density through some parameters of the dual permeability model. Histograms of certain parameters are found to display bi- or tri- modal characteristics. We believe that this is not a peculiarity of the posterior distribution but reflects the sequence of flow processes of the matrix, macropore, and/or the interface region. This is similar to observations in natural systems, where macropores are predominantly active at and near saturation, the micropores get active at a relatively lower pressure, and the interface at a variety of pressure heads in between the extremes. Results indicate that the degree of local non-equilibrium in the matrix-macropore interface is controlled not only by the transfer term parameter (K_a) and macropore tortuosity (l_f) but also by other parameters governing the shape of water retention curves for the matrix and macropore domains. This result is important from the perspective of understanding the physical meaning and effect of dual permeability parameters, and incorporating uncertainty in certain parameters to better account for lateral flow processes through the matrix-macropore interface region.

We must note that theoretical concepts derived from this one-dimensional column study are applicable to multi-dimensional settings of structured soils. This is because preferential flow causes majority of the flow (disregarding macropore tortuosity

and dead ends) to be carried through macropores and fractures, making the flow essentially one-dimensional [*Flury et al.*, 1994; *Mohanty et al.*, 1998]. Therefore, specific results like existence of correlation among DPM parameters, the need for requisite changes to *Ks* to account for increase in macropore density, and the dominance of interface region in any flow process are all transferrable to the field scale. A recent study by *Kodeŝová et al.* [2010] also demonstrates correlations with respect to Ks_f with K_a, and Ks_f with shape parameters of the macropore domain for an experimental field setting. In addition, three-dimensional field settings can only enhance the problem of correlated parameters by introducing spatial correlation in the added dimension [*Mallants et al.*, 1997; *Coppola et al.*, 2009].

CHAPTER IV

REDOX GEOCHEMISTRY WITHIN HOMOGENEOUS AND LAYERED SOIL COLUMNS UNDER VARYING HYDROLOGICAL CONDITIONS

4.1 Synopsis

A fundamental issue in predicting the fate and transport of contaminants in subsurface systems is the complex interaction between transport and redox processes. These predictions are further complicated by variable flow dynamics, transient redox states, and structural heterogeneity of the unsaturated zone. Thus, the objective of this study is to identify the dominant biogeochemical processes and evaluate the effect of varying hydrologic conditions on these processes in soil columns with known structural heterogeneity. In particular, underlying redox processes and hydrological variations within repacked homogeneous sand and loam columns are compared with a layered sand-over-loam configuration. A principal component analysis (PCA) is performed to infer the dominant redox processes, and HP1 modeling is used to conduct numerical perturbations corresponding to rainfall intensity, water chemistry (pH), and hydrologic boundary conditions to analyze the variations within these dominant processes.

PCA results indicate that the dominant process controlling biogeochemical variations is advective transport in the homogeneous sand column, advective transport and oxidation of iron sulfide in the homogeneous loam, and sulfate dynamics at the textural interface in the layered column. HP1 findings suggest that redox gradients in the homogeneous columns are controlled by the type of hydrologic boundary condition

(infiltration, drainage, etc.) whereas textural layering is paramount in controlling redox gradients in the layered sand-over-loam column. This textural interface enhances biogeochemical activity in the layered column as compared to the homogeneous columns and highlights the need to incorporate structural heterogeneity in contaminant fate and transport models. A conceptual model is described for such structurally heterogeneous variably-saturated media that can account for distinct water chemistries across similar heterogeneous formations (layered interfaces, clay lenses, etc.).

4.2 Introduction

Contamination of subsurface water resources is a significant environmental concern. Much of this contamination occurs in the unsaturated zone in the form of leaking underground storage tanks, municipal solids and hazardous waste landfills, waste management sites, unlined pits, ponds, and lagoons, household septic systems, etc. [*LaGrega et al.*, 1994; *National Research Council*, 1994]. Several physical and biogeochemical processes (dilution, precipitation, adsorption, redox transformation, diffusion, etc.) have the ability to control and attenuate contamination [*Bagchi*, 1987; *Christensen et al.*, 1994]. However, there is a general lack of knowledge about the understanding of coupled hydrological, microbial, and geochemical processes or key biogeochemical parameters that can trigger, sustain or discontinue biodegradation in subsurface systems.

Biodegradation of contaminants in the unsaturated zone is governed by the presence of electron acceptors, nutrients, and growth and decay of microorganisms. Theoretically, in closed groundwater systems, redox conditions can indicate which

biogeochemical transformations can occur, and the progression of redox zones is based on thermodynamic energy yields as: aerobic respiration, nitrate reduction, manganese reduction, iron reduction, sulfate reduction, and methanogenesis [*Champ et al.*, 1979; *Chapelle*, 2001; *Megonigal et al.*, 2004]. However, studies have found that formation of redox zones could be simultaneous and non-sequential in dynamic systems [*McGuire et al.*, 2000, 2002]. In unsaturated zones, hydrologic and geochemical conditions are time-variant and can affect the redox reactions occurring in situ. For example, *Scholl et al.* [2006] studied the impact of seasonal rainfall events on redox processes at an alluvial aquifer contaminated with leachate from an unlined municipal landfill. They concluded that sulfur (and possibly nitrogen) redox processes were directly related to recharge timing, and that seasonal rainfall events were significant drivers of biodegradation processes. Similarly, *Han et al.* [2001] observed that the wetting-drying moisture regime in arid soils resulted in redistribution and fractionation of heavy metals such as Ni, Zn and Cu. Thus, the variability of soil moisture regime and rainfall recharge events of the unsaturated zone are all dominant controls on soil redox potential and can govern the transport and release of metals and contaminants in subsurface systems [*Abrams and Loague*, 2000].

Elemental speciation and mobility of metals is also affected by pH variation in soils. *Mayer et al.* [2001] treated chromium contaminated waters by increasing the pH of groundwater using a zero-valent iron barrier at the Elizabeth City site. Similarly, *Jansen et al.* [2002] investigated the effect of small pH changes (3.5-4.5) on soluble complexation of Fe^{2+}, Fe^{3+} and Al^{3+} with dissolved organic matter. They concluded that

pH and redox potential have serious implications for promoting or reducing the mobility of these metals in soils. Previous studies have indicated that the influence of pH and even small variations in redox conditions can have drastic effects on sorptive properties and transport of metals and contaminants [*Masscheleyn et al.*, 1991; *Cao et al.*, 2001]. It is therefore important to develop an understanding of the complex interactions between hydrological variability (rainfall events, pH, etc.) and redox conditions in unsaturated zones.

Apart from the variably-saturated conditions, fate and transport of contaminants in the unsaturated zone is further complicated by subsurface heterogeneity. Heterogeneity in the form of interfaces has been studied under various experimental and field scenarios. Interfaces can be defined as transition zones between distinct water masses (e.g., recharge water-contaminant plume), lithological variations (e.g., sand-clay lens), or sediment-water boundaries (e.g., contaminant plume fringe). The most important aspect of an interface is that mixing between waters is a driver of biodegradation processes [*Baez-Cazull et al.*, 2007; *Kneeshaw et al.*, 2007]. As a result, most biogeochemical processes are strongly affected by layering and interfaces. For example, *McGuire et al.* [2005] studied the impact of a moderate-sized rainfall event on redox processes at a shallow, sandy aquifer contaminated with petroleum hydrocarbons and chlorinated solvents. They concluded that recharge effects on progression of redox zones existed primarily at the interface between infiltrating water and the aquifer, and not at the average aquifer scale. *Van Breukelen and Griffioen* [2004] also analyzed redox reactions at the top fringe of a landfill leachate plume in Banisveld, Netherlands. They

suggested that the plume fringe is an important zone for degradation of dissolved organic carbon but secondary redox reactions like methane oxidation can reduce the potential of natural attenuation in these zones. Similarly, wetland-aquifer interfaces have been identified as important zones of biogeochemical cycling and secondary redox reactions [*Baez-Cazull et al.*, 2007, 2008]. Although previous studies have analyzed the importance of interfaces and heterogeneous mediums, little information is available on redox processes across textural boundaries under variably-saturated conditions.

Several characteristics of the unsaturated zone add complexity to modeling and understanding biogeochemical processes. First, subsurface heterogeneity can manifest itself in the form of variable solid-phase constituents, lithology, microbial population, and/or physical features such as macropores, soil type, textural layering. Second, unsaturated zone processes are complicated by soil moisture conditions, pH variations, and seasonality of flow. Therefore, the purpose of this study is to isolate and understand the contribution of various hydrological conditions that can trigger, sustain, or discontinue the biogeochemical processes in experimental soil columns with homogeneous and layered configurations. Thus, this study combines the effect of subsurface heterogeneity (textural interface) with hydrologic variability to understand the complex interaction between transport and redox processes in the unsaturated zone. The objectives of this study are: i) to understand the dominant processes controlling biogeochemical variations in homogeneous sand, homogeneous loam, and layered sand-over-loam soil columns, and ii) to evaluate and compare the effect of hydrologic

perturbations in terms of variable boundary conditions, pH, and rainfall intensity on redox conditions in homogeneous and layered columns.

4.3 Experimental procedures

4.3.1 Site description

The Norman Landfill is a municipal solid waste landfill that operated from 1922 to 1985 in the city of Norman, Oklahoma (Figure 4.1). The site sits on permeable Canadian River alluvium which is about 10 to 15 meters thick and overlies a low-permeability shale and mudstone confining unit known as the Hennessey Group. The aquifer material is predominantly sand and silty sand with intermittent mud layers and clay lenses [*Scholl and Christenson*, 1998]. Aquifer mineralogy is comprised of quartz, illite-smectite, feldspars, and minor calcite and dolomite for the sand layers, and higher clay content for the mud layers [*Breit et al.*, 2005]. Authigenic constituents in the aquifer include iron monosulfide, pyrite, barite, and ferric oxides, with ephemeral surface accumulations of mirabilite and gypsum [*Tuttle*, 2009]. Figure 4.1 also depicts an adjacent abandoned river channel known as the slough which was intermittently exposed to landfill leachate [*Becker*, 2002].

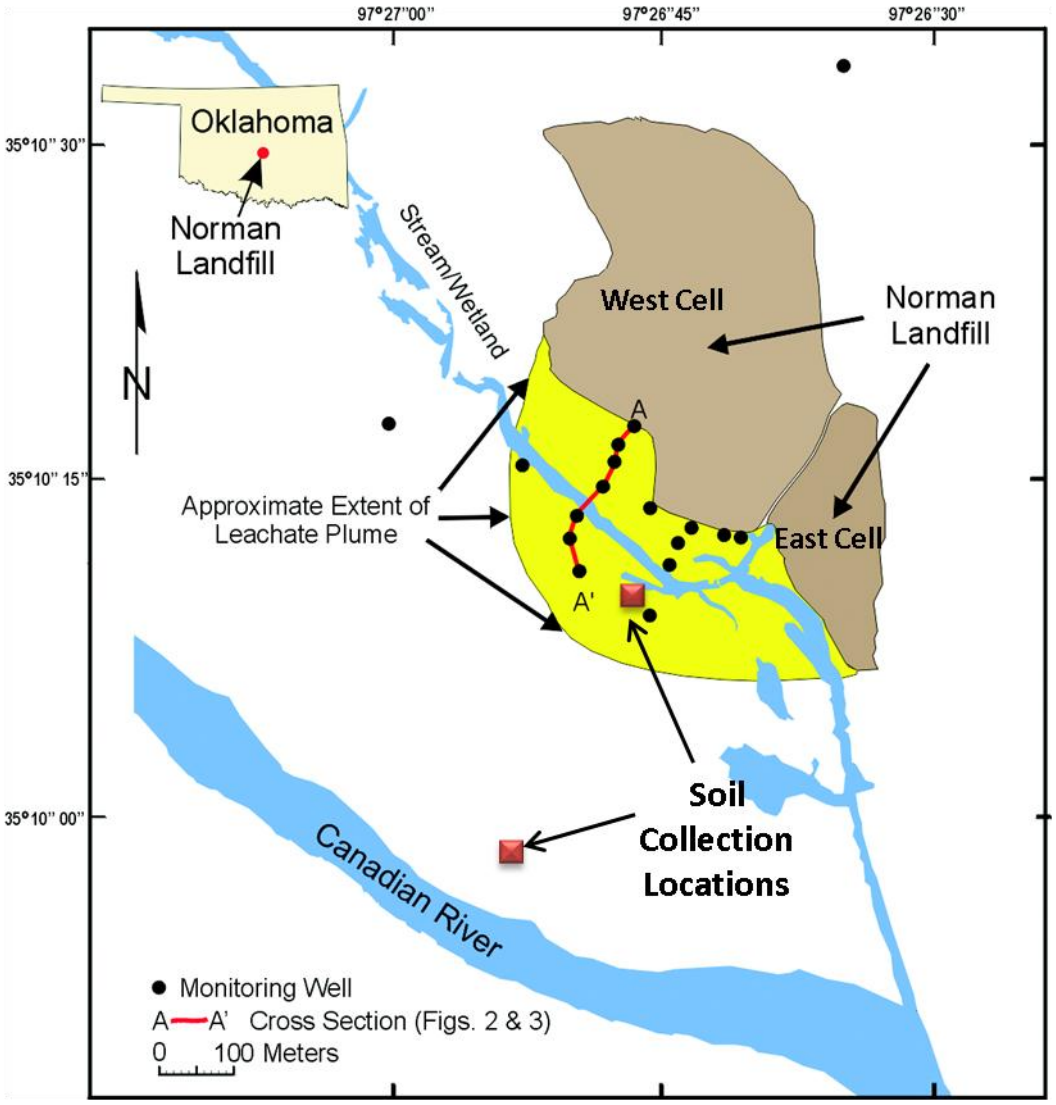

Figure 4.1: Location of the Norman Landfill site. Modified from *Scholl and Christenson* [1998].

The Norman Landfill has been designated as a U.S. Geological Survey research site and active investigations on the biogeochemistry of the leachate plume have been conducted since 1995. Research indicates that the groundwater between the landfill and the Canadian River is contaminated, with toxicity diminishing as distance from the landfill increases [*Bruner et al.*, 1998; *Cozzarelli et al.*, 2000; *Harris et al.*, 2006]. The biogeochemistry of the site indicates sulfate reduction, iron reduction, and methanogenesis to be important processes for degradation of organic matter [*Cozzarelli et al.*, 2000; *Eganhouse et al.*, 2001; *Grossman et al.*, 2002]. Recharge from precipitation and interaction of groundwater with the unsaturated zone control the availability and reoxidation of electron acceptors [*Scholl et al.*, 2006; *Baez-Cazull et al.*, 2008]. Soil cores were collected from unsaturated zone of the slough and the alluvium, and repacked to form laboratory soil columns (Figure 4.1).

4.3.2 Soil column setup

Three soil columns were constructed to understand the underlying redox processes and to evaluate the effect of layering: a homogenized fine-grained sand, homogenized organic-rich loam, and a sand-over-loam layered column (Figure 4.2). The soil cores collected from the Norman landfill site were air-dried, ground, and repacked using a piston compactor to attain a dry bulk density of 1.4 Mg/m^3 for sand and 1.0 Mg/m^3 for loam soil columns. The cylindrical soil columns were 40 cm in length and 15 cm in diameter. The layered column had 18 cm of sand over 22 cm of loam.

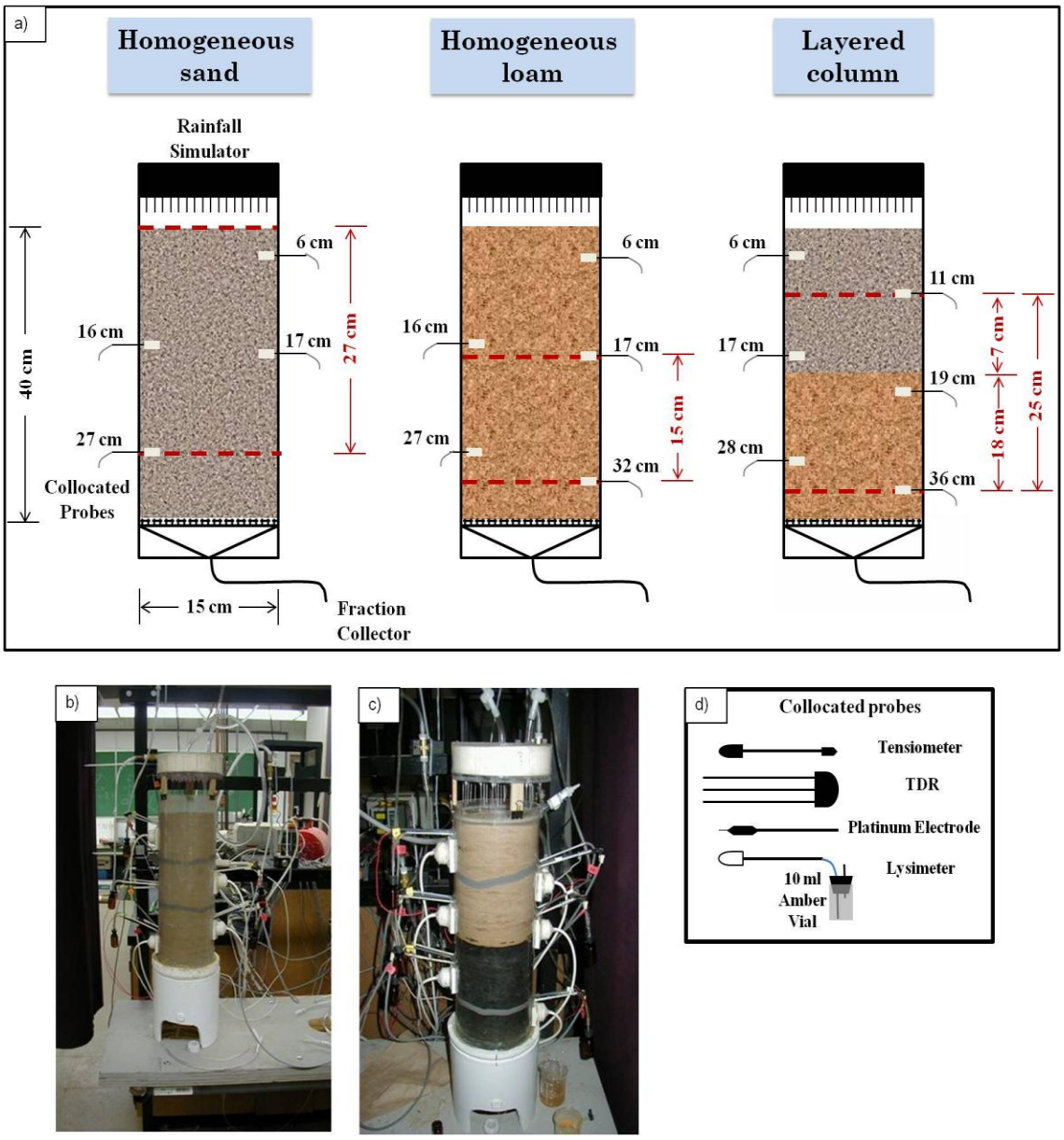

Figure 4.2: Schematic of a) the homogenous sand, homogeneous loam, and layered sand-over-loam columns with description of the modeling domains (dashed red lines) (Modified from *Hansen et al.*, 2011), b) the experimental layout of the homogenous sand column, c) the experimental layout of the layered column, and d) the collocated probe.

Rainwater was introduced using a rainfall simulator through a matching diameter disc (15 cm) installed with gauge needles [*Köhne and Mohanty*, 2005]. Boundary conditions were maintained using a tension infiltrometer at the top of the soil column. Tensiometer and time-domain reflectometry (TDR) probes were installed at various depths throughout the columns to monitor pressure head and water content profiles, respectively (Figure 4.2).

For geochemical analyses, lysimeters with amber vials were installed at various depths in the columns (Table 4.1) and used to collect low volume porewater (less than 7 ml). This porewater was used to analyze pH, alkalinity, and concentrations for major anions (Cl^-, Br^-, SO_4^{2-}, and NO_3^-) and cations (Ca^{2+}, K^+, Na^+, and NH_4^+). Reduced species of iron and sulfur, and redox potential (Eh) were quantified voltammetrically using a hanging drop mercury electrode. A fraction collector was used intermittently to analyze concentration profiles from the bottom of the soil columns. Microbiological analysis and soil imaging were done on soil cores extracted from the columns after the experiments were completed. These basically enumerated the type and most probable number (MPN) for iron and sulfate reducing bacteria [*Hansen et al.*, 2012a]. Further information on the experimental setup and analyses can be obtained elsewhere [*Hansen et al.*, 2011].

Table 4.1: Location of collocated probes (tensiometers, TDRs, and lysimeters) from the top of the soil columns.

Columns	Depth of collocated probes in cm
Homogeneous Sand	6, 16, 17, 27
Homogeneous Loam	6#, 16#, 17, 27, 32
Layered Column	6#, 11, 17, 19, 28, 36

Collocated probe not working at the given depth.

4.4 Modeling framework

4.4.1 Statistical analysis

Exploratory data analysis is performed on all geochemical measurements as well as TDR and tensiometer data to establish normality conditions (or lack thereof). Probability density functions based on the Kolmogorov-Smirnov test reject the null hypothesis and indicate non-normal distributions for almost all variables. As a result, only conservative, non-parametric statistics are used for analyzing correlations among physical (e.g. flow rate, hydraulic conductivity) and chemical factors (e.g. aqueous concentrations, pH, Eh). Standardization of the data is done using z-scores and a Spearman's Rho correlation is performed on the dataset. Correlations with rho values greater than 0.5 and p-values less than 0.0001 are considered significant as large datasets typically result in lower p-values [*Baez-Cazull et al.*, 2008; *Hansen et al.*, 2012b]. Principal component analysis (PCA) is employed to identify trends and interpret processes that could explain the most variability within the dataset. A varimax orthogonal rotation is used in this study and factors are assigned to dominant processes

that highlight the differences between homogeneous and layered soil columns. The selection of factors is based on eigenvectors whose eigenvalues are greater than one according to the Kaiser criterion [*Kaiser*, 1960].

4.4.2 Simulation model

This study uses HP1 for modeling observed infiltration and drainage events as well as for simulated perturbation experiments to derive an understanding of the underlying redox processes within the soil columns. HP1 integrates the flow and solute transport code of HYDRUS-1D with geochemical simulations of PHREEQC [*Parkhurst and Appelo*, 1999; *Jacques and Šimůnek*, 2005; *Šimůnek et al.*, 2008]. The combined HP1 model permits simultaneous simulations of variably-saturated water flow, multicomponent solute transport, and coupled reactive transport under a broad range of transient flow conditions and heterogeneous soil profiles. HP1 uses an operator-splitting approach where flow and solute transport are first implemented using the Richards' (equation 4.1) and convection-dispersion equations (CDE) (equation 4.6), respectively, and then equilibrium and kinetic biogeochemical reactions are solved:

$$\frac{\partial \theta(h)}{\partial t} = \frac{\partial}{\partial z}\left[K(h)\left(\frac{\partial h}{\partial z} + 1 \right) \right] - S \qquad (4.1)$$

where z is the vertical coordinate positive upwards [L], t is time [T], θ is the volumetric water content [L^3L^{-3}], h is the soil water pressure head [L], K is the unsaturated hydraulic conductivity [LT^{-1}], and S is a sink term [L^3L^{-3} T^{-1}]. To describe the relation between $\theta(h)$ and $K(h)$, which is required to solve the Richards' equation, a set of closed-form equations is used [*van Genuchten*, 1980]:

$$K(h) = KsS_e^l \left\{1 - \left[1 - (S_e^{1/m})\right]^m\right\}^2 \tag{4.2}$$

$$S_e = \frac{\theta(h) - \theta r}{\theta s - \theta r} \tag{4.3}$$

$$m = 1 - \frac{1}{n} \tag{4.4}$$

where θr and θs are the residual and saturated water contents [L^3L^{-3}], respectively, Ks is the saturated hydraulic conductivity [LT^{-1}], α is a shape parameter related to the inverse of air-entry suction [L^{-1}], n is a measure of the pore-size distribution [-], l is a pore connectivity parameter [-], and S_e is the effective saturation.

Solute transport in HP1 is achieved by writing the geochemical reactions in terms of aqueous master species and their stoichiometric components [*Morel and Hering*, 1993]:

$$\sum_{j=1}^{N_m} v_{ji} A_j^m = A_i \tag{4.5}$$

where N_m is the number of aqueous master species, i=1,…., N_s, N_s are the number of aqueous secondary species, v_{ji} are the stoichiometric coefficients in the reaction, and A_j^m and A_i are the chemical formula for the master and secondary species, respectively. CDE for each aqueous component is then described as [*Mayer*, 1999; *Jacques et al.*, 2008]:

$$\frac{\partial \theta c_j}{\partial t} = \frac{\partial}{\partial z}\left(\theta D \frac{\partial c_j}{\partial z}\right) - \frac{\partial q c_j}{\partial z} - SC_{r,j} + R_{o,j} \tag{4.6}$$

where j=1,…., N_m, D is the dispersion coefficient in the liquid phase [L^2T^{-1}], q is the volumetric flux density [LT^{-1}], S is the sink term (from equation 4.1), $C_{r,j}$ is the total concentration of the sink term [ML^{-3}], $R_{o,j}$ is the source/sink term that represents aqueous

kinetic reactions and/or heterogeneous equilibrium and kinetic reactions, and C_j is the total liquid concentration defined as:

$$C_j = c_j + \sum_{j=1}^{N_a} \nu_{j,i} c_i \tag{4.7}$$

The non-iterative sequential approach of the HP1 simulator is described in detail by *Jacques et al.* [2006].

4.4.3 Numerical implementation

Observed experiments and simulated perturbations are used to infer the dominant processes causing biogeochemical variations in all experimental columns. The soil columns are represented by a one-dimensional mesh with 100 elements. An initial time-step of 0.5 min, and minimum and maximum time steps of 0.05 and 5 min are used for all experiments. Boundary conditions for the soil columns are based on the transient conditions observed at the uppermost and lowermost collocated probes within the columns. As the uppermost probe malfunctioned, the top of the soil profile is truncated to the depth of the next working probe (Table 4.1). Similarly, to assign a bottom boundary condition, 13, 8 and 4 cm of the homogeneous sand, homogeneous loam, and layered columns are respectively truncated based on the location of the lowest probe. The numerical domain and modeling depth for all soil columns are shown in Figure 4.2.

Table 4.2: Boundary conditions (BC) as specified at the soil surface ($z=L$) and bottom of the soil profile (z=0) for different experiments of the soil columns*.

Columns	Experiment	Upper BC	Lower BC
Homogeneous sand	Infiltration	$h_{z=L}(t)=\begin{cases}1.37, 0<t<t_r\\ \vdots, t_r<t<t_e\\ -2.67, t=t_e\end{cases}$	$h_{z=0}(t)=\begin{cases}0.18, 0<t<t_r\\ \vdots, t_r<t<t_e\\ -2.86, t=t_e\end{cases}$
	Numerical Perturbation##	$h_{z=L}(t)$ = 10 cm, 0<t<t_e	$q_{z=0}(t)$ = 0, if $h_{z=0}(t)$ < 0 $h_{z=0}(t)$ = 0, else#
	Drainage	$h_{z=L}(t)=\begin{cases}-2.75, 0<t<t_r\\ \vdots, t_r<t<t_e\\ 0.19, t=t_e\end{cases}$	$h_{z=0}(t)=\begin{cases}-2.88, 0<t<t_r\\ \vdots, t_r<t<t_e\\ -0.21, t=t_e\end{cases}$
Homogeneous loam	Infiltration	$h_{z=L}(t)=\begin{cases}-70.82, 0<t<t_r\\ \vdots, t_r<t<t_e\\ -8.48, t=t_e\end{cases}$	$h_{z=0}(t)=\begin{cases}-70.17, 0<t<t_r\\ \vdots, t_r<t<t_e\\ -17.23, t=t_e\end{cases}$
	Drainage	$h_{z=L}(t)=\begin{cases}-26.75, 0<t<t_r\\ \vdots, t_r<t<t_e\\ -37.91, t=t_e\end{cases}$	$h_{z=0}(t)=\begin{cases}-22.49, 0<t<t_r\\ \vdots, t_r<t<t_e\\ -26.31, t=t_e\end{cases}$
	Numerical Perturbation##	$h_{z=L}(t)$ = -5 cm, 0<t<t_e	$q_{z=0}(t)$ = 0, if $h_{z=0}(t)$ < 0 $h_{z=0}(t)$ = 0, else#
Layered sand-over-loam column	Infiltration	$h_{z=L}(t)=\begin{cases}-69.34, 0<t<t_r\\ \vdots, t_r<t<t_e\\ 1.72, t=t_e\end{cases}$	$h_{z=0}(t)=\begin{cases}-50.21, 0<t<t_r\\ \vdots, t_r<t<t_e\\ 4.30, t=t_e\end{cases}$
	Drainage	$h_{z=L}(t)=\begin{cases}1.34, 0<t<t_r\\ \vdots, t_r<t<t_e\\ -27.06, t=t_e\end{cases}$	$h_{z=0}(t)=\begin{cases}4.78, 0<t<t_r\\ \vdots, t_r<t<t_e\\ -5.25, t=t_e\end{cases}$
All columns	Constant flux	$q_{z=L}(t)$ = -1 cm/min, 0<t<t_e	$q_{z=0}(t)$ = 0, if $h_{z=0}(t)$ < 0 $h_{z=0}(t)$ = 0, else#

*Symbols: h, pressure head; q, flux; z, vertical coordinate positive upwards; L, column length; t, time; with BCs specified as h values linearly interpolated for time, where t_r represents the time of tensiometer reading, and t_e represents the duration of the experiment.

These conditions represent a seepage face boundary condition [*Šimůnek et al.*, 1998].

Initial conditions correspond to the infiltration (drainage) experiment for perturbation to the homogeneous sand (loam) column.

Upper and lower hydraulic boundary conditions for observed infiltration and drainage experiments are set according to the transient flow conditions of the experiments (Table 4.2). Observations at different tensiometer locations in the soil are used to describe initial hydraulic conditions at various depths in the soil columns. These can be obtained from Table 4.2 for time t=0. For example, initial pressure head condition for a drainage experiment of the homogeneous loam column is given by:

$$h_z(t=0) = \begin{cases} -26.75, L < z < d_r \\ \vdots, d_r < z < 0 \\ -22.49, z = 0 \end{cases} \tag{4.8}$$

where L represents the truncated length of the soil column [L], and d_r represents the depth at which a working tensiometer is installed [L].

Solute analysis includes thirteen chemical species - Ba^{2+}, total carbon, Ca^{2+}, Cl^-, Fe^{2+}, Fe^{3+}, K^+, Mg^{2+}, Na^+, NH_4^+, NO_3^-, total P, and SO_4^{2-}. Ambient air temperature 22^0C (±2) as observed during the experiment is used for geochemical modeling. Initial chemical concentrations in the columns are based on geochemical analyses conducted on the soil cores (Table 4.3). Appropriate amounts of barium and carbon are also included in this solution. Exchanges among minerals like greigite (Fe_3S_4), pyrite (FeS_2), mackinawite (FeS), and Fe^{2+} and S^{2-} ions are included in the model. The top chemical boundary condition is associated with the rainwater composition (Table 4.4) while the bottom boundary is free drainage.

Table 4.3: Initial geochemical composition of the soil columns.

Columns	Constituent type	Concentration (mg/l)
Homogeneous sand	pH	8.5
	Ca	1688
	K	19
	Mg	56
	Na	154
	P	4
	S	40
	Fe	2.83
	NO_3^- - N	4
Homogeneous loam	pH	7.9
	Ca	24833
	K	86
	Mg	802
	Na	374
	P	5
	S	694
	Fe	88.3
	NO_3^- - N	2

Table 4.4: Rainwater composition from standards prepared by the National Bureau of Standards (SRM 2694).

Constituent type	Concentration (mg/l)
pH	4.3
Ca	0.014
Cl	0.24
K	0.052
Mg	0.024
Na	0.205
SO42-	2.69
F	0.054
NO_3^-	0.501

4.4.4 Model parameters

The main focus of this study is to analyze dominant biogeochemical processes and the effect of hydrological conditions on redox processes within homogeneous and layered soil profiles. Therefore, only results corresponding to forward simulations of water flow and transport of major cations and anions for the experimental soil columns will be described in detail. The soil water retention parameters for forward modeling are either obtained from laboratory measurements or inversely estimated using HYDRUS-1D. Saturated hydraulic conductivity parameters are obtained from soil cores, and matrix tortuosity parameters are fixed at 0.5 for both homogeneous sand and loam columns [*Mualem*, 1976]. In organic degradation studies, water retention characteristics of the soils have been reported to change [*Kalbitz et al.*, 2003; *Dexter et al.*, 2008]. Therefore, inverse estimation of some of the parameters (θr, θs, α, and n) is conducted using transient infiltration and drainage experiments of the soil columns. Table 4.5 enlists the soil water retention parameters for both homogeneous sand and loam configurations. Inverse analysis reveals a higher n value for the homogeneous loam column as compared to the sand column. Various studies have shown that higher organic content leads to an increase in porosity, which is reflected here by the soil retention parameter n [*Haynes and Naidu*, 1998; *Zhang et al.*, 2007]. As mentioned earlier, the organic-rich loam was collected from the leachate contaminated wetland.

Table 4.5: Water retention characteristics of the homogeneous sand and loam configurations [*Hansen et al.*, 2011].

Column	θr (-)	θs (-)	α (cm^{-1})	n (-)	Ks ($cm.min^{-1}$)	l (-)
Homogeneous sand	0.027	0.321	3.18	1.60	0.636	0.50
Homogeneous loam	0.015	0.385	2.02	1.86	0.141	0.50

4.5 Results and discussion

4.5.1 Principal component analysis

Spearman's rho correlation is unable to provide information about dominant biogeochemical processes within the columns as no significant correlations are found between any variables. As a result, factor analysis was conducted to identify dominant factors that can explain the variability within the experimental datasets of homogeneous sand, homogeneous loam and layered soil columns. PCA was performed on hydrological (depth, pressure head, water content values) and geochemical parameters (Cl^-, Br^-, SO_4^{2-}, NO_3^-, acetate, pH, alkalinity, K^+, Ca^{2+}, Na^+, Mg^{2+}, NH_4^+ and Eh). Table 4.6 indicates the constituents of each factor and their contribution is indicated in brackets. Only constituents with significant contributions (i.e. factor loadings > ±0.75) are reported. See appendix for other consitutents.

For the homogeneous sand column, the maximum variability (95.45%) of an infiltration experiment is explained by a single factor which is bromide. Since bromide is considered to be a conservative tracer, the process assigned to this factor is advective transport.

Table 4.6: Varimax orthogonal factor rotation obtained from principal component analysis of infiltration experiments of the soil columns.

Column	Factor	Percent	Constituent (loadings)
Homogeneous sand	Factor 1	95.45	Br^-(0.98)
Homogeneous loam	Factor 1	59.62	SO_4^{2-} (0.95)
	Factor 2	34.76	Br^- (0.88)
	Factor 3	3.86	Alkalinity (0.82)
Layered column	Factor 1	74.62	Alkalinity (-0.70), SO_4^{2-} (-0.50)
	Factor 2	24.42	SO_4^{2-} (0.90), Alkalinity (-0.80)

The most dominating factor of the homogeneous loam column has a positive loading of sulfate, which is interpreted to be FeS oxidation and/or sulfate mineral dissolution. Our interpretations are consistent with those reported by *Baez-Cazull et al.* [2008] in their analysis of the Norman Landfill dataset of 3 years. They suggested that positive loading of sulfate corresponds to sulfide oxidation and observations at the landfill site indicate that a decrease in water table re-oxidizes iron sulfide minerals thereby providing a fresh supply of sulfate. The second factor of the homogeneous loam column includes bromide and indicates advective transport. The third factor has a positive loading of alkalinity and also suggests advection processes. This is consistent with associations reported by *Baez-Cazull et al.* [2008] in evaluating dominant biogeochemical processes at the Norman landfill site. In our homogeneous loam column, it seems that the infiltrating water is oxidizing FeS minerals. This suggests that this column is affected by coupled geochemical reactions (iron-sulfide oxidation) and hydrological transport.

The infiltration experiment of the layered column is associated with two factors that are both affected by sulfate and alkalinity but to different extents. A negative loading of alkalinity in both factors is associated with decrease in water flow with depth and could be attributed to ponding at the sand-loam interface of the layered column. This is consistent with our previous interpretation that alkalinity is related to advection processes. Sulfate also has a negative loading in factor 1 of the layered column and could be connected to sulfate reduction. Previous research has indicated that the first factor is a good indicator of bacterial degradation processes [*Dauwe et al.*, 1999; *Sheridan et al.*, 2002]. Our study confirms this information as sulfate reduction is an important biogeochemical process for both our layered column and the Norman landfill site [*Cozzarelli et al.*, 2000; *Grossman et al.*, 2002; *Hansen et al.*, 2012a]. A positive loading of sulfate in factor 2 indicates secondary redox processes such as FeS oxidation and/or sulfate mineral dissolution. It seems that this column is strongly affected by impedance of water flow at the interface, indicated by negative loading of alkalinity in both factors, and redox cycling of sulfur, indicated by changing signs of sulfur loading. This dominance of interface over other biogeochemical processes reflects the importance of including subsurface heterogeneity in contaminant fate and transport studies in the vadose zone.

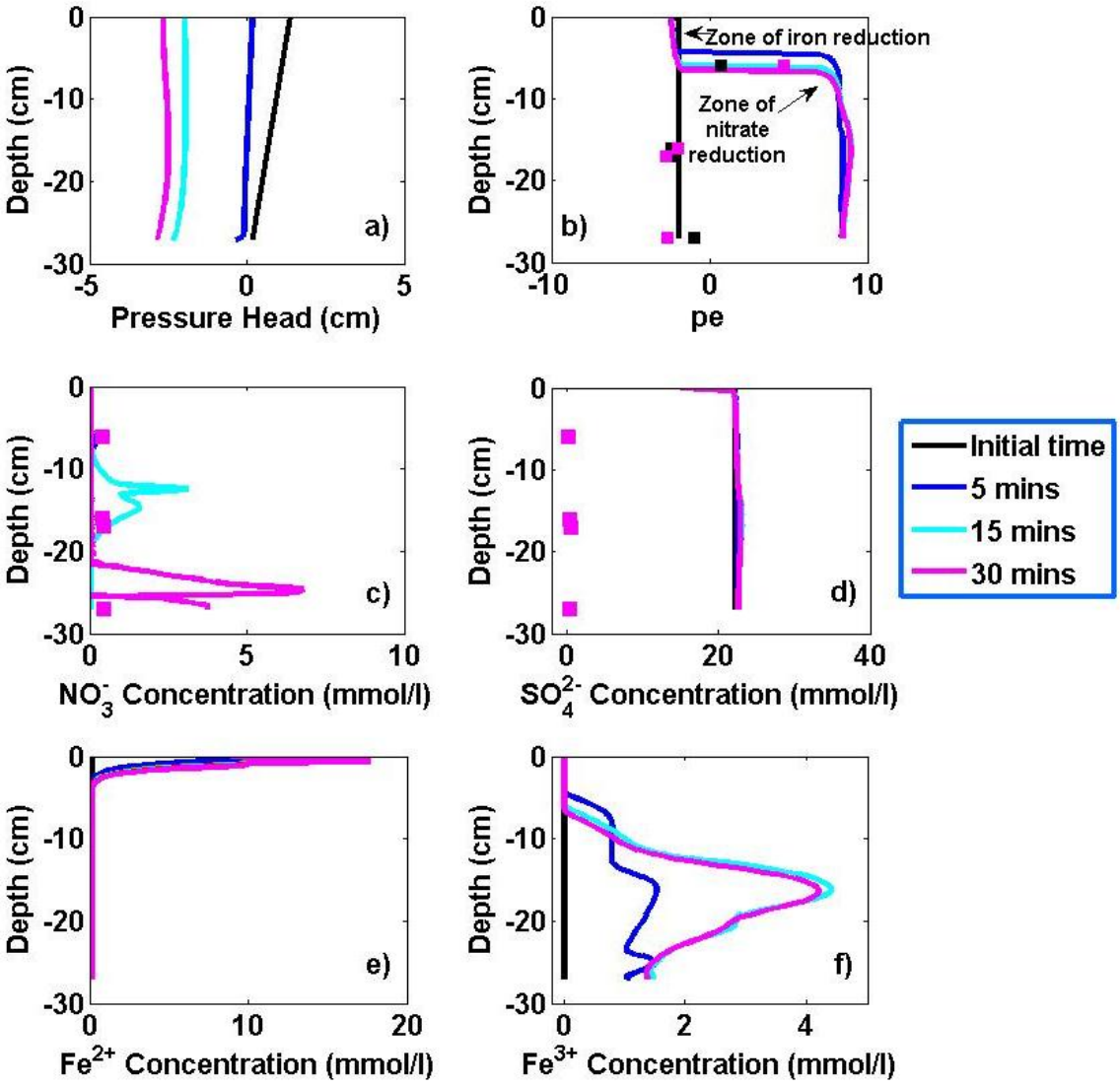

Figure 4.3: Simulated and observed time series of a) pressure head, b) pe, c) NO_3^-, d) SO_4^{2-}, e) Fe^{2+}, and f) Fe^{3+} concentrations for a transient drainage experiment of the homogeneous sand column. Solid lines indicate model predictions, solid squares indicate observations, and color scheme corresponds to time. Note that observations are not available for all times.

4.5.2 Effect of hydrologic conditions

Experimental observations are analyzed and compared with HP1 modeling simulations to understand the dominant redox processes occurring within the homogeneous and layered soil columns, and numerical perturbations are used to illustrate the effect of hydrologic variability on these dominant redox processes. pe, which is a measure of electron activity, and Eh, which is the redox potential, are used throughout this study to describe redox states within these columns.

4.5.3 Homogeneous sand column

Predictions of forward modeling and observations of flow experiments of the homogeneous sand column are documented briefly (Figures 4.3 and 4.4). Figure 4.3 depicts the dominant processes in the homogeneous sand column while Figure 4.4 evaluates the effect of hydrologic perturbations on these dominant processes. Figure 4.3 demonstrates variations in simulated and observed pressure head, pe, and concentration profiles of NO_3^-, SO_4^{2-}, Fe^{2+}, and Fe^{3+} for the vertical depth of the homogeneous sand column during a transient drainage experiment. HP1 simulations suggest that NO_3^- reduction (Figure 4.3c) is occurring below 5-7 cm in the column where predicted nitrate concentrations first reach a peak value, then decrease, and the remaining concentrations get transported through the column.

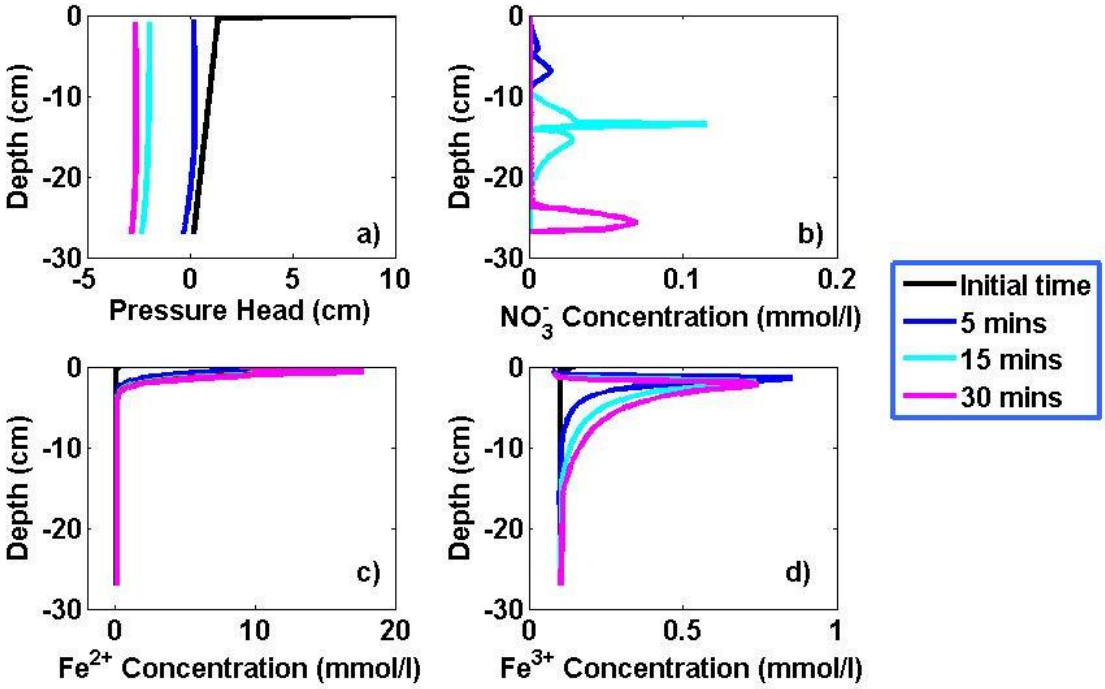

Figure 4.4: Simulated time series of a) pressure head, b) NO_3^-, c) Fe^{2+}, and d) Fe^{3+} concentrations for perturbed drainage experiment of the homogeneous sand column. Solid lines indicate model predictions, and color scheme corresponds to time.

Forward modeling further indicates iron reduction to be occurring in the top 0-5 cm of the homogeneous sand column where Fe^{2+} concentrations increase with time (Figure 4.3e) and Fe^{3+} concentrations decrease (Figure 4.3f). Figure 4.3d shows that sulfate concentrations increase at the top boundary and then remain fixed at 22 mmol/l for the entire duration of the transient drainage experiment. Therefore, HP1 modeling indicates thermodynamic controls where nitrate and iron reduction are occurring in the column while sulfate is just being transported through the column. These predictions are confirmed by simulated pe (Figure 4.3b) which is close to -2 in the zone of iron reduction (0-5 cm) and increases to 8 in the zone of nitrate reduction (5-7 cm). It seems

that the depth and predictions of nitrate and iron reduction, presence of Fe^{2+}, and absence of sulfate reduction are all being controlled by pe. This is confirmed by numerically perturbing the system and introducing a constant head of 10 cm at the top of the soil profile (Table 4.2). Figure 4.4 illustrates that the pe variations (under perturbed top boundary condition) are focused around the top 2 cm of the soil column such that iron reduction and presence of Fe^{2+} are concentrated in this particular zone instead of 0-5 cm (as in Figure 4.3), and nitrate reduction is observed below 2 cm instead of 5-7 cm in Figure 4.3. These results demonstrate that predicted pe is the controlling factor in establishing aqueous speciations and geochemical concentrations at different depths within the sand column, while predicted pe is regulated by hydrologic boundary conditions for this column.

Observations from the transient drainage experiment in Figure 4.3 suggest that nitrate is still present in the system while sulfate has been consumed. Observed pe (Figure 4.3b) is also close to -2 and suggests that sulfate reduction is occurring at least below 10 cm in this column. This mismatch between observed and predicted concentrations can be a result of redox disequilibrium caused by active sulfate reducing bacteria (SRB). Observations of SRB have been made in MPN and microbiological analysis for this column [*Hansen et al.*, 2012a] and at the Norman landfill site [*Beeman and Suflita*, 1987; *Tanner*, 1989; *Ulrich et al.*, 2003]. Figure 4.5 illustrates a better agreement between HP1 predictions and observations of sulfate concentration and redox potential when reaction kinetics for sulfate reduction are considered. A Michaelis-Menten type relationship is used and the corresponding reaction rate parameters are

comparable within an order of magnitude with parameters suggested by *Ulrich et al.* [2003] in their analysis of aquifer sediments for sulfate reduction rates at the Norman landfill site.

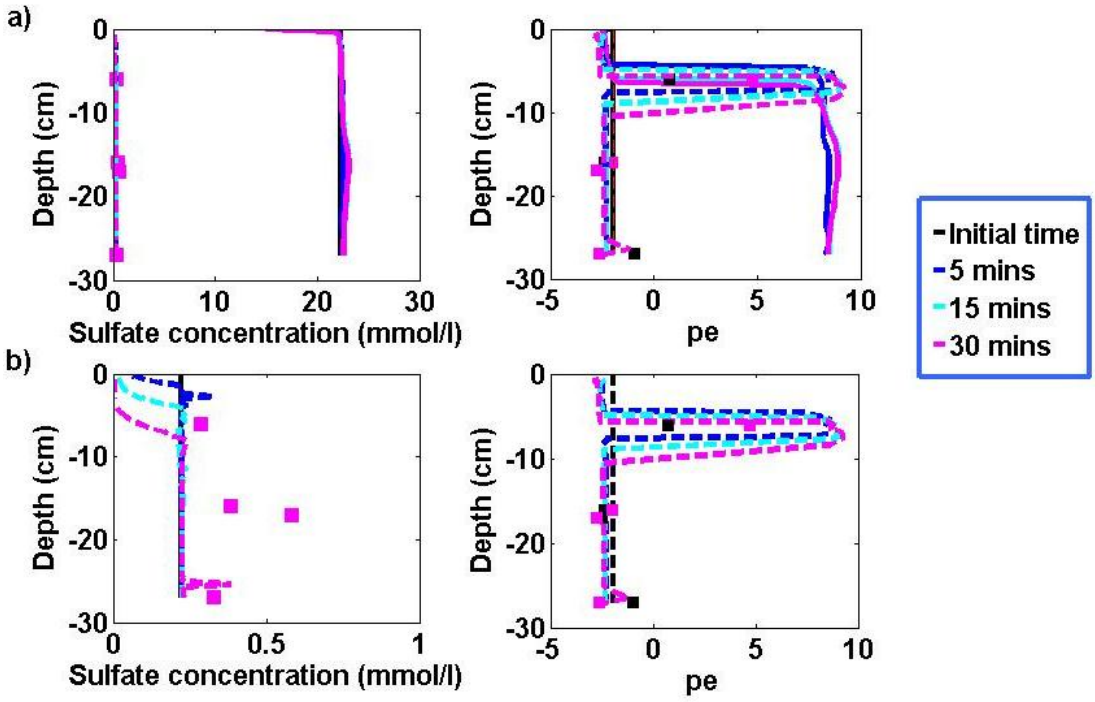

Figure 4.5: Simulated and observed sulfate concentration and pe a) comparing model predictions before and after considering reaction kinetics, and b) considering reaction kinetics only for the homogeneous sand column. Solid lines indicate model predictions without reaction kinetics, dashed lines indicate model predictions considering reaction kinetics, solid squares indicate observations, and color scheme corresponds to time. Note that observations are not available for all times.

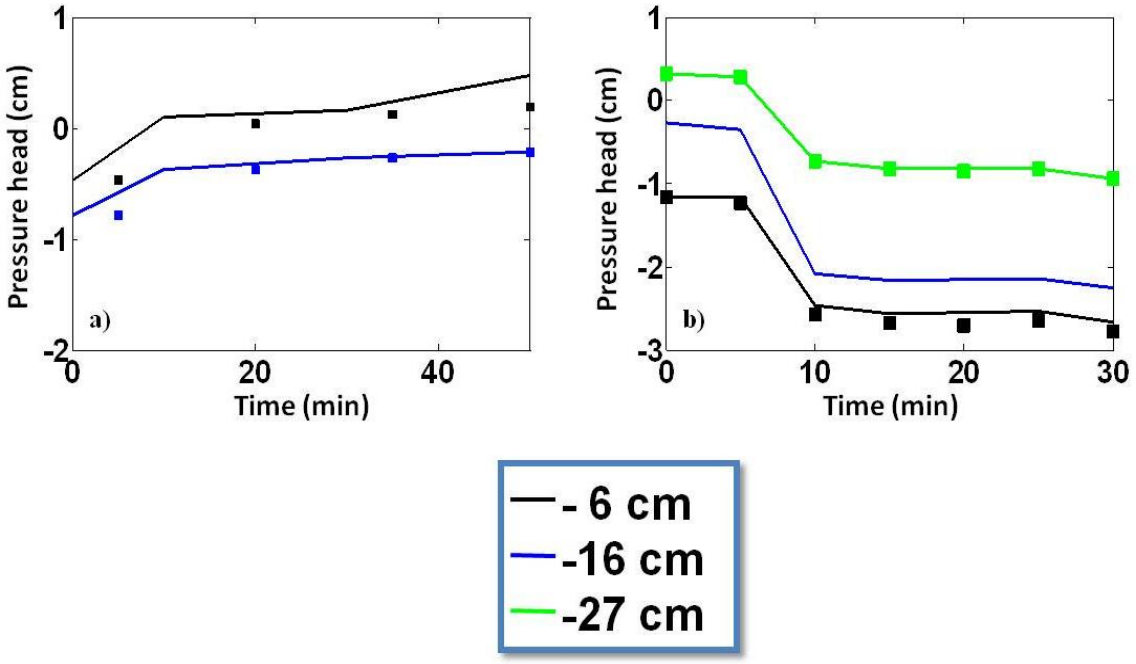

Figure 4.6: Simulated and observed pressure head profiles for a) infiltration and b) drainage experiments of the homogeneous sand column. Solid lines indicate model predictions, solid squares indicate observations, and color scheme corresponds to depth. Note that observations are not available for all depths.

Figure 4.6 shows pressure head measurements at 6, 16 and 27 cm for transient infiltration and drainage experiments. The estimated soil hydraulic parameters for the homogeneous sand column are able to reproduce sufficient details of the pressure head profiles. Separate adjustments of parameters for the infiltration and drainage experiments are not done to maintain consistency in parameters. In summary, HP1 modeling indicates that hydrologic perturbations especially boundary conditions affect redox processes (such as initiation of nitrate reduction) in the homogeneous sand column while experimental observations indicate redox disequilibrium with respect to sulfate reduction within the column.

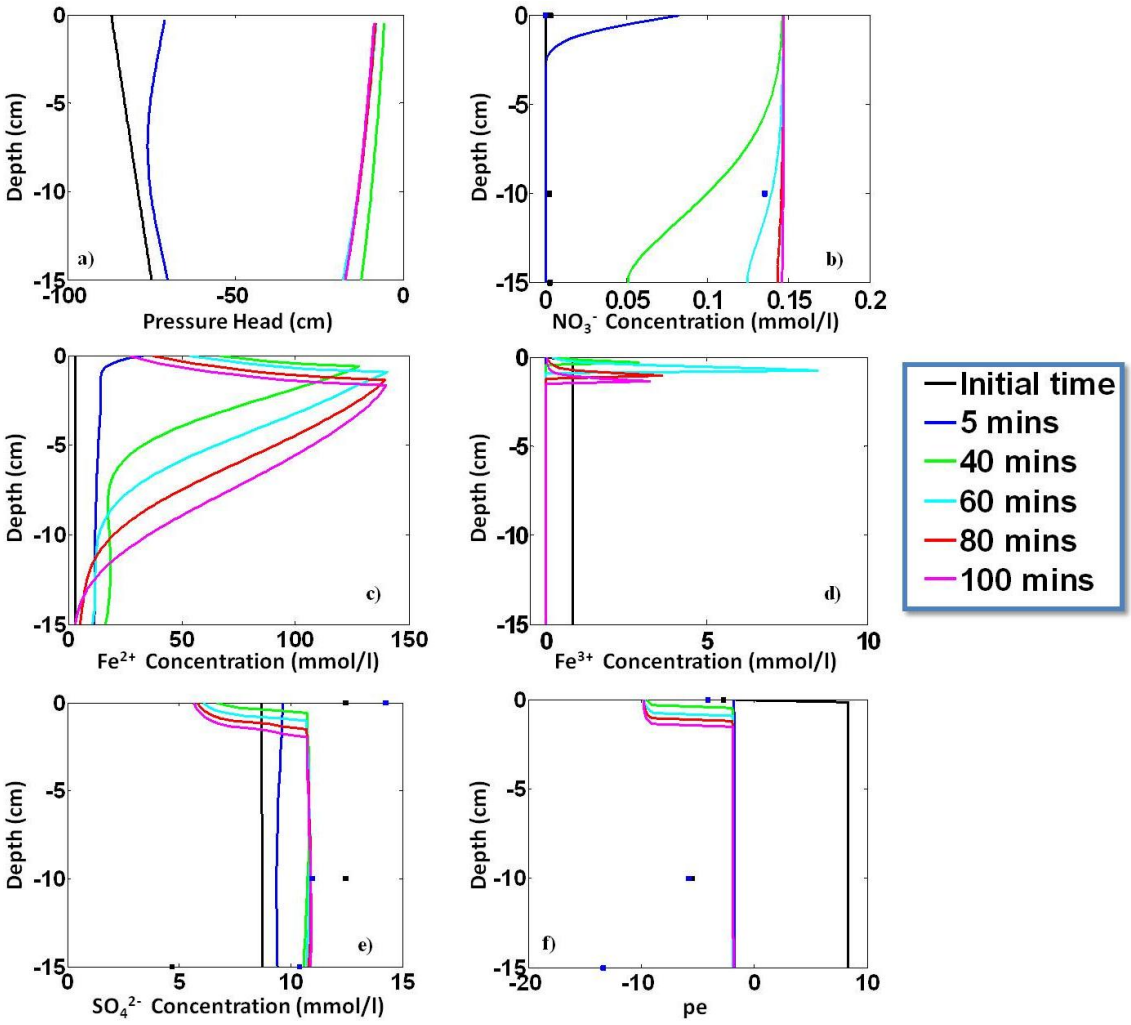

Figure 4.7: Simulated and observed time series of a) pressure head, b) NO_3^- concentrations, c) Fe^{2+} concentrations, d) Fe^{3+} concentrations, e) SO_4^{2-} concentrations, and f) pe for a transient infiltration experiment of the homogeneous loam column. Solid lines indicate model predictions, solid squares indicate observations, and color scheme corresponds to time. Note that observations are not available for all times.

4.5.4 Homogeneous loam column

An observed infiltration experiment under transient flow conditions is used to infer the aqueous speciation (Figure 4.7), and a perturbed drainage experiment is used to evaluate the effect of hydrologic variations on the redox geochemistry of the homogeneous loam column (Figure 4.8). Model predictions in Figure 4.7 indicate that the boundary/hydrologic conditions hold much importance as the initial two times with unsaturated conditions (pressure head values < -50 cm in Figure 4.7a) have different concentration patterns (e.g., Figure 4.7b, c, e) than later times when pressure head is close to saturation. Forward modeling further indicates iron oxidation to be occurring in the top 0-3 cm of the homogeneous loam column where Fe^{2+} concentrations decrease (Figure 4.7c) and Fe^{3+} concentrations increase (Figure 4.7d). This is the reason that Fe^{3+} presence is limited to the top few cms of the homogeneous loam column (Figure 4.7d). Figure 4.7c illustrates that Fe^{2+} that has not been oxidized is transported through the profile as is nitrate (Figure 4.7b) which is present in the infiltrating rainwater (Table 4.4). HP1 results suggest that iron is being oxidized from nitrate. This interpretation is confirmed by perturbing the hydrologic conditions and introducing a constant head at the top of the soil column for a transient drainage experiment (Table 4.2).

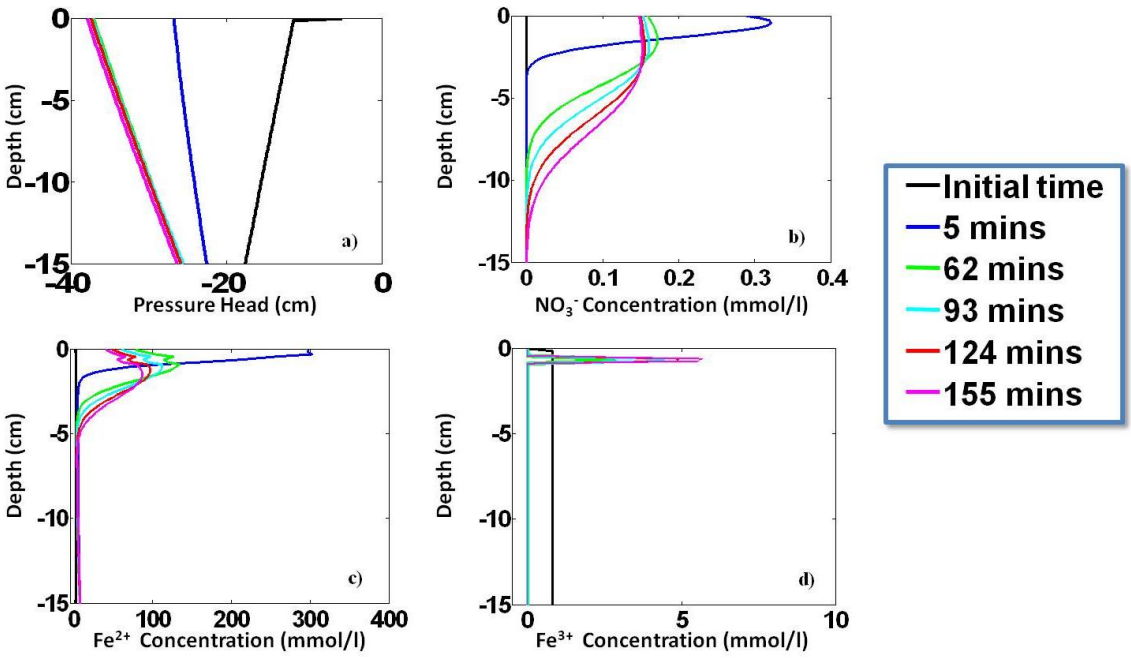

Figure 4.8: Simulated time series of a) pressure head, b) NO_3^-, c) Fe^{2+}, and d) Fe^{3+} concentrations (mmol/l) for perturbed drainage experiment of the homogeneous loam column. Solid lines indicate model predictions, and color scheme corresponds to time.

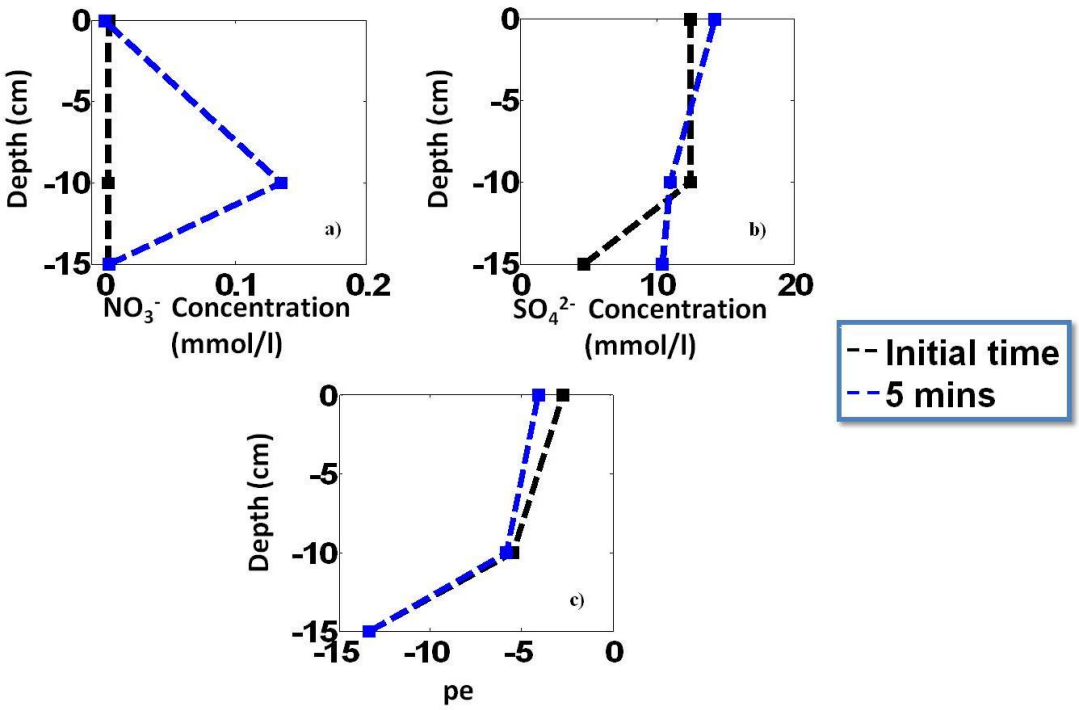

Figure 4.9: Observed gradients of a) NO_3^- concentrations, b) SO_4^{2-} concentrations, and c) pe for a transient infiltration experiment of the homogeneous loam column. Dashed lines indicate gradients, solid squares indicate observations, and color scheme corresponds to time.

Figure 4.8a depicts the perturbations induced using initial pressure head conditions (solid black line). With ponding conditions, simulations (blue line) at 5 min depict an increase in nitrate (Figure 4.8b) and ferrous iron (Figure 4.8c) concentrations. The decrease in NO_3^- (Figure 4.8b) and Fe^{2+} (Figure 4.8c) concentrations at all other times is related to ferrous iron being oxidized from nitrate and causing an increase in Fe^{3+} concentrations (Figure 4.8d) in the top 1-2 cm of the soil column.

In the loam column, Figure 4.7 indicates that our predictions are closer to observations for both sulfate (Figure 4.7e) and nitrate concentrations (Figure 4.7b) in terms of orders of magnitude as compared to the homogeneous sand column. However, observation trends corresponding to these suggest a significant decrease in transport processes especially in the bottom 5 cm of the modeled column (see Figure 4.9). This is consistent with our experimental observations that suggest a decrease in hydraulic conductivity with depth due to the presence of FeS precipitates [*Hansen et al.*, 2011]. Therefore, the mismatch between trends of sulfate and other data indicates the importance of including feedback mechanism from geochemical processes (FeS precipitates) to hydraulic transport (reduced advection) to improve model predictions. HP1 modeling results indicate iron oxidation from nitrate reduction to be a dominant redox process and again emphasize the significance of hydrologic boundary conditions for the homogeneous loam column.

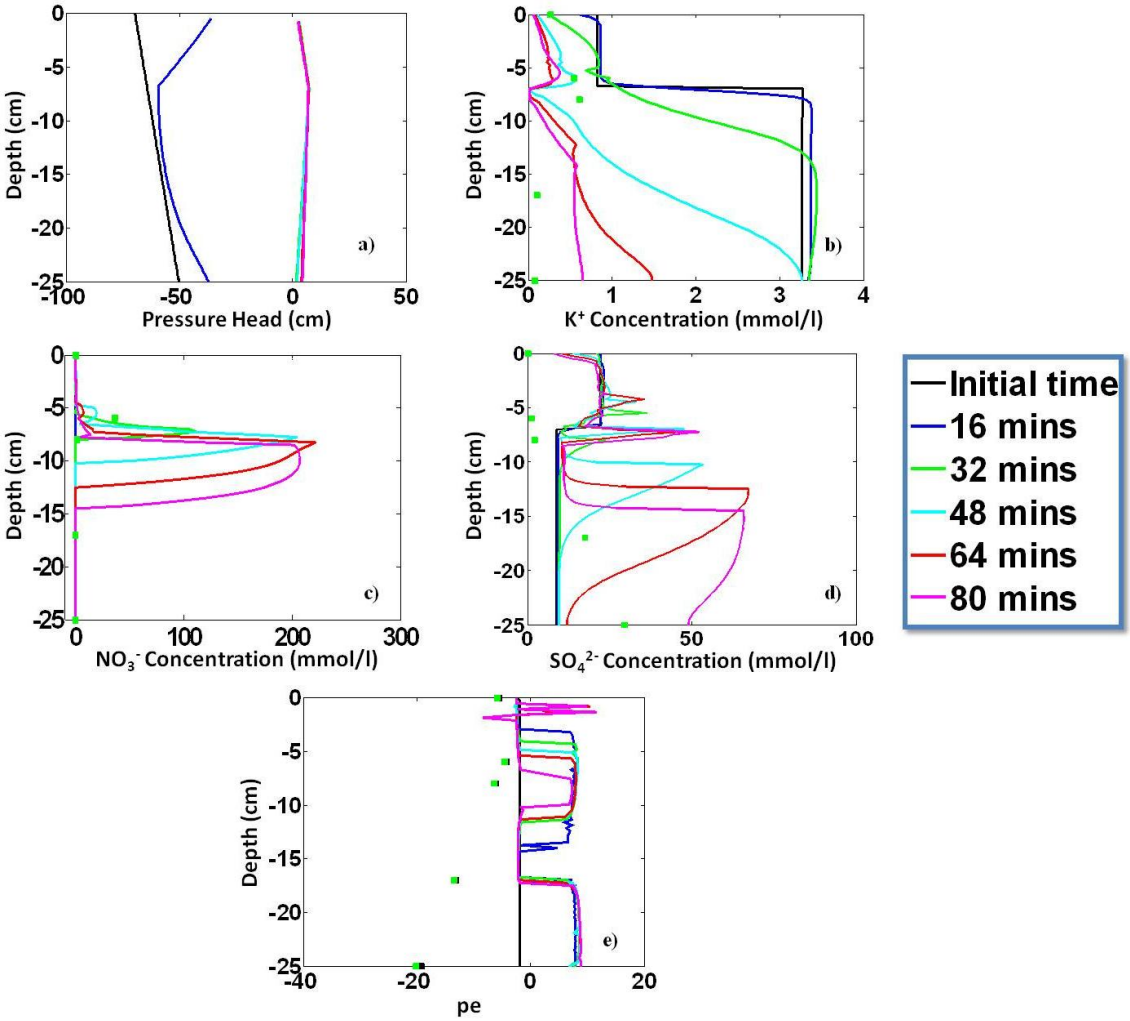

Figure 4.10: Simulated and observed depth profiles of a) pressure head, b) K^+, c) NO_3^-, d) SO_4^{2-}, and e) pe for a transient infiltration experiment of the layered column (textural layering at 7 cm). Solid lines indicate model predictions, solid squares indicate observations, and color scheme corresponds to time. Note that observations are not available for all times.

4.5.5 Layered sand-over-loam column

Figure 4.10 illustrates simulation of a transient infiltration experiment of the layered sand over loam column. The layering at 7 cm for the simulated 25 cm of the column is visible within all graphs as the point of shift in pressure head (Figure 4.10a) and concentration profiles (e.g. Figures 4.10b-d). Observations and predictions of nitrate (Figure 4.10c) suggest excessive accumulation at the interface, and slow transport in the bottom loam layer due to the lower saturated hydraulic conductivity (0.141 cm/min) as compared to the top sand layer (0.636 cm/min). HP1 predictions indicate that sulfate (Figure 4.10d) is present at different concentrations above and below the 7 cm textural interface. Figure 4.11a demonstrates that as time proceeds, more sulfate is accumulated above the layering, and is slowly being reduced between 7-10 cm. Below the reducing zone, HP1 predictions indicate that sulfate is being transported through the loam layer. Modeled Fe^{2+} profile (Figure 4.11b) suggests that iron reduction is occurring and Fe^{2+} is being transported in the same zones, encompassing slightly larger zones than those predicted for sulfate (Figure 4.11a), as Eh conditions for iron reduction are slightly lower than for sulfate reduction. The absence of Fe^{2+} concentrations (Figure 4.11b) in non-reducing zones indicate the formation of iron sulfide precipitates within the layered column which corroborates well with our observations of this column [*Hansen et al.*, 2012a].

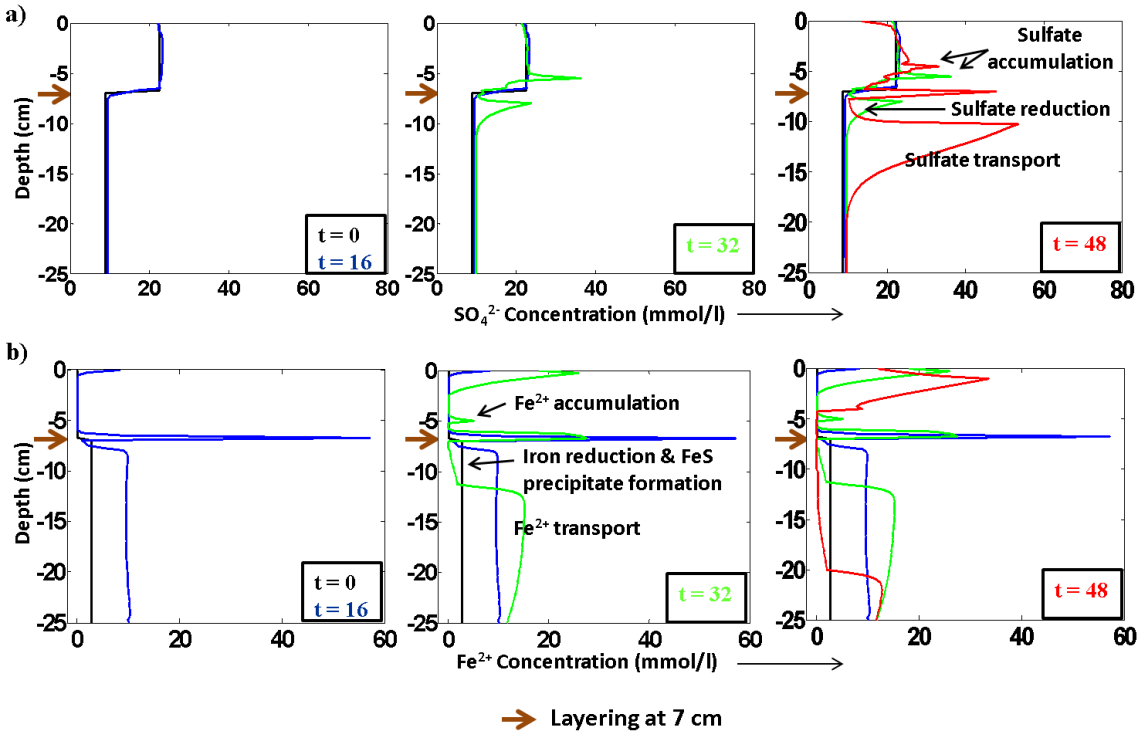

Figure 4.11: Time progression of simulated vertical profiles of a) SO_4^{2-}, and b) Fe^{2+} concentrations for a transient infiltration experiment of the layered column. Solid lines indicate model predictions, and color scheme corresponds to time.

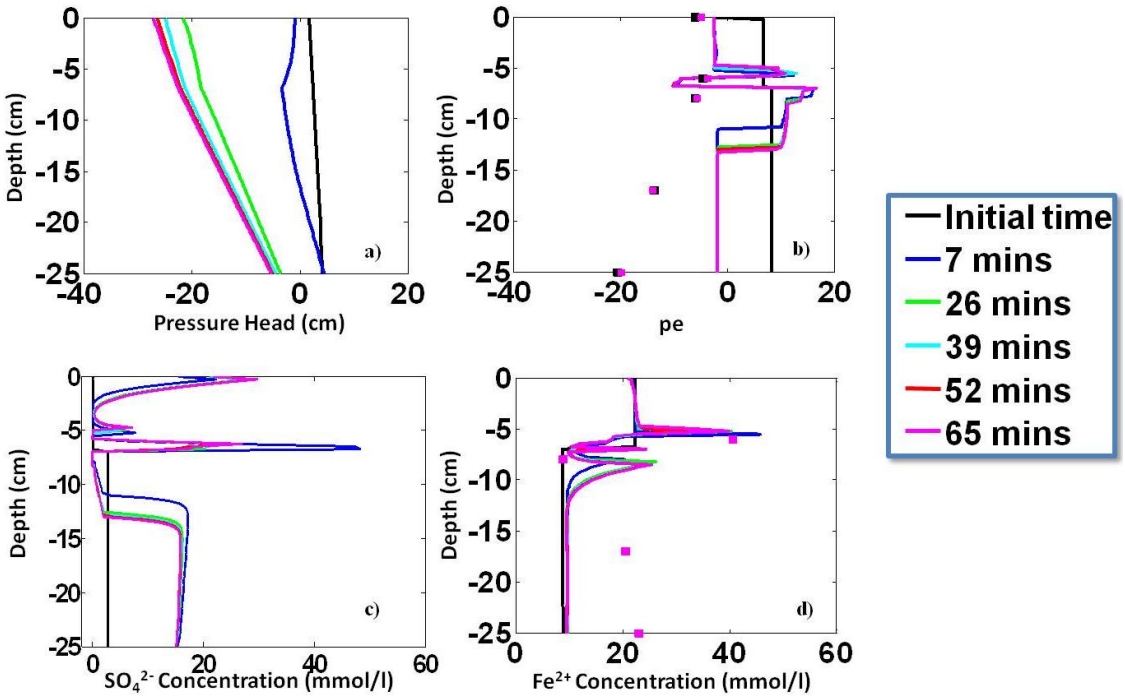

Figure 4.12: Simulated and observed depth profiles of a) pressure head, b) pe, c) SO_4^{2-}, and d) Fe^{2+} concentrations for a transient drainage experiment of the layered column. Solid lines indicate model predictions, solid squares indicate observations, and color scheme corresponds to time. Note that observations are not available for all times.

Predictions for a transient drainage experiment of the layered column confirm the presence of iron and sulfate reduction as significant biogeochemical processes for this column (Figure 4.12). The regions of iron reduction during drainage (Figure 4.12d) are quite similar to the transient infiltration experiment (Figure 4.11b) as peaks in ferrous iron concentrations for both experiments are observed above (~5 cm), at (7 cm), and below (~9 cm) the interface. HP1 predictions indicate that sulfate (Figure 4.12c) is being reduced near the interface and below 13 cm. Predicted pe (Figure 4.12b) confirms reducing conditions both above 6 cm and below 15 cm. It is interesting to note that predicted pe has a point of inflection at the interface while it is continuously decreasing below the interface. Therefore, it seems that the zone of redox perturbation is located around the interface at 7 cm.

Observations of pe (Figure 4.10e) agree with model analysis and indicate reducing conditions in the loam layer of the layered column. Observed K^+ (Figure 4.10b) in the lower layer supports increased potassium uptake due to high microbial activity. The mismatch between HP1 predictions and observations of sulfate, potassium and pe can again be improved by including reaction kinetics for sulfate reduction processes (Figure 4.13). But, notice that pe observations (Figure 4.10e) are close to -20 and therefore, require four orders of magnitude higher reduction rates than used for the homogeneous sand column to account for the increased sulfate reduction dynamics observed in this column. Both experimental observations and HP1 predictions for the layered sand over loam column emphasize the importance of including heterogeneity to

account for 'enhanced' biogeochemical activity (including sulfate reduction) in contaminant fate and transport models.

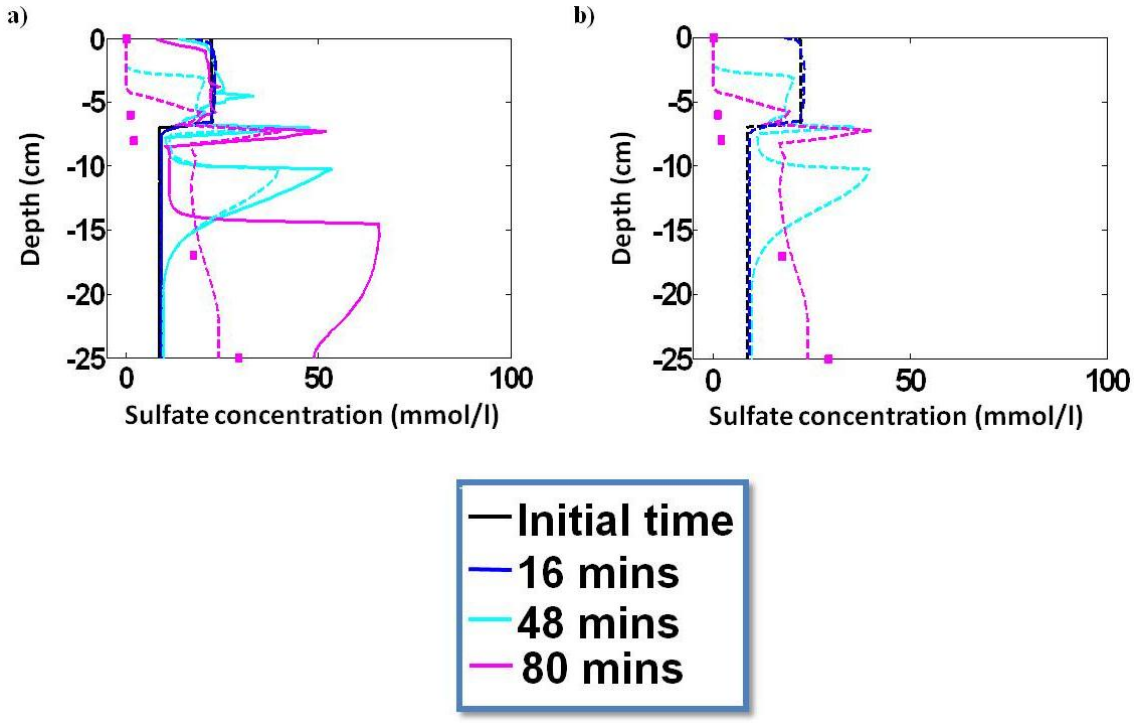

Figure 4.13: Simulated and observed sulfate concentration a) comparing model predictions before and after considering reaction kinetics, and b) considering reaction kinetics only for the layered column. Solid lines indicate model predictions without reaction kinetics, dashed lines indicate model predictions considering reaction kinetics, solid squares indicate observations, and color scheme corresponds to time. Note that observations are not available for all times.

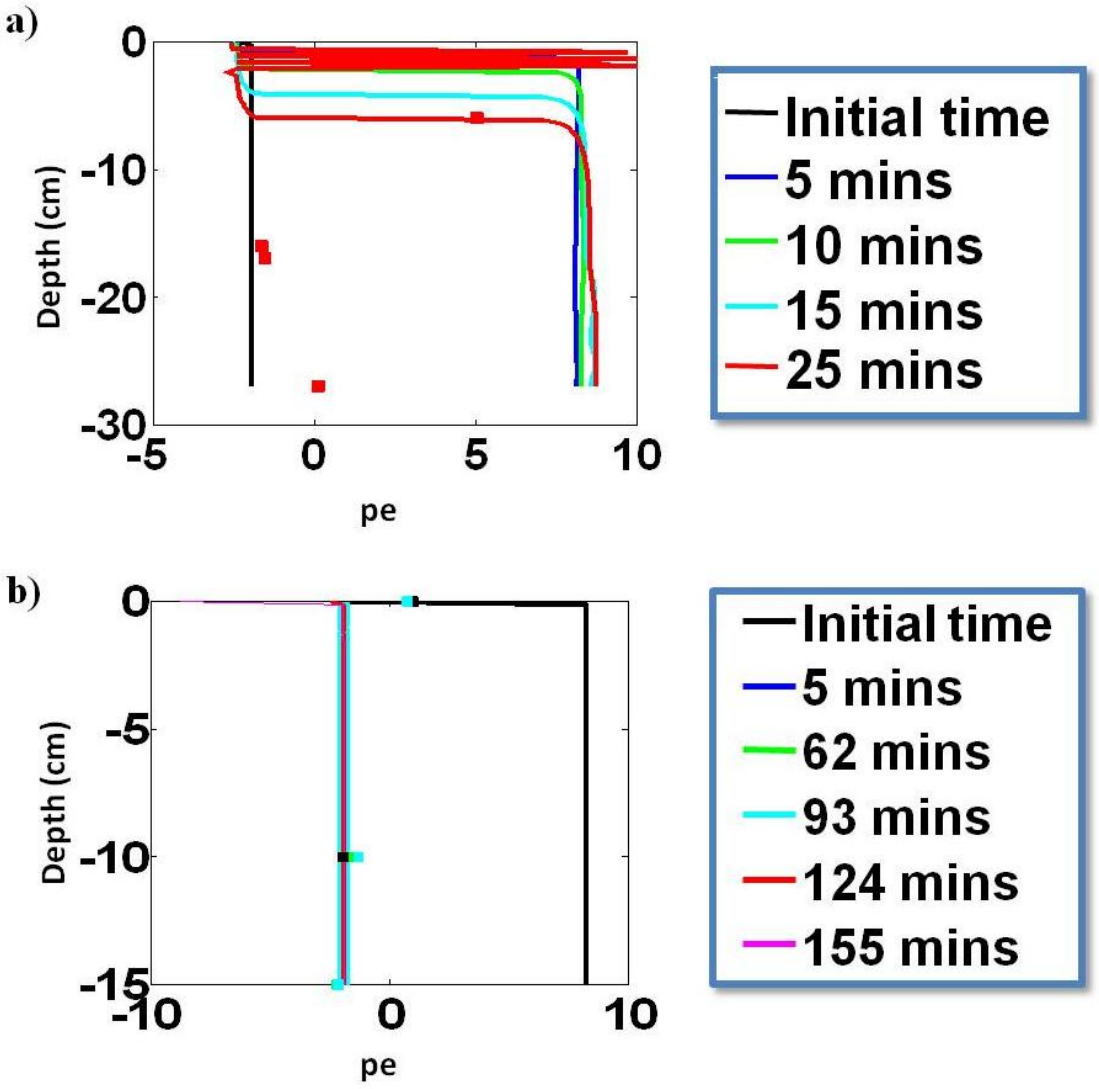

Figure 4.14: Time progression of observed and simulated pe (without reaction kinetics) for a) infiltration experiment of the homogeneous sand and b) drainage experiment of the homogeneous loam column. Solid lines indicate model predictions, solid squares indicate observations, and color scheme corresponds to time. Note that observations are not available for all times.

4.5.6 Dominant redox controls for homogeneous and layered columns

It is interesting to note that redox gradients are dependent on hydrologic conditions (infiltration, drainage, etc.) for both homogeneous sand and loam columns (Figures 4.3, 4.7, and 4.14). Comparing simulated pe for the homogeneous sand column, it seems that the infiltration experiment (Figure 4.3b) has a difference in pe only at the top 0-3 cm of the column as compared to the drainage experiment (Figure 4.14a). Similarly, the infiltration experiment for the homogeneous loam column (Figure 4.7f) showcases a difference from the drainage experiment (Figure 4.14b) only in the top 0-3 cm zone of perturbation (infiltration). However, it is the interface and textural heterogeneity of the layered column that exerts control over redox gradients and consequently geochemical reactions in the layered configuration. Figures 4.10e and 4.12b portray that the differences between the redox gradients for the infiltration and drainage experiments of the layered column are not limited to perturbation in the top few cms (as in homogeneous columns) but showcase completely different profiles. In fact, the zones of sulfate reduction (especially below the interface) are completely different for the two (infiltration and drainage) experiments.

Observations of pe used in these figures correspond to short time hydrologic experiments and therefore do not vary within all experiments. For example, pe observations for infiltration (Figure 4.3b) and drainage events (Figure 4.14a) of the homogeneous sand column match completely. The same is true for the layered column (Figures 4.10e and 4.12b). However, variations in redox potential with different experimental controls (rainfall, drainage, dry spell) have been explored by *Hansen et al.*

[2011] and support our interpretation. We conclude that redox processes in homogeneous systems are strongly affected by flow conditions while a layered configuration is strongly affected by layering and structural heterogeneity.

4.5.7 Effect of increased flux and pH

The effect of increased flux is verified by applying a constant water flux of 1 cm/min at the top boundary for the duration of the experiment for all soil columns (Table 4.2). The increased water flux is found to increase the transport of various cations and anions in the homogenous sand column, cause higher oxidation of iron in the homogeneous loam column, and increase the production of FeS precipitates in the layered column. The analysis of hydrologic perturbations in boundary conditions in the previous section essentially conveys the same results as that of increased flux in the system. However, changes in pH fail to produce any difference in the results of the experiments as compared to variation in hydrologic conditions. The infiltrating water pH used for initial analysis is 4.3, which is the same as observed in Norman, Oklahoma according to the National Bureau of Standards (SRM 2694). When the pH of rainwater is increased to 8 or decreased to 4, no major differences in redox gradients or cation and anion concentrations within the experimental columns are detected. High pH conditions typically promote the precipitation of a number of secondary minerals that usually consume alkalinity, and act to buffer further increases in pH [*Mayer et al.*, 2001]. Iron sulfide minerals (present in our columns) also provide a strong driving force for precipitation of carbonate and hydroxide mineral phases [*Stoessell*, 1992]. It seems that

our experimental columns are buffered with respect to pH, and therefore do not show significant variations in chemical concentrations with changes to pH.

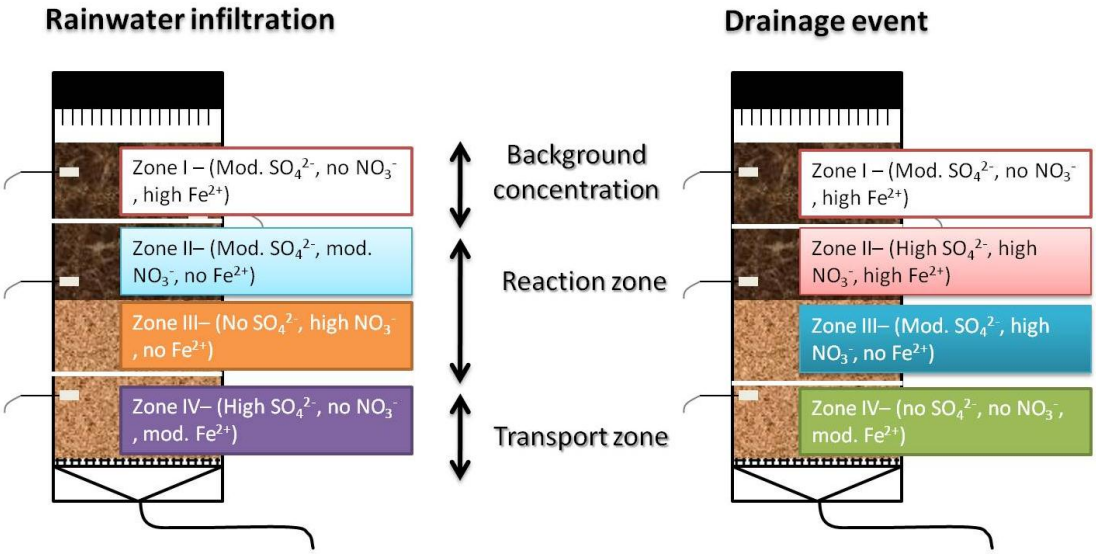

Figure 4.15: Conceptual model for spatially heterogonous formations in variably-saturated media.

4.6 Development of a conceptual model

A conceptual model is presented here that can account for heterogeneous formations in variably-saturated media (Figure 4.15). This model is derived from distinct water chemistries observed in the layered soil column when different types of experiments (infiltration, drainage, perturbation, etc.) are conducted on this column. As Figure 4.15 suggests four distinct geochemical zones (colored boxes) can be identified in both infiltration and drainage events. These zones or distinct water chemistries can be associated with background concentration at the top, followed by a reaction zone which is associated with the interface and combines the geochemical zones above and below

the heterogeneity, and a transport zone that carries either the background concentrations or the reaction products through the column. The background concentration zone is essentially free of the effects of the interface or the heterogeneous formation (showcased by similar colored boxes for both infiltration and drainage events). The reaction zone is the area of activity where distinct geochemistry can be encountered both above and below the layering or the interface. The lowest zone is the transport zone which is also free of the interface effects but can carry reaction products or background concentrations depending upon the type of hydrologic conditions. This conceptual model doesn't specify the lengths of the different zones. The extent of the three characteristic zones is dependent on the thickness and magnitude of heterogeneity/layering encountered, progression of geochemical reactions, and type of perturbation of hydrologic conditions within the porous media. This conceptual model can be applied to other subsurface heterogeneities such as clay lenses, macropores, etc. and used to describe the formation of distinct water chemistries across textural interfaces and other similar heterogeneities.

4.7 Conclusions

A conceptual model is presented here that can account for heterogeneous formations in variably-saturated media (Figure 4.15). Few studies have evaluated the effect of subsurface heterogeneity on transport and redox processes in the vadose zone. The vadose zone is subject to large transient variations both in terms of atmospheric inputs and subsurface heterogeneity, which can significantly alter the fate and transport of contaminants. Therefore, this study aims at identifying the dominant redox processes and evaluating the individual contribution of hydrological perturbations (such as pH,

flux, and boundary conditions) on these processes in homogeneous versus layered systems. The use of soil columns with geochemical (contaminated vs. uncontaminated) and textural differences (sand vs. loam) provide insight on the interplay of dominant processes in different repacked configurations. The soil cores for the columns were obtained from the Norman Landfill site in Norman, Oklahoma which is contaminated with landfill leachate. Factor analysis indicates that the dominant process controlling biogeochemical variations is different for the different soil columns. Advective transport explains the maximum variability in the homogeneous sand column, coupled hydrological and geochemical processes control the variability within the homogeneous loam column, while the sand-loam interface of the layered column is the dominant feature controlling biogeochemical variability within the layered column.

HP1 simulations indicate thermodynamic control in the homogeneous sand column with concentrations of various chemicals changing with (predicted) pe. According to HP1 analysis, pe is driven by hydrologic fluxes. Both the observed (infiltration and drainage) and numerical perturbation experiments of this column suggest that the depth of peak chemical concentrations and sharp redox variations are strongly guided by hydrologic boundary conditions. However, observations indicate redox disequilibrium in this column as sulfate reduction is occurring in the absence of nitrate reduction. A better agreement between model predictions and observations is obtained when this redox disequilibrium is accounted for and reaction kinetics are included in the HP1 model.

In the homogeneous loam column, HP1 predictions suggest that nitrate reduction is coupled with iron oxidation. HP1 modeling again demonstrates that dominant processes (nitrate reduction and iron oxidation) and redox gradients are strongly affected by hydrologic gradients. Visual snapshots and observation gradients of the homogeneous loam column highlight the presence of iron sulfide precipitates and reduced hydraulic conductivity as a result of precipitate formation in this column [*Hansen et al.*, 2011].

For the layered column, experimental observations and model predictions indicate that iron and sulfate reduction are the dominant biogeochemical processes, and major differences between them can be improved by including reaction kinetics (at rates higher than those employed for homogeneous systems). Unlike the homogeneous columns, hydrologic properties in the layered column are found to be affected only by the textural interface. The different hydrologic perturbations conducted using HP1 have minimal to no effect as to the positioning of chemical gradients in this particular column. The textural interface displays the transition with respect to geochemical concentrations and both HP1 predictions and experimental observations agree that this interface is a hotspot of biogeochemical activity. Therefore, we conclude that in homogeneous soil systems, hydrologic conditions are important drivers of redox processes while heterogeneous formations are affected more by layering and interfaces.

A conceptual model, which is developed through a comparison of the homogeneous and layered column experiments, represents the geochemical variability in and around a heterogeneous formation in variably-saturated media. This conceptual model divides the system into three characteristic zones around the subsurface

heterogeneity: a ‘background’ concentration zone that is in contact with the system and at a quasi steady state composition, a ‘reaction’ zone that is the center of activity around the heterogeneous formation, and a ‘transport’ zone that carries the reaction products or background concentrations.

4.8 Implications for future reactive transport modeling

The analysis and comparison of HP1 modeling results and experimental observations for the different experimental soil columns provide several implications for improving future reactive transport modeling. First, an inclusion of feedback mechanisms between hydraulic properties, geochemical processes, and microbiological analysis is crucial to better characterize the fate and transport of chemicals. The homogenous loam column portrays the effect of redox processes (FeS precipitate formation) on hydraulic conductivity within the column and consequent mismatch obtained with model predictions. Similarly, redox disequilibrium resulting from the presence of sulfate reducing bacteria in the homogeneous sand and layered sand-over-loam columns demonstrate the importance of including microbially-mediated reaction rates in obtaining better predictions of sulfate and pe. This feedback is shown to improve agreement between predictions and observations of sulfate concentrations in both the columns. Future models must consider the possibility of updating hydraulic properties or geochemical concentrations based on positive feedback mechanism between the coupled biogeochemical processes. Second, the characterization of any heterogeneous soil profile according to the conceptual model would greatly improve this feedback mechanism. Inclusion of a conceptual model that separates the reaction zone for the heterogeneous

soil profile would ensure that only the feedbacks centered on the zone of activity are analyzed and thereby reduce the numerical cumbersomeness of the models.

CHAPTER V

TEMPORAL DYNAMICS OF BIOGEOCHEMICAL PROCESSES AT THE NORMAN LANDFILL SITE

5.1 Synopsis

Little is known, however, about the physical controls that govern the temporal variability of redox-sensitive biogeochemistry. These biogeochemical variations are typically non-stationary, and distributed across various time scales. Therefore, the purpose of this study is to investigate biogeochemical datasets from a municipal landfill site to identify the dominant modes of variation and determine the physical controls that become significant at different time scales. Three wells with different proximities to the leachate plume provide locations with varied geochemical characteristics and hydrological interactions at the Norman Landfill site. A continuous wavelet transform is used to obtain a complete time-frequency representation of the Norman Landfill geochemical dataset and a wavelet decomposition technique is used to infer the dominant physical controls on geochemical parameters at four dyadic time scales (2, 4, 8, and 16 months).

Wavelet analysis indicates that variations in reactive and conservative concentrations are strongly coupled to hydrologic variability (water table elevation and precipitation) at 8 month scales, and to individual eco-hydrogeologic framework (such as seasonality of vegetation, surface-groundwater dynamics) at 16 month scales. Apart from hydrologic variations, temporal variability in sulfate concentrations can be

associated with different sources (FeS cycling, recharge events) and sinks (uptake by vegetation) depending on the well location and proximity to the leachate plume. Results suggest that nitrate concentrations show multi-scale behavior across temporal scales for different well locations, and dominant variability in dissolved organic carbon for a closed municipal landfill can be larger than 2 years due to its decomposition and changing content.

5.2 Introduction

The leaching of reactive contaminants from landfill and waste management sites is controlled by multiple geochemical, hydrological, and microbiological factors, and occurs across various time scales [*Christensen et al.*, 2001; *Cozzarelli et al.*, 2001; *Jardine*, 2008; *Bjerg et al.*, 2011]. Knowledge about the temporal variability of reactive contaminants in groundwater is important to assess contaminant plume migration, evaluate associated health risks, and undertake timely action. However, temporal patterns and non-linear interactions in biogeochemical processes controlling this variability are poorly understood in groundwater systems.

The majority of organic and inorganic contaminants in the subsurface are affected by the hydrological and geochemical properties of the porous media [*Mercer*, 1983]. Hydrologic variations including water table elevation and precipitation play a pivotal role in the migration and distribution of contaminants in groundwater. For example, *Fendorf et al.* [2010] suggested that the patterns of recharge and discharge of groundwater, especially groundwater pumping and time since recharge, were important factors influencing arsenic concentrations in South and Southeast Asia. The impact of

seasonal rainfall events on redox processes at a shallow, sandy aquifer contaminated with petroleum hydrocarbons and chlorinated solvents was addressed by *McGuire et al.* [2000]. They concluded that changes in concentrations of redox-sensitive chemicals appeared to be related to rainfall events at monthly and larger (3 yr) time scales. The previous chapter also emphasizes the importance of hydrologic boundary conditions (such as infiltration, drainage events) on redox conditions in soil columns with homogeneous and layered profiles. Several other studies have documented the influence of hydrologic controls (changes in direction and seasonality of flow, recharge timing, etc.) on geochemical concentrations at both column and landfill scales [*Mitchell and Branfireun*, 2005; *Cozzarelli et al.*, 2011; *Hansen et al.*, 2012b]. Topographic and landscape controls such as shifts in vegetation structure and density can also contribute to spatio-temporal dynamics of water content availability and infiltration characteristics of the porous media [*Asseng et al.*, 2001; *Raz-Yaseef et al.*, 2010; *Jana and Mohanty*, 2012].

Apart from hydrologic variations, geochemical processes are also known to affect redox dynamics in groundwater systems. The progression of redox reactions and subsequent transformation of contaminants is based on thermodynamic energy yields as: aerobic respiration, nitrate reduction, manganese reduction, iron reduction, sulfate reduction, and methanogenesis [*Chapelle*, 2001; *Megonigal et al.*, 2004]. However, heterogeneities in contaminant load (e.g., changes in organic carbon content, metals), aquifer composition (e.g., presence of iron and/or manganese oxides), geologic framework, etc. can result in a departure from the characteristic spatial sequence of

redox zones [*Champ et al.*, 1979; *Christensen et al.*, 2000; *Van Breukelen et al.*, 2003; *Harris et al.*, 2006]. Redox dynamics can be spatially variable and intensified at the plume fringe, where they are governed by the differences between the composition of the landfill and the mineralogy of the aquifer as well as by seasonal biogeochemical cycling [*Sinke et al.*, 1998; *McGuire et al.*, 2002; *Scholl et al.*, 2006]. Apart from being spatially heterogeneous, the distribution of redox species can be temporally variable as many of the redox reactions are microbially-mediated. Differences in microbial populations, community structures and their biotic interactions (e.g., biomass accumulation, competition) can add to the temporal heterogeneity of the distribution of contaminants [*Roling et al.*, 2001; *Jolley et al.*, 2003; *Haack et al.*, 2004].

Therefore, the release of contaminants is a function of the complex interactions between physical factors (e.g., porosity, permeability, dilution), chemical mechanisms (e.g., adsorption, redox, precipitation), geological controls (e.g., lithologic variations, depositional patterns, presence of fractured rock), ecological interactions (e.g., type of vegetation, rooting depth) and microbial activities (e.g., biodegradation, biotransformation) [*Christensen et al.*, 2000; *Bjerg et al.*, 2003, 2011; *Wanty and Berger*, 2006; *Pacific et al.*, 2011]. For example, the progression of redox zones is affected by the supply rate of terminal electron acceptors, which is governed by permeability and hydrologic recharge events, and by the presence of oxidized minerals, which is controlled by the geologic framework of the aquifer [*Lovley and Chapelle*, 1995; *Kamolpornwijit et al.*, 2003; *Mukherjee et al.*, 2008]. Consequently, microbial activity is influenced by hydrological and geological processes that control the transport

of terminal electron acceptors and the distribution of redox and other reactant species [*Hunter et al.*, 1998; *Haack and Bekins*, 2000; *Geesey and Mitchell*, 2008]. In return, microbial processes utilize these reactants and modify the chemical composition of the groundwater. Biotic degradation of organic carbon can change pH and groundwater alkalinity, thus affecting geochemical mechanisms (such as precipitation, sorption), while biomass accumulation can impede flow, thus affecting hydrological variables (such as permeability, aquifer porosity) [*Mills et al.*, 1989; *Taylor and Jaffe*, 1990; *Kusel*, 2003]. Therefore, the distribution of redox-sensitive compounds is governed by an aggregation of linked hydrological and biogeochemical processes.

Since these biogeochemical interactions are non-linear and complex, changes to measured water chemistry parameters (such as pH, SO_4^{2-}) can indicate the influence of multiple processes simultaneously. Moreover, the time frame of analysis is an important factor when considering changes in chemical composition, redox state, microbial community structure, vegetation growth, or other external forcing [*Bloschl and Sivapalan*, 1995; *Langmuir*, 1997; *Smith*, 2007]. Therefore, wavelet analysis is used to extract the natural frequencies and identify the governing processes that exert control over redox patterns at different time scales. Wavelet analysis is a technique that analyzes the data with a window that can be stretched and translated with a flexible resolution in both time and frequency domains [*Foufoula-Georgiou and Kumar*, 1994]. The time-frequency localization property of wavelets is meaningful as it examines the biogeochemical dataset with a detail matched to its scale, thus providing the opportunity

to identify transient, seasonal and long-term patterns of the dataset [*Lau and Weng*, 1995; *Torrence and Compo*, 1998].

In summary, determining the governing processes in a landfill environment is challenging due to the complex linkages between hydrologic, geochemical, and microbiological processes, and the knowledge about how these processes evolve temporally. Variations in water chemistry parameters are difficult to interpret as soil hydraulic properties, chemical reactions, microbial composition, and external forcing (such as rainfall events, aquifer withdrawal) change with time. Therefore, the objectives of this study are to: i) extract the natural variability of the biogeochemical dataset from a closed municipal landfill site, and ii) identify the dominant processes that control this temporal variability.

5.3 Field procedures

5.3.1 Site description

The Norman Landfill is a closed municipal landfill that operated for 63 years in the city of Norman, Oklahoma (Figure 5.1). By the mid 1990s, the leachate plume from the site extended approximately 250m downgradient towards the Canadian River [*Scholl and Christenson*, 1998]. Near the landfill, the groundwater is shallow and ranges to about two meters from the land surface [*Scholl et al.*, 2006; *Cozzarelli et al.*, 2011].

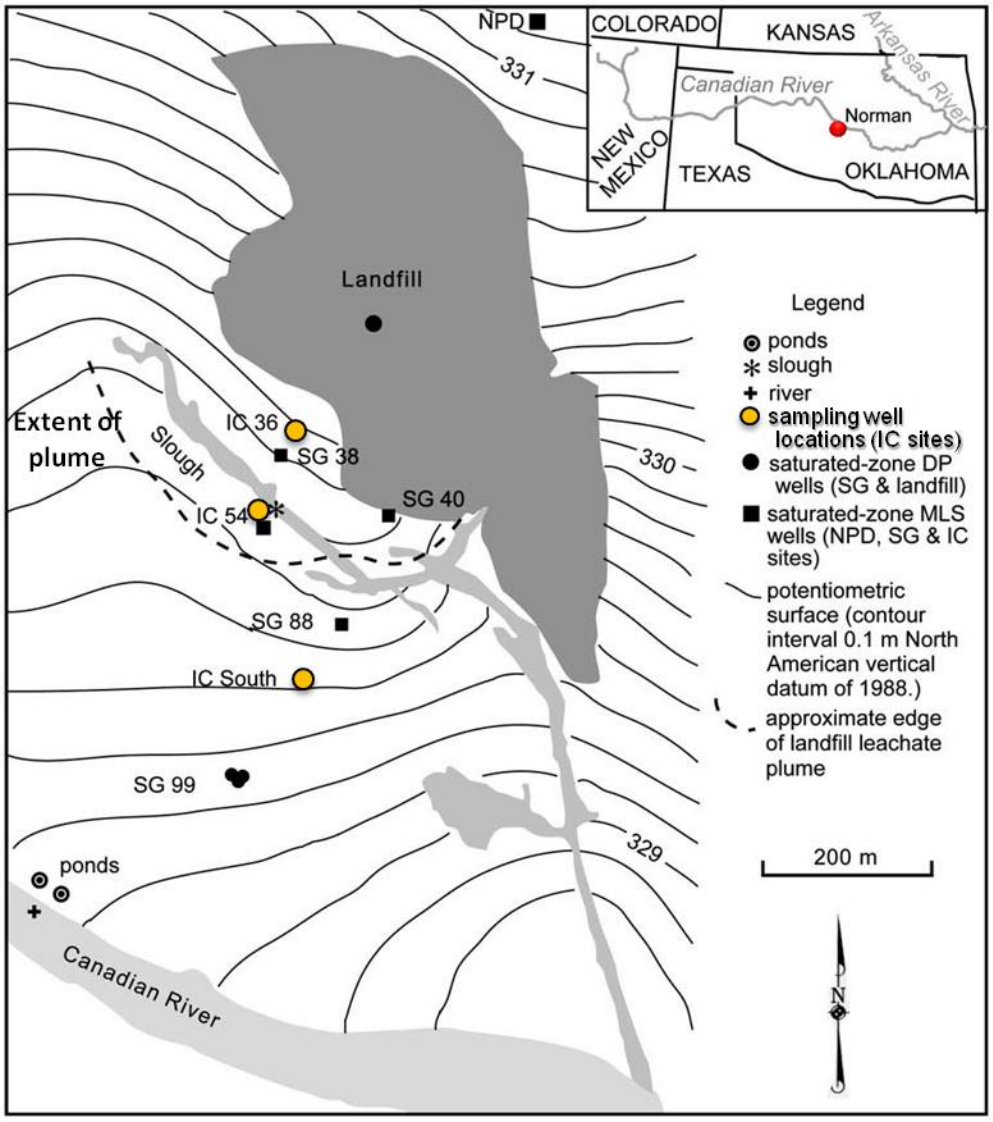

Figure 5.1: Map depicting the location of the Norman Landfill site and the multi-level sampling wells (IC 36, IC 54, and IC South) overlain on the potentiometric surface.

Previous hydrologic investigations on the site reveal its dynamic nature with diurnal water-table fluctuations in response to transpiration, observed seasonal variations as large as 1.4 m from winter to summer, and rapid variations in response to rainfall events [*Scholl et al.*, 2005]. The seasonality of the water table is primarily attributed to rainfall and evapotranspiration. Oklahoma has a continental climate, and the character of rainfall varies with the seasons. On an average, the climatological maximum for rainfall occurs in May and a secondary maximum occurs in September [*Comrie and Glenn*, 1998]. In their study, *Scholl et al.* [2005] indicated that rainfall events can elevate the water table within 0.6-2 days, and the residence time of the groundwater is on the order of days depending on the season and other recharge events. The riparian zone near the landfill is responsible for water level decline during the growing season (mid-April to October) [*Scholl et al.*, 2005].

Analyses of groundwater samples have indicated that the leachate also interacts with a former Canadian River channel, referred to as the slough [*Becker*, 2002] (Figure 5.1). The slough is an ephemeral wetland that is an expression of the local water dynamics. Seasonal variations in the slough water depth can be as much as 1m deep in the spring to dry in summer, and occur in response to groundwater and precipitation [*Christenson et al.*, 1999; *Lorah et al.*, 2009]. The slough and the leachate contaminated groundwater are hydrologically connected such that the groundwater discharges into the slough along the northeast bank while the slough recharges the groundwater along the southwest bank [*Scholl et al.*, 2005; *Lorah et al.*, 2009].

The biogeochemistry of the site indicates sulfate reduction, iron reduction, and methanogenesis to be important processes for degradation of organic matter [*Cozzarelli et al.*, 2000; *Eganhouse et al.*, 2001; *Grossman et al.*, 2002]. *Báez-Cazull et al.* [2008] reported that seasonal rainfall patterns were dominant controls on redox zonations, especially for iron and sulfate reduction, while analyzing 3-year of data from the slough. They also concluded that exact temporal controls on the fate of iron could not be determined because of multiple biogeochemical controls. *Cozzarelli et al.* [2011] confirmed that chemical concentrations in the plume boundaries are affected by hydrologic processes at various time scales. Their analysis of the plume-scale data revealed that the upper boundary of the leachate plume is an active redox location while the center of the plume is depleted in sulfate and has low oxidation capacity. The spatial variability of biogeochemical processes is also evident in the existing conceptual framework of the Norman Landfill site (Figure 5.2). Therefore, the Norman Landfill provides an opportunity to study the temporal variability of biogeochemical processes in the leachate plume and identify the physical controls governing contaminant distributions at different locations within the site.

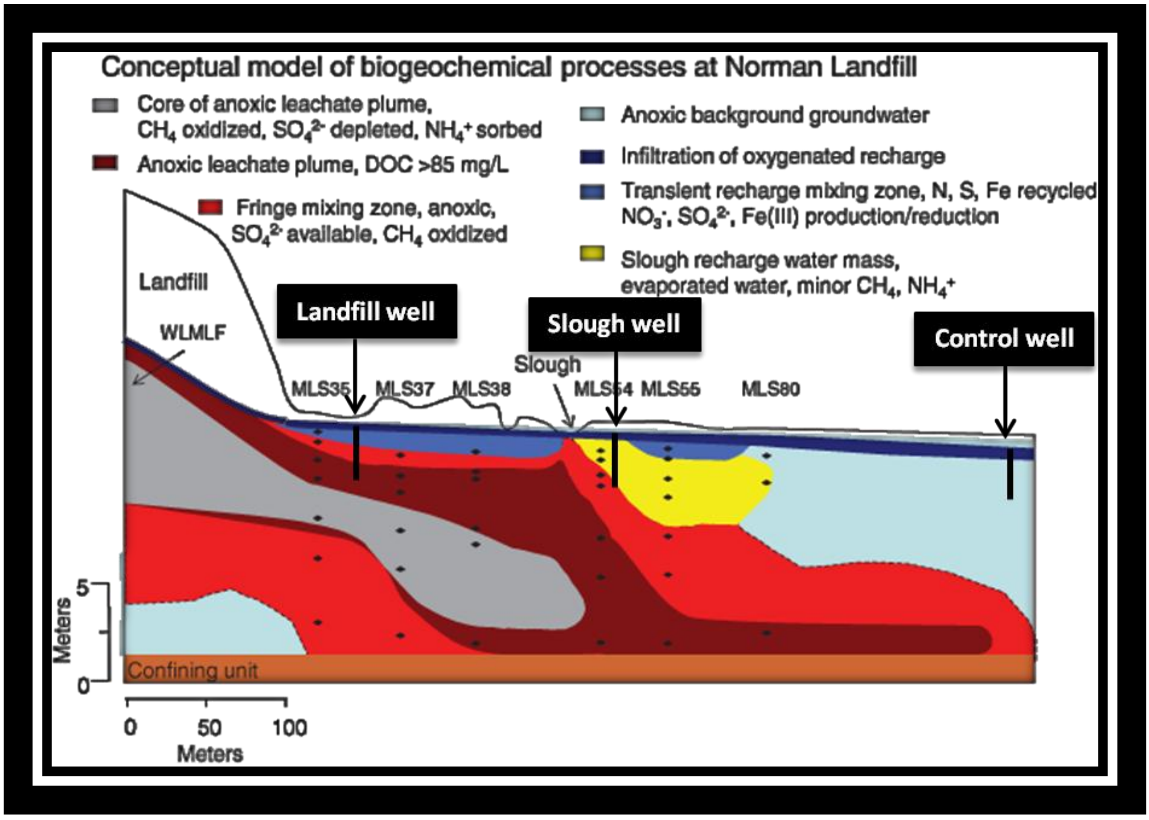

Figure 5.2: Conceptual map showing the location of the multi-level wells with respect to the biogeochemical zones (Modified from *Cozzarelli et al.*, 2011).

5.3.2 Field measurements

Three multilevel wells located on a transect parallel to the groundwater flow were used to analyze the biogeochemical variability at the Norman Landfill site (Figure 5.1). These wells have screens set at different elevations to capture the dynamics of the local water table [*Scholl et al.*, 2006]. The landfill well (IC 36) is located 35m from the edge of the landfill mound, the slough well (IC 54) is located 7m south of the slough, and the control well (IC South) is 85m downgradient from the slough [*Breit et al.*, 2005]. The wells are named as such because the chemical characteristics of the IC 36 well suggest its interactions with the leachate plume, the IC 54 well with the slough and the leachate plume, and the IC South with background groundwater concentrations or recharged slough water [*Breit et al.*, 2005]. The control well (IC South) is located in an area that was prone to flooding during the 1980s and has sparse vegetation due to the activity of the river channel [*Schlottmann*, 2001]. In contrast, the vegetation is quite dense near the landfill and slough wells with mature trees and understory [*Tuttle et al.*, 2009]. The differences in chemical characteristics and hydrologic interactions between the three well locations are evident in Figure 5.2 which represents the distinct biogeochemical zones for the wells using the conceptual framework of the Norman Landfill site.

Hydrological and geochemical indicators including hydraulic head, specific conductance, δ^2H, chloride, sulfate, nitrate, and non-volatile dissolved organic carbon (NVDOC) were measured at all well locations. Data was collected at a minimum of three depth levels for each well [*Scholl et al.*, 2006]. Specific conductance was measured

using a portable meter, anions were analyzed using ion chromatograph, NVDOC concentrations were determined following the method of *Qian and Mopper* [1996], and isotopic analyses were done by equilibration with gaseous hydrogen for δ^2H. A more detailed description of the chemical methods can be obtained from *Scholl et al.* [2006]. This time-series data was collected on a monthly to semi-monthly time scale [*Cozzarelli et al.*, 2011].

5.4 Wavelet analysis

Since groundwater systems are complicated by linked biogeochemical processes, wavelets offer a powerful technique to analyze the observed redox patterns and identify the dominant processes that control water chemistry variations in the temporal domain. Wavelets have the ability to provide high inter-scale decorrelation especially when the contributing biogeochemical processes are inter-linked and have multi-scalar characteristics [*Diou et al.*, 1999]. Therefore, a wavelet transform is performed on the Norman Landfill dataset to obtain a comprehensive view of the frequency variations over time, and a multilevel decomposition (MLD) analysis is conducted to obtain the physical controls governing biogeochemical patterns at different time scales. These techniques are described in the following sections.

5.4.1 Time-frequency analysis

Since their inception, wavelet transforms have been used to characterize multi-scale, non-stationary processes across spatial and temporal scales [*Shao et al.*, 2003; *Das and Mohanty*, 2008; *Beecham and Chowdhury*, 2010]. The continuous wavelet transform (CWT) is useful to obtain a complete representation of the localized, intermediate, and

long-term patterns observed across different time scales [*Kumar and Foufoula-Georgiou*, 1997]. The continuous wavelet transform is obtained by decomposing the data $\boldsymbol{D}(t)$ with the wavelet function $\boldsymbol{\psi}(t)$:

$$W_D(a,b) = \int_{-\infty}^{\infty} \boldsymbol{\Psi}^*_{a,b}(t) D(t) dt \tag{5.1}$$

where $\boldsymbol{W}$ are wavelet coefficients, t is time, * denotes the complex conjugate of the wavelet function, and the wavelet function is described by:

$$\boldsymbol{\Psi}_{a,b}(t) = \frac{1}{\sqrt{a}} \boldsymbol{\Psi}\left(\frac{t-b}{a}\right), \qquad a>0,\ -\infty<b<\infty \tag{5.2}$$

where a is the scale parameter that controls the dilation or contraction, and b is the shift parameter that determines the location of the wavelet. This wavelet function is not arbitrary and must satisfy the basic properties of i) zero mean ($\int_{-\infty}^{\infty} \boldsymbol{\Psi}(t) dt = 0$), ii) unit energy ($\int_{-\infty}^{\infty} \boldsymbol{\Psi}^2(t) dt = 1$), and iii) conservation of energy during transformation [*Daubechies*, 1992; *Farge*, 1992].

In this study, Morlet wavelet is used to extract the dominant frequencies within the biogeochemical dataset as it has a shape similar to the time-series data of the Norman Landfill site. Morlet wavelet is obtained by localizing a complex sine wave with a Gaussian envelope. This wavelet has both complex and real parts and therefore, enables the identification and fine tuning of significant frequencies [*Lau and Weng*, 1995; *Hariprasath and Mohan*, 2009].

5.4.2 Wavelet spectrum and cross-spectrum analysis

The modulus of the wavelet coefficients is used to develop a continuous-time power spectrum $p_D(a,b)$ defined as:

$$p_D(a,b) = W_D(a,b)W_D^*(a,b) = |W_D(a,b)|^2 \tag{5.3}$$

This wavelet power spectrum is advantageous as it provides the variance of the time-series in both frequency and time domains [*Guan et al.*, 2011]. This power spectrum can be averaged over time to obtain the variance distribution across different time scales [*Torrence and Compo*, 1998]. This is known as the global wavelet power spectrum. Wavelet software provided by C. Torrence and G. Compo (http://atoc.colorado.edu/research/wavelets/) is used in this study for obtaining the wavelet power spectrum and global variance distribution.

For the Norman Landfill dataset, it is desirable to know how two non-stationary geochemical variables vary in time. The physical relationship between two time-series in the time frequency domain can be obtained using wavelet cross-spectrum and wavelet coherence analyses. A wavelet cross-spectrum provides the opportunity to quantify the correlation between the wavelet power spectra of two variables ($D1$, $D2$) [*Grinsted et al.*, 2004]:

$$p_{D1,D2}(a,b) = W_{D1}(a,b)W_{D2}^*(a,b) \tag{5.4}$$

The wavelet coherence provides the association between these variables by normalizing the cross-spectrum with the individual spectrum of both the variables [*Cazelles et al.*, 2008]:

$$p_{D1,D2}(a,b) = \frac{\left\| \left\langle W_{D1}(a,b) W_{D2}^{*}(a,b) \right\rangle \right\|}{\sqrt{\left\| \left\langle W_{D1}(a,b) \right\rangle \right\| \sqrt{\left\| \left\langle W_{D1}(a,b) \right\rangle \right\|}}} \tag{5.5}$$

where <> denotes a smoothing operator in time and scale.

5.4.3 Multilevel decomposition

The wavelet decomposition technique, as the name implies, decomposes the original data into a number of frequency bands at discrete levels or time scales. At the first step, the time-series data is split into two to reveal the high-pass bandwidth or the detailed components, and the low-pass bandwidth or the approximate components [*Misiti et al.*, 2008; *Kia et al.*, 2009; *Quiroz et al.*, 2011]. Each low-pass bandwidth is further decomposed to obtain the next level of hierarchy. The decomposition levels are based on the total number of data points and the sampling frequency [*Mallat*, 1999].

The hierarchical details and approximations are obtained by iteratively applying a high-pass filter and an associated low-pass filter, which must satisfy certain conditions including orthonormality [*Labat et al.*, 2000; *Percival and Walden*, 2000]. In the wavelet analysis, a wavelet function $\psi(t)$ constitutes the high-pass filter, and its scaling function $\varphi(t)$ forms the low-pass filter. The choice of the wavelet function is such that it is orthogonal to both translates and dilates, while the scaling function is only orthogonal to the translates [*Kumar and Foufoula-Georgiou*, 1997]. The detail (D_m) and approximation (A_m) components at any decomposition level m are thus given by:

$$D_m(t) = \sum_{k=-\infty}^{\infty} W(m,k) \psi_{m,k}(t) \tag{5.6}$$

$$A_m(t) = \sum_{k=-\infty}^{\infty} S(m,k)\phi_{m,k}(t) \tag{5.7}$$

where k is a discrete location index, and S are the scaling coefficients analogous to the wavelet coefficients. In multilevel decomposition (MLD), a discretized version of equation 5.1 is used where the wavelet function is scaled by powers of two such that $a=2^m$ and shifted by integers such that $b = k2^m$ [*Martinez and Gilabert*, 2009].

In this study, the wavelet decomposition is carried out using the Daubechies 5 (Db5) wavelet and scaling functions, which satisfy the orthogonality requirement. Figure 5.3 illustrates the shape of the Db5 wavelet and scaling functions and the four levels of decomposition obtained from them. The hierarchical decompositions follow dyadic sampling (powers of two).

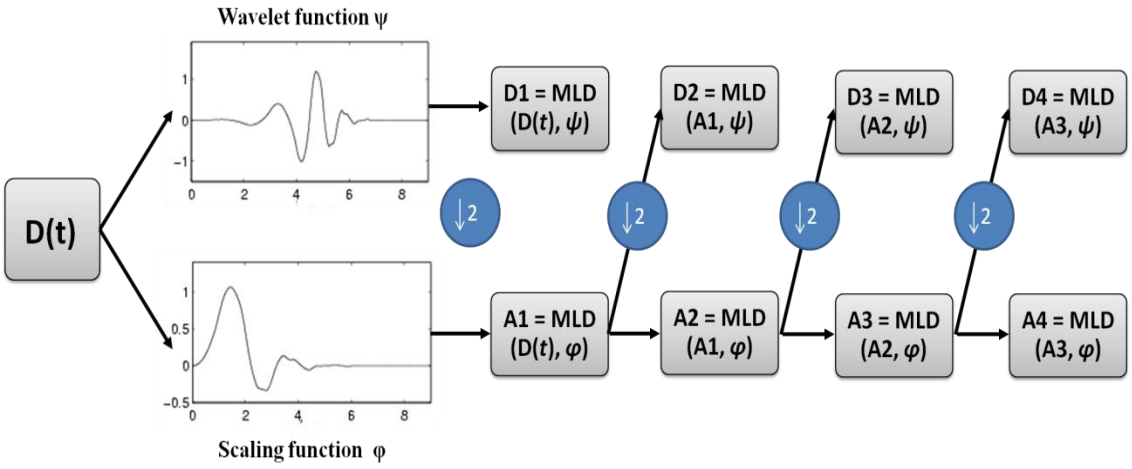

Figure 5.3: Scheme of the multi-level decomposition (MLD) using Db5 wavelet and scaling functions. ↓2 represents the decomposition by a power of two.

5.5 Results and discussion

Wavelet analysis is used in this study to obtain the dominant variations in the biogeochemical dataset and identify the different processes that control these variations at dominant time scales. This section demonstrates the use of continuous and discrete wavelet techniques described in the previous section to investigate the time-series behavior of geochemical variables at the control, landfill, and slough wells.

5.5.1 Temporal variations and governing processes at the control well

Figure 5.4 depicts the temporal characteristics of chloride, sulfate, and bromide at the control (IC South) well from May 1998 to May 2000. The temporal characteristics for the geochemical variables are described as a function of depth. As described in the previous section, Morlet wavelet is employed to study the temporal variations in the dataset. The edge effects of time frequency analysis, represented by the cone of influence (indicated by cross-hatched regions in the continuous wavelet spectrum), are excluded from this analysis [*Guan et al.*, 2011].

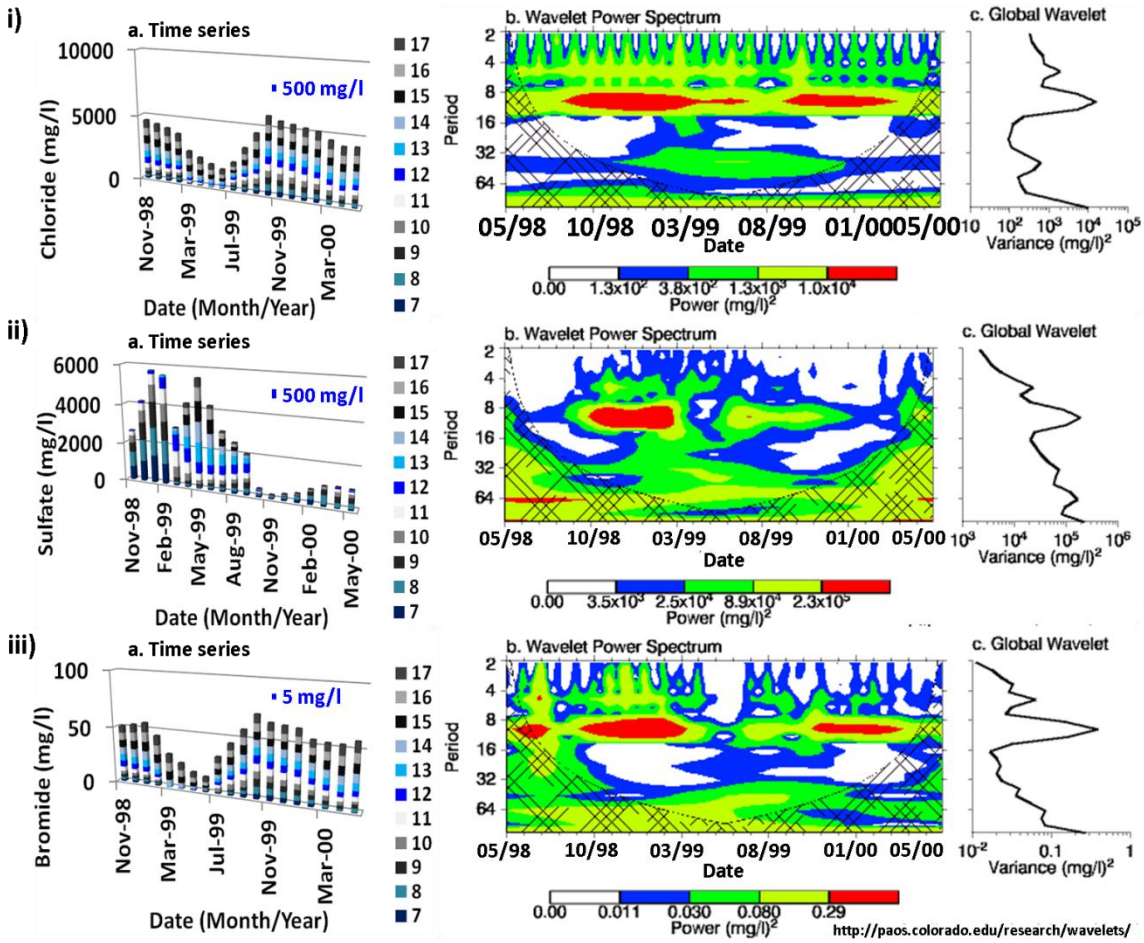

Figure 5.4: Time frequency analysis at the control well for i) chloride, ii) sulfate, and iii) bromide data displaying time record, continuous wavelet spectrum, and global variance distribution. In the time series graphs, the thickness of the cylinder signifies the concentration value, and the colors represent the well screens 7-17 with water elevation level between 329.73 and 328.38. In the wavelet power spectrum, the cross-hatched regions signify the cone of influence, and the color bar signifies the strength of power in the global wavelet spectrum.

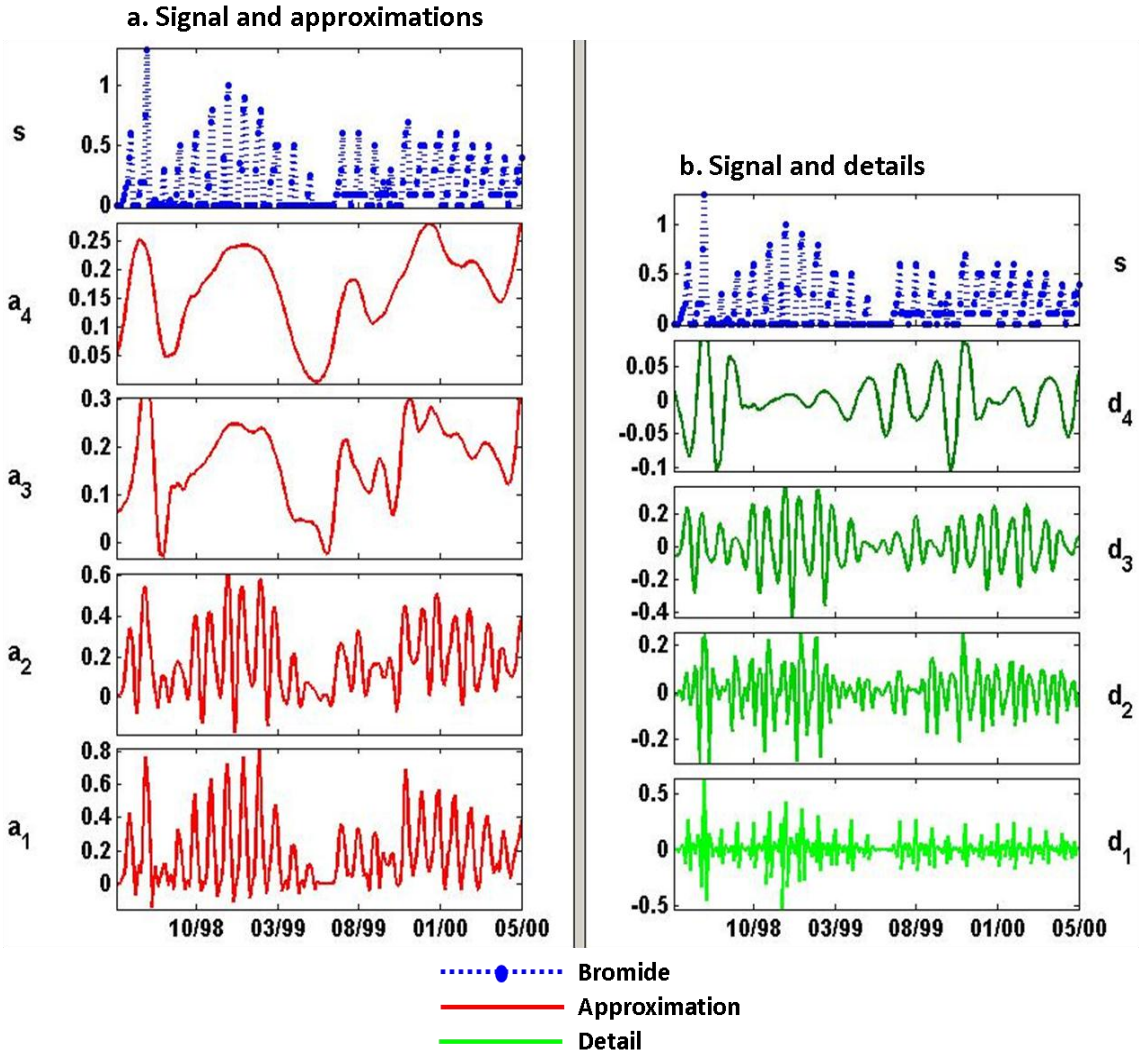

Figure 5.5: Multilevel decomposition of bromide at the control well with approximations and detail coefficients at dyadic scales of 2 (a_1), 4 (a_2), 8(a_3) and 16 (a_4) from May 1998 to May 2000.

Based on the Morlet wavelet, all three time-series depict a single dominant scale close to 12 month period in their wavelet power spectra (Figure 5.4b). This dominant frequency is also evident in the global variance distribution (Figure 5.4c) for all three geochemical variables despite the large differences in their temporal dataset (Figure 5.4a). There is however a discontinuity in the dominant frequency at different times for the three variables, with chloride displaying this discontinuity between August-September 1999, bromide between April-November 1999, and sulfate beyond April 1999. The reasons for this temporal disparity will be explored using MLD analysis. Another interesting feature in the wavelet power spectra is the small-scale behavior that shows consistent patterns (wavelet coefficients with significant power) at 4 month period for chloride data, and somewhat repetitive behavior for bromide data. Since chloride and bromide act mainly as conservative indicators of water flow, these small scale patterns could be representative of seasonal hydrologic events.

To further analyze and temporally isolate the processes affecting these dominant frequencies, a multilevel decomposition is performed on the bromide data (Figure 5.5). Db5 wavelet is applied to the original signal and the results at four levels of decomposition are shown. As mentioned in the previous section, this filtering removes the noise (detailed components) from the data and keeps only the approximations at each scale. The approximations reveal the smoothed trend in the bromide data and are therefore compared with water table elevation and rainfall data to further isolate and identify the hydrologic processes affecting bromide time-series (Figure 5.6).

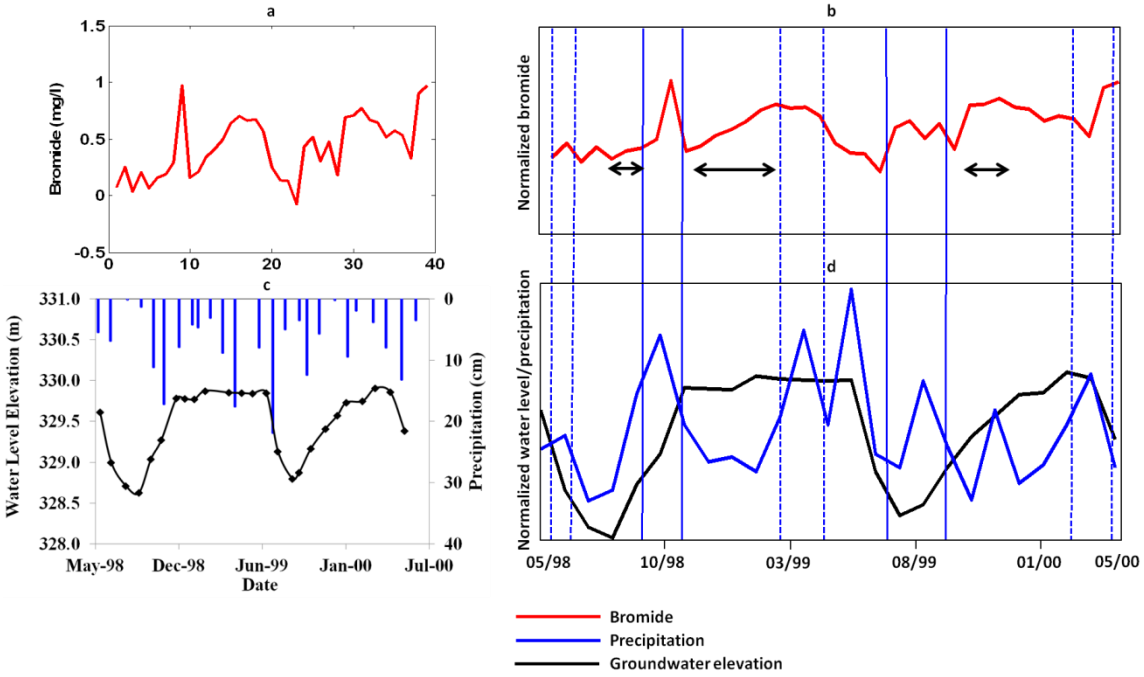

Figure 5.6: Multilevel decomposition of bromide data at the control well: a) bromide "approximation" at 8 months, b) normalized "approximation" signal, c) time record of monthly groundwater elevation data and precipitation at the control well, and d) normalized water level and precipitation signals. Two consecutive dashed/solid lines show trends matching between the normalized bromide signal and the precipitation data, and arrows show trends matching between the normalized bromide signal and groundwater elevation data.

Figure 5.6d illustrates that normalized monthly precipitation events exceeding certain limit act as discrete episodes that correspond to the normalized "approximation" of bromide (Figure 5.6b). A significant portion of these temporal trends are also associated with water table elevation data (indicated by arrows in Figure 5.6b). The detailed components in Figure 5.5 reveal frequency specific behavior and the d_4 component reveals a peak around September 1998 that coincides with the rainfall peak (Figure 5.6c). As mentioned earlier, rainfall in Oklahoma has a secondary maximum in September, and therefore exhibits a prevalent peak in this "detail" component of bromide. The detailed components (d_1-d_3) further confirm the discontinuity in dominant frequency as suggested by the continuous wavelet spectrum. The annual periodic component in the bromide time-series is therefore replaced by 5-7 month components that correspond to hydrologic data. Therefore, rainfall recharge events and seasonal variability of groundwater table affect wavelet coefficients at semi-annual scales (~8 months) and can be associated with the temporal dynamics of bromide concentrations at the control well.

A multilevel decomposition is also performed on sulfate data to identify the governing processes controlling its temporal variability at the control well. Previous studies have identified several sources of sulfate at the landfill site (such as organosulfur compounds, mineral weathering from barite, pyrite, iron oxide minerals, etc.) and demonstrated the influence of recharge events on sulfur cycling and its transport to deeper depths [*Scholl et al.*, 2006; *Tuttle et al.*, 2009]. However, this study compares the approximations at the scale of the dominant frequency (a_3) and hydrologic data to reveal

the temporal dynamics of processes controlling sulfate concentrations at the control well (Figure 5.7). As expected, there are striking similarities between the seasonal groundwater variations (indicated by arrows) and rainfall events (indicated by consecutive dashed/solid blue lines) with trends in sulfate data (Figure 5.7b, d). Notice the low levels of sulfate concentrations observed following a rainfall event even with an increasing water table elevation. This decrease in sulfate concentrations is attributed to sulfate reduction processes at the control well [*Scholl et al.*, 2006], and is evident after the rainfall events of September 1998 and September 1999.

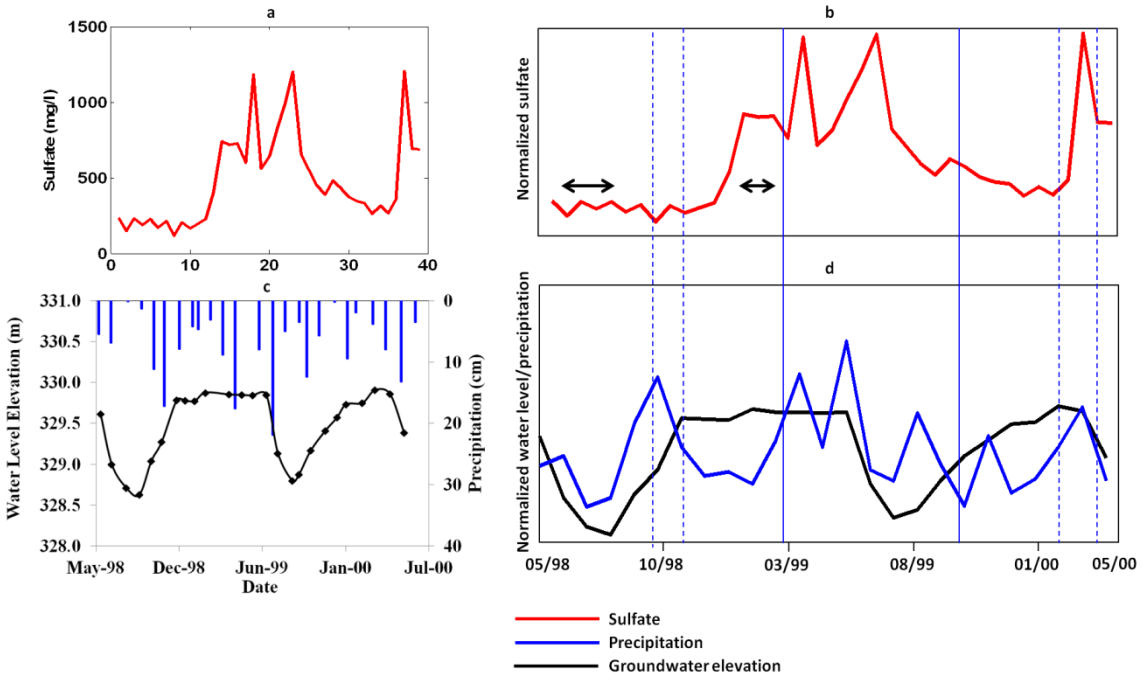

Figure 5.7: Multilevel decomposition of sulfate data at the control well: a) sulfate "approximation" at 8 months, b) normalized "approximation" signal, c) time record of monthly groundwater elevation data and precipitation at the control well, and d) normalized water level and precipitation signals. Two consecutive dashed/solid lines show trends matching between the normalized sulfate signal and the precipitation data, and arrows show trends matching between the normalized sulfate signal and groundwater elevation data.

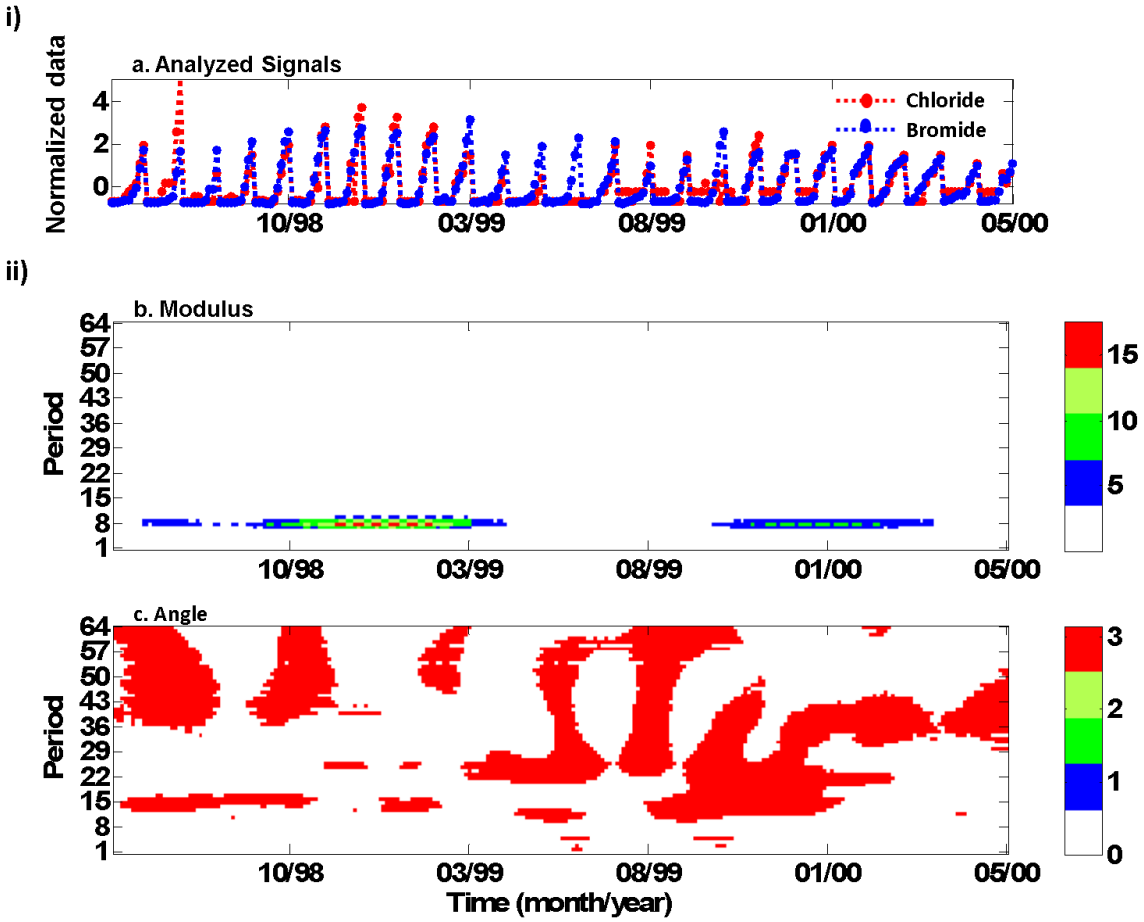

Figure 5.8: Cross wavelet analysis of bromide and chloride signals at the control well from May 1998 to May 2000: i) time records of normalized bromide and chloride data, and ii) modulus and angle of the wavelet cross-spectrum.

The cross wavelet transform is used in this study to describe the physical relationships between bromide and chloride data in the time frequency space. The modulus of the cross wavelet transform indicates that both signals have significant correlation around scale 8 except in the interval between April-October 1999, which reveals the quasi-periodic nature of this correlation (Figure 5.8b). The phase plot (Figure 5.8c) of the normalized data also reveals the out-of-phase behavior of the two signals that is not consistent throughout the dataset. This again suggests the time-localized correlation between bromide and chloride, which could be attributed to different sources that augment bromide and chloride concentrations at the landfill site. As both signals are conservative indicators of water flow, results pertaining to bromide only will be described. Cross wavelet analysis with respect to other variables is provided in the appendix.

In summary, temporal variations in bromide and sulfate data at the control well show annual periodicity (~12 month), and are significantly dominated by water table variability and precipitation events. The temporal anomalies at the dominant scale of variation are related to hydrologic variability for bromide, and sulfate reduction processes for sulfate.

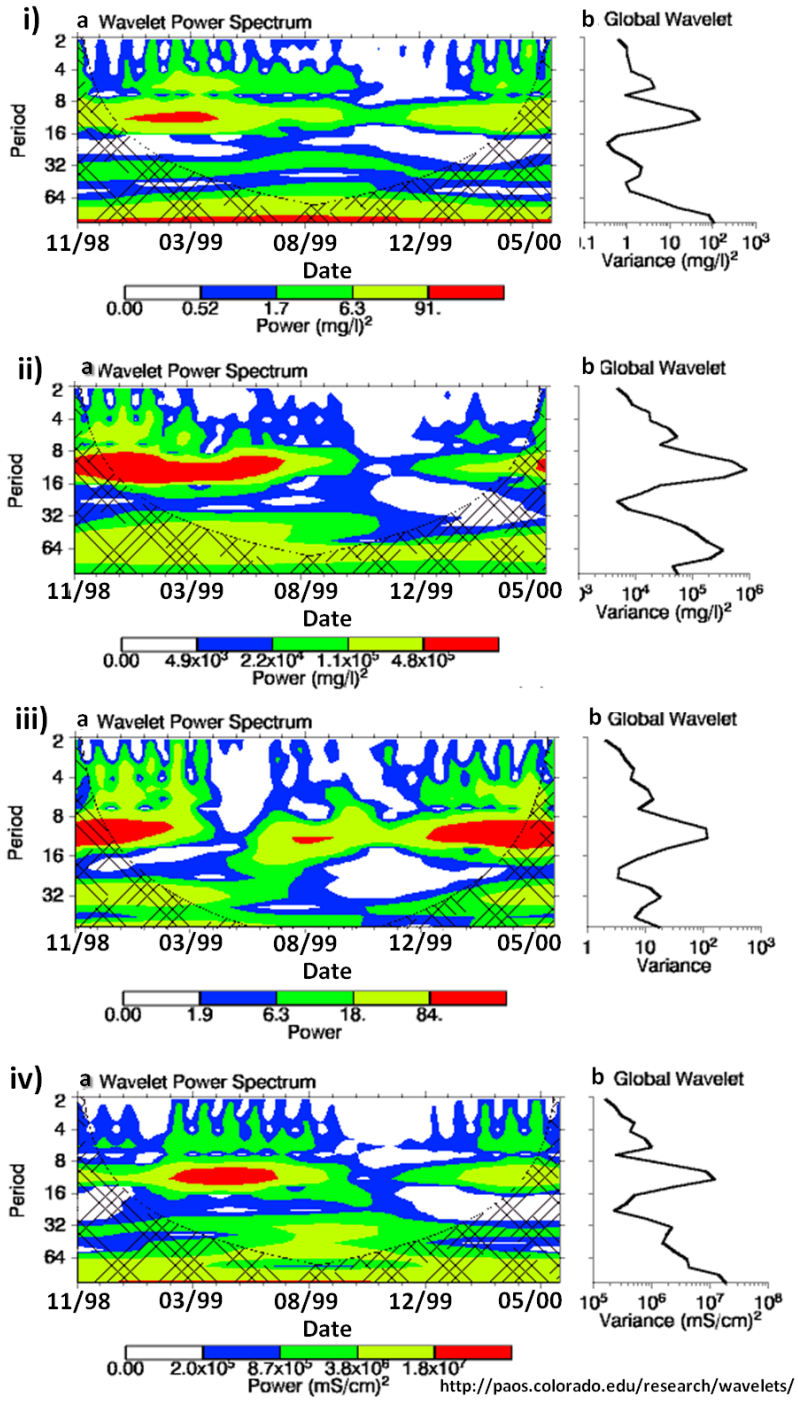

Figure 5.9: Time frequency analysis at the landfill well for i) bromide, ii) δ^2H, iii) sulfate, and iii) specific conductivity data displaying continuous power spectrum and global variance distribution. The cross-hatched regions in the wavelet power spectrum signify the cone of influence, and the color bar signifies the strength of power in the global wavelet spectrum.

5.5.2 Temporal variations and governing processes at the landfill well

Figure 5.9 represents the temporal dynamics of bromide, δ^2H, sulfate, and specific conductivity at the landfill (IC 36) well from November 1998 to May 2000. An annual periodic component is again visible in the wavelet spectra for all time-series data (Figure 5.9a), and this component shows dominance in the global variance distribution as well (Figure 5.9b). These periodic structures show time localization and disappear beyond April 1999 for bromide, beyond July 1999 for sulfate and specific conductivity, and show temporal irregularity in δ^2H data. These annual components are therefore replaced by 4-month components for bromide and specific conductivity, and a 7-month component for δ^2H. Regarding the small scales (2-4 months), structures with significant power are again visible for bromide, δ^2H, and sulfate time-series but not for specific conductivity. Since these variables have different contributing processes, the temporal discrepancies present in the wavelet power spectrum for each signal are different.

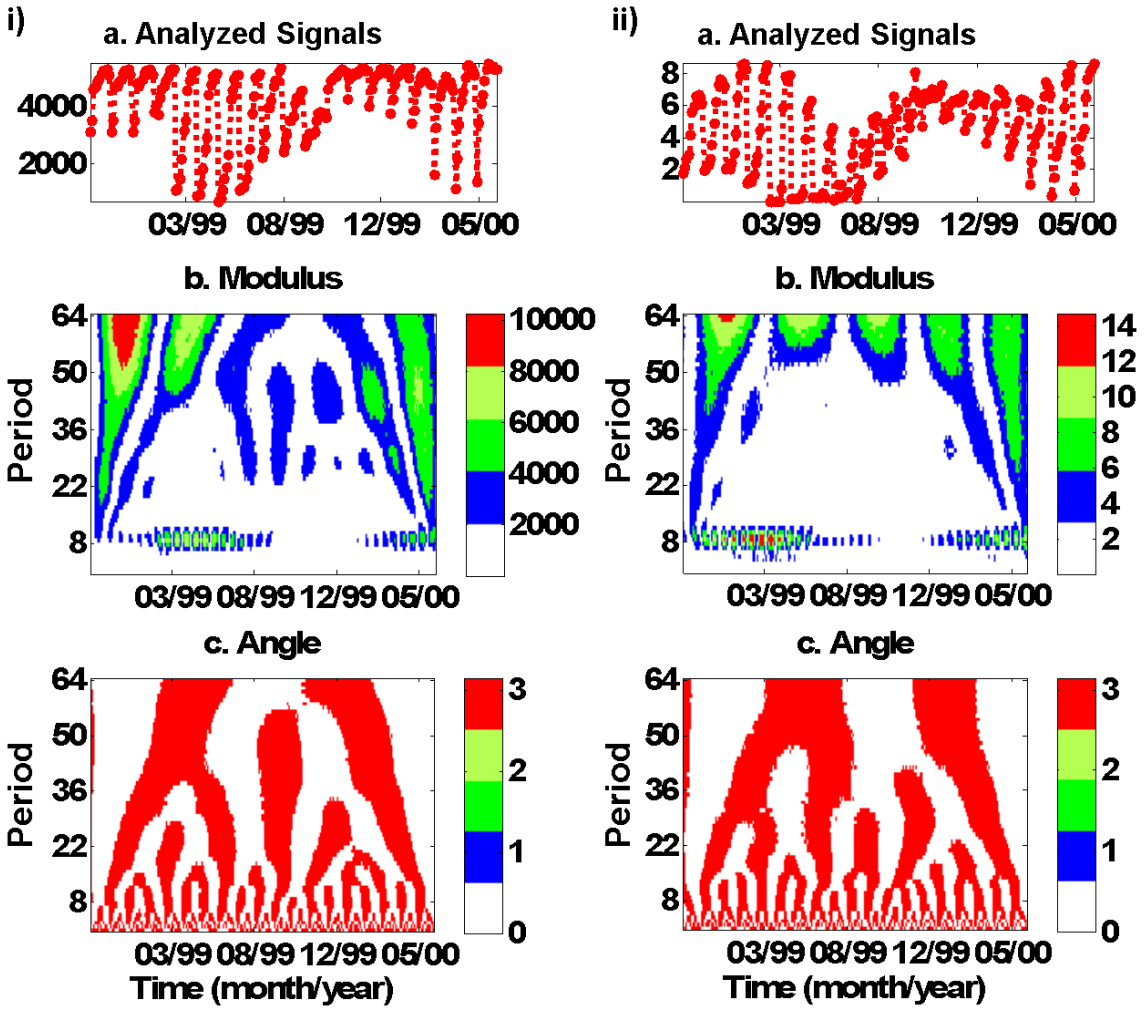

Figure 5.10: Wavelet coherence analysis at the landfill well from November 1998 to May 2000: i) specific conductivity and ii) bromide displaying analyzed signals, and modulus and angle of the continuous wavelet spectrum.

Wavelet coherence analysis conducted on bromide and specific conductivity is illustrated in Figure 5.10. Although the analysis reveals different structures at higher time scales, similar contributing processes at the dominant scale of variation (scale 8) are observed (Figure 5.10b). The angle plots (Figure 5.10c) also reveal a consistent out-of-phase behavior at the smaller scales suggesting a high correlation between the two time-series. Wavelet cross spectrum and coherence analyses also suggest a high correlation between bromide and δ^2H signals in displaying the periodic annual component. As a result, a multilevel decomposition is performed only with respect to bromide and sulfate at the landfill well. Cross wavelet analysis with respect to other variables is provided in the appendix.

After removing the noise components, the "approximation" of bromide is again compared with hydrologic variations at the landfill well (Figure 5.11). Apart from November-February time frames for both 1998-1999 and 1999-2000 years, the normalized patterns of bromide show considerable matching with groundwater table and rainfall data. Since the region around the landfill well is densely vegetated, a decrease in evapotranspiration processes observed during the winter months (represented by ovals in Figure 5.11e) seems to be contributing to variations in bromide transport processes during these time frames. Therefore, a comprehensive analysis of the hydrologic interactions at the landfill well is able to explain the variability in bromide concentrations at this location.

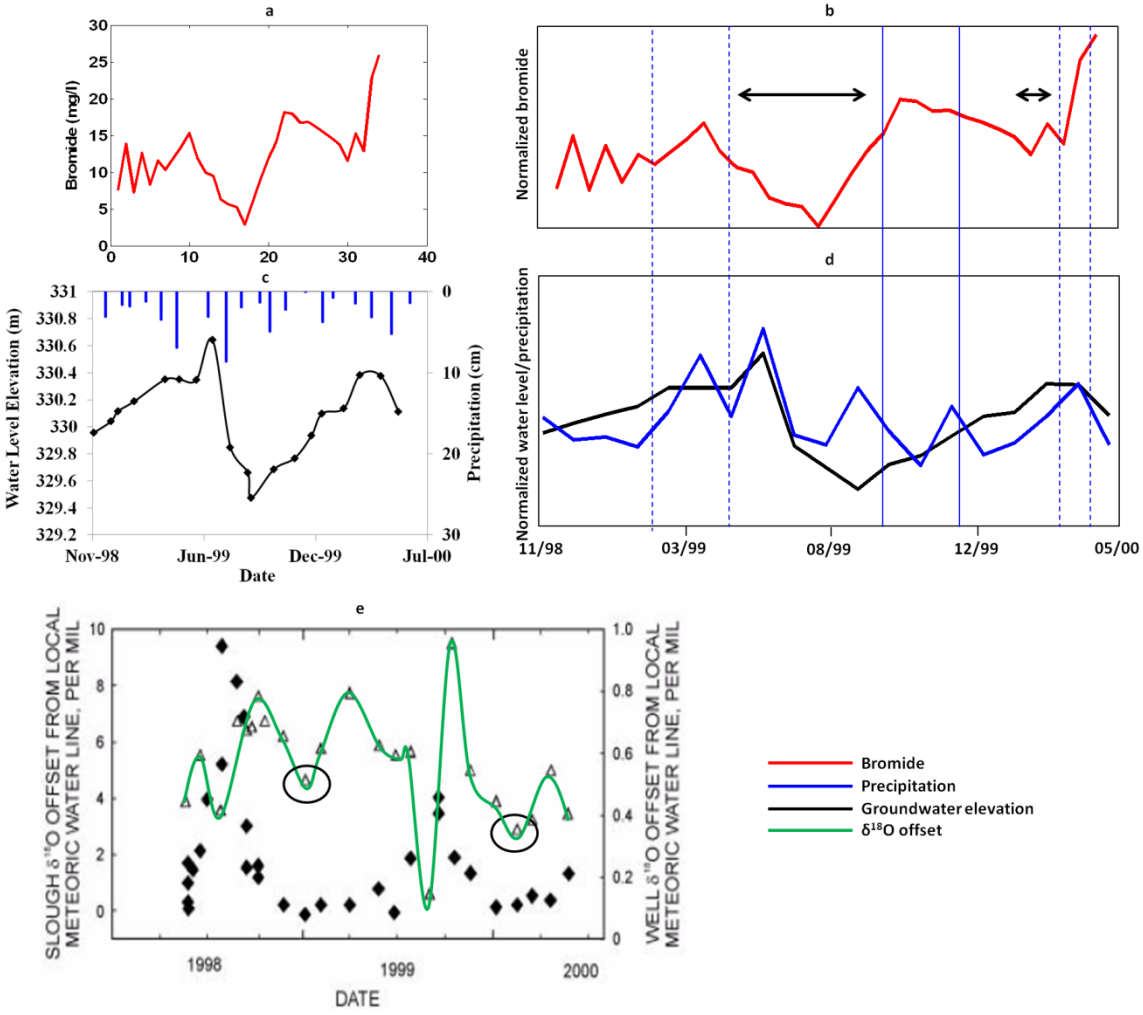

Figure 5.11: Multilevel decomposition of bromide data at the landfill well: a) bromide "approximation" at 8 months, b) normalized "approximation" signal, c) time record of monthly groundwater elevation data and precipitation at the landfill well, d) normalized water level and precipitation signals, and e) time record of $\delta^{18}O$ offset representing evapotranspiration processes [modified from *Scholl et al.*, 2005]. Two consecutive dashed/solid lines show trends matching between the normalized bromide signal and the precipitation data, arrows show trends matching between the normalized bromide signal and groundwater elevation data, and ovals represent decrease in evapotranspiration levels that can be located in the normalized bromide signal.

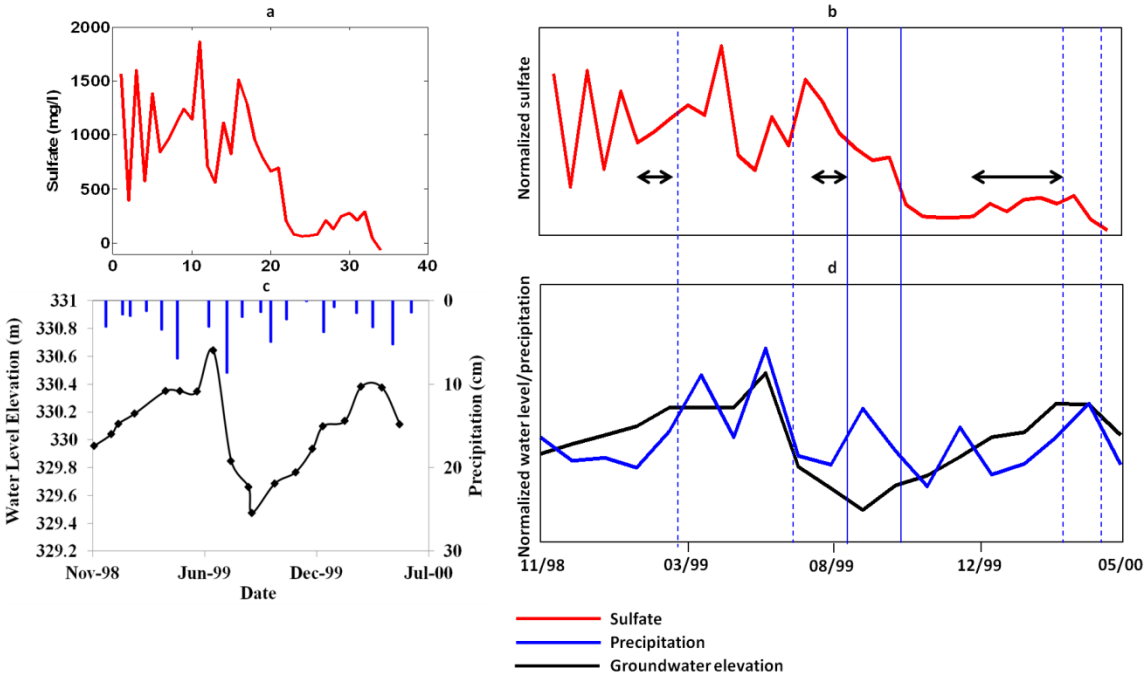

Figure 5.12: Multilevel decomposition of sulfate data at the landfill well: a) sulfate "approximation" at 8 months, b) normalized "approximation" signal, c) time record of monthly groundwater elevation data and precipitation at the landfill well, and d) normalized water level and precipitation signals. Two consecutive dashed/solid lines show trends matching between the normalized sulfate signal and the precipitation data, and arrows show trends matching between the normalized sulfate signal and groundwater elevation data.

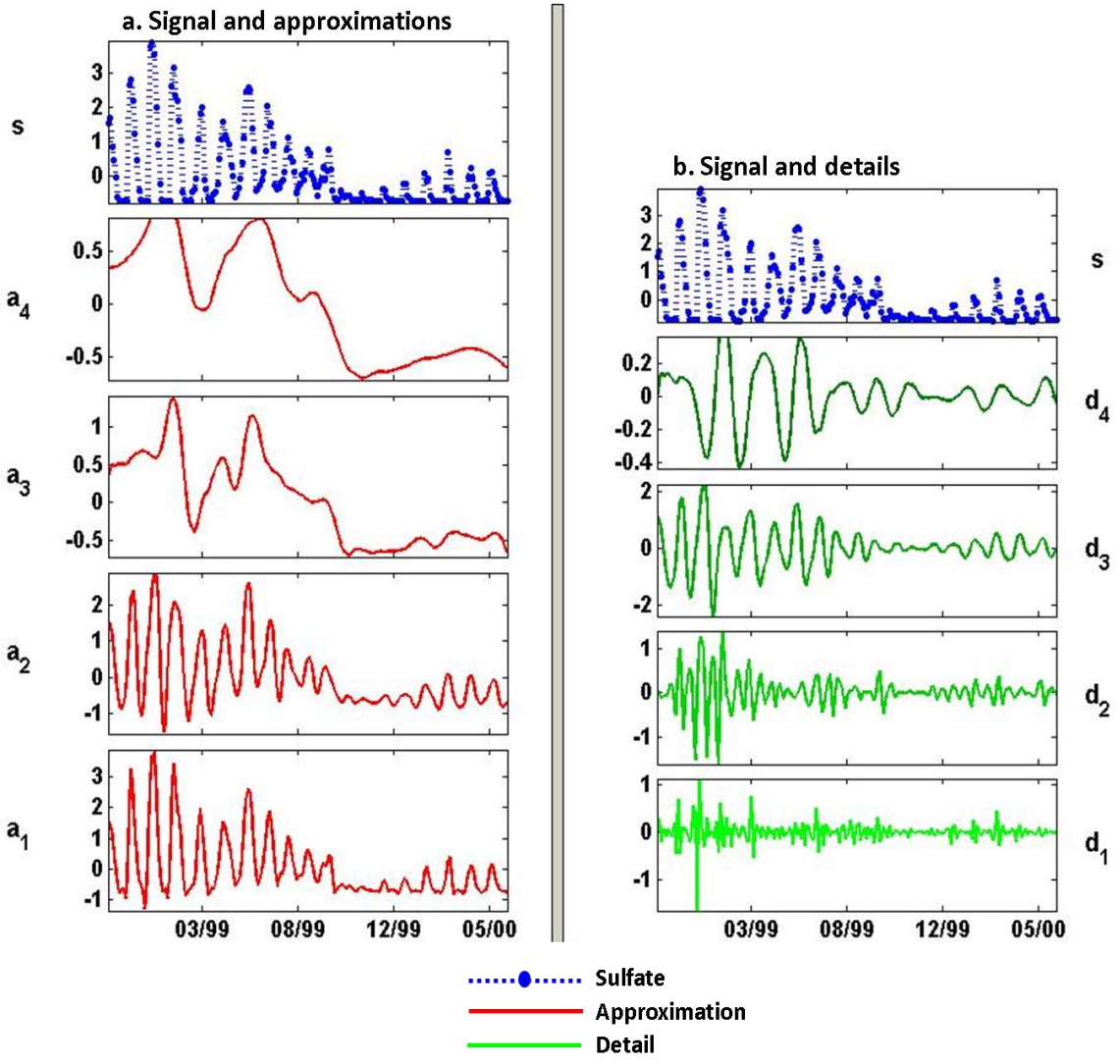

Figure 5.13: Multilevel decomposition of sulfate at the landfill well with approximations and detail coefficients at dyadic scales of 2 (a_1), 4 (a_2), 8(a_3) and 16 (a_4) from November 1998 to May 2000.

The "approximation" component of sulfate at the dominant scale of variation is also compared with hydrologic fluctuations (Figure 5.12). Again, the November-February time frames for both 1998-1999 and 1999-2000 years show poor matching. The trend analysis also reveals a mismatch with a peak in sulfate concentrations around July 1999. Therefore, scale decomposition with all approximations and details of sulfate time-series is illustrated in Figure 5.13. The decomposition in the details of sulfate concentrations at the landfill well leads to the identification of three components with very different behaviors. First, a large peak is located around January 1999, second, several smaller peaks are located around December 1998, February, March, and July of 1999, and April 2000, and third, a discontinuity is observed around November1999-March 2000 in the d_1 component. The d_2 component also reveals an amplitude reduction in sulfate frequency from November 1998-March 1999 to the rest of the time-series. These detailed components suggest that large peaks in sulfate concentrations in the beginning time frame (November 1998-March 1999) correspond to a large reoxidation event that possibly lead to the dissolution of aquifer solids (barite, iron sulfide minerals) because such high sulfate concentrations cannot be attributed to background groundwater or rainfall alone, or that the aggregation of various processes (rainfall recharge, vegetative decay, mineral dissolution, etc.) simultaneously resulted in such an event [*Schlottmann*, 2001]. Previous studies have documented the importance of barite dissolution and its influence on sulfate concentrations at the landfill site [*Tuttle et al.*, 2009; *Cozzarelli et al.*, 2011]. Also, these larger peaks occur immediately following low sulfate concentrations and several factors (water table variations, undersaturation with

respect to sulfate due to increased sulfate reduction and/or iron sulfide formation, etc.) can contribute to an increase in the dissolution rate [*Ulrich et al.*, 2003; *Cozzarelli et al.*, 2011]. The smaller peaks that are spread across different times indicate an increase in sulfate concentrations in response to rainfall events or sulfur cycling as a result of reoxidation of iron sulfide minerals with an increase in groundwater table [*Ulrich et al.*, 2003; *Baez-Cazull et al.*, 2008]. This sulfur cycling also constitutes a sulfate reduction step which is visible as the decrease in sulfate concentrations immediately following a rainfall event (Figure 5.12b, d). The discontinuity around November 1999-March 2000 constitutes a significant decrease in sulfate concentrations (greater than those observed for November 1998-March 1999) and may stem from strong vegetation dynamics at the site. Uptake of sulfate by plant roots is an important process near the landfill well [*Tuttle et al.*, 2009] and this frequency may be reduced during the winter months as suggested by $\delta^{18}O$ offset patterns (Figure 5.11e).

In summary, an annual periodic component again dominates different geochemical concentrations at the landfill well. The temporal patterns of geochemical variables are strongly guided by hydrologic variations and affected by vegetation dynamics in the winter months. The multilevel decomposition of sulfate reveals sources (FeS cycling, rainfall events, increased barite dissolution rate) and sinks (uptake by plant roots) of sulfate at different time frames between November 1998 and May 2000.

i)

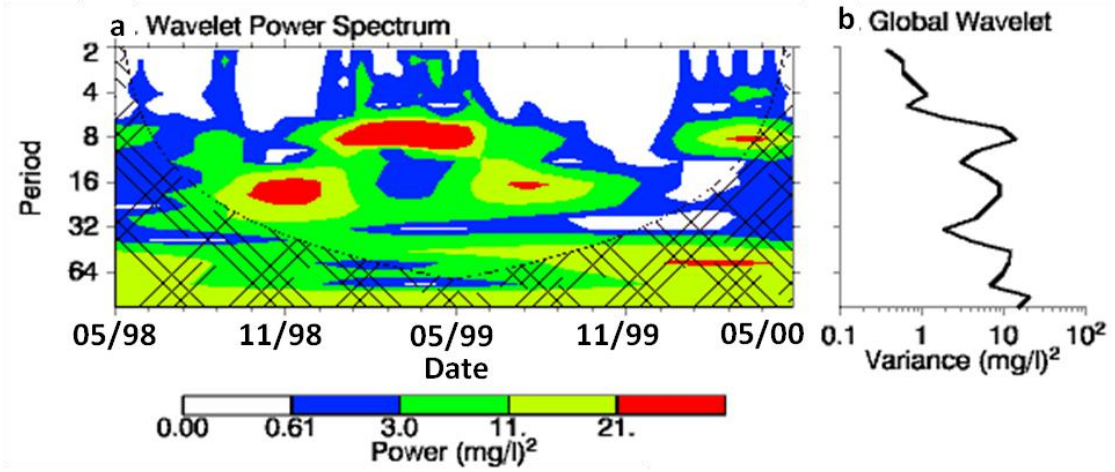

ii)

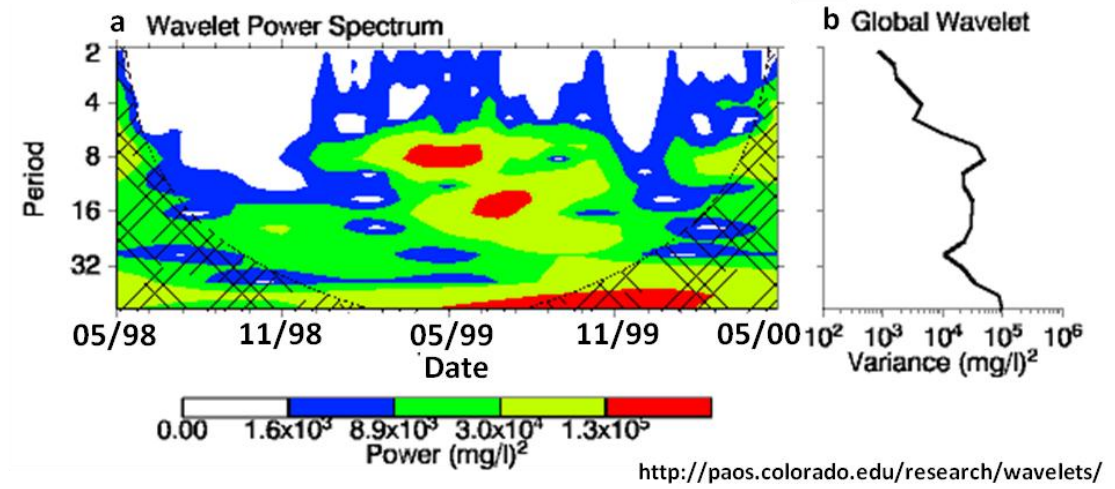

Figure 5.14: Time frequency analysis at the slough well for i) bromide and ii) sulfate data displaying continuous power spectrum and global variance distribution. The cross-hatched regions in the wavelet power spectrum signify the cone of influence, and the color bar signifies the strength of power in the global wavelet spectrum.

5.5.3 Temporal variations and governing processes at the slough well

Figure 5.14 demonstrates the temporal evolution of bromide and sulfate at the slough (IC 54) well. The wavelet power spectra (Figure 5.14a) reveal two dominant scales of variation with annual and bi-annual periodic components for both signals. Notice that the smaller scales contain negligible power for both time-series. The annual component (~12 months) is replaced by a 2-month component for sulfate and a 5-month component for bromide that reappears in the last phase of the time-series. The bi-annual component (~20 months) is replaced by a 1-2 month component for bromide and a 2-month component for sulfate.

To further evaluate the processes affecting temporal variability at the slough well, a multilevel decomposition is conducted on the bromide time-series. This trend analysis (Figure 5.15b, d) at the semi-annual scale (8 months) portrays significant matching with rainfall data in the second year of analysis (July 1999-May 2000). In the first year of analysis (May 1998 to July 1999), there are discrete patterns of decreasing, increasing, and constant water table elevation that match with the normalized "approximation" of bromide. The mismatch between the smoothed "approximation" and hydrologic data can be explained by groundwater-surface water interactions between the wetland and the slough well (Figure 5.15e). Notice the peak in the normalized bromide signal around July 1999 (Figure 5.15b) that matches with the increase in wetland water levels (represented by a circle in Figure 5.15e).

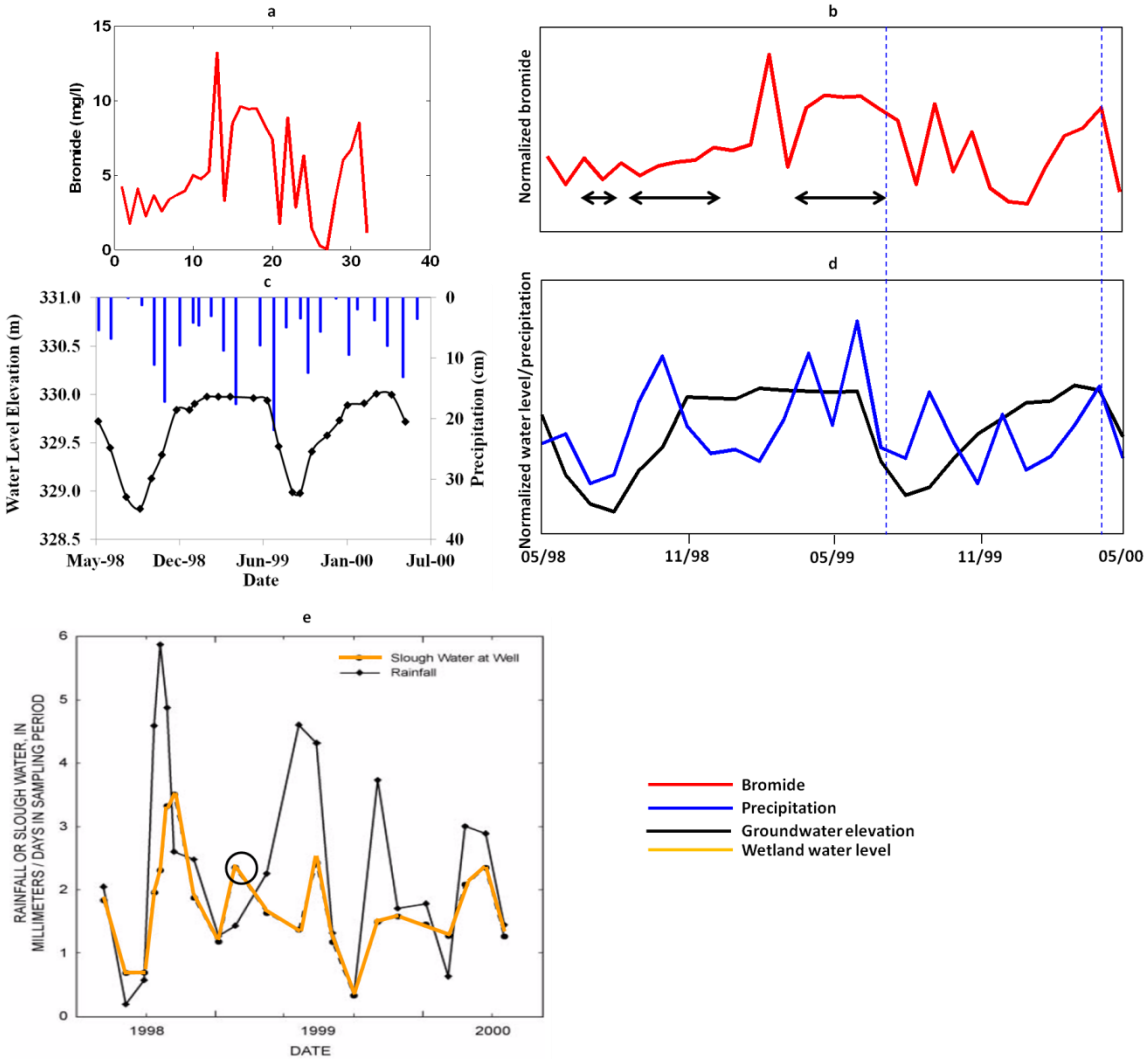

Figure 5.15: Multilevel decomposition of bromide data at the slough well: a) bromide "approximation" at 8 months, b) normalized "approximation" signal, c) time record of monthly groundwater elevation data and precipitation at the slough well, d) normalized water level and precipitation signals, and e) time record of wetland water level [modified from *Scholl et al.*, 2005]. Two consecutive dashed/solid lines show trends matching between the normalized bromide signal and the precipitation data, arrows show trends matching between the normalized bromide signal and groundwater elevation data, and circle represents peak in the wetland water level that can be located in the normalized bromide signal.

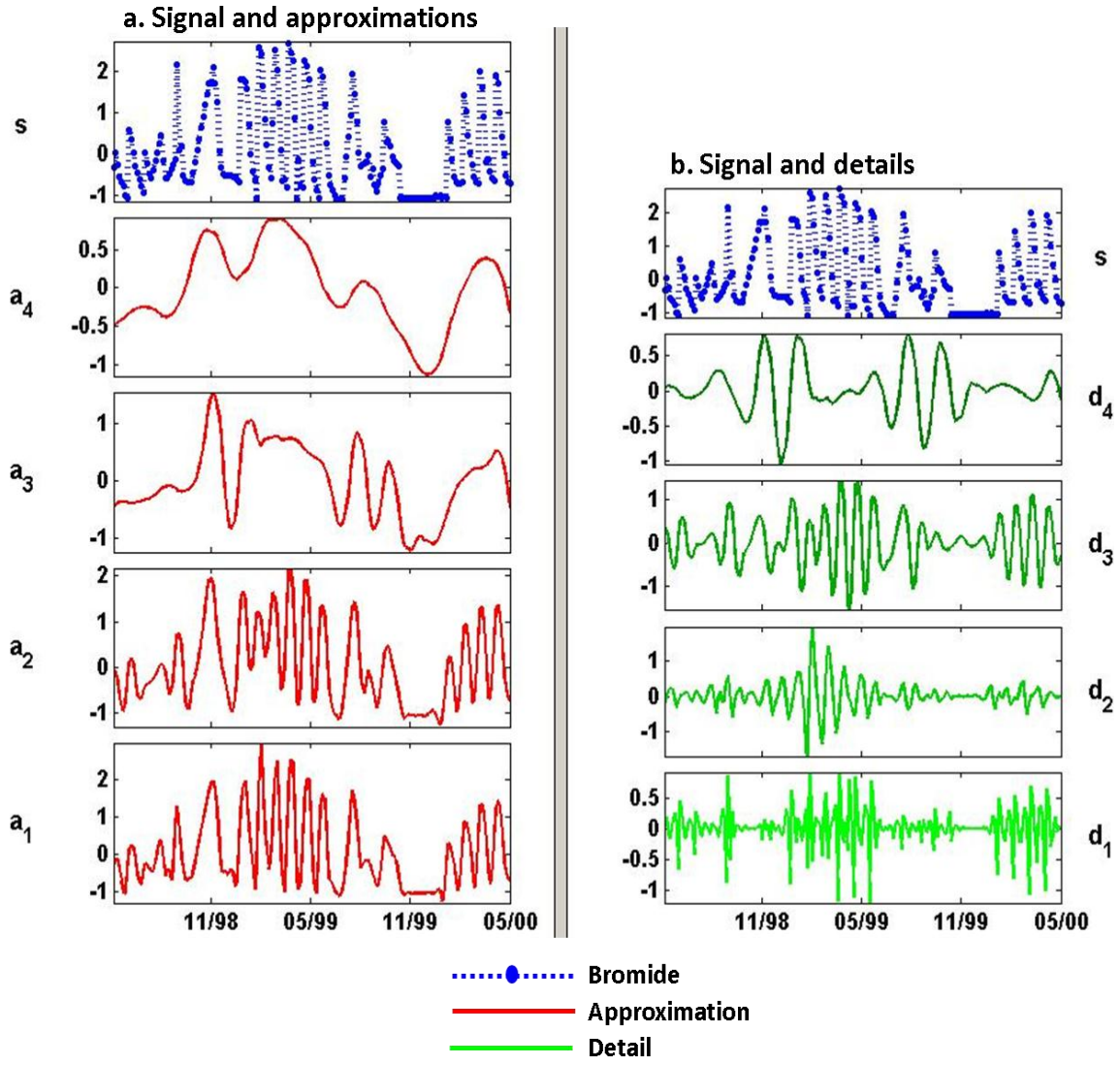

Figure 5.16: Multilevel decomposition of bromide data at the slough well with approximations and detail coefficients at dyadic scales of 2 (a_1), 4 (a_2), 8(a_3) and 16 (a_4) from May 1998 to May 2000.

The detailed components d_1-d_3 (Figure 5.16) also identify a frequency around March-July 1999 that is visible in the last phase of the time-series as well and corresponds to an increase in wetland water level during the spring season [*Scholl et al.*, 2005]. The d_4 component reveals another frequency that is localized around October-November 1999 and October 2000. This bi-annual component is reflective of the end of the growing season. The withdrawal of water from the water table by vegetation affects hydrologic dynamics at the site and consequently alters transport of conservative indicators.

In summary, the wavelet spectra for bromide and sulfate at the slough well reveal two frequencies that are more or less localized in time. The annual periodic component in the signal corresponds to slough interactions and showcases a 5-month component that spans the months of March to July, while the biannual component is a function of vegetation dynamics at the slough well and showcases a 1-2 month component that spans the months of October and November.

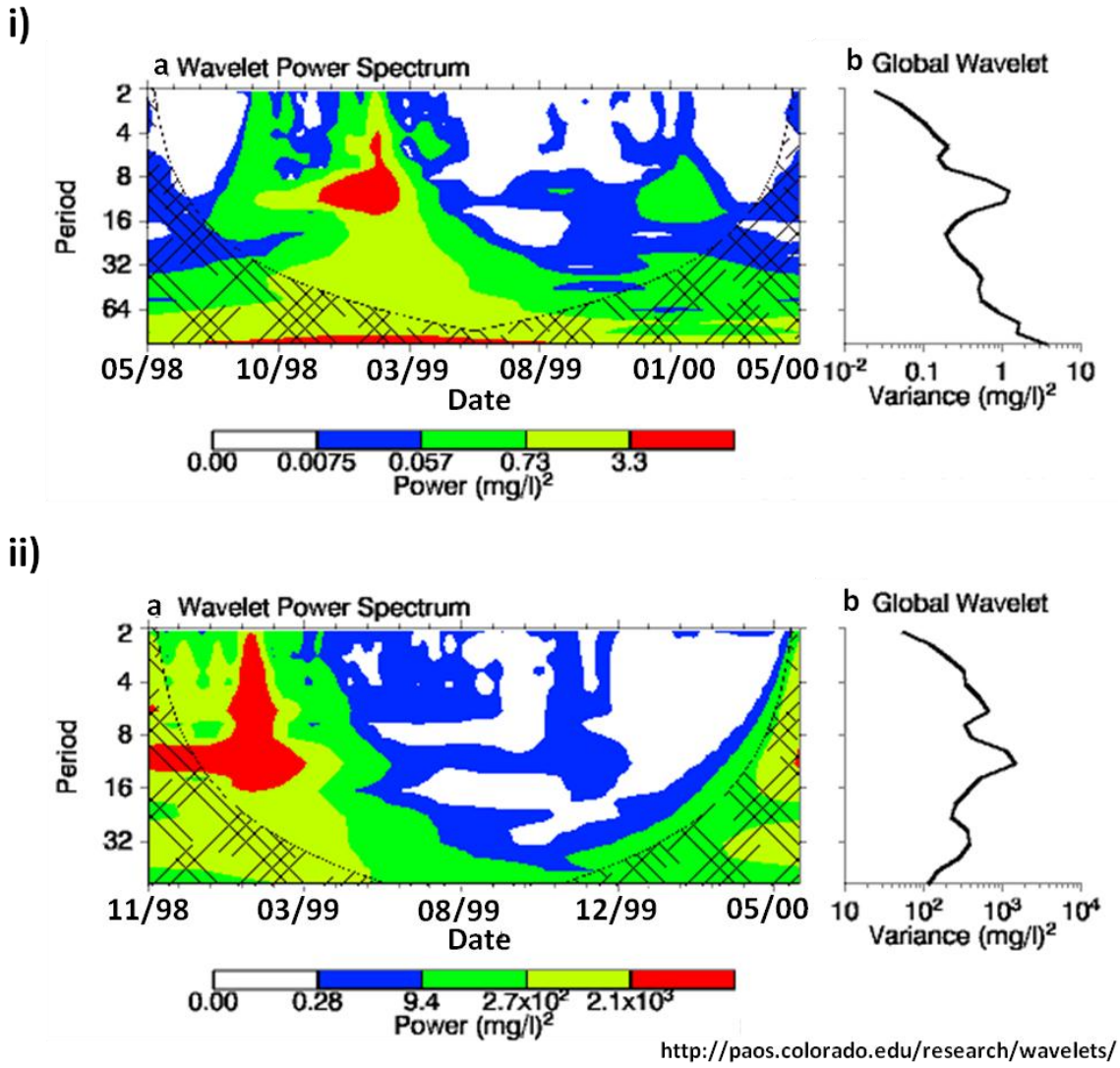

Figure 5.17: Time frequency analysis of nitrate at the i) control and ii) landfill wells displaying continuous power spectrum and global variance distribution. The cross-hatched regions in the wavelet power spectrum signify the cone of influence, and the color bar signifies the strength of power in the global wavelet spectrum.

5.5.4 Exceptions to the dominant frequency rule

There are two exceptions to the dominant scales of variation obtained for the geochemical variables at the control (scale 8), landfill (scale 8), and slough wells (scales 8 and 16). First, nitrate data are inherently multi-scalar and this is demonstrated in Figure 5.17. The wavelet power spectra of nitrate time-series (Figure 5.17a) reveal high power wavelet coefficients across scales 4-16 for the control well, and across scales 2-16 for the landfill well. The global variance distributions (Figure 5.17b) also suggest power to be distributed across multiple scales. This clearly indicates that different processes with different frequency ranges are contributing to the total wavelet spectra. Notice that the regions of significant power are limited to November 1998-March 1999 for both wells. The dominant variability in nitrate concentrations during these winter months could be a result of several concomitant processes such as external climate forcing (e.g., snow storms), plant decay, and bacterial decomposition of stored nitrogen, which produced a similar time frame of November-March for both wells.

Second, dissolved organic carbon (DOC) concentrations follow the dominant scales of variation for both the control and slough wells but not for the landfill well. The wavelet power spectrum (Figure 5.18a) and global variance distribution (Figure 5.18b) for the landfill (IC 36) well suggest that although the annual periodic component carries significant power, the dominant frequency may well lie outside the time scale of analysis.

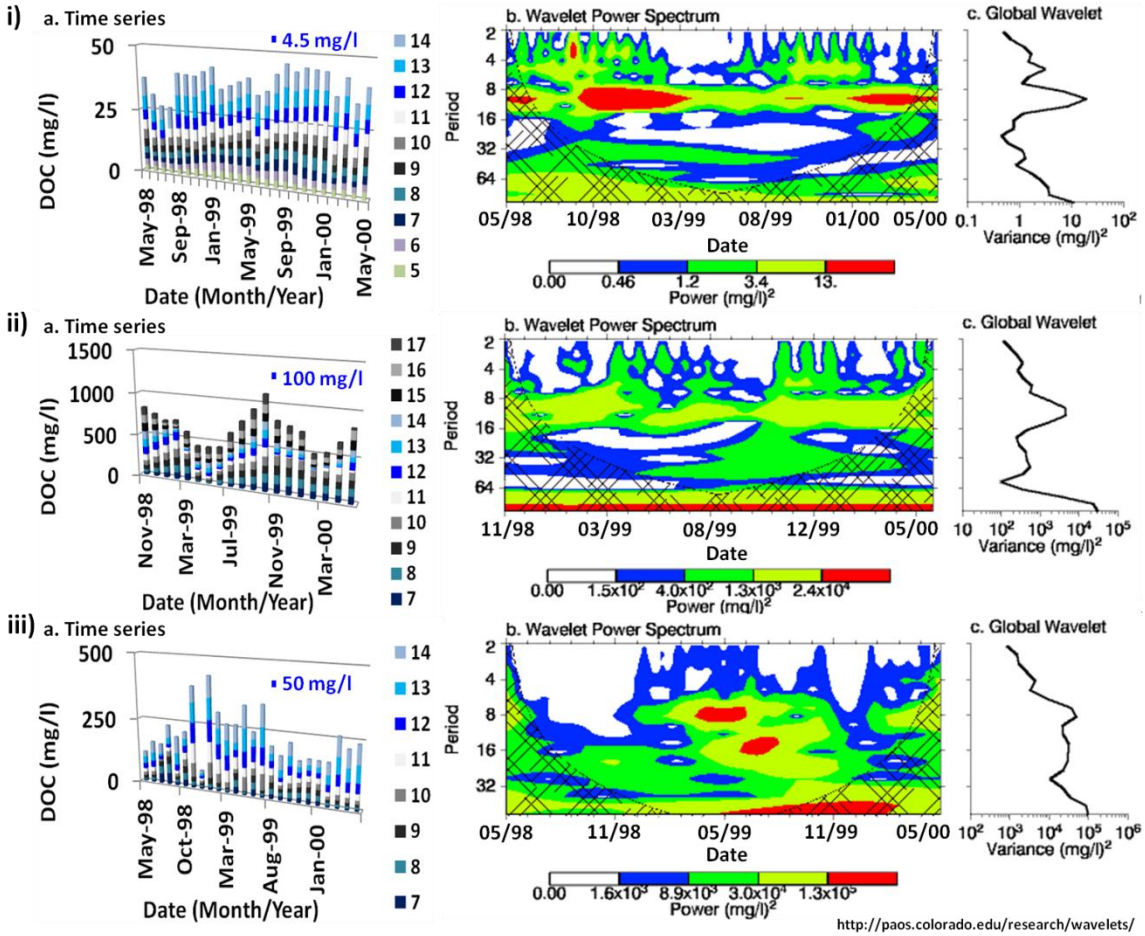

Figure 5.18: Time frequency analysis of DOC at the i) control, ii) landfill and iii) slough wells displaying time-series data, continuous power spectrum and global variance distribution. In the time series graphs, the thickness of the cylinder signifies the concentration value, and the colors represent the well screens. In the wavelet power spectrum, the cross-hatched regions signify the cone of influence, and the color bar signifies the strength of power in the global wavelet spectrum.

This is expected as the temporal variability in DOC concentrations are not limited to hydrologic events. Changes in the carbon content as a result of organic degradation can itself contribute to the temporal variability in the data [*Cozzarelli et al.*, 2011].

5.6 Conclusions

Biogeochemical processes and redox reactions are often characterized by high temporal variability. Analyses of biogeochemical datasets using correlation, principal component analysis, or other statistical techniques are not always able to identify the processes driving this temporal variability. Therefore, the focus of this study is to extract the complex linkages among biogeochemical processes and identify the temporal scales at which they exert dominant control. A continuous wavelet transform (CWT) is employed to understand the temporal variations in redox-sensitive chemicals at the Norman Landfill site and a multilevel decomposition technique (MLD) is used to identify the coupled processes that govern the fate of landfill contaminants at the dominant scale of variation. The Norman Landfill is a closed landfill site with prevalent organic contamination, and three wells at the landfill site are used to elucidate the complex processes and external factors that govern the chemical composition of water.

The wavelet analysis (CWT) reveals that the chemical dataset of the Norman landfill site has single-scale characteristics for different geochemical variables at the landfill (IC 36) and control (IC South) wells despite the large differences in their geochemical characteristics and conceptual redox frameworks. The IC 36 well is located closest to the landfill mound and contaminated with the leachate plume, while the IC

South well is located farthest from the landfill and is devoid of any influence from contamination. The single-scale characteristics show that a dominant scale of variation lies in an annual (~12 months) periodic component. Wavelet decomposition analysis further suggests that this annual component is usually replaced by smaller cycles (5-7 month components) that are guided by hydrologic fluctuations. Bromide concentrations typically show strong associations with rainfall recharge events and seasonality of the groundwater. Sulfate concentrations reveal sources and sinks that are related to hydrologic (rainfall recharge, water table dynamics) and geologic frameworks (aquifer composition). The vegetation around the landfill well also demonstrates its influence on the dominant frequency for both conservative and reactive concentrations during the winter months. Wavelet cross-spectrum and coherence analyses between bromide and other variables (specific conductivity, chloride, etc.) reveal high common power and similar contributing processes at scale 8. This local phase-locked behavior is again indicative of hydrologic variations to be important drivers of redox geochemistry at both landfill and control wells. Temporal discrepancies between different conservative indicators like bromide and chloride indicate differences in contributing sources.

At the slough well, the continuous wavelet transform suggests two dominant scales of variation for diverse geochemical variables such as DOC, sulfate, bromide. These dominant scales contain annual (~12 months) and bi-annual (~20 months) periodic components that are significantly localized in time. The annual periodic component is replaced by a 5-month component and associated with a local feature, which is the surface-groundwater interaction between the wetland and the IC 54 well.

The bi-annual component is replaced by a 1-2 month component and associated with vegetation dynamics around the slough well.

There are two major exceptions to the dominant scale(s) of variation across the three well locations. First, nitrate displays a multi-scale behavior with significant power between scales 4-16 for the control well, and scales 2-16 for the landfill well. This clearly indicates the influence of several concomitant processes (such as plant decay, microbiological decomposition, effect of climate) with different frequencies on nitrate concentrations. Second, dissolved organic carbon concentrations illustrate that the dominant scale of variation is beyond scale 16 for the landfill well. This behavior is not unexpected as several studies have documented the persistence of organic carbon at the Norman landfill site [*Cozzarelli et al.*, 2000, 2011; *Eganhouse et al.*, 2001].

Based on our analysis of the biogeochemical dataset of 2 years, we hypothesize that the information in conservative and redox signals at large scales can be explained by linked biogeochemical processes such as increased xenophobicity of the carbon content (Figure 5.19). Figure 5.19 demonstrates the temporal characteristics of redox-sensitive chemicals at any landfill site. This time-series data can be further decomposed with variability being explained by site-specific interactions at the bi-annual scales, and hydrologic fluctuations at the annual scales.

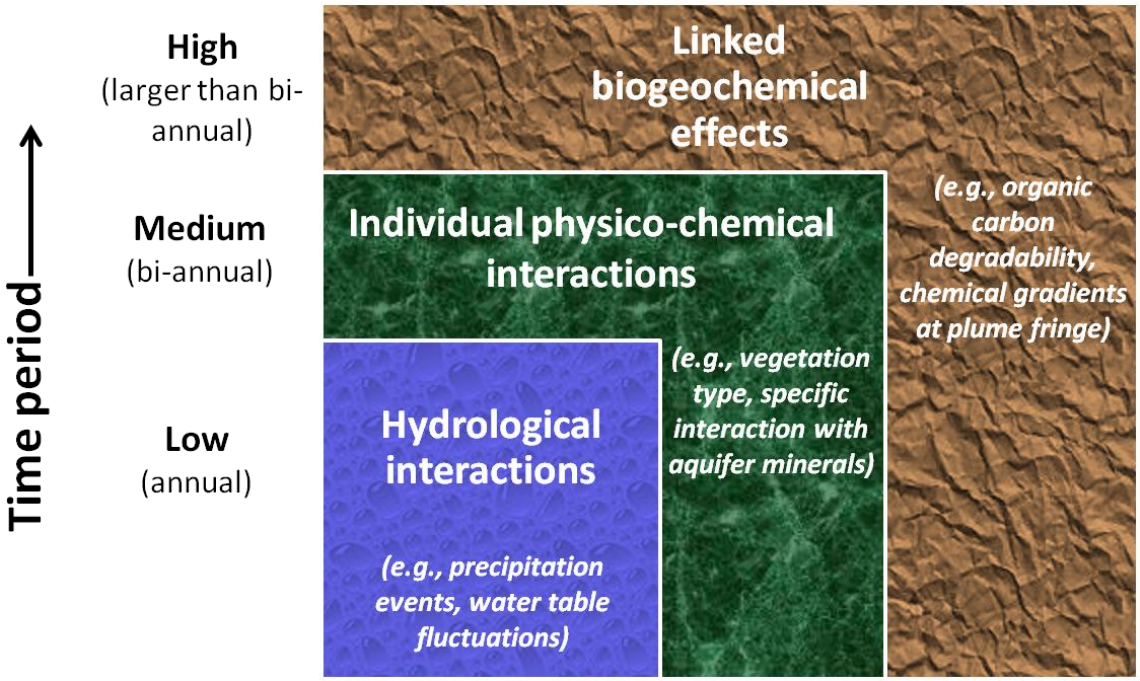

Figure 5.19: Conceptual diagram showing the governing controls of redox geochemistry at increasing time scales.

CHAPTER VI

AN INTEGRATED MARKOV CHAIN MONTE CARLO ALGORITHM FOR UPSCALING HYDROLOGICAL AND GEOCHEMICAL PARAMETERS FROM COLUMN TO THE FIELD SCALE

6.1 Synopsis

Predicting and controlling the concentrations of redox-sensitive elements is a primary concern for environmental remediation of contaminated sites. These predictions are complicated by dynamic flow processes as hydrologic variability is a governing control on conservative and reactive chemical concentrations. In addition, subsurface heterogeneity in the form of layers and lenses further complicates the flow dynamics of the system. Therefore, this study investigates the role of heterogeneity and hydrologic processes on an effective parameter upscaling scheme from the column to the landfill scale. A Markov chain Monte Carlo algorithm (MCMC) is used to derive upscaling coefficients for hydrologic and geochemical parameters, which are tested for variations across heterogeneous systems (layers and lenses) and interaction of flow processes based on output uncertainty of dominant biogeochemical concentrations at the Norman landfill site. The Norman landfill is a closed municipal landfill with prevalent organic contamination.

The results from the MCMC analysis indicate that geochemical upscaling coefficients based on effective concentration ratios incorporating local heterogeneity across layered and lensed systems produce better estimates of redox-sensitive

biogeochemistry at the field scale. The MCMC scheme also suggests that inclusion of hydrological parameters reduces output uncertainty of effective mean geochemical concentrations by orders of magnitude at the Norman Landfill site. This is further confirmed by posterior density plots of the scaling coefficients that reveal unimodal characteristics when only geochemical processes are involved, but produce multi-modal distributions when hydrological parameters are included. The multi-modality again suggests the effect of heterogeneity and lithologic variability on redox processes at the Norman landfill site.

6.2 Introduction

Knowledge about effective hydrologic and geochemical properties at field scales is pertinent in predicting and managing the fate and transport of reactive contaminants from landfill and waste management sites. However, the transition of biogeochemical processes across scales is not well understood. Therefore, the challenge is to acquire detailed knowledge of key processes at individual scales and identify the dominant linkages to predict geochemical dynamics from one scale to the other.

Reactive transport is strongly influenced by hydrological processes across different spatial scales [*Kimball et al.*, 1994; *Vogel and Roth*, 2003; *Jardine*, 2008]. Hydrologic variations including water table elevation and precipitation play a pivotal role in the migration and distribution of contaminants in groundwater. Several studies have identified the impact of rainfall events on redox processes at column [*Hansen et al.*, 2011] and field scales [*McGuire et al.*, 2000; *Scholl et al.*, 2006]. Other studies have documented the importance of seasonality and direction of groundwater flow on the

variability of geochemical concentrations [*Prommer et al.*, 1998; *Mitchell and Branfireun*, 2005; *Cozzarelli et al.*, 2011]. For example, *Fendorf et al.* [2010] suggested that the patterns of recharge and discharge of groundwater, especially groundwater pumping and time since recharge, were important factors influencing arsenic concentrations in South and Southeast Asia.

Apart from hydrologic variations, the uncertainty in predicting redox dynamics is also affected by geochemical and microbiological characteristics of groundwater systems. Various studies have reported that the progression of redox reactions can be spatially variable and intensified at the plume fringe, and temporally variable and governed by changes in chemical composition, redox state, microbial community structure, or other external forcing [*Champ et al.*, 1979; *Roling et al.*, 2001; *Van Breukelen and Griiffioen*, 2004]. Chapter V identifies the temporal variability of different processes that affect the distribution of conservative and reactive concentrations at the Norman landfill site. Thus, the variability in redox processes across scales can result from interactions of different processes simultaneously [*Christensen et al.*, 2001; *Bjerg*, 2011; *Pacific et al.*, 2011].

Despite several decades of research on redox processes and considerable knowledge about individual physical (e.g., advection, dilution), geochemical (e.g., adsorption, precipitation, complexation) and microbiological processes (e.g., microbial biodegradation, biotransformation), the interactions among these processes and their influence across scales is not well understood. Rate laws, hydrological parameters or interactions that are applicable at one scale may not necessarily be applicable to other

scales [*van Grinsven and van Riemsdijk*, 1992; *White and Brantley*, 2003]. For example, variations in hydraulic conductivity parameter, which are known to affect contaminant transport, have to be evaluated based on the scale of study [*Hunt*, 2003; *Schulze-Makuch and Cherkauer*, 2004]. Hydrologic processes themselves exhibit scale variability [*Bloschl and Sivapalan*, 1995] and are affected by a number of physical attributes such as topography, vegetation, and other characteristics of the porous media [*Sharma et al.*, 2006; *Das et al.*, 2008; *Jana and Mohanty*, 2012]. It is therefore viable to isolate and understand the contribution of hydrological processes that can influence biogeochemical processes across scales.

In addition, understanding the natural variability of biogeochemical processes is difficult from the standpoint of heterogeneity in the subsurface. Structural heterogeneity resulting from the presence of macropores and fractures leads to preferential flow movement and faster gateways for contaminants to reach groundwater [*Mohanty et al.*, 1998; *Jarvis et al.*, 2007]. Heterogeneity in the form of textural interfaces and lithological variations is known to intensify biogeochemical activity and affect the distribution of chemical concentrations. In their study, *Hansen et al.* [2011] clearly demonstrated that heightened redox activity was observed at small scale interfaces of a layered soil column as compared to two texturally homogeneous soil columns. Similarly, *Schilling and Jacobson* [2012] indicated that variations in nutrient concentrations were closely related to lithologic variations within the Cedar River floodplain in Iowa. They demonstrated that water beneath sand-dominated ridges was aerobic, had higher concentrations of NO_3-N and lower concentrations of dissolved organic carbon (DOC)

as compared to the anaerobic groundwater beneath shales that had lower NO_3-N and higher DOC. Therefore, an ability to accurately model subsurface heterogeneity and relate this phenomenon to biogeochemical processes is important to address the issue of upscaling from fine (e.g., column) to coarse (e.g., field) scales.

Upscaling is the process of replacing such heterogeneous systems with effective mean properties that capture the key field scale behavior (by matching hydrologic fluxes and geochemistry data from the field site) [*Rubin*, 2003; *Zhu and Mohanty*, 2002, 2003, 2004; *Vereecken et al.*, 2007]. Most upscaling schemes for soil hydraulic parameters homogenize the effect of heterogeneity in their derivation of effective parameter values [e.g., *Zhu and Mohanty*, 2006; *Mohanty and Zhu*, 2007; *Vereecken et al.*, 2007]. However, real-world applications of solute scaling schemes require that the effect of small-scale heterogeneity on redox activity and geochemical parameters be incorporated into these schemes. For example, *Onsoy et al.* [2005] concluded that the mismatch between effective mean concentrations and nitrate observations at the field scale was a result of the heterogeneous flux conditions that were not accounted for by the mass balance approach used in their study. In the same way, *Khaleel et al.* [2002] indicated that dispersivity values at the field scale were dependent on geologic formations, and averaged concentration profiles for flow parallel to bedding were highly skewed and affected by geologic layering. Therefore, we present a study that isolates and quantifies the influence of hydrologic conditions (such as infiltration, drainage) and heterogeneity (such as lenses, layers) on the effective upscaled geochemical concentrations at the field scale.

In summary, determining the governing rules for upscaling to a landfill environment is difficult due to the complex linkages between hydrologic, geochemical, and microbiological processes, and the knowledge about how these processes transition across scales. The characteristics of the porous media and subsurface heterogeneity in the form of lithological variations also add complexity to modeling and upscaling biogeochemical processes. Therefore, the objective of this study is to examine the scale dependency of geochemical concentrations while incorporating the influence of subsurface heterogeneity (lenses and layers) and hydrologic variability (infiltration and drainage scenarios) into the scaling algorithm.

6.3 Approach

In this study, the uncertainties associated with the scale dependency of hydrological and geochemical parameters as a result of subsurface heterogeneity and influence of coupled processes is the focus of the development of an upscaling algorithm. Figure 6.1 illustrates the framework for developing such an algorithm using Bayesian methods. The hypothesis of using the Bayesian methodology is that the characterization of redox-sensitive elements at the field scale can be realized by an ensemble of effective upscaled soil hydraulic and geochemical parameters that are derived from column scale setups with similar heterogeneous systems.

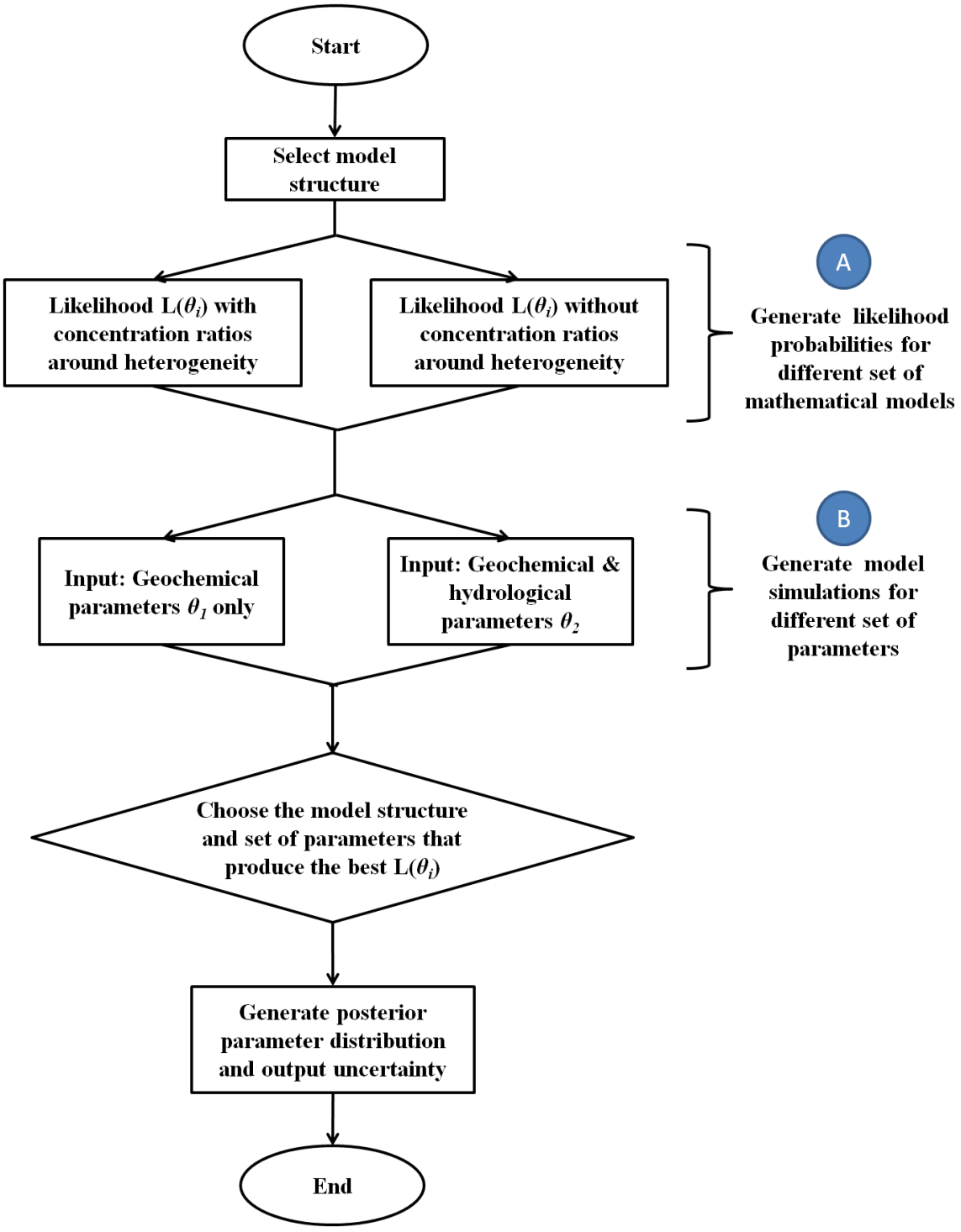

Figure 6.1: Schematic of the upscaling algorithm for testing the heterogeneity hypothesis (part A) and integrated modeling framework (part B).

For verifying the effect of heterogeneity on upscaling coefficients, two different mathematical structures, i.e. with and without heterogeneous formulations, are proposed. For verifying the effect of hydrologic processes, two different sets of input parameters, i.e. with and without the inclusion of soil water retention parameters, are considered. As Figure 6.1 illustrates, the upscaling algorithm requires the selection of the mathematical structure of the model (with or without considering heterogeneous formulations). Next, prior probabilities of model parameters are established based on the choice of the parameter set (with or without the soil water retention parameters). Then, likelihood probabilities are generated depending on the choice of the mathematical model and the parameter set. The upscaling algorithm established is thus able to produce full probability distributions for the selected parameters.

The heterogeneity formulations are based on the conceptual model framework of Chapter IV. This conceptual model developed in § 4.6 describes the distribution of geochemical concentrations in close proximity to spatial heterogeneities and has been validated at the column scale for both infiltration and drainage scenarios. Figure 6.2 demonstrates the application of this model for describing the distribution of sulfate concentrations (associated with the dominant redox processes) as affected by the presence of a clay lens.

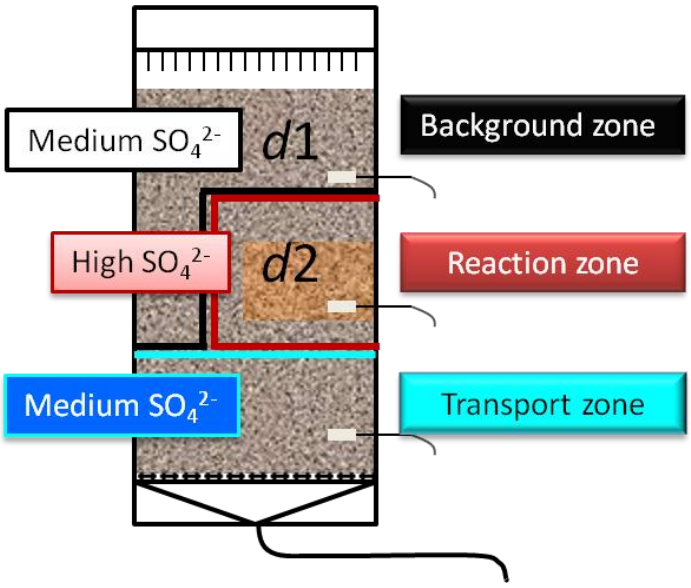

Figure 6.2: Conceptual framework for part A showing the effect of heterogeneity on sulfate concentrations at depths *d*1 and *d*2.

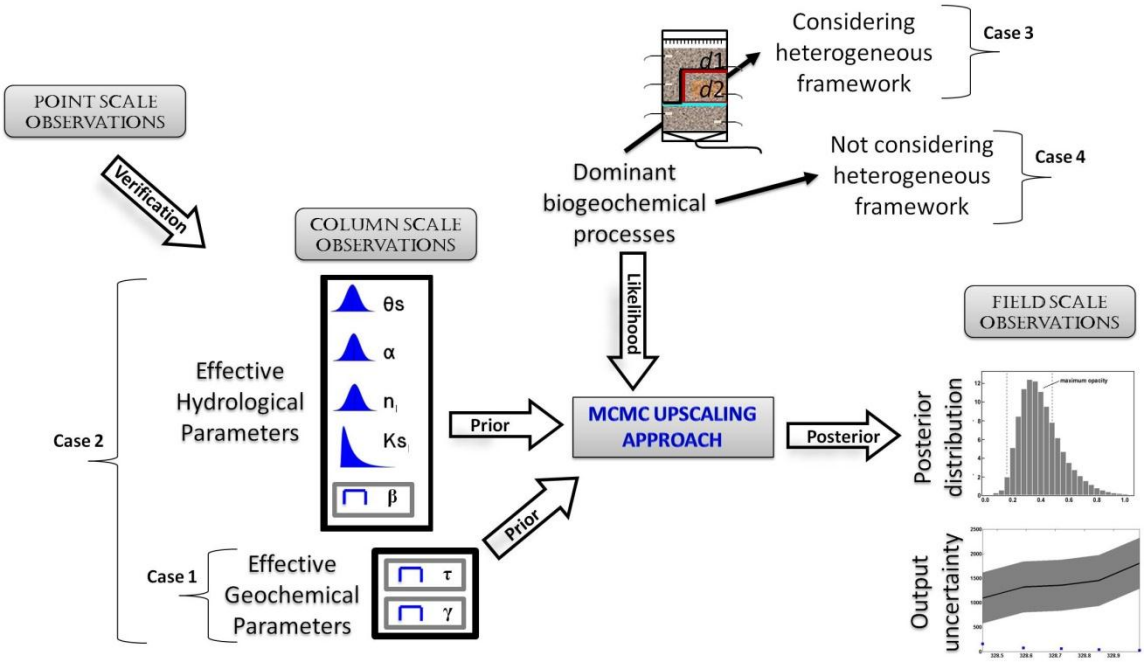

Figure 6.3: Markov chain Monte Carlo based upscaling algorithm for part B deriving scaling coefficients for hydrologic and geochemical parameters.

An adaptive model that preserves the spatial characteristics of the conceptual model is proposed to include the influence of heterogeneity in the scaling scheme. Therefore, the effective mean chemical concentrations <*U*> at the field scale as a function of depth *d* are given by [*Evans et al.*, 2003]:

$$\left\langle U_{field,d} \right\rangle = \frac{\left(U_{column,d} - \overline{U}_{field,d1}\right)}{U^{\tau}_{column,d}\,\overline{U}^{\gamma}_{field,d1}R^{1-\tau-\gamma}},\ d \in d1 \tag{6.1}$$

where the subscript *field* and *column* represent the corresponding scale of observation/prediction, U is the chemical concentration at the given depth of observation, $\bar{U}$ is the average chemical concentration for a homogeneous layer *d1* at the field scale, *d1* belongs to the set of *x* homogeneous layers within the soil system at the corresponding scale {*d1*, *d2*,.., *dx*}, and τ and γ are scaling coefficients. Both τ and γ are restrained such that $\tau + \gamma < 1$ and the correct relation between variables across scales is preserved. R is a characteristic overall ratio, which considering the heterogeneous formulation is given by:

$$R = \frac{U_{column,d}}{\overline{U}_{field,d1}} \tag{6.2}$$

and is 1 otherwise. The choice of U is site specific, and is dependent on the dominant redox processes (e.g., sulfate or iron reduction at the Norman Landfill site).

6.3.1 Description of Bayesian methods

The primary aim of this study is to develop an integrated upscaling algorithm, using Bayesian methods, for estimating effective mean concentrations across a heterogeneous formation. Bayesian methods provide a statistical framework for

obtaining an improved estimate of parameter distributions by combining preexisting (prior) knowledge with what is known about those parameters through observed data and model output. Figure 6.3 illustrates the methodology of the Bayesian framework where cases 1 and 2 are used for testing the influence of hydrological parameters, and cases 3 and 4 are used for verifying the hypothesis regarding the heterogeneity formulations. A scaling parameter β is used to account for scale disparity for hydrological parameters and as described above, two such parameters (τ and γ) are used for upscaling geochemical parameters. A non-informative prior is assigned to these parameters (e.g., $\beta \sim U[0,1]$) so that no preference is given to any specific parameter domain. Here, the likelihood is a function of the time series of observations of redox-sensitive elements at the field scale as a function of depth. Therefore, the general relationship applied for upscaling geochemical parameters is given by equations 6.1 and 6.2, and for soil hydraulic parameters is given by [*Das et al.*, 2008]:

$$(\theta_s)_{eff} = \theta_s^{\beta} \tag{6.3}$$

where $(\theta_s)_{\text{eff}}$ is the effective value of the saturated water content at the field scale. The scaling coefficient β has a value of 1 for homogeneous soil systems, and less than 1 for heterogeneous systems such that the effect of variations in soil type and lithology are accounted for. Figure 6.3 further illustrates that this Bayesian algorithm is also tested for upscaling observations from the point to the column scale.

The resulting upscaling algorithm is able to provide the conditional posterior distribution using the Bayes' framework:

$$p(\boldsymbol{\Theta} \mid \mathbf{D}) = \frac{f(\mathbf{D} \mid \boldsymbol{\Theta})\pi(\boldsymbol{\Theta})}{\pi(\mathbf{D})} \tag{6.4}$$

where **D** is the observed data at the field scale, $f(\mathbf{D}|\boldsymbol{\Theta})$ is the likelihood function summarizing the model for the data given the parameters, $\pi(\mathbf{D})$ is a normalizing constant, $\pi(\boldsymbol{\Theta})$ is the prior joint probability for the upscaled parameters, and $\boldsymbol{\Theta}$ is the parameter set $\{\theta_r^{\beta}, \theta_s^{\beta}, \alpha^{\beta}, n^{\beta}, K_s^{\beta}, \tau, \gamma\}$ while including the hydraulic parameters and $\{\tau, \gamma\}$ otherwise. Once the conditional posterior probability is known, the marginal posterior distribution $p(.|\mathbf{D})$ for any upscaled parameter (e.g., saturated soil water content for the matrix domain, θ_s^{β}) is given by integrating over the set of all other geochemical and soil hydraulic parameters ($\theta_2, \theta_3, \ldots, \theta_{tot}$) included in the analysis:

$$p(\theta_s^{\beta} \mid \mathbf{D}) = \frac{\int\int\int_{\theta_2,..,\theta_{tot}} f(\mathbf{D} \mid \boldsymbol{\Theta}) \times \pi(\boldsymbol{\Theta}) d\theta_2 .. d\theta_{tot}}{\pi(\mathbf{D})} \tag{6.5}$$

The main complication in solving equation 6.5 is the intractability of the multi-dimensional integration and the computation of $\pi(\mathbf{D})$. A possible solution is to use any MCMC algorithm that generates a sequence of parameter sets, $\{\boldsymbol{\Theta}(0), \boldsymbol{\Theta}(1),.., \boldsymbol{\Theta}(t)\}$ that converge to the stationary target distribution for large number of iterations t [*Gelman et al.*, 1995].

An adaptive MCMC scheme of *Harrio et al.* [2001], which caters to our need for resolving a large number of hydrological and geochemical parameters, is used in this study. *Harrio et al.* [2001] chose a multivariate normal distribution as the proposal density, and resolved correlation among parameters by employing a fixed covariance matrix $\sum$ for a finite number of initial iterations (t_0), and then updating $\sum$ as a function of all the previous iterations:

$$\Sigma_i = \begin{cases} \Sigma_0, i \le t_0 \\ s_d \mathrm{Cov}\left(\Theta_1, \Theta_2, ..., \Theta_{iter-1}\right) + s_d \varepsilon \boldsymbol{I}_d, i > t_0 \end{cases} \tag{6.6}$$

where i is the current iteration, $\sum_0$ is the initial covariance matrix based on prior information, d is the dimension of $\boldsymbol{\Theta}$, ϵ is a small parameter chosen to ensure $\sum_i$ does not become singular, $\boldsymbol{I_d}$ is the d-dimensional identity matrix, and s_d is a scaling parameter that depends only on d. A basic choice for the scaling parameter can be $s_d = (2.4)^2/d$ for Gaussian targets and Gaussian proposals [*Gelman et al.*, 1995]. To decrease the computational cost, *Harrio et al.* [2001] also described the method to obtain $\sum$ at the next iteration (i+1) as:

$$\Sigma_{i+1} = \frac{i-1}{i}\Sigma_i + \frac{s_d}{i}\left(i\overline{\Theta}_{i-1}\overline{\Theta}_i^T - (i+1)\overline{\Theta}_i\overline{\Theta}_i^T + \varepsilon \boldsymbol{I}_d\right) \tag{6.7}$$

The AMCMC algorithm used in this study has been described in the previous chapter (§ 3.3.4).

6.4 Data

6.4.1 Site description

The field scale data for verifying the upscaling algorithm is obtained from the Norman Landfill site. The Norman Landfill is a closed municipal landfill that operated for 63 years in the city of Norman, Oklahoma (Figure 6.4a).

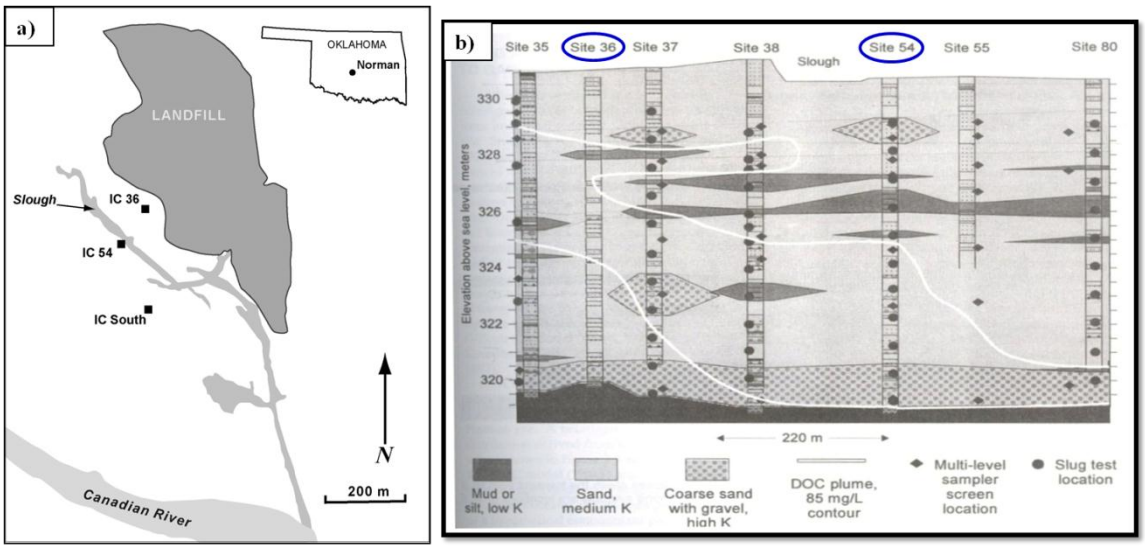

Figure 6.4: Map showing a) the location of the Norman Landfill site [*Breit et al.*, 2005], and b) the spatial heterogeneity encountered across different well locations at the site [*Scholl et al.*, 1999]. The ovals in the spatial heterogeneity map represent the well locations used in this study.

The site sits on permeable Canadian River alluvium which is about 10 to 15 meters thick and overlies a low-permeability shale and mudstone confining unit known as the Hennessey Group. The aquifer material is predominantly sand and silty sand with intermittent mud layers and clay lenses [*Scholl and Christenson*, 1998].

Near the landfill, the groundwater is shallow and ranges to about four meters from the land surface [*Scholl and Christenson*, 1998]. The leachate plume from the site extends approximately 250m in the direction of groundwater towards the Canadian River [*Scholl and Christenson*, 1998]. Previous hydrologic investigations have indicated that the leachate flows directly beneath a former Canadian River channel, referred to as the slough (Figure 6.4a) [*Becker*, 2002]. The slough is an ephemeral wetland that was intermittently exposed to the landfill leachate.

The Norman Landfill has been designated as a U.S. Geological Survey research site and active investigations have been conducted on its biogeochemistry since 1995. Several studies have indicated that sulfate reduction, iron reduction, and methanogenesis are important biogeochemical processes at the Norman Landfill site [*Cozzarelli et al.*, 2000; *Eganhouse et al.*, 2001; *Grossman et al.*, 2002]. In their study, *Báez-Cazull et al.* [2008] reported that seasonal rainfall patterns were dominant factors in controlling iron and sulfate reduction while analyzing 3 year data from the slough. *Cozzarelli et al.* [2011] confirmed that chemical concentrations in the plume boundaries are affected by hydrologic processes at various time scales. Their analysis further revealed the spatial variability in chemical concentrations across the leachate plume. They concluded that the upper boundary of the leachate plume is an active redox location while the center of the plume is depleted in sulfate and has low oxidation capacity. Therefore, the Norman Landfill provides an opportunity to develop and verify an upscaling algorithm that incorporates hydrologic variability and spatial heterogeneity within the site.

6.4.2 Field scale measurements

The performance of the upscaled parameters can be tested using selected wells at the Norman Landfill that have vertical heterogeneity similar to the experimental soil columns. Two multilevel wells located on a transect parallel to the groundwater flow are employed for verifying the integrated MCMC algorithm at this site. Figure 6.4b illustrates the geologic map of the Norman Landfill site including the location of IC 36 and IC 54 wells (represented by ovals) with intermittent mud layers. The landfill well (IC 36) is located 35m from the edge of the landfill mound, and the slough well (IC 54)

is located 7m south of the slough [*Breit et al.*, 2005]. The wells are named as such because of their distinct chemical characteristics and hydrologic interactions. The IC 36 well closely interacts with the leachate plume, and the IC 54 well is hydrologically connected with the slough.

Both wells have screens set at different elevations to capture the dynamics of the local water table [*Scholl et al.*, 2006]. Apart from hydraulic head measurements, geochemical data including specific conductance, δ^2H, chloride, sulfate, nitrate, and non-volatile dissolved organic carbon (NVDOC) were collected at both well locations. Specific conductance was measured using a portable meter, anions were analyzed using ion chromatograph, NVDOC concentrations were determined following the method of *Qian and Mopper* [1996], and isotopic analyses were done by equilibration with gaseous hydrogen for δ^2H. Further details of the chemical methods are provided elsewhere [*Scholl et al.*, 2006; *Cozzarelli et al.*, 2011].

6.4.3 Soil column setup

Two soil columns with similar spatial heterogeneities were used to verify the integrated upscaling algorithm: a layered column and a lensed column (Figure 6.5). The soil cores for both columns were collected from the Norman Landfill site. Two soil types were collected from this site: an alluvial, fine-grained sand from the banks of the Canadian River and an organic-rich loam from the slough. The soil cores were air-dried, ground, and repacked using a piston compactor to attain a dry bulk density of 1.4 Mg/m^3 for the sand and 1.0 Mg/m^3 for the loam soil.

The schematics of the layered and lensed columns are given in Figure 6.5a. The sand-over-loam layered soil column was 40 cm in length and 15 cm in diameter. It had 18 cm of sand over 22 cm of loam. The lensed column had two horizontally offset lenses of loam within a matrix of sand. The lensed soil column was 60 cm in length and 15 cm in diameter.

The experimental setup was such that a rainfall simulator with a matching diameter disc (15 cm) was used for introducing rainwater to the columns (Figure 6.5b) [*Kohne and Mohanty*, 2005]. Boundary conditions were maintained using a tension infiltrometer at the top of the soil column. The bottom boundary was open to atmosphere. A fraction collector was used intermittently to analyze concentration profiles from the bottom of the soil columns.

6.4.4 Column scale measurements

Hydrologic and geochemical data were monitored using collocated probes installed at various depths within the columns (Figure 6.5b, c). In particular, tensiometer and time-domain reflectometry (TDR) probes were used to monitor pressure head and water content profiles, respectively.

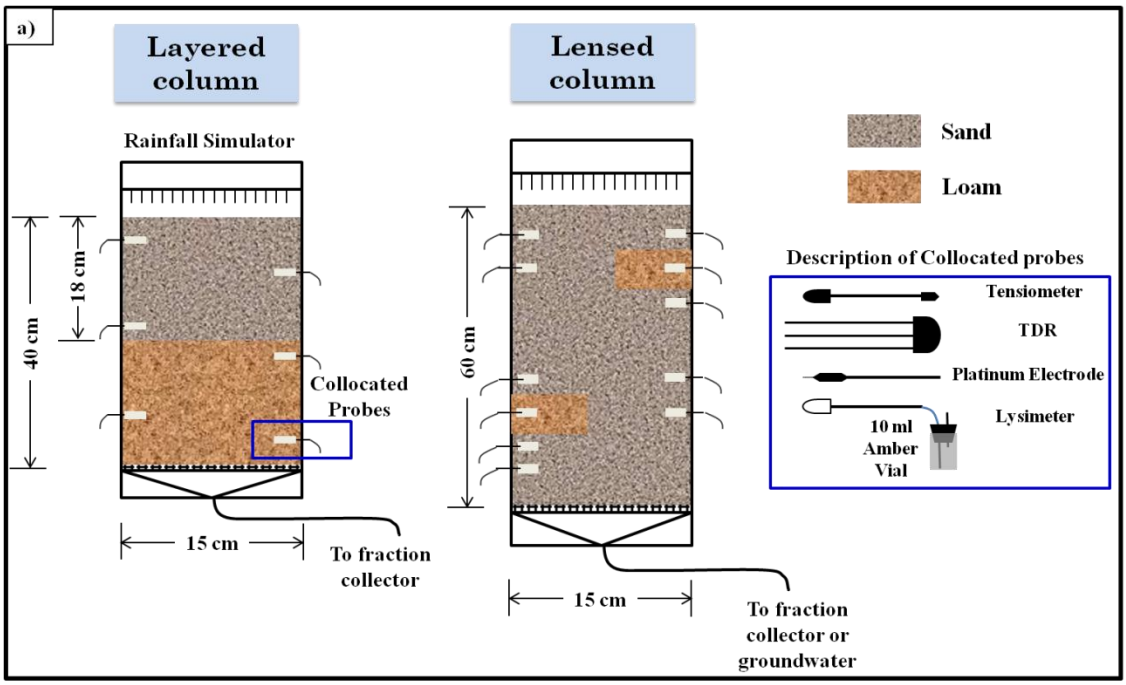

Figure 6.5: Schematic of a) the layered and lensed columns with instrumentation, b) the experimental setup of the layered sand-over-loam column, and c) the experimental setup of the lensed column.

Lysimeters with amber vials were used to collect low volume porewater (less than 7 ml) for geochemical analyses. This porewater was used to analyze pH and alkalinity measurements. The concentrations of major anions (Cl^-, Br^-, SO_4^{2-}, and NO_3^-) and cations (Ca^{2+}, K^+, Na^+, and NH_4^+) obtained from this porewater. In addition, reduced species of iron and sulfur, and redox potential (Eh) were quantified voltammetrically using a hanging drop mercury electrode. Further information on the experimental setup and analyses can be obtained elsewhere [*Hansen et al.*, 2011; *Hansen et al.*, 2012b].

6.5 Results and discussion

Bayesian methods are used in this study to upscale dominant redox concentrations, i.e. sulfate concentrations, from the column scale to the Norman Landfill site. As described in Figure 6.3, the MCMC algorithm is used to upscale the layered column data to the IC 36 well, and lensed column data to the IC 54 well. This upscaling algorithm is then verified by using point scale data measured in one of the lens to obtain column scale data encompassing the heterogeneity around the other lens. For both the layered and lensed columns, the upscaling algorithm is used to verify the effect of heterogeneity and influence of coupled parameters on sulfate concentrations at the Norman Landfill site.

6.5.1 Upscaling from the layered soil column to the IC 36 well

The approach described above is applied to upscale dominant redox concentrations from the layered heterogeneity at the column scale to a similar vertical heterogeneity setup of the landfill well. MCMC iterations are run for verifying each hypothesis, i.e. the heterogeneity formulation and the influence of hydrological

parameters. It is worthwhile to mention that the observed data (represented by squares) for infiltration and drainage scenarios at the field scale correspond to the monthly data for May and September, respectively. The choice of the months is based on Chapter V where the influence of infiltration and drainage events on conservative indicator and reactive concentrations were specifically identified on a temporal scale. Efforts were also made to ensure that the rainwater composition used for the infiltration experiments at the column scale matched the rainfall chemistry at the landfill site (see previous chapter, Table 4.4).

Figure 6.6 compares the effective sulfate and ferrous iron concentrations obtained as a function of depth at the landfill well with and without the heterogeneity formulations (equations 6.1 and 6.2) for an infiltration scenario. Figure 6.6 demonstrates that the predictions of sulfate are included within the 95% uncertainty bounds when the heterogeneity formulation is used in the upscaling algorithm. The predictions of Fe^{2+} are also significantly improved with the heterogeneity formulation even though the geochemical scaling coefficients are derived by considering the dominant sulfate reduction processes and employing sulfate as U in equation 6.2.

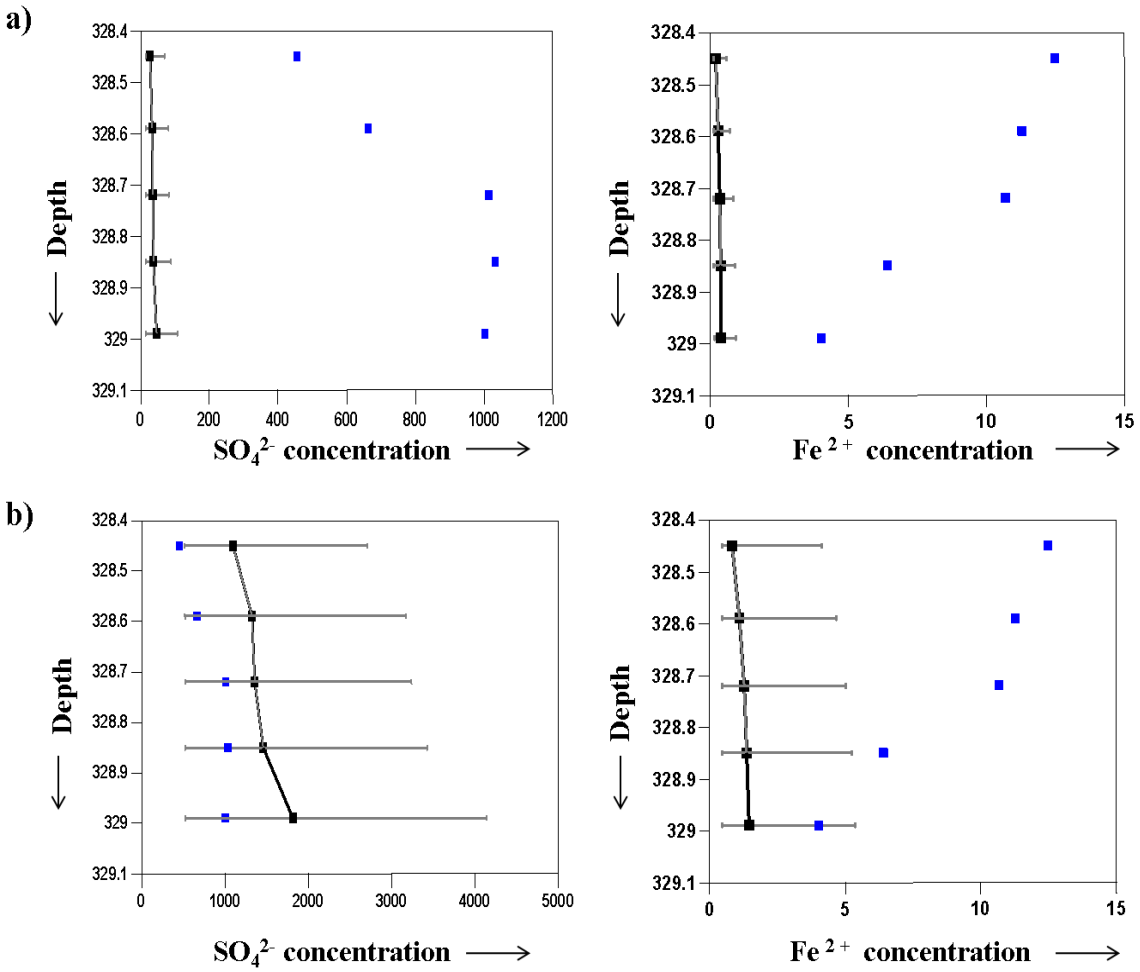

Figure 6.6: Uncertainty in estimating effective sulfate and ferrous iron concentrations (mg/l) at the landfill well from an infiltration experiment of the layered soil column with geochemical parameter ratios a) without and b) with the heterogeneity formulation. The solid line represents the average output from the MCMC simulations, the bars represent the 95% prediction uncertainty range, and the squares correspond to field observations below the heterogeneity.

To further evaluate the integrated upscaling approach, the effective sulfate and bromide concentrations are compared without (Figure 6.7a) and with the heterogeneity formulation (Figure 6.7b), as well as without (Figure 6.7a, b) and with the inclusion of hydrological parameters (Figure 6.7c) for a drainage scenario. Table 6.1 summarizes the initial soil hydraulic parameter values and their uncertainty ranges employed for the MCMC simulations. The initial values for the soil water retention parameters are either obtained from laboratory measurements or inversely estimated using HYDRUS-1D as mentioned in § 4.4.4. The initial uncertainty range included herein is based on the UNSODA database for sand and loam soil types [*Nemes et al.*, 1999, 2001]. A normal distribution is assigned as a prior to the soil hydraulic parameters based on previous experiences with upscaling using Bayesian methods [*Das et al.*, 2008]. The results from the MCMC iterations indicate that a significant improvement is observed in the predictions of the reactive component (SO_4^{2-}) using the integrated upscaling approach, while orders of magnitude improvement is obtained for the tracer component (Br^-) as can be seen in the transition from Figure 6.7a to Figure 6.7c. Comparatively, an order of magnitude improvement in sulfate concentrations is not obtained because the geochemical scaling coefficients are already based on sulfate concentrations.

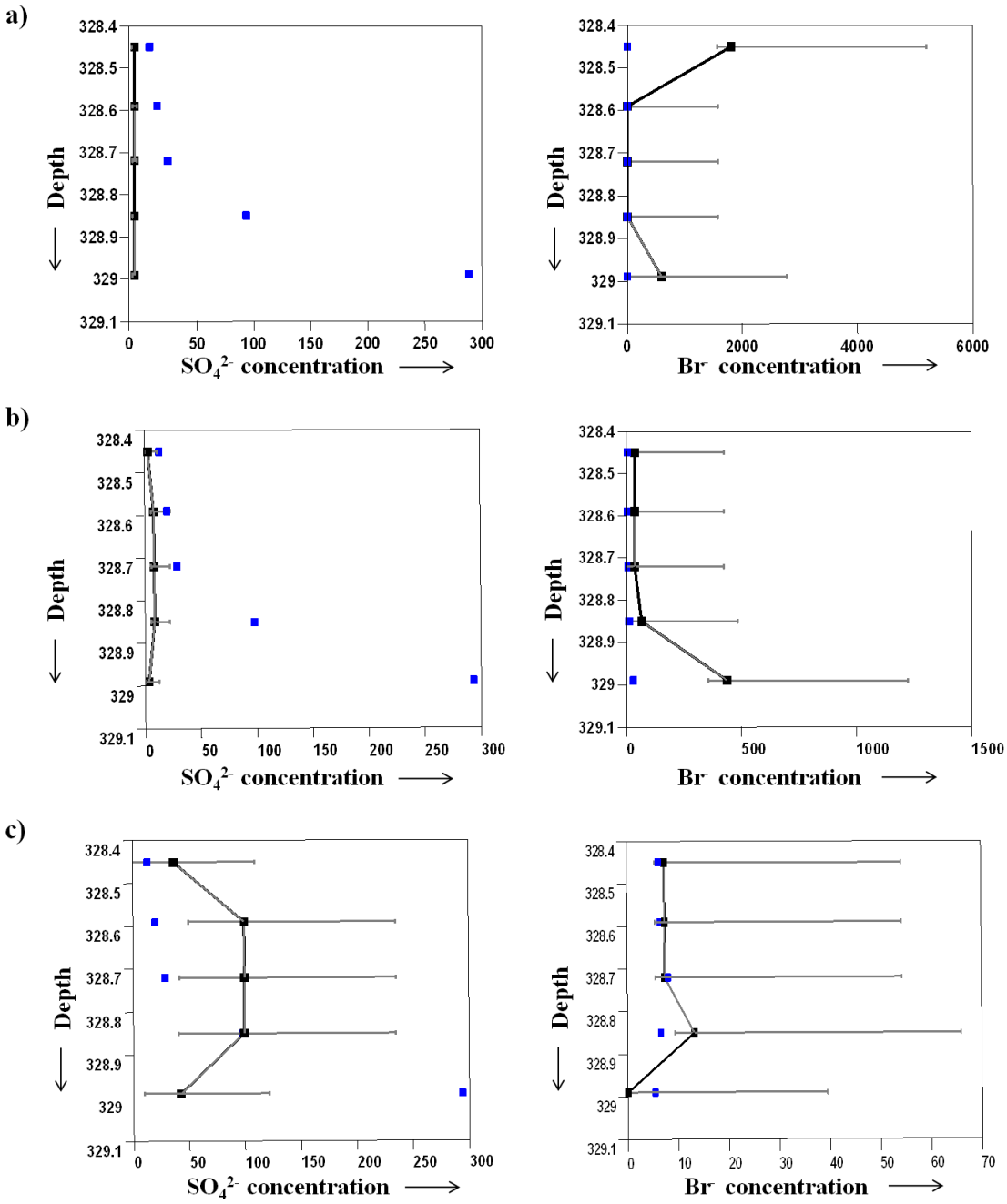

Figure 6.7: Uncertainty in estimating effective sulfate and bromide concentrations (mg/l) at the landfill well from a drainage experiment of the layered soil column with geochemical parameter ratios a) without and b) with the heterogeneity formulation, and c) in combination with hydrological parameters. The solid line represents the average output from the MCMC simulations, the bars represent the 95% prediction uncertainty range, and the squares correspond to field observations below the heterogeneity.

Table 6.1: Initial parameter values and uncertainty range of soil hydraulic parameters used in the MCMC simulations.

Soil hydraulic parameters		Initial values	Initial uncertainty range
Sand	θr (-)	0.027	Fixed*
	θs (-)	0.321	0.36-0.42
	α (cm^{-1})	3.18	0-0.14
	n (-)	1.60	1.1-2.9
	Ks ($cm.min^{-1}$)	0.636	1.85-37
	l (-)	0.50	Fixed**
Loam	θr (-)	0.015	Fixed*
	θs (-)	0.385	0.35-0.41
	α (cm^{-1})	2.02	0-0.14
	n (-)	1.86	1.38-2.22
	Ks ($cm.min^{-1}$)	0.141	0.003-5.53
	l (-)	0.50	Fixed**

* to reduce the number of fitting parameters, some parameters were fixed based on optimal HYDRUS simulation

** tortuosity parameter was fixed at 0.5 [*Mualem*, 1976].

Figures 6.8 and 6.9 show the trace plots and the posterior distributions of the geochemical scaling coefficients (τ and γ) using the AMCMC technique for drainage and infiltration experiments of the layered soil column, respectively. A key issue in successful implementation of the MCMC algorithm is the choice of the burn-in period and thinning of the chain. For this study, each MCMC chain was run for 10000 iterations, and the initial 1000 iterations were regarded as the burn-in length. The posterior density plots of τ and γ with and without the heterogeneity formulation in Figures 6.8 and 6.9 are realized after discarding the burn-in length and thinning of the MCMC chain.

For both infiltration and drainage events, the trace plots of Figures 6.8 and 6.9 indicate good mixing of the chain as the AMCMC iterates seem to traverse the entire parameter distribution to yield good estimates of the geochemical scaling parameters. It can be easily seen that the sequence of draws converges quickly to the true target density, within 10000 iterations, using the AMCMC technique with 25-28% acceptance ratio.

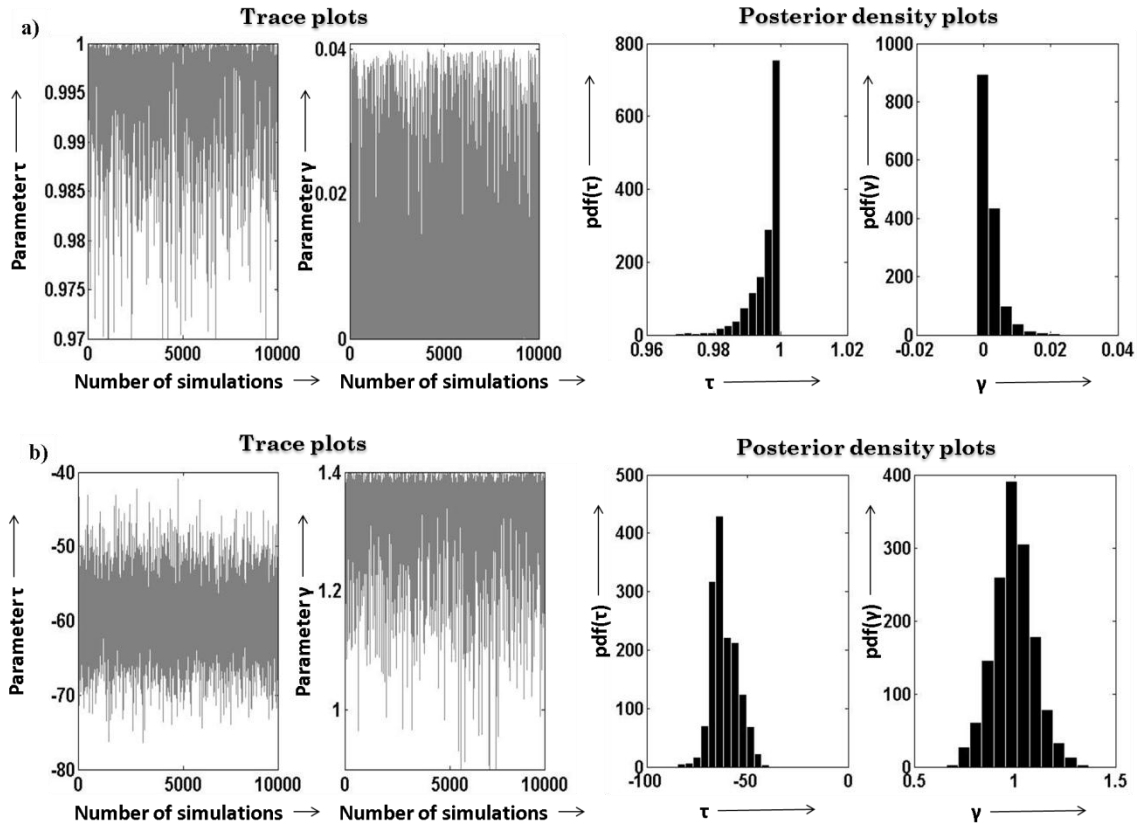

Figure 6.8: Parameter trace plots and posterior density plots of geochemical scaling coefficients a) without and b) with the heterogeneity formulation for a drainage experiment of the layered soil column.

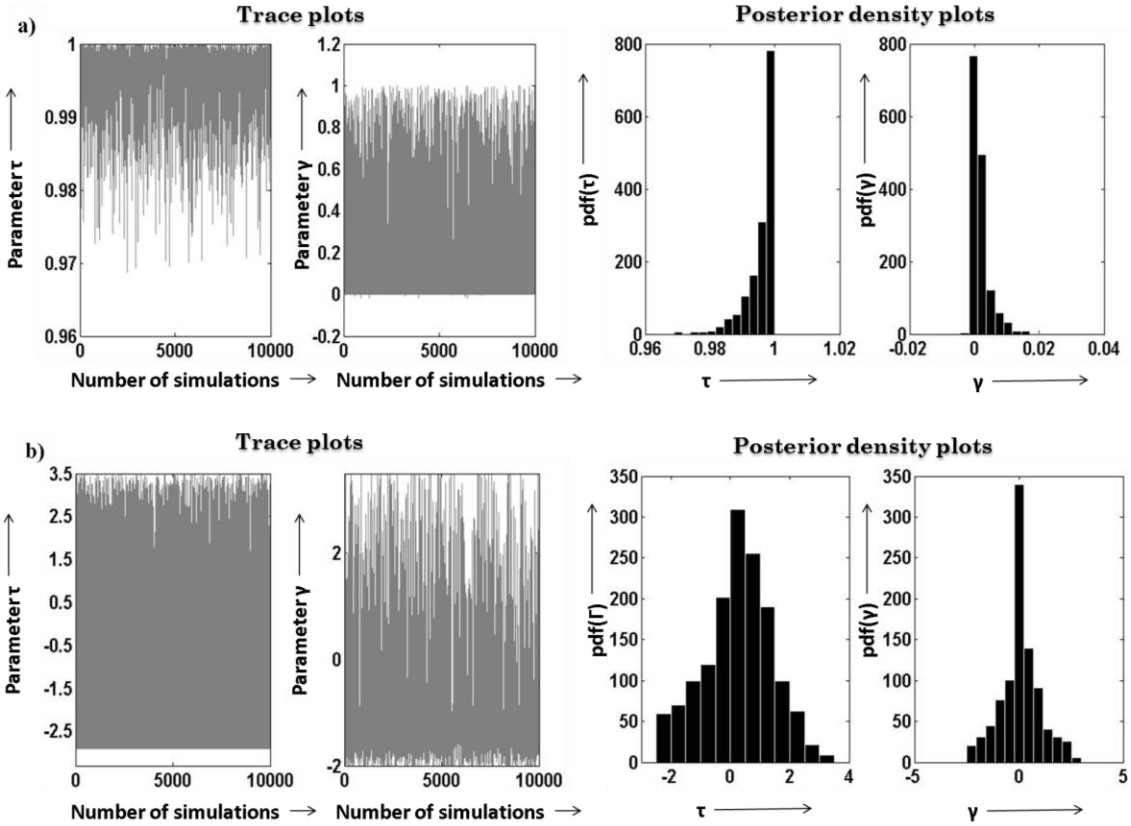

Figure 6.9: Parameter trace plots and posterior density plots of geochemical scaling coefficients a) without and b) with the heterogeneity formulation for an infiltration experiment of the layered soil column.

An interesting thing to note is that the posterior density plots for both τ and γ portray skewed distributions without the heterogeneity formulation (Figures 6.8a and 6.9a), and are strongly correlated to each other as $\tau = 1-\gamma-e$ (where e is a small number, even less than 0.01, for both infiltration and drainage scenarios). The means of the geochemical scaling coefficients are also quite similar for both scenarios. This clearly indicates that the geochemical scaling coefficients are unable to reproduce the behavior of hydrologic events (infiltration, drainage, etc.) and distribution of chemicals around the heterogeneity through this formulation, and therefore exhibit an unnecessary correlation. This can be further confirmed when the heterogeneity formulation is considered and the geochemical scaling coefficients are normally distributed and not correlated as the relationship described above. In fact, the means and the correlation structure between τ and γ are different for the infiltration and drainage scenarios as indicated by their different ranges and density plots (Figures 6.8b and 6.9b).

Figure 6.10 demonstrates that the posterior density distribution of the hydrologic scaling coefficient (β) is multimodal for both infiltration and drainage events as compared to the unimodal nature of the posterior distributions for both geochemical scaling coefficients (Figures 6.8 and 6.9). The multimodality can result from the inherent structure of the prior, such as the use of a multivariate normal prior applied in this study [*Escobar and West*, 1995]. However, several studies have indicated that these modes in the posterior distribution are related to the different domains or layers of a soil system. For example, de *Rooij et al.* [2004] obtained different modes for soil hydraulic parameters within the same parametric distribution in their analysis of undisturbed soil

cores from an arable field near Andelfingen in northern Switzerland. In their study, the different modes were reflective of the different soil depths and retention functions of the plough layer and the subsoil. For our study, the posterior distribution of β is again suggestive of the effect of layering and heterogeneity, especially the different retention and hydraulic conductivity functions of the sand and loam soil types.

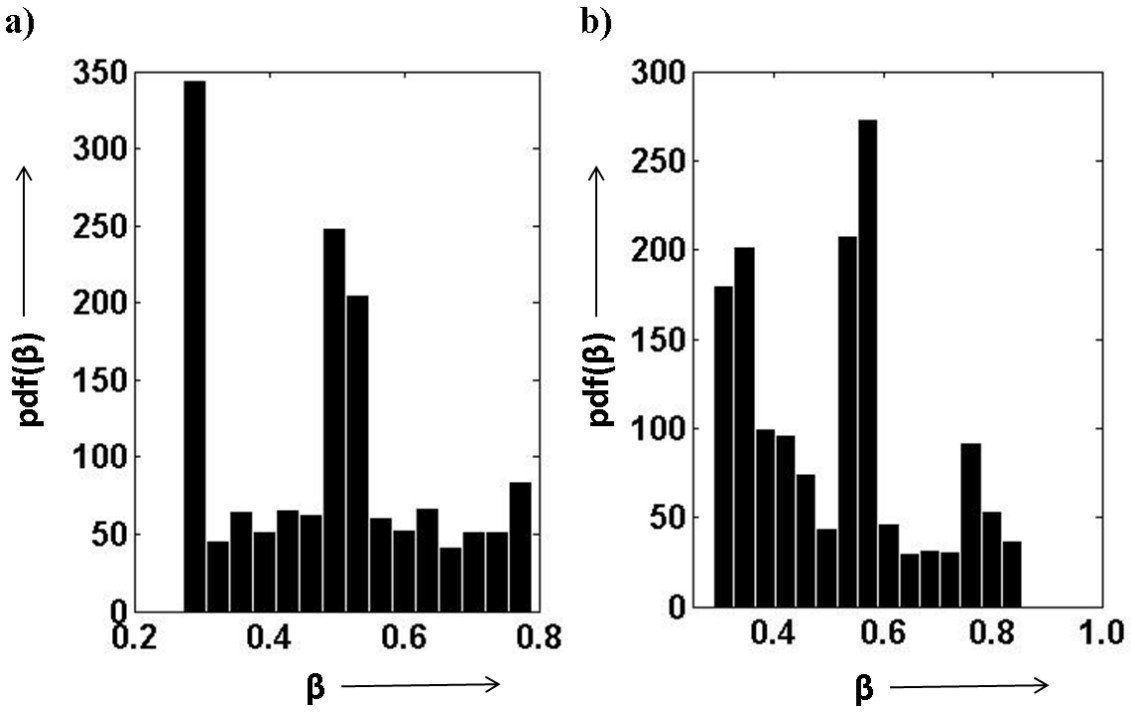

Figure 6.10: Posterior density plots of the hydrologic scaling coefficient using the integrated upscaling framework for i) infiltration and ii) drainage experiments of the layered soil column.

6.5.2 Verifying the upscaling algorithm

The upscaling algorithm is verified on two criteria: i) to test its applicability from any fine scale measurement (e.g., point) to the coarse scale (e.g., column), and ii) to confirm the choice of the adaptive conceptual model that preserves the spatial distribution of dominant redox processes. For the first criterion, the upscaling algorithm is verified on the lensed column by upscaling point scale observations of sulfate from one lens to the other lens, and matching these upscaled values with the column scale data. For the second criterion, the adaptive model is again verified on the lensed column by upscaling from the point to the column scale. If the geochemical parameters are truly independent of the spatial characteristics of the adaptive model, then a single effective concentration obtained without the heterogeneity formulation would be representative of sulfate concentrations around the lensed heterogeneity. Figure 6.11 represents the observed SO_4^{2-} concentrations (represented by squares) around the lower lens of the column and predicted SO_4^{2-} concentrations obtained from upscaling of data from the upper lens with (represented by solid lines) and without (represented by dashed lines) the heterogeneity formulation. As the results indicate, the distribution and both the increasing and decreasing trends of sulfate around the lower lens are well captured when the effect of heterogeneity is accounted for as opposed to a single effective value obtained from the upscaling algorithm without the heterogeneity formulation. The lower sum of squares error (SSE) also supports the use of an adaptive conceptual model that preserves the trend of the local depth variations at the point scale as compared to a single effective value. The single effective concentrations display a higher SSE only in nitrate

concentrations for the infiltration experiment of the lensed column. However, the adaptive model appropriately reproduces the spatial distribution of nitrate concentrations at the column scale. A satisfactory match of the effective sulfate concentrations to the column data confirms the applicability of this upscaling algorithm across any fine to coarse scales.

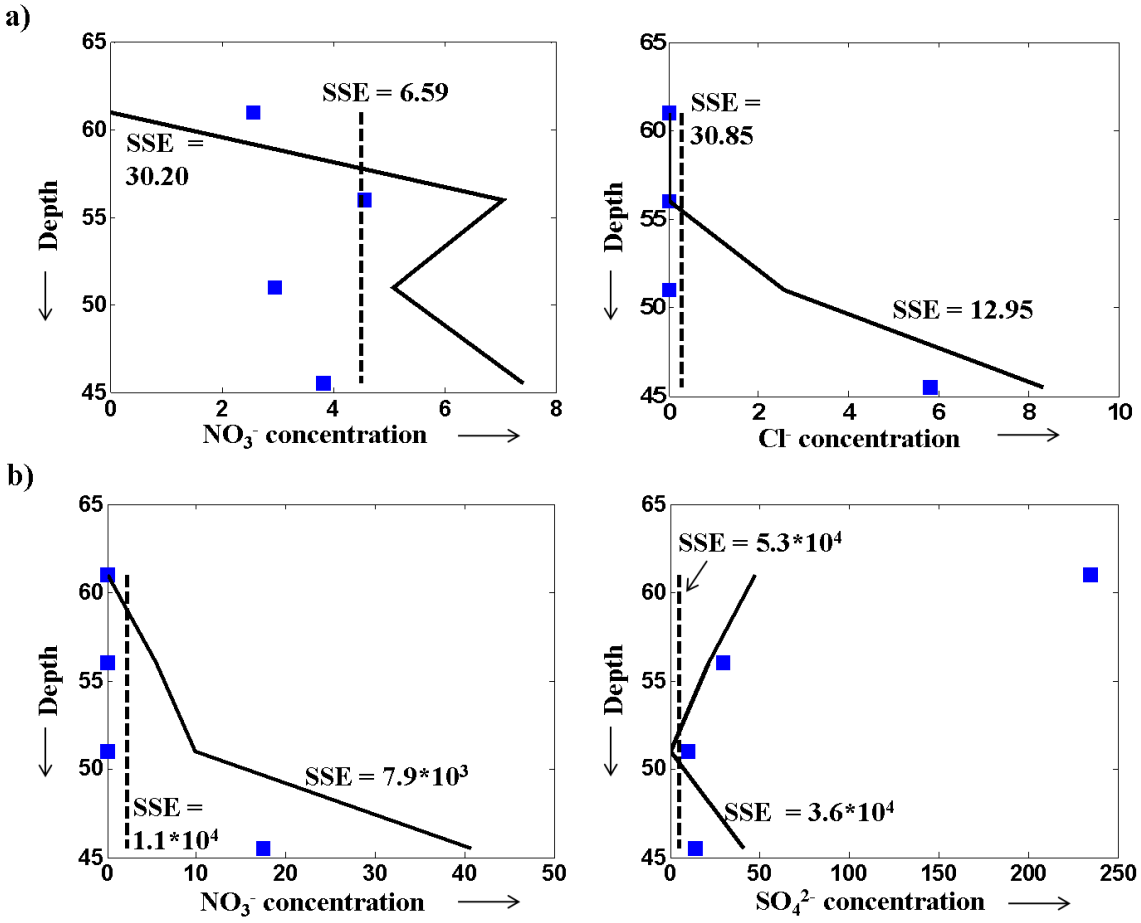

Figure 6.11: Observed and predicted effective concentrations (mg/l) for a) infiltration and b) drainage experiments of the lensed column. The solid line represents the average output at the columns scale using the heterogeneity formulation, the dashed line represents the average output at the columns scale without using the heterogeneity formulation, and the squares correspond to observations. Symbol: SSE, sum of squares error.

6.5.3 Upscaling from the lensed soil column to the IC 54 well

Figures 6.12 and 6.13 show a series of plots for assessing the fit of upscaled concentrations to the IC 54 well data. As mentioned earlier, the vertical heterogeneities between the slough well and the lensed column are quite similar, and the infiltrating water chemistry used for column scale experiments is similar to the observed rainfall at the landfill site (see previous chapter, Table 4.4). Figure 6.12 indicates that a reasonable fit is achieved for a drainage event when the heterogeneity formulation is applied for both nitrate and bromide concentrations, even though the geochemical scaling coefficients are again derived using sulfate. The results indicate that the prediction accuracy has significantly improved as predicted nitrate concentrations are between 0-0.05 mg/l using the heterogeneity formulation and between 0-6000 mg/l without the heterogeneity formulation while observations lie between 0.2-0.3 mg/l. Figure 6.13 emphasizes the role of soil hydraulic parameters in improving the predictions of geochemical concentrations at the field scale for an infiltration event. Again, the improvement obtained in conservative indicator concentrations (i.e., chloride) is much larger than that obtained in reactive concentrations (i.e., sulfate) when soil hydraulic parameters are included in the integrated upscaling framework. Figure 6.13 demonstrates that almost all predictions of chloride are included within the 95% uncertainty bounds when soil hydraulic parameters are included in the upscaling algorithm.

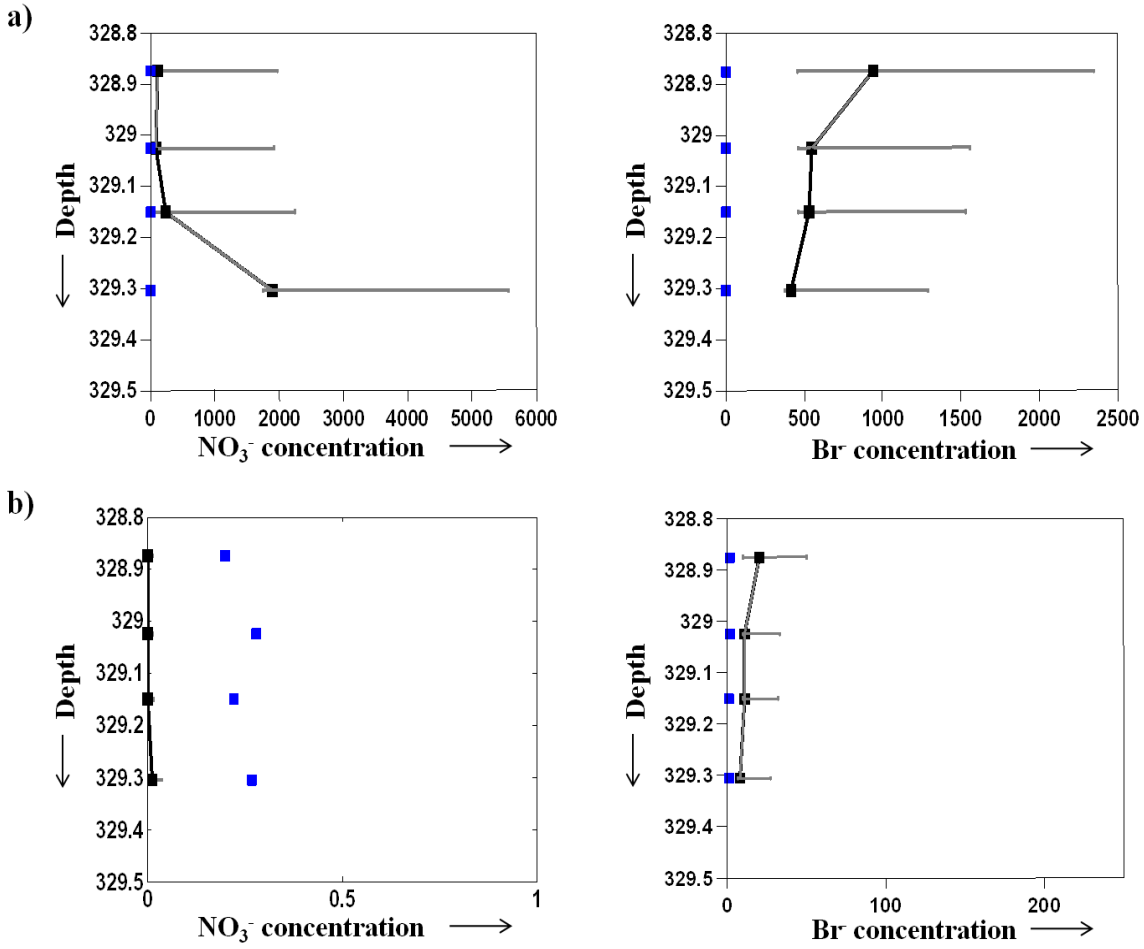

Figure 6.12: Uncertainty in estimating effective nitrate and bromide concentrations (mg/l) at the slough well from a drainage experiment of the lensed soil column with geochemical parameter ratios a) without and b) with the heterogeneity formulation. The solid line represents the average output from the MCMC simulations, the bars represent the 95% prediction uncertainty range, and the squares correspond to field observations above the heterogeneity.

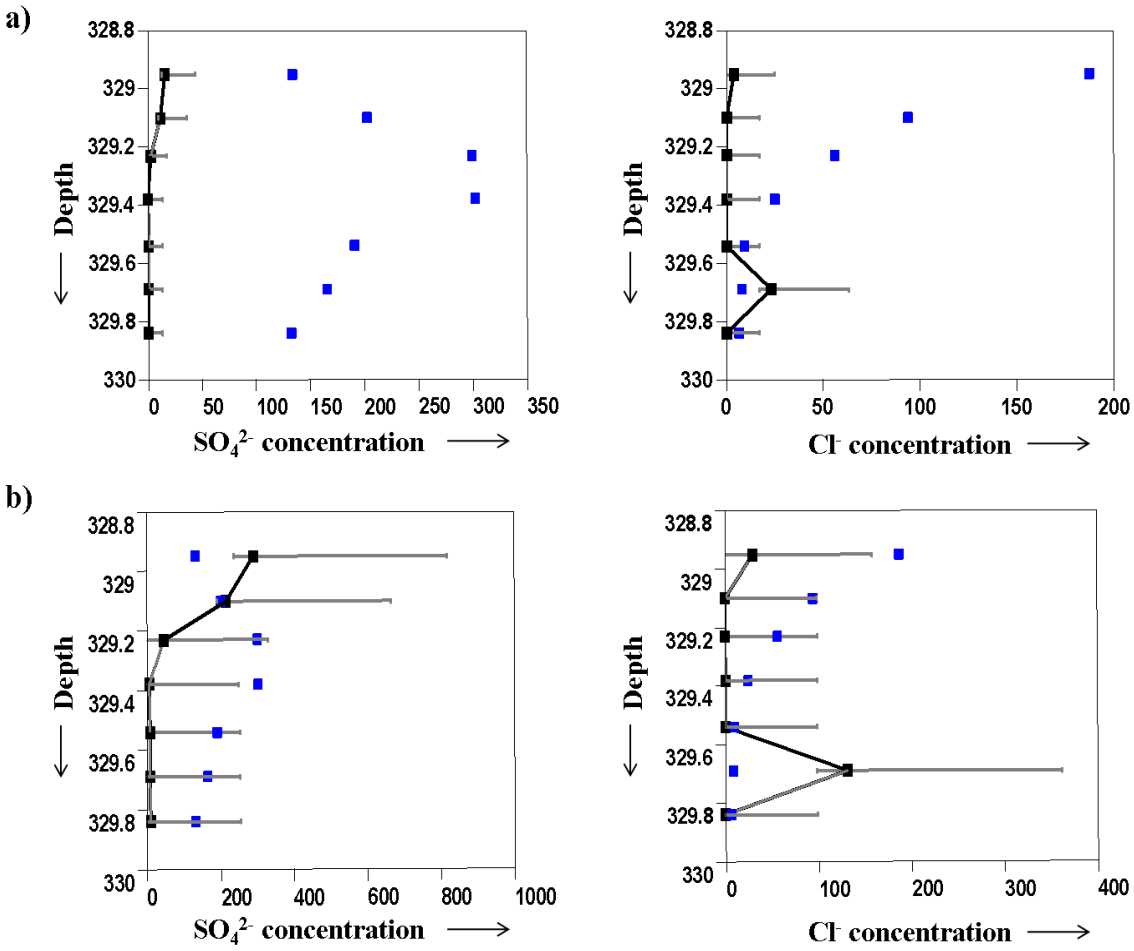

Figure 6.13: Uncertainty in estimating effective sulfate and chloride concentrations (mg/l) at the slough well from an infiltration experiment of the lensed soil column with geochemical parameter ratios i) without and ii) with hydrological parameters. The solid line represents the average output from the MCMC simulations, the bars represent the 95% prediction uncertainty range, and the squares correspond to field observations above the heterogeneity.

For the scaling coefficients, the convergence of MCMC chains to the true posterior density can be assessed using the Geweke z statistic apart from using the trace plots [*Geweke*, 1992]. The Geweke test splits the MCMC chain into two "windows": the first window contains the beginning 20% of the chain, and the second contains the last 50% of the chain. If the MCMC chain has converged to a stationary distribution, the mean of the two windows is equal and the Geweke test statistic or the chi-squared marginal significance for the two means yields a value greater than 2. A value of less than 2 for the Geweke chi-squared estimate indicates autocorrelation in the chain. For the integrated upscaling framework, Table 6.2 confirms the convergence of all scaling coefficients using the AMCMC algorithm.

6.5.4 Effect of parameter correlation on upscaling

Table 6.3 summarizes the prior and posterior correlation structure of the soil hydraulic parameters for a drainage experiment of the lensed column using the AMCMC algorithm. The results presented in Table 6.3 illustrate that we end up with different correlation coefficients for all parameters. The difference in initial and posterior covariance matrices could be a result of the adaptive nature of the MCMC algorithm. However, the posterior correlation coefficients are less than 0.6 for all parameters suggesting that the interaction among parameters is not restricting us from obtaining a unique parameter set for the upscaling coefficients. Infact, by employing the adaptive MCMC algorithm that updates the parameter correlation simultaneously, we have strengthened the upscaling framework used in this study.

Table 6.2: Geweke convergence statistic for MCMC chains using the integrated upscaling framework.

Scaling coefficient	Geweke z score
τ	1.21
γ	1.97
β	1.80

Table 6.3: Prior and posterior covariance matrix for a drainage experiment of the lensed column.

Covariance matrix	Soil hydraulic parameters					
		θr	θs	α	n	Ks
Prior*	θr	1				
	θs	-0.07	1			
	α	-0.19	-0.55	1		
	n	-0.42	0.42	-0.40	1	
	Ks	0.0	0.04	-0.03	0.03	1
Posterior	θr	1				
	θs	0.14	1			
	α	0.40	-0.47	1		
	n	-0.57	0.25	0.44	1	
	Ks	-0.23	0.27	-0.27	-0.57	1

* The initial covariance structure is obtained from previous experience (see § 3.4.3) with the model for this data [*Vrugt et al.*, 2003].

6.6 Limitations of the study

Despite the multi-scale verification and advanced stochastic techniques used in this study, there are certain limitations to our approach. First, this study does not evaluate the effect of thickness, lateral positions, or the interaction among multiple heterogeneous structures on the upscaled hydrologic and geochemical coefficients. Several studies have shown that upscaled parameters are affected by the geological characteristics and arrangement of lithologic units in the subsurface system [*Khaleel et al.*, 2002; *Onsoy et al.*, 2005; *Deng*, 2009]. Although a complete representation of spatial heterogeneity will definitely improve the upscaling framework and predictions of conservative and reactive concentrations at the field scale, this detailed analysis is beyond the scope of the current study.

Second, the geochemical scaling coefficients used for obtaining the conservative and reactive chemical concentrations at the field scale are based on the dominant biogeochemical processes. For the case of the Norman Landfill site, we used sulfate reduction as a dominant process and incorporated the distribution of sulfate around the heterogeneity in the upscaling framework. The scaling coefficients obtained are quite similar when nitrate concentrations are used but are different when iron is used instead of sulfate (Figure 6.14). This is because iron reduction is also a dominant biogeochemical process at the Norman Landfill site [*Cozzarelli et al.*, 2000; *Eganhouse et al.*, 2001; *Grossman et al.*, 2002]. If geochemical concentrations for the dominant processes are unavailable at one or both scales or knowledge about the dominant processes is lacking, then this upscaling framework is limited in its applicability.

Therefore, we encourage the users to identify the dominant redox processes and evaluate the results for upscaling geochemical concentrations for thess processes before transferring results from our study.

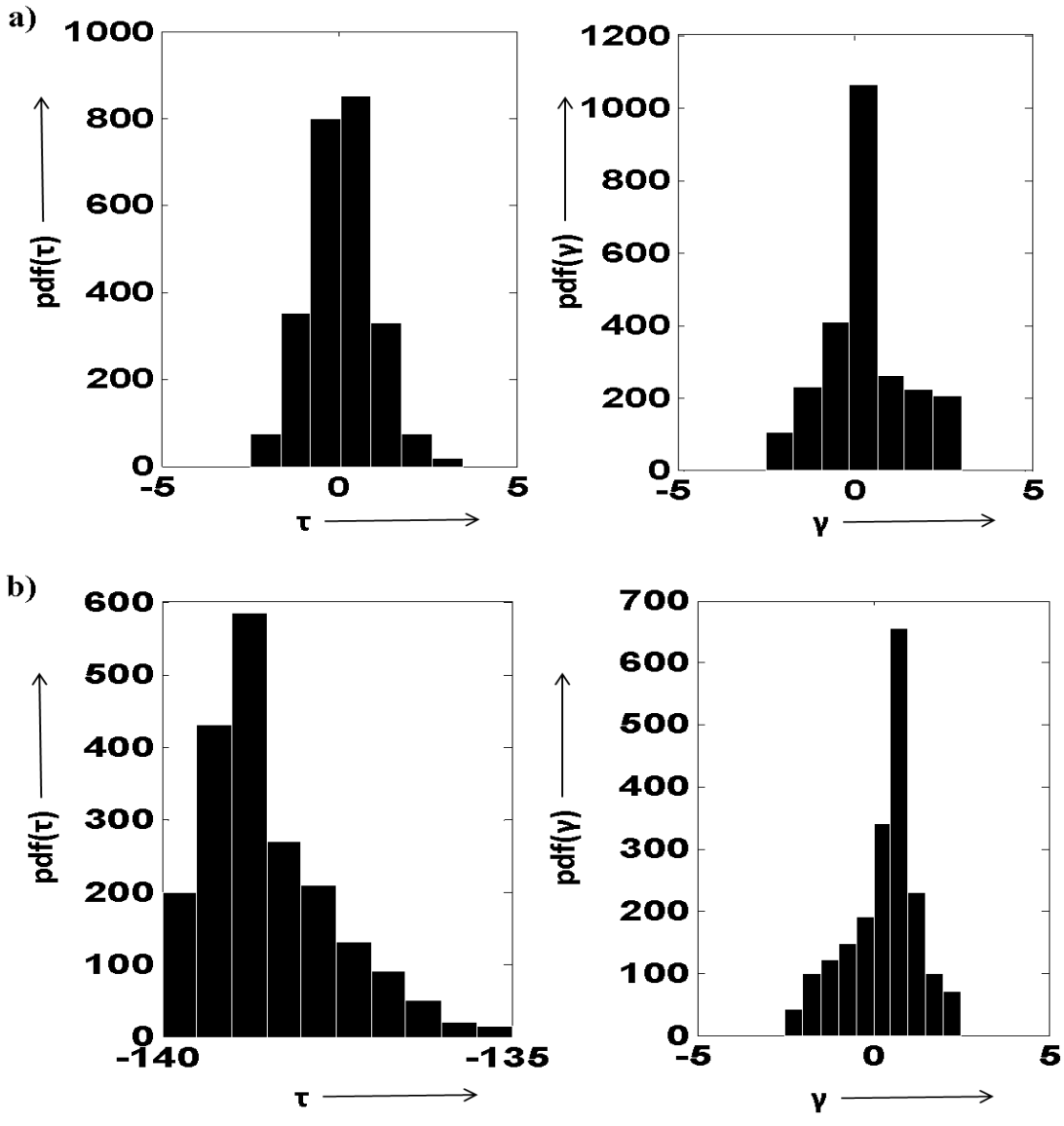

Figure 6.14: Posterior density plots of the geochemical scaling coefficients using i) nitrate and ii) iron concentrations in the integrated upscaling framework for an infiltration experiment of the layered soil column.

6.7 Conclusions

Geochemical concentrations of conservative and reactive contaminants in groundwater are key parameters for assessing contaminant plume migration, evaluating health risks, and planning remedial actions. A significant challenge in predicting these concentrations at large scales is the lack of an efficient upscaling methodology that serves as a link between knowledge gained at the laboratory scale and application needed at the field scale. We present a study that develops scale-appropriate parameters to represent the transition of biogeochemical processes that impact contaminant migration and prediction from the column to landfill scales. A new integrated upscaling framework is developed using Bayesian methods that addresses the effect of structural heterogeneity (lenses and layers) and coupled processes (influence of hydrologic variability) on dominant redox concentrations at the Norman Landfill site.

A Bayesian upscaling approach with simulations performed using an adaptive Markov chain Monte Carlo (AMCMC) algorithm is presented in this study. The Bayesian methods provide an objective framework for the selection of the likelihood function, the choice of model parameters, and the development of an integrated upscaling framework. The results of the MCMC simulations indicate that the use of a heterogeneity formulation in the likelihood function significantly improves the prediction of geochemical concentrations at the landfill site. The inclusion of soil hydraulic parameters along with the geochemical scaling coefficients increases the prediction accuracy, especially for conservative indicators, by orders of magnitude. These results using 10000 MCMC simulations for two different soil column setups help

in the development of an integrated upscaling algorithm that employs an adaptive conceptual model that preserves the effect of structural heterogeneity and influence of hydrologic variability on dominant redox processes.

The scale-dependent geochemical coefficients (τ and γ) derived through the upscaling algorithm demonstrate unimodal characteristics in the posterior distribution while the hydrologic scaling coefficient (β) is multimodal in nature. This multimodality again emphasizes the influence of subsurface heterogeneity and two different soil types (sand and loam) on posterior distribution of β. This is similar to conclusions made in Chapter III and other studies where the multimodality in soil hydraulic parameters is primarily affected by the different soil water retention functions due to different matrix or macropore domains, or soil layers [de *Rooij et al.*, 2004].

For implementing the upscaling algorithm, MCMC convergence diagnostics are considered using both graphical and statistical techniques. The influence of parameter correlation on scale-dependent upscaling coefficients is also considered. The integrated framework is developed by upscaling from the column to the field scale, and verified by upscaling from point measurements to the column scale. Therefore, this integrated upscaling algorithm can cater to most fine or coarse scale datasets as long as the dominant redox processes are known and representative concentrations are available at both scales.

CHAPTER VII

GENERAL CONCLUSIONS

The fate and transport of contaminants in the subsurface is affected by the reduction-oxidation (redox) potential of a system. Previous studies have indicated that redox can be non-linearly coupled with other biogeochemical processes that have the ability to change the reactivity and transport of contaminants before they reach the saturated zone. The research reported in this dissertation was specifically focused on understanding the interaction among coupled biogeochemical processes, extracting the influence of heterogeneity and hydrologic variability on these interactions, and quantifying how these interactions change across scales.

Results from Chapters II and III analyzed the effect of macropore heterogeneity on experimental soil columns with no macropore, single macropore, and multiple macropore distributions. This study was the first of its kind to describe the behavior of preferential flow and tracer transport under heterogeneous macropore distributions. Comparison between commonly applied continuum-scale models (single porosity, mobile-immobile, dual permeability) recommended the use of a more complex model with an increase in macropore density to generate forecasts with greater accuracy. This study also demonstrated that domain-specific measurements should be used and macropore density should be accounted for to reduce errors when using complex continuum scale models.

When the dual permeability model (DPM) is applied within a Bayesian framework, as demonstrated in Chapter III, the uncertainty in parameters and preferential flow outputs from the single and multiple macropore columns can be quantified. This is important from the perspective that complex continuum scale models require identification of a large number of parameters associated with the additional macropore domain and the matrix-macropore interface. The comparison between deterministic and stochastic approaches helped in interpreting the physical role of interface parameters in a dual permeability model, and outlined the need for efficient sampling algorithms or additional datasets to yield unique (equifinal) soil hydraulic parameters. In addition, the results also indicated that the effect of macropore density should be accounted for by changing certain parameters (e.g., saturated hydraulic conducitivity of the fracture domain) of the DPM framework.

Apart from macropore distributions, this study (Chapter IV) also analyzed the effect of structural heterogeneity on redox processes by comparing two texturally homogeneous with a heterogeneous (layered) soil column. The results from this study indicate that enhanced biogeochemical activity is observed around the textural interface of the layered sand-over-loam column as compared to the homogeneous sand and loam columns, and highlights the need to incorporate structural heterogeneity in contaminant fate and transport models. A conceptual model is proposed that can account for distinct water chemistries across such heterogeneous formations (such as layered interfaces, clay lenses). This study also demonstrates that the type of hydrologic boundary conditions

(infiltration, drainage, etc.) stongly influence redox processes within the experimental soil columns.

Results from the Norman Landfill site (Chapter V) also demonstrated the intricate linkages between redox geochemistry and hydrologic variability. This relationship was tested in the upscaling framework developed in Chapter VI.

A new upscaling algorithm which accounts for reactive concentration ratios around heterogeneous formations and incorporates hydrologic upscaling in addition to geochemical upscaling was developed and successfully tested in Chapter VI.

Therefore, the different studies presented in this dissertation clearly demonstrate that modeling fate and transport of contaminants can be improved by including the effect of subsurface heterogeneity and influence of hydrologic variability from column to landfill scales.

REFERENCES

Abbasi, F., J. Šimůnek, J. Feyen, M. Th. van Genuchten, and P. J. Shouse (2003), Simultaneous inverse estimation of soil hydraulic and solute transport parameters from transient field experiments: Homogeneous soil, *Trans. ASAE*, *46*(4), 1085–1095.

Abrams, R. H., and K. Loague (2000), A compartmentalized solute transport model for redox zones in contaminated aquifers, *Water Resour. Res.*, *36* (8), 2001-2013.

Ahuja, L. R., and C. Hebson (1992), Root zone water quality model, in *GPSR Technical Report*, *2*, USDA, ARS, Fort Collins, CO.

Ahuja, L. R., K. E. Johnsen, and G. C. Heathman (1995), Macropore transport of a surface-applied bromide tracer: Model evaluation and refinement, *Soil Sci. Soc. Am. J.*, *59*, 1234–1241.

Asseng, S., I. R. P. Fillery, F. X. Dunin, B. A. Keating, and H. Meinke (2001), Potential deep drainage under wheat crops in a Mediterranean climate. I. Temporal and spatial variability, *Aust. J. Agric. Res.*, *52*, 45–56.

Atchadé, Y. F., and J. S. Rosenthal (2005), On adaptive Markov chain Monte Carlo algorithms, *Bernoulli*, *11*(5), 815-828.

Atkins, P. W. (1990), *Physical chemistry*, 4th ed., 995 pp., W. H. Freeman and Company, New York.

Báez-Cazull, S. E., J. T. McGuire, I. M. Cozzarelli, A. Raymond, and L. Welsh (2007), Centimeter-scale characterization of biogeochemical gradients at a wetland-

aquifer interface using capillary electrophoresis, *Appl. Geochem.*, *22* (12), 2664-2683.

Báez-Cazull, S. E., J. T. McGuire, I. M. Cozzarelli, and M. A. Voytek (2008), Determination of dominant biogeochemical processes in a contaminated aquifer-wetland system using multivariate statistical analysis, *J. Environ. Qual.*, *37*, 30-46, doi:10.2134/jeq2007.0169.

Bagchi, A. (1987), Natural attenuation mechanisms of landfill leachate and effects of various factors on the mechanisms, *Waste Manage. Res.*, *5* (4), 453-463.

Becker, C. J. (2002), Hydrogeology and leachate plume delineation at a closed municipal landfill, Norman, Oklahoma, *U.S. Geological Survey Water-Resources Investigations Report 01–4168*, 36 pp.

Beecham, S., and R. K. Chowdhury (2010), Temporal characteristics and variability of point rainfall: A statistical and wavelet analysis, *Int. J. Climatol.*, *30*, 458-473.

Beeman, R. E., and J. M. Suflita (1987), Microbial ecology of a shallow unconfined groundwater aquifer polluted by municipal landfill leachate, *Microb. Ecol.*, *14*, 39–54.

Beven, K., and P. Germann (1982), Macropores and water flow in soils, *Water Resour. Res.*, *18*, 1311-1325.

Biggar, J. W., and D. R. Nielsen (1962), Miscible displacement: II. Behavior of tracers, *Soil Sci. Soc. Am. J.*, *25*, 1–25.

Bjerg, P. L., H. J. Albrechtsen, P. Kjeldsen, T. H. Christensen, and I. Cozzarelli (2003), The groundwater geochemistry of waste disposal facilities, in *Treatise on*

Geochemistry, vol. 9, *Environmental Geochemistry*, edited by H. D. Holland, K. K. Turekian, and B. Sherwood Lollar, pp. 579 – 612, Elsevier, New York.

Bjerg, P. L., N. Tuxen, L. A. Reitzel, H. J. Albrechtsen, and P. Kjeldsen (2011), Natural attenuation processes in landfill leachate plumes at three Danish sites, *Ground Water*, *49* (5), 688-705.

Bloschl, G., and M. Sivapalan (1995), Scale issues in hydrological modeling: A review, *Hydrol. Process.*, *9*, 251-290.

Böhlke, J.-K. (2002), Groundwater recharge and agricultural contamination, *Hydrogeol. J.*, *10*, 153-179.

Breit, G. N., M. L. W. Tuttle, I. M. Cozzarelli, S. C. Christenson, J. B. Jaeschke, D. L. Fey, and C. J. Berry (2005), Results of chemical and isotopic analyses of sediment and ground water form alluvium of the Canadian river near a closed municipal landfill, Norman, Oklahoma, Part 2, *U.S. Geological Survey Open-File Report 2008–1134*, 35 pp.

Bruner, M. A., M. Rao, J. N. Dumont, M. Hull, T. Jones, and J. A. Bantle (1998), Ground and surface water developmental toxicity at a municipal landfill: Description and weather-related variation, *Ecotoxicol. Environ. Saf.*, *39*, 215-226.

Brusseau, M. L., and P. S. C. Rao (1990), Modeling solute transport in structured soils: A review, *Geoderma*, *46*(1), 169-192.

Cao, X., Y. Chen, X. Wang, and X. Deng (2001), Effects of redox potential and pH value on the release of rare earth elements from soil, *Chemosphere*, *44* (4), 655-661.

Carrera, J., and S. P. Neumann (1986), Estimation of aquifer parameters under transient and steady-state conditions: 2. Uniqueness, stability and solution algorithms, *Water Resour. Res.*, *22*, 211–227.

Castiglione, P., B. P. Mohanty, P. J. Shouse, J. Simunek, M. T. Van Genuchten, and A. Santini (2003), Lateral water diffusion in an artificial macroporous system: Modeling and experimental evidence, *Vadose Zone J.*, *2*, 212– 221.

Cazelles, B., M. Chavez, D. Berteaux, F. Menard, J. O. Vik, S. Jenouvrier, N. C. Stenseth (2008), Wavelet analysis of ecological time series, *Oecologia*, *156*, 287–304.

Champ, D. R., J. Gulens, and R. E. Jackson (1979), Oxidation-reduction sequences in groundwater flow systems, *Can. J. Earth Sci.*, *127*, 85-108.

Chapelle, F. H. (2001), *Ground-water microbiology and geochemistry*, John Wiley & Sons Inc., New York.

Chen, C., and R. J. Wagenet (1992), Simulation of water and chemicals in macropore soils. Part 1. Representation of the equivalent macropore influence and its effect on soil water flow, *J. Hydrol.*, *130*, 105–126.

Christensen, T. H., P. Kjeldsen, H. Albrechtsen, G. Heron, P. H. Nielsen, P. L. Bjerg, P. E. Holm (1994), Attenuation of landfill leachate pollutants in aquifers, *Crit. Rev. Environ. Sci. Technol.*, *24* (2), 119-202.

Christensen, T. H., P. L. Bjerg, S. Banwart, R. Jakobsen, G. Heron, and H.-J. Albrechtsen (2000), Characterization of redox conditions in groundwater contaminant plumes, *J. Contam. Hydrol.*, *45*, 165-241.

Christensen, T. H., P. Kjeldsen, P. L. Bjerg, D. L. Jensen, J. B. Christensen, A. Baun, H.-J. Albrechtsen, and G. Heron (2001), Biogeochemistry of landfill leachate plumes, *Appl. Geochem.*, *16*, 659-718.

Christenson, S., M. A. Scholl, J. L. Schlottmann, and C. J. Becker (1999), Ground-water and surface-water hydrology of the Norman Landfill research site, in *U.S. Geological Survey Toxic Substances Hydrology Program—Proceedings of the Technical Meeting*, *Water-Resources Investigations Report 99-4018C*, pp. 501–507, Charleston, SC.

Clausnitzer, V., and J. W. Hopmans (1995), Non-linear parameter estimation: LM_OPT, General-purpose optimization code based on the Levenberg-Marquardt algorithm, *Land, Air and Water Resour. Pap. 100032*, University of Calif., Davis.

Comrie, A. C., and E. C. Glenn (1998), Principal components-based regionalization of precipitation regimes across the southwest United States and northern Mexico, with an application to monsoon precipitation variability, *Clim. Res.*, *10*, 201–215.

Coppola, A., A. Basile, A. Comegna, and N. Lamaddalena (2009), Monte Carlo analysis of field water flow comparing uni- and bimodal effective hydraulic parameters for structured soil, *J. Contam. Hydrol.*, *104*(1-4), 153–165.

Cowles, M. K., and B. P. Carlin (1996), Markov chain Monte Carlo convergence diagnostics: A comparative review, *J. Am. Statistics Assoc.*, *91*, 883-904.

Cozzarelli, I. M., B. A. Bekins, M. J. Baedecker, G. R. Aiken, R. P. Eganhouse, and M. E. Tuccillo (2001), Progression of natural attenuation processes at a crude-oil spill site: I. Geochemical evolution of the plume, *J. Contam. Hydrol.*, *53* (3-4), 369-385.

Cozzarelli, I. M., J. K. Bohlke, J. Masoner, G. N. Breit, M. M. Lorah, M. L. W. Tuttle, and J. B. Jaeschke (2011), Biogeochemical evolution of a landfill leachate plume, Norman, Oklahoma, *Ground Water*, *49* (5), 663-687.

Cozzarelli, I. M., J. M. Suflita, G. A. Ulrich, S. H. Harris, J. L. Schlottmann, and S. Christenson (2000), Geochemical and microbiological methods for evaluating anaerobic processes in an aquifer contaminated by landfill leachate, *Environ. Sci. Technol.*, *34* (18), 4025-4033.

Das, N. N., and B. P. Mohanty (2008), Temporal dynamics of PSR-based soil moisture across spatial scales in an agricultural landscape using SMEX02: A wavelet approach, *Remote Sens. Environ.*, *112*, 522-534.

Das, N. N., B. P. Mohanty, and E. G. Njoku (2008), A Markov chain Monte Carlo algorithm for upscaled soil-vegetation-atmosphere-transfer modeling to evaluate satellite-based soil moisture measurements, *Water Resour. Res.*, *44*, W05416, doi:10.1029/2007WR006472.

Dasgupta, S., B. P. Mohanty, and J. M. Köhne (2006), Soil hydraulic conductivities and their spatial and temporal variations in a vertisol, *Soil Sci. Soc. Am. J.*, *70*, 1872–1881.

Daubechies, I. (1992), *Ten lectures on wavelets*, SIAM, Philadelphia.

Dauwe, B., J. J. Middelburg, P. M. J. Herman, C. H. R. Heip (1999), Linking diagenetic alteration of amino acids and bulk organic matter reactivity, *Limnol. Oceanogr.*, *44*, 1809–1814.

de Rooij, G. H., R. T. A. Kasteel, A. Papritz, and H. Flühler (2004), Joint distributions of the unsaturated soil hydraulic parameters and their effect on other variates, *Vadose Zone J.*, *3*, 947-955.

Deng, H. (2009), Upscaling reactive transport parameters for porous and fractured porous media, Ph.D. Thesis, Department of Geological Sciences, The Florida State University, Florida, USA.

Dexter, A. R., G. Richard, D. Arrouays, E. A. Czyz, C. Jolivet, and O. Duval (2008), Complexed organic matter controls soil physical properties, *Geoderma*, *144* (3-4), 620-627.

Diou, A., C. Dumont, O. Laligant, M. Toubin, F. Truchetet, E.P. Verrecchia, M. A. Abidi (1999), Multiscale analysis of range image: Its use for growth increment characterization, *Opt. Eng.*, *38* (12), 2016-2021.

Dousset, S., M. Thevenot, V. Pot, J. Šimůnek, and F. Andreux (2007), Evaluating equilibrium and non-equilibrium transport of bromide and isoproturon in

disturbed and undisturbed soil columns, *J. Contam. Hydrol.*, *94*(3-4), 261-276, doi:10.1016/j.jconhyd.2007.07.002.

Dubus, I. G., S. Beulke, and C. D. Brown (2002), Calibration of pesticide leaching models: Critical review and guidance for reporting, *Pest. Manage. Sci.*, *58*, 745–758.

Durner, W., E. B. Schultze, and T. Zurmühl, (1999), State-of-the-art in inverse modeling of inflow/outflow experiments, in: *Characterization and measurement of the hydraulic properties of unsaturated porous media*, edited by M.Th. van Genuchten et al., Proceedings of international workshop, Riverside, CA. 22–24 Oct. 1997, USDA-ARS, U.S. Salinity Laboratory, Riverside, CA.

Eganhouse, R. P., I. M. Cozzarelli, M. A. Scholl, and L. L. Matthews (2001), Natural attenuation of volatile organic compounds (VOCs) in the leachate plume of a municipal landfill: Using alkylbenzenes as a process probe, *Ground Water*, *39* (2), 192-202.

Escobar, M. D., and M. West (1995), Bayesian density estimation and inference using mixtures, *J. Am. Statistics Assoc.*, *90*, 577-588.

Evans, G. T. (2003), Defining misfit between biogeochemical models and data sets, *J. Mar. Sys.*, *40-41*, 49-54.

Farge, M. (1992), Wavelet transforms and their applications to turbulence, *Annu. Rev. Fluid Mech.*, *24*, 395–457.

Fendorf, S., H. A. Michael, and A. van Geen (2010), Spatial and temporal variations of groundwater arsenic in South and Southeast Asia, *Science*, *328* (5982), 1123-1127.

Feyen, J., D. Jacques, A. Timmerman, and J. Vanderborght (1998), Modelling water flow and solute transport in heterogeneous soils: A review of recent approaches, *J. Agr. Eng. Res.*, *70*(3), 231-256, doi:10.1006/jaer.1998.0272.

Flores, A. N., D. Entekhabi, R. L. Bras (2010), Reproducibility of soil moisture ensembles when representing soil parameter uncertainty using a Latin hypercube–based approach with correlation control, *Water Resour. Res.*, W04506, doi:10.1029/2009WR008155.

Flury, M., H. Fluhler, W. A. Jury, and J. Leuenberger (1994), Susceptibility of soils to preferential flow of water: A field study, *Water Resour. Res.*, *30*(7), 1945–1954.

Foufoula-Georgiou, E., and P. Kumar (1994), *Wavelets in geophysics*, Academic Press, San Diego.

Franzluebbers, A. J., F. M. Hons, and D. A. Zuberer (1995), Tillage-induced seasonal changes in soil physical properties affecting soil CO_2 evolution under intensive cropping, *Soil Tillage Res.*, *34*, 41-60.

Freeze, R. A. (1975), A stochastic-conceptual analysis of one-dimensional groundwater flow in nonuniform homogeneous media, *Water Resour. Res.*, *11*(5), 725-741.

Gee, G. W., C. T. Kincaid, R. J. Lenhard, C. S. Simmons (1991), Recent studies of flow and transport in the vadose zone, *U.S. Nat. Rep. Int. Union Geod. Geophys. 1987-1990*, *Rev. Geophys.*, *29*, 227-239.

Geesey, G. G., and A. C. Mitchell (2008), Need for direct measurements of coupled microbiological and hydrological processes at different scales in porous media Systems, *J. Hydrol. Eng.*, *13*, 28-36.

Gelman, A., J. B. Carlin, H. S. Stern, and D. B. Rubin (1995), *Bayesian data analysis*, Chapman and Hall, London.

Gerke, H. H. (2006), Preferential flow descriptions for structured soils, *J. Plant Nutr. Soil Sci.*, *169*(3), 382-400.

Gerke, H. H., and J. M. Köhne (2004), Dual-permeability modeling of preferential bromide leaching from a tile-drained glacial till agricultural field, *J. Hydrol.*, *289*(1-4), 239-257.

Gerke, H. H., and M. T. van Genuchten (1993a), A dual-porosity model for simulating the preferential movement of water and solutes in structured porous media, *Water Resour. Res.*, *29*, 305–319.

Gerke, H. H., and M. T. van Genuchten (1993b), Evaluation of a first-order water transfer term for variably-saturated dual-porosity models, *Water Resour. Res.*, *29*, 1225–1238.

Gerke, H. H., and M. T. van Genuchten (1996), Macroscopic representation of structural geometry for simulating water and solute mass transfer in dual-porosity media, *Adv. Water Resour.*, *19*, 343–357.

Germann, P. F. (1985), Kinematic wave approach to infiltration and drainage into and from soil macropores, *T. ASAE*, *28*(3), 745–749.

Geweke, J. (1992), Evaluating the accuracy of sampling-based approaches to the calculation of posterior moments, in *Bayesian Statistics* 4, edited by J. M. Bernado et al., pp. 169– 193, Oxford Press, Oxford, UK.

Ginn, T. R., and J. H. Cushman (1990), Inverse methods for subsurface flow: A critical review of stochastic techniques, *Stochastic Hydrol. Hydraul.*, *4*, 1-26.

Grinsted, A., S. Jevrejeva, and J. Moore (2004), Application of the crosswavelet transform and wavelet coherence to geophysical time series, *Nonlinear Processes Geophys.*, *11*, 561–566.

Grossman, E. L., L. A. Cifuentes, and I. M. Cozzarelli (2002), Anaerobic methane oxidation in a landfill-leachate plume, *Environ. Sci. Technol.*, *36* (11), 2436-2442.

Guan, K., S. E. Thompson, C. J. Harman, N. B. Basu, P. S. C. Rao, M. Sivapalan, A. I. Packman, and P. K. Kalita (2011), Spatiotemporal scaling of hydrological and agrochemical export dynamics in a tile-drained Midwestern watershed, *Water Resour. Res.*, *47*, W00J02, doi:10.1029/2010WR009997.

Gwo, J. P., P. M. Jardine, G. V. Wilson, and G. T. Yeh (1995), A multiple-pore-region concept to modeling mass transfer in subsurface media, *J. Hydrol.*, *164*, 217–237.

Haack, S. K., and B. A. Bekins (2000), Microbial populations in contaminant plumes, *Hydrogeol. J.*, *8* (1), 63-76.

Haack, S. K., L. R. Fogarty, T. G. West, E. W. Alm, J. T. McGuire, D. T. Long, D. W. Hyndman, and L. J. Forney (2004), Spatial and temporal changes in microbial

community structure associated with recharge-influenced chemical gradients in a contaminated aquifer, *Environ. Microbiol.*, *6* (5), 438-448.

Han, F. X., A. Banin, and G. B. Triplett (2001), Redistribution of heavy metals in arid-zone soils under a wetting-drying cycle soil moisture regime, *Soil Sci.*, *166*, 18-28.

Hansen, D. J., J. T. McGuire, and B. P. Mohanty (2011), Enhanced biogeochemical cycling and subsequent reduction of hydraulic conductivity associated with soil-layer interfaces in the vadose zone, *J. Environ. Qual.*, *40* (6), 1941-1954.

Hansen, D. J., J. T. McGuire, and B. P. Mohanty (2012a), Evidence of aqueous FeS clusters in the vadose zone and implications for dynamic soil structure, *Biogeochemistry*, submitted manuscript.

Hansen, D. J., J. T. McGuire, and B. P. Mohanty (2012b), Biogeochemical cycling in heterogeneous unsaturated soils: A comparison between live and sterilized sediments, *Vadose Zone J.*, submitted manuscript.

Hariprasath, S., and V. Mohan (2009), Iris pattern recognition using complex wavelet and wavelet packet transform, *J. Computer Applications*, *2* (2), 18-23.

Harrio, H., E. Saksman, and J. Tamminen (2001), An adaptive Metropolis algorithm, *Bernoulli 7*(2), 223-242.

Harris, S. H. Jr, J. D. Istok, and J. M. Suflita (2006), Changes in organic matter biodegradability influencing sulfate reduction in an aquifer contaminated by landfill leachate, *Microb. Ecol.*, *51* (4), 535–542.

Hastings, W. K. (1970), Monte Carlo sampling methods using Markov chains and their applications, *Biometrika*, *57*, 97-109.

Haynes, R. J., and R. Naidu (1998), Influence of lime, fertilizer and manure applications on soil organic matter content and soil physical conditions: A review, *Nutr. Cycling Agroecosyst.*, *51* (2), 123-137.

Hendrickx, J. M. H., and M. Flury (2001), Conceptual models of flow and transport in the fractured vadose zone, in *Uniform and preferential flow mechanisms in the vadose zone*, pp. 149–187, Natl. Academy Press, Washington, D. C.

Hunt, A. G. (2003), Some comments on the scale dependence of the hydraulic conductivity in the presence of nested heterogeneity, *Adv. Water Resour.*, *26* (1), 71-77.

Hunter, K. S., Y. Wang, and P. van Cappellen (1998), Kinetic modeling of microbially-driven redox chemistry of subsurface environments: Coupling transport, microbial metabolism, and geochemistry, *J. Hydrol.*, *209*, 53-80.

Jacques, D., and J. Šimůnek (2005), User manual of the multicomponent variably-saturated flow and transport model HP1, description, verification and examples, Version 1.0, *Open Report SCK•CEN-BLG-998*, Nuclear Regulatory Commission, Mol, Belgium, 79 pp.

Jacques, D., J. Šimůnek, D. Mallants, and M. Th. Van Genuchten (2006), Operator-splitting errors in coupled reactive transport codes for transient variably saturated flow and contaminant transport in layered soil profiles, *J. Contam. Hydrol.*, *88*, 197-218.

Jacques, D., J. Šimůnek, D. Mallants, and M. Th. Van Genuchten (2008), Modeling coupled hydrological and chemical processes: Long-term uranium transport following mineral phosphorus fertilization, *Vadose Zone J.*, *7* (2), 698-711.

Jamieson, R. C., R. J. Gordon, K. E. Sharples, G. W. Stratton, and A. Madani (2002), Movement and persistence of fecal bacteria in agricultural soils and subsurface drainage water—A review, *Can. Biosys. Eng.*, *44*, 1.1-1.9.

Jana, R. B., and B. P. Mohanty (2011), Enhancing PTFs with remotely sensed data for multi-scale soil water retention estimation, *J. Hydrol.*, *399*(3-4), 201-211.

Jana, R. B., and B. P. Mohanty (2012), On topographic controls of soil hydraulic parameter scaling at hill-slope scales, *Water Resour. Res.*, *48*, W02518, doi:10.1029/2011WR011204.

Jansen, B., K. G. J. Nierop, J. M. Verstraten (2002), Influence of pH and metal/carbon ratios on soluble organic complexation of Fe(II), Fe(III) and Al(III) in soil solutions determined by diffusive gradients in thin films, *Anal. Chem. Acta*, *454*, 259–270.

Jansson, C., B. Espeby, and P.-E. Jansson (2005), Preferential water flow in a glacial till soil, *Nord. Hydrol.*, *36*, 1-11, doi:10.1029/1999WR00310.

Jardine, P. M. (2008), Influence of coupled processes on contaminant fate and transport in subsurface environments, *Adv. Agronomy*, *99*, 1-99, doi:10.1016/S0065-2113(08)00401-X.

Jarvis, N. J. (1994), The MACRO Model (Version 3.1): Technical description and sample simulations, in *Reports and Dissertations no. 19*, Dept. Soil Sci., Swedish Univ. of Agric. Sci., Uppsala, Sweden.

Jarvis, N. J. (2007), A review of non-equilibrium water flow and solute transport in soil macropores: Principles, controlling factors and consequences for water quality, *Eur. J. Soil Sci.*, *58*, 523–546, doi:10.1111/j.1365-2389.2007.00915.x

Jarvis, N., M. Larsbo, S. Roulier, A. Lindahl, and L. Persson (2007), The role of soil properties in regulating non-equilibrium macropore flow and solute transport in agricultural topsoils, *Europ. J. Soil Sci.*, *58*(1), 282-292.

Jolley, D. M., T. F. Ehrhorn, and J. Horn (2003), microbial impacts to the near-field environment geochemistry: A model for estimating microbial communities in repository drifts at Yucca mountain, *J. Contam. Hydrol.*, *62-63*, 553-575.

Jury, W. A., and H. Flühler (1992), Transport of chemicals through soil: Mechanisms, models and field applications, *Adv. Agron.*, *47*, 141-201.

Kaiser, H. F. (1960), The application of electronic computers to factor analysis, *Educational and Physiological Measurement*, *20*, 141-151.

Kalbitz, K., D. Schwesig, J. Schmerwitz, K. Kaiser, L. Haumaier, B. Glaser, R. Ellerbrock, and P. Leinweber (2003), Changes in properties of soil-derived dissolved organic matter induced by biodegradation, *Soil Biol. Biochem.*, *35* (8), 1129-1142.

Kamolpornwijit, W., L. Liang, O. R. West, G. R. Moline, A. B. Sullivan (2003), Preferential flow path development and its influence on long-term PRB performance: Column study, *J. Contam. Hydrol.*, *66*, 161-178.

Khaleel, R., T.-C. J. Yeh, and Z. Lu (2002), Upscaled flow and transport properties for heterogeneous unsaturated media, *Water Resour. Res.*, *38* (5), doi:10.1029/2000WR000072.

Kia, S. H., H. Henao, and G.-A. Capolino (2009), Diagnosis of broken-bar fault in induction machines using discrete wavelet transform without slip estimation, *IEEE Trans. Ind. Appl.*, 45 (4), 1395-1404.

Kimball, B. A., R. E. Broshears, K. E. Bencala, D. M. McKnight (1994), Coupling of hydrologic transport and chemical reactions in a stream affected by acid mine drainage, *Environ. Sci. Technol.*, *28* (12), 2065-2073.

Kladivko, E. J., L. C. Brown, and J. L. Baker (2001), Pesticide transport to subsurface tile drains in humid regions of North America, *Crit. Rev. Env. Sci. Tec.*, *31*, 1-62.

Kneeshaw, T. A., J. T. McGuire, E. W. Smith, and I. M. Cozzarelli (2007), Evaluation of sulfate reduction at experimentally induced mixing interfaces using small-scale push–pull tests in an aquifer–wetland system, *Appl. Geochem.*, *22* (12), 2618-2629.

Kodeŝová, R., J. Šimůnek, A. Nikodem, and V. Jirku (2010), Estimation of the dual-permeability model parameters using tension disk infiltrometer and Guelph permeameter, *Vadose Zone J.*, *9*(2), 213– 225.

Kodešová, R., M. Kočárek, V. Kodeš, J. Šimůnek, and J. Kozák (2008), Impact of soil micromorphological features on water flow and herbicide transport in soils, *Vadose Zone J.*, *7*, 798-809.

Kohne, J. M., and B. P. Mohanty (2005), Water flow processes in a soil column with a cylindrical macropore: Experiment and hierarchical modeling, *Water Resour. Res.*, *41*, W03010, doi:10.1029/2004WR003303.

Köhne, J. M., B. P. Mohanty, J. Šimůnek, and H. H. Gerke (2004), Numerical evaluation of a second-order water transfer term for variably saturated dual-permeability models, *Water Resour. Res.*, *40*, W07409, doi:10.1029/2004WR003285.

Köhne, J. M., S. Köhne, and H. H. Gerke (2002), Estimating the hydraulic functions of dual-permeability models from bulk soil data, *Water Resour. Res.*, *38*(7), doi:10.1029/2001WR000492.

Köhne, J. M., S. Köhne, and J. Šimůnek (2006a), Multi-process herbicide transport in structured soil columns: Experiments and model analysis, *J. Contam. Hydrol.*, *85*, 1-32, doi:10.1016/j.jconhyd.2006.01.001.

Köhne, J. M., S. Köhne, and J. Šimůnek (2009), A review of model applications for structured soils: a) Water flow and solute transport, *J. Contam. Hydrol.*, *104*, 4-35, doi:10.1016/j.jconhyd.2008.10.002.

Köhne, S., B. Lennartz, J. M. Köhne, and J. Šimůnek (2006b) Bromide transport at a tile-drained field site: Experiment, and one- and two-dimensional equilibrium and non-equilibrium numerical modeling, *J. Hydrol.*, *321*(1-4), 390-408, doi:10.1016/j.jhydrol.2005.08.010.

Kool, J. B., and J. C. Parker (1988), Analysis of the inverse problem for transient unsaturated flow, *Water Resour. Res.*, *24*, 817-830.

Kramers, G., J. C. van Dam, C. J. Ritsema, F. Stagnitti, K. Oostindie, and L. W. Dekker (2005), A new modelling approach to simulate preferential flow and transport in water repellent porous media: Parameter sensitivity, and effects on crop growth and solute leaching, *Austr. J. Soil Res.*, *43*, 371-382.

Kumar, P., and E. Foufoula-Georgiou (1997), Wavelet analysis for geophysical applications, *Rev. Geophys.*, *35* (4), 385-412.

Kusel, K. (2003), Microbial cycling of iron and sulfur in acidic coal mining lake sediments, Water, Air Soil Pollut., *3* (1), 67-90.

Labat, D., R. Ababou, and A. Mangin (2000), Rainfall-runoff relations for karstic springs. Part II: Continuous wavelet and discrete orthogonal multiresolution analyses, *J. Hydrol.*, *238*, 149-178.

LaGrega, M. D., P. L. Buckingham, and J. C. Evans (1994), *Hazardous waste management*, McGraw-Hill Inc., New York.

Langmuir, D. (1997), *Aqueous environmental geochemistry*, Prentice Hall, New Jersey.

Larsbo, M., S. Roulier, F. Stenemo, R. Kasteel, and N. Jarvis (2005), An improved dual-permeability model of water flow and solute transport in the vadose zone, *Vadose Zone J.*, *4*, 398-406.

Larsson, M. H., N. J. Jarvis, G. Torstensson and R. Kasteel (1999), Quantifying the impact of preferential flow on solute transport to tile drains in a sandy field soil, *J. Hydrol.*, *215*, 116–134, doi:10.1016/S0022-1694(98)00265-0.

Lau, K.-M., and H. Weng (1995), Climate signal detection using wavelet transform: How to make a time series sing, *Bull. Am. Meteorol. Soc.*, *76* (12), 2391-2402.

Legates, D. R., and G. J. McCabe Jr. (1999), Evaluating the use of "goodness-of-fit" measures in hydrologic and hydroclimatic model validation, *Water Resour. Res.*, *35*(1), 233-241.

Liu, K. H., C. G. Enfield, and S. C. Mravik (1991), Evaluation of sorption models in the simulation of naphthalene transport through saturated soils, *Ground Water*, *29*(5), 685–692.

Logsdon, S. D., and D. B. Jaynes (1996), Spatial variability of hydraulic conductivity in a cultivated field at different times, *Soil Sci. Soc. Am. J.*, *60*, 703–709.

Lorah, M. M., I. M. Cozzarelli, and J. K. Böhlke (2009), Biogeochemistry at a wetland sediment-alluvial aquifer interface in a landfill leachate plume, *J. Contam. Hydrol.*, *105*, 99-117.

Lovley, D. R., and F. H. Chapelle (1995), Deep subsurface microbial processes, *Rev. Geophys.*, *33*, 365-381.

Mallants, D., B. P. Mohanty, A. Vervoort, and J. Feyen (1997), Spatial analysis of saturated hydraulic conductivity in a soil with macropores, *Soil Tec.*, *10*(2), 115-131.

Mallat, S. (1999), *A wavelet tour of signal processing*, Academic Press, New York.

Marshall, L., D. Nott, and A. Sharma (2004), A comparative study of Markov chain Monte Carlo methods for conceptual rainfall-runoff modeling, *Water Resour. Res.*, *40*, W02501, doi:10.1029/2003WR002378.

Martinez, B., and M. A. Gilabert (2009), Vegetation dynamics from NDVI time series analysis using the wavelet transform, *Remote Sens. Environ.*, *113*, 1823–1842.

Masscheleyn, P. H., R. D. Delaune, and W. H. Patrick (1991), Effect of redox potential and pH on arsenic speciation and solubility in a contaminated soil, *Environ. Sci. Technol.*, *25* (8), 1414-1419.

Mayer, U. (1999), A numerical model for multicomponent reactive transport in variably saturated porous media, Ph.D. thesis, Department of Earth Sciences, University of Waterloo, Waterloo, Canada.

Mayer, K. U., D. W. Blowes, and E. O. Frind (2001), Reactive transport modeling of an in situ reactive barrier for the treatment of hexavaelent chromium and trichloroethylene in groundwater, *Water Resour. Res.*, *37* (12), 3091-3103.

McGuire, J. T., D. T. Long, and D. W. Hyndman (2005), Analysis of recharge-induced geochemical change in a contaminated aquifer, *Ground Water*, *43* (4), 518-530.

McGuire, J. T., D. T. Long, M. J. Klug, S. K. Haack, and D. W. Hyndman (2002), Evaluating behavior of oxygen, nitrate, and sulfate during recharge and quantifying reaction rates in a contaminated aquifer, *Environ. Sci. Technol.*, *36* (12), 2693-2700.

McGuire, J. T., E. W. Smith, D. T. Long, D. W. Hyndman, S. K. Haack, M. J. Klug, and M. A. Velbel (2000), Temporal variations in parameters reflecting terminal-electron-accepting processes in an aquifer contaminated with waste fuel and chlorinated solvents, *Chem. Geol.*, *169* (3-4), 471-485.

Megonigal, J. P., M. E. Hines, and P. T. Visscher (2004), *Anaerobic metabolism: Linkages to trace gases and anaerobic processes*, Elsevier-Pergamon, Oxford, UK.

Mercer, J. W. (1983), *The role of the unsaturated zone in radioactive and hazardous waste disposal*, Butterworth-Heinemann, Oxford, UK.

Metropolis, N., A. W. Rosenbluth, M. N. Rosenbluth, A. H. Teller, and E. Teller (1953), Equations of state calculations by fast computing machines, *J. Chem. Phys.*, *21*, 1087-1091.

Miller, J. J., B. J. Lamond, N. J. Sweetland, and F. J. Larney (1999), Preferential leaching in large undisturbed soil blocks from conventional tillage and no-till fields in southern Alberta, *Water Qual. Res. J. Can.*, *34*(2), 249-266.

Mills, A. L., P. E. Bell, and A. T. Herlihy (1989), Microbes, sediments, and acidified waters: The importance of biological buffering, in *Acid stress and aquatic microbial interactions*, edited by S.S. Rao, CRC Press, Inc., pp. 1–19, Boca Raton, FL.

Misiti, M., Y. Misiti, G. Oppenheim, and J. M. Poggi (2008), *Matlab user's guide: Wavelet toolbox™ 4*, The Math Works Inc, Natick, MA.

Mitchell, C. P. J., and B. A. Branfireun (2005), Hydrogeomorphic controls on reduction–oxidation conditions across boreal upland–peatland interfaces, *Ecosystems*, *8* (7), 731-747.

Mohanty, B. P., and J. Zhu (2007), Effective hydraulic parameters in horizontally and vertically heterogeneous soils for steady-state land–atmosphere interaction, *J. Hydrometerol.*, *8* (4), 715–729.

Mohanty, B. P., R. S. Bowman, J. M. H. Hendrickx, and M. Th. van Genuchten (1997), New piecewise-continuous hydraulic functions for modeling preferential flow in an intermittent-flood-irrigated field, *Water Resour. Res.*, *33*(9), 2049-2063.

Mohanty, B. P., R. S. Bowman, J. M. H. Hendrickx, J. Šimůnek, and M. Th. van Genuchten (1998), Preferential transport of nitrate to a tile drain in an intermittent-flood-irrigated field: Model development and experimental evaluation, *Water Resour. Res.*, *34* (5), 1061-1076.

Morel, F., and J. Hering (1993), *Principles and applications of aquatic chemistry*, John Wiley & Sons Inc., New York.

Mualem, Y. (1976), A new model for predicting the hydraulic conductivity of unsaturated soils, *Water Resour. Res.*, *12*, 513-522.

Mukherjee, A., M. von Brömssen, B. R. Scanlon, P. Bhattacharya, A. E. Fryar, M. A. Hasan, K. M. Ahmed, D. Chatterjee, G. Jacks, and O. Sracek (2008), Hydrogeochemical comparison and effects of overlapping redox zones on groundwater arsenic near the Western (Bhagirathi sub-basin, India) and Eastern (Meghna sub-basin, Bangladesh) margins of the Bengal basin, *J. Contam. Hydrol.*, *99*, 31-48.

National Research Council (1994), *Ground water recharge using waters of impaired quality*, 283 pp., Natl. Academy Press, Washington, D. C.

Nemes, A., M. G. Schaap, and F. J. Leij (1999), The UNSODA unsaturated soil hydraulic database, version 2.0, U. S. Salinity Laboratory, U. S. Department of Agriculture, Agricultural Research Service, Riverside, California.

Nemes, A., M. G. Schaap, F. J. Leij, and J. H. M. Wosten (2001), Description of the unsaturated soil hydraulic database UNSODA version 2.0, *J. Hydrol.*, *251*(3-4), 151-162.

Novák, V., J. Šimůnek, and M. T. van Genuchten (2000), Infiltration of water into soils with cracks, *J. Irrig. Drain. Engg.*, *126*(1), 41–47.

Onsoy, Y. S., T. Harter, T. R. Ginn, and W. R. Horwath (2005), Spatial variability and transport of nitrate in a deep alluvial vadose zone, *Vadose Zone J.*, *4*, 41-54.

Pacific, V. J., B. L. McGlynn, D. A. Riveros-Iregui, D. L. Welsch, and H. E. Epstein (2011), Landscape structure, groundwater dynamics, and soil water content influence soil respiration across riparian-hillslope transitions in the Tenderfoot Creek experimental forest, Montana, *Hydrol. Processes*, *25* (5), 811–827.

Parkhurst, D. L., and C. A. J. Appelo (1999), User's guide to PHREEQC (Version 2) — A computer program for speciation, batch-reaction, one-dimensional transport and inverse geochemical calculations, *Water-Resources Investigations Report 99-4259*, Denver, Colorado, 312 pp.

Percival, D. B., and A. T. Walden (2000), *Wavelet methods for time series analysis*, Cambridge University Press, Cambridge.

Peters, G. W., B. Kannan, B. Lasscock, and C. Mellen (2009), Model selection and adaptive Markov chain Monte Carlo for Bayesian cointegrated VAR model,

paper presented at 15th International conference on computing in economics and finance, Sydney, Australia.

Pollacco, J. A. P., J. M. S. Ugalde, R. Angulo-Jaramillo, I. Braud, and B. Saugier (2008), A linking test to reduce the number of hydraulic parameters necessary to simulate groundwater recharge in unsaturated soils, *Adv. Water Resour.*, *31*(2), 355-369.

Prommer, H., D. A. Barry, and G. B. Davis (1998), The effect of seasonal variability on intrinsic biodégradation of a BTEX plume, in *Groundwater quality: Remediation and protection GQ'98*, IAHS Publ. No. 250, edited by M. Herbert and K. Kovar, pp. 213–220. Tubingen, Germany.

Qian, J., and K. Mopper (1996), Automated high performance, high temperature combustion total organic carbon analyzer, *Anal. Chem.*, *68*, 3090–3097.

Quiroz, R., C. Yarleque, A. Posadas, V. Mares, and W. W. Immerzeel (2011), Improving daily rainfall estimation from NDVI using a wavelet transform, *Environ. Modell. Softw.*, *26*, 201-209.

Raftery, A. E., and S. Lewis (1992), "How many iterations in the Gibbs sampler?", in *Bayesian statistics* 4, edited by J. M. Bernardo et al., pp. 763-773, Oxford University Press, Oxford, UK.

Raz-Yaseef, N., E. Rotenberg, and D. Yakir (2010), Effects of spatial variations in soil evaporation caused by tree shading on water flux partitioning in a semi-arid pine forest, *Agric. Forest Meteorol.*, *150*, 454–462.

Reis, D. S., and J. R. Stedinger (2005), Bayesian MCMC flood frequency analysis with historical information, *J. Hydrol.*, *313*, 97–116.

Röling, W. F. M., B. M. van Breukelen, M. Braster, B. Lin, and H. W. van Verseveld (2001), Relationships between microbial community structure and hydrochemistry in a landfill leachate-polluted aquifer, *Appl. Environ. Microbiol.*, *67* (10), 4619-4629.

Roulier, S., and N. Jarvis (2003), Analysis of inverse procedures for estimating parameters controlling macropore flow and solute transport in the dual-permeability model MACRO, *Vadose Zone J.*, *2*, 349-357.

Rubin, Y. (2003), *Applied stochastic hydrogeology*, Oxford Univ. Press, New York.

Schäffer, B., M. Stauber, T. L. Mueller, R. Müller, and R. Schulin (2008), Soil and macro-pores under uniaxial compression. I. Mechanical stability of repacked soil and deformation of different types of macro-pores, *Geoderma*, *146*(1-2), 183-191.

Scharnagl, B., J. A. Vrugt, H. Vereecken, and M. Herbst (2011), Inverse modelling of in situ soil water dynamics: Investigating the effect of different prior distributions of the soil hydraulic parameters, *Hydrol. Earth Syst. Sci.*, *8*(1), 2019-2063.

Schilling, K. E. and P. Jacobson (2012), Spatial relations of topography, lithology and water quality in a large river floodplain, *River Res. Applic.*, doi:10.1002/rra.1531.

Schlottmann, J. L. (2001), Water chemistry near the closed Norman Landfill, Cleveland County, Oklahoma, 1995, *U.S. Geological Survey Water-Resources Investigation Report 00-4238*, 44 pp.

Scholl, M. A., and S. C. Christenson (1998), Spatial variation in hydraulic conductivity determined by slug tests in the Canadian River alluvium near the Norman Landfill, Norman, Oklahoma, *U.S. Geological Survey Water-Resources Investigation Report 97-4292*, 28 pp.

Scholl, M. A., I. M. Cozzarelli, and S. C. Christenson (2006), Recharge processes drive sulfate reduction in an alluvial aquifer contaminated with landfill leachate, *J. Contam. Hydrol.*, *104*, 4-35, doi:10.1016/j.jconhyd.2008.10.002.

Scholl, M. A., I. M. Cozzarelli, S. C. Christenson, G. N. Breit, and J. L. Schlottmann (1999), Aquifer heterogeneity at Norman Landfill and its effect on observations of biodegradation processes, In *U.S. Geological Survey Toxic Substances Hydrology Program: Proceedings of the Technical Meeting, Charleston, South Carolina, March 8-12, 1999 Subsurface contamination from point source (eds. D. W. Morganwalp and H. T. Buxton), U.S. Geological Survey Water-Resources Investigation Report 99-4018C,* West Trenton, NJ, vol. 3, pp. 557-568.

Scholl, M. A., S. C. Christenson, and I. M. Cozzarelli (2005), Recharge processes in an alluvial aquifer riparian zone, Norman Landfill, Norman, Oklahoma, 1998–2000, *U.S. Geological Survey Water-Resources Investigation Report 2004-5238*, 60 pp.

Schoups, G., and J. A. Vrugt (2010), A formal likelihood function for parameter and predictive inference of hydrologic models with correlated, heteroscedastic, and non-Gaussian errors, *Water Resour. Res.*, *46*, W10531, doi:10.1029/2009WR008933.

Schulze-Makuch, D., and D. S. Cherkauer (2004), Variations in hydraulic conductivity with scale of measurement during aquifer tests in heterogeneous, porous carbonate rocks, *Hydrogeology J.*, *6* (2), 204-215.

Schwartz, R. C., A. S. R. Juo, and K. J. McInnes (2000), Estimating parameters for a dual-porosity model to describe non-equilibrium, reactive transport in a fine textured soil, *J. Hydrol.*, *229*, 149–167.

Shao, X.-G., A. K.-M. Leung, and F.-T. Chau (2003), Wavelet: A new trend in chemistry, *Acc. Chem. Res.*, *36* (4), 276–283.

Sharma, S. K., B. P. Mohanty, and J. Zhu (2006), Including topography and vegetation attributes for developing pedotransfer functions, *Soil Sci. Am. J.*, *70*, 1430-1440.

Sheridan, C. C., C. Lee, S. G. Wakeham, and J. K. B. Bishop (2002), Suspended particle organic composition and cycling in surface and midwaters of the equatorial Pacific Ocean, *Deep-Sea Res. I*, *49*, 1983–2008.

Šimůnek, J., and M. T. van Genuchten (2008), Modeling nonequilibrium flow and transport processes using HYDRUS, *Vadose Zone J.*, *7*(2), 782-797.

Šimůnek, J., M. Šejna, and M. Th. van Genuchten (1998), The HYDRUS-1D software package for simulating the one-dimensional movement of water, heat, and multiple solutes in variably-saturated media (Version 2.0), *IGWMC - TPS - 70,* International Ground Water Modeling Center, Colorado School of Mines, Golden, Colorado, 202 pp.

Šimůnek, J., M. Šejna, H. Saito, M. Sakai, and M. Th. Van Genuchten (2008), The HYDRUS-1D software package for simulating the movement of water, heat, and

multiple solutes in variably-saturated media, Version 4.0, HYDRUS Software Series 3, Department of Environmental Sciences, University of California Riverside, Riverside, California, 315 pp.

Šimůnek, J., N. J. Jarvis, M. T. van Genuchten, and A. Gärdenäs (2003), Review and comparison of models for describing non-equilibrium and preferential flow and transport in the vadose zone, *J. Hydrol.*, *272*, 14-35, doi:10.1016/S0022-1694(02)00252-4.

Šimůnek, J., O. Wendroth, and M. T. van Genuchten (1999), Estimating unsaturated soil hydraulic properties from laboratory tension disc infiltrometer experiments, *Water Resour. Res.*, *35*(10), 2965-2979.

Šimůnek, J., O. Wendroth, N. Wypler, and M. Th. van Genuchten (2001), Non–equilibrium water flow characterized by means of upward infiltration experiments, *Eur. J. Soil Sci.*, *52*(1), 13–24.

Sinke, A. J. C., O. Dury, and J. Zobrist (1998), Effects of a fluctuating water table: Column study on redox dynamics and fate of some organic pollutants, *J. Contam. Hydrol.*, *33* (1-2), 231-246.

Smith, K. S. (2007), Strategies to predict metal mobility in surficial mining environments, in *Reviews in Engineering Geology, Volume XVII: Understanding and responding to hazardous substances at mine sites in the western United States*, vol. 17, edited by J. V. DeGraff, pp. 25-45, The Geological Society of America, USA.

Stoessell, R. K. (1992), Effects of sulfate reduction on $CaCO_3$ dissolution and precipitation in mixing-zone fluids, *J. Sedimentary Petrol.*, *62* (5), 873-880.

Tanner, R. S. (1989), Monitoring sulfate-reducing bacteria: Comparison of enumeration media, *J. Microbiol. Methods*, *10* (2), 83-90.

Taylor, S. W., and P. R. Jaffe (1990), Biofilm growth and the related changes in the physical properties porous medium, *Water Resour. Res.*, *26* (9), 2153–2159.

Torrence, C., and G. P. Compo (1998), A practical guide to wavelet analysis, *Bull. Am. Meteorol. Soc.*, *79* (1), 61-78.

Tuttle, M. L. W., G. N. Breit, and I. M. Cozzarelli (2009), Processes affecting $\delta^{34}S$ and $\delta^{18}O$ values of dissolved sulfate in alluvium along the Canadian River, central Oklahoma, USA, *Chem. Geol.*, *265*, 455-467.

Ulrich, G. A., G. N. Breit, I. M. Cozzarelli, and J. M. Suflita (2003), Sources of sulfate supporting anaerobic metabolism in a contaminated aquifer, *Environ. Sci. Technol.*, *37* (6), 1093-1099.

van Breukelen, B. M., and J. Griffioen (2004), Biogeochemical processes at the fringe of a landfill leachate pollution plume: Potential for dissolved organic carbon, Fe(II), Mn(II), NH_4, and CH_4 oxidation, *J. Contam. Hydrol.*, *73*, 181-205, doi:10.1016/j.jconhyd.2004.01.001.

van Breukelen, B. M., W. F. M Röling, J. Groen, J. Griffioen, and H. W. Van Verseveld (2003), Biogeochemistry and isotope geochemistry of a landfill leachate plume, *J. Contam. Hydrol.*, *65* (3-4), 245–268.

van Genuchten, M. T. (1980), A closed-form equation for predicting the hydraulic conductivity of unsaturated soils, *Soil Sci. Soc. Am. J.*, *44*, 892–898.

van Genuchten, M. T., and P. J. Wierenga (1976), Mass transfer studies in sorbing porous media, I, Analytical solutions, *Soil Sci. Soc. Am. J.*, *40*, 473–481.

van Genuchten, M. T., D. E. Rolston, and P. F. Germann (1990), Transport of water and solutes in macropores, *Geoderma*, *46*(1), 1-297.

van Grinsven, J. J. M., and W. H. van Riemsdijk (1992), Evaluation of batch and column techniques to measure weathering rates in soils, *Geoderma*, 52 (1-2), 42-57.

Vereecken, H., R. Kasteel, J. Vanderborght, and T. Harter (2007), Upscaling hydraulic properties and soil water flow processes in heterogeneous soils: A review, *Vadose Zone J.*, *6*, 1-28.

Villholth, K. G., and K. H. Jensen (1998), Flow and transport processes in a macroporous subsurface drained glacial till soil. II. Model analysis, *J. Hydrol.*, *207*, 121–135, doi:10.1016/S0022-1694(98)00129-2.

Vogel, H.-J., and K. Roth (2003), Moving through scales of flow and transport in soil, *J. Hydrol.*, *272* (1-4), 95–106.

Vogel, T., H. H. Gerke, R. Zhang, and M. T. van Genuchten (2000), Modeling flow and transport in a two-dimensional dual-permeability system with spatially variable hydraulic properties, *J. Hydrol.*, *238*, 78-79, doi: 10.1016/S0022-1694(00)00327-9.

Vrugt, J. A., P. H. Stauffer, Th. Wöhling, B. A. Robinson, and V. V. Vesselinov (2008), Inverse modeling of subsurface flow and transport properties: A review with new developments, *Vadose Zone J.*, *7*, 843-864.

Vrugt, J. A., W. Bouten, H. V. Gupta, and J. W. Hopmans (2003), Toward improved identifiability of soil hydraulic parameters: On the selection of a suitable parametric model, *Vadose Zone J.*, *2*, 98-113.

Wanty, R. B., and B. R. Berger (2006), Geologic, hydrologic, and geochemical interpretations of mineral deposits as analogs for understanding transport of environmental contaminants, *J. Geochem. Explor.*, *88*, 162–165.

Weiler, M. (2005), An infiltration model based on flow variability in macropores: Development, sensitivity analysis and applications, *J. Hydrol.*, *310*(1-4), 294-315, doi: 10.1016/j.jhydrol.2005.01.010.

White, A. F., and S. L Brantley (2003), The effect of time on the weathering of silicate minerals: Why do weathering rates differ in the laboratory and field?, *Chem. Geol.*, *202* (3-4), 479-506.

Wu, C.-M., T.-C. J. Yeh, J. Zhu, T. H. Lee, N.-S. Hsu. C.-H. Chen, and A. F. Sancho (2005), Traditional analysis of aquifer tests: Comparing apples to oranges?, *Water Resour. Res.*, *41*, W09402, doi:10.1029/2004WR003717.

Wu, W., J. S. Clark, and J. M. Vose (2010), Assimilating multi-source uncertainties of a parsimonious conceptual hydrological model using hierarchical Bayesian modeling, *J. Hydrol.*, *394*(3-4), 436-446.

Zachmann, D. W., P. C. Duchateau, and A. Klute (1981), The calibration of the Richards' flow equation for a draining column by parameter identification, *Soil Sci. Soc. Am. J.*, *45*, 1012–1015.

Zhang, B. H., Z. J. Wang, Z. T. Liu, A. M. Huang, Q. X. Tang, Y. R. He (2007), Influence of soil organic matter contents on soil water characteristics of forests on east slope of Gongga Mountain, *J. For. Res.*, *18* (1), 78-80.

Zhang, K., Y. S. Wu, and J. Houseworth (2006), Sensitivity analysis of hydrological parameters in modeling flow and transport in the unsaturated zone of Yucca Mountain, Nevada, USA, *Hydrogeol. J.*, *14*(8), 1599-1619, doi:10.1007/s10040-006-0055-y.

Zhu, J., and B. P. Mohanty (2002), Spatial Averaging of van Genuchten Hydraulic Parameters for Steady-State Flow in Heterogeneous Soils: A Numerical Study, *Vadose Zone J.*, *1*, 261-272.

Zhu, J., and B. P. Mohanty (2003), Effective hydraulic parameters for steady state vertical flow in heterogeneous soils, *Water Resour. Res.*, *39(8)*, doi:10.1029/2002WR001831.

Zhu, J., and B. P. Mohanty (2004), Soil hydraulic parameter upscaling for steady-state flow with root water uptake, *Vadose Zone J.*, *3*, 1464-1470.

Zhu, J., and B. P. Mohanty (2006), Effective scaling factor for transient infiltration in heterogeneous soils, *J. Hydrol.*, *319*, 96–108.

Zurmuhl, T. and W. Durner (1998), Determination of parameters for bimodal hydraulic functions by inverse modeling, *Soil Sci. Soc. Am. J.*, *4620*, 874–880.

APPENDIX A

PRINCIPAL COMPONENT ANALYSIS

A complete summary of the principal component analysis used for extracting the dominant processes of the homogeneous sand, homogeneous loam and layered columns is provided in the following tables.

Table A1: Component Score Coefficient Matrix for the homogeneous sand column.

Parameter	Component 1
Depth	1.62E-02
Tensiometer located at the top of the column	4.00E-10
Tensiometer located at the bottom of the column	1.62E-09
TDR located at the top of the column	-7.65E-07
TDR located at the bottom of the column	8.95E-09
Redox potential measurement at the top of the column	4.97E-05
Redox potential measurement at the top of the column	-1.04E-04
Cl^-	-9.00E-03
Br^-	9.78E-01
SO_4^{2-}	9.47E-04
NO_3^-	3.82E-03
Alkalinity	8.37E-03
Temperature	2.37E-08

Table A2: Component Score Coefficient Matrix for the homogeneous loam column.

Parameter	Component 1	Component 2	Component 3
Depth	-5.84E-03	5.81E-03	-5.50E-04
Tensiometer located at the top of the column	-4.70E-09	9.15E-09	5.53E-09
Tensiometer located at the bottom of the column	1.62E-06	-2.20E-06	-4.60E-07
TDR located at the top of the column	-1.50E-07	3.58E-07	1.16E-07
TDR located at the bottom of the column	3.39E-10	-7.00E-10	-1.50E-11
Redox potential measurement at the top of the column	-5.20E-05	9.67E-05	1.86E-05
Redox potential measurement at the top of the column	1.15E-04	-2.50E-04	-4.20E-05
Cl^-	-5.11E-02	1.35E-01	2.04E-02
Br^-	-3.43E-01	8.83E-01	1.37E-01
SO_4^{2-}	1.06E+00	-8.73E-02	2.61E-01
NO_3^-	1.79E-09	-3.12E-08	-2.79E-08
Alkalinity	-1.60E-01	4.17E-02	1.03E+00
Temperature	2.00E-04	-3.53E-04	-7.94E-05
K	-4.30E-03	1.00E-02	1.75E-03
Ca	-1.43E-03	1.46E-02	-8.83E-03
Na	-1.89E-02	5.23E-02	4.69E-03
Mg	2.35E-04	-4.08E-04	-4.37E-05
NH_4	8.70E-04	-3.17E-03	-1.21E-03

Table A3: Component Score Coefficient Matrix for the layered sand-over-loam column.

Parameter	Component 1	Component 2
Depth	-2.88E-04	-5.00E-04
Tensiometer located at the top of the column	2.10E-09	2.59E-10
Tensiometer located at the bottom of the column	7.76E-09	7.58E-09
TDR located at the top of the column	-1.34E-09	-2.88E-08
TDR located at the bottom of the column	-7.03E-11	1.12E-11
Redox potential measurement at the top of the column	2.09E-07	1.31E-07
Redox potential measurement at the top of the column	1.38E-07	-1.41E-08
Cl^-	2.21E-03	6.22E-03
Br^-	-8.05E-04	-6.38E-04
SO_4^{2-}	-5.41E-01	8.90E-01
NO_3^-	7.14E-08	2.67E-08
Alkalinity	-6.98E-01	-7.72E-01
Temperature	3.94E-08	3.65E-08
K	2.94E-04	1.14E-04
Ca	-1.38E-04	6.53E-04
Na	7.27E-04	-1.40E-04
Mg	-2.32E-04	1.03E-04
NH_4	-8.57E-04	-2.23E-03

APPENDIX B

CROSS WAVELET ANALYSIS

The following figures provide detailed results of the cross wavelet analysis that establish similar temporal frequencies for different indicator and reactive chemicals.

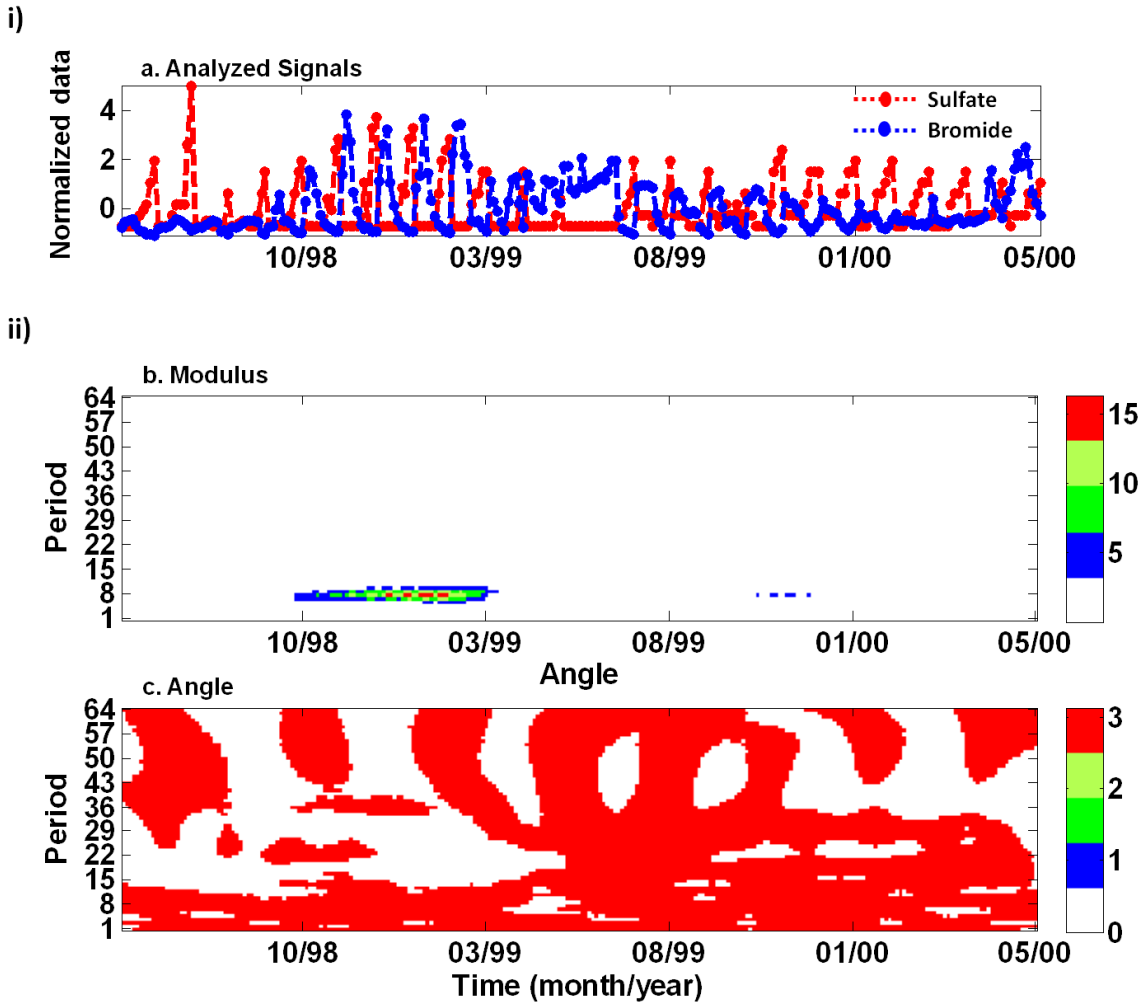

Figure B1: Cross wavelet analysis of bromide and sulfate signals at the control well from May 1998 to May 2000: i) time records of normalized bromide and sulfate data, and ii) modulus and angle of the wavelet cross-spectrum.

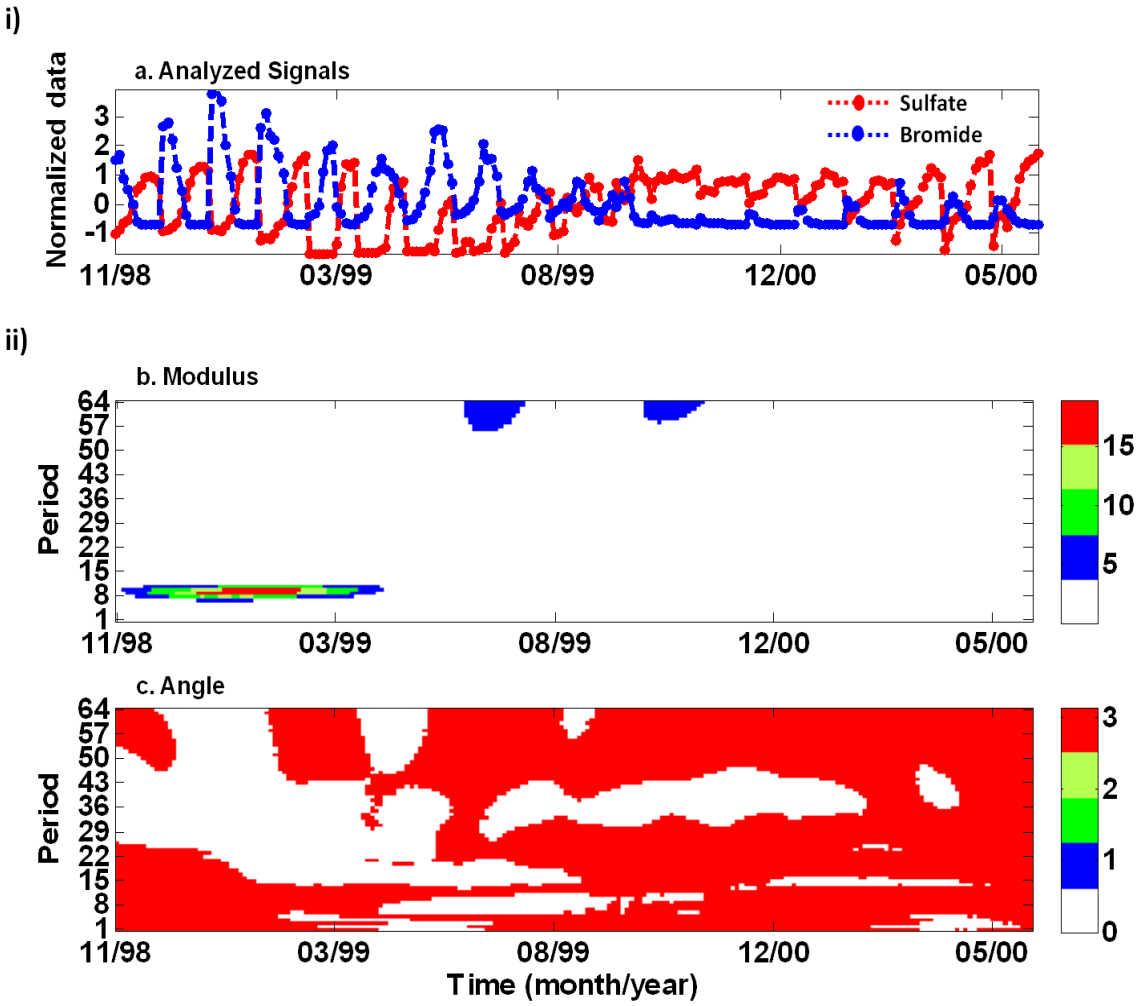

Figure B2: Cross wavelet analysis of bromide and sulfate signals at the landfill well from November 1998 to May 2000: i) time records of normalized bromide and sulfate data, and ii) modulus and angle of the wavelet cross-spectrum.

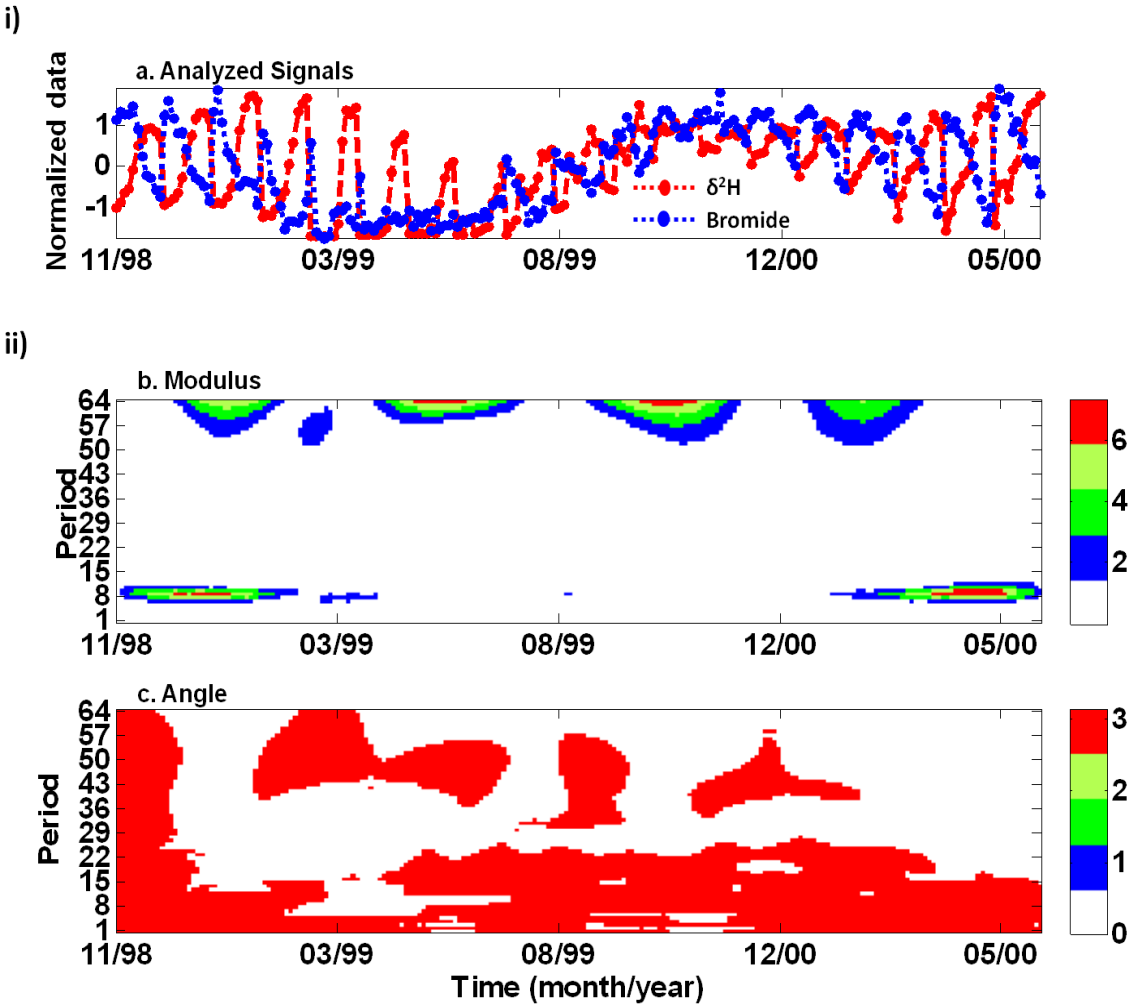

Figure B3: Cross wavelet analysis of bromide and δ^2H signals at the landfill well from November 1998 to May 2000: i) time records of normalized bromide and δ^2H data, and ii) modulus and angle of the wavelet cross-spectrum.

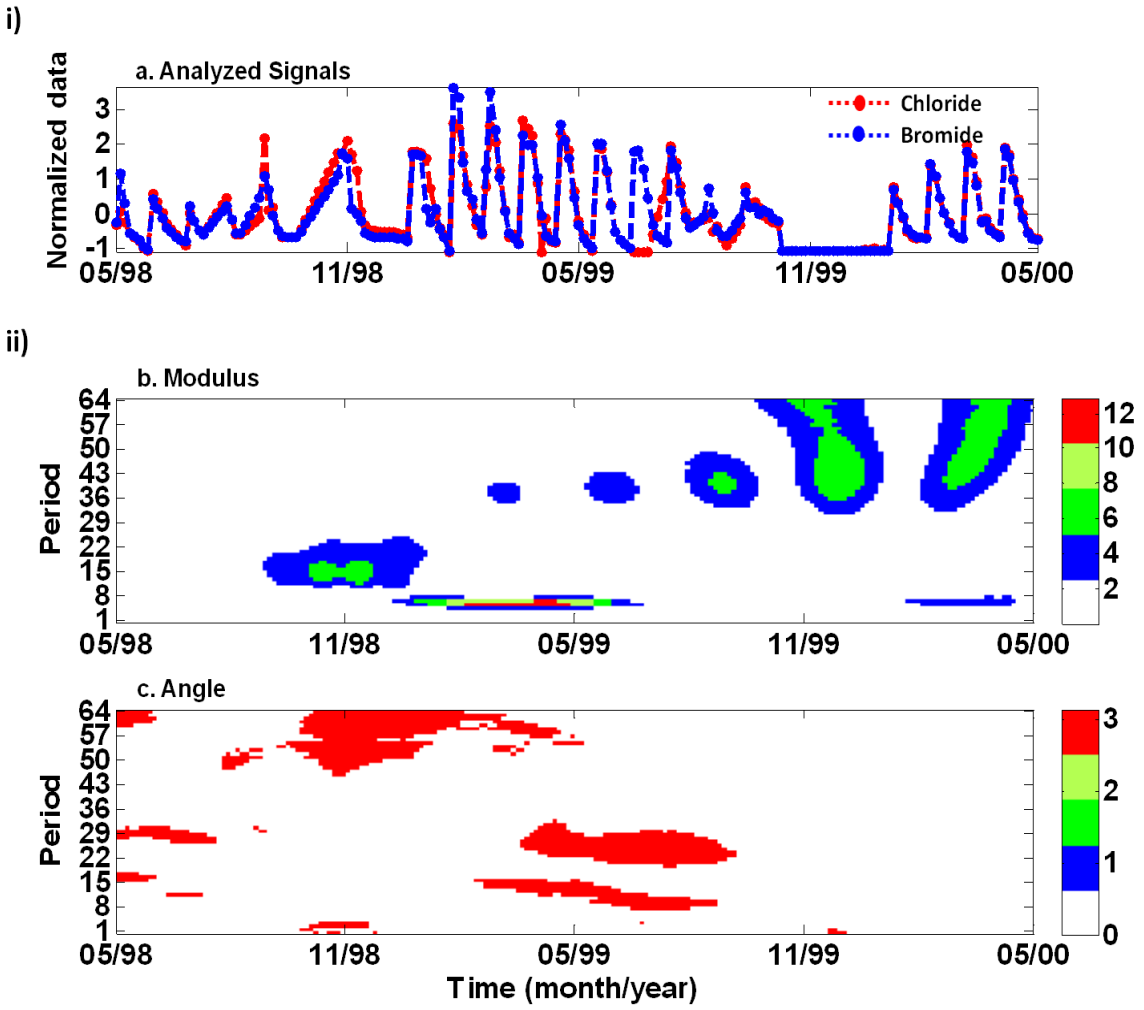

Figure B4: Cross wavelet analysis of bromide and chloride signals at the slough well from May 1998 to May 2000: i) time records of normalized bromide and chloride data, and ii) modulus and angle of the wavelet cross-spectrum.

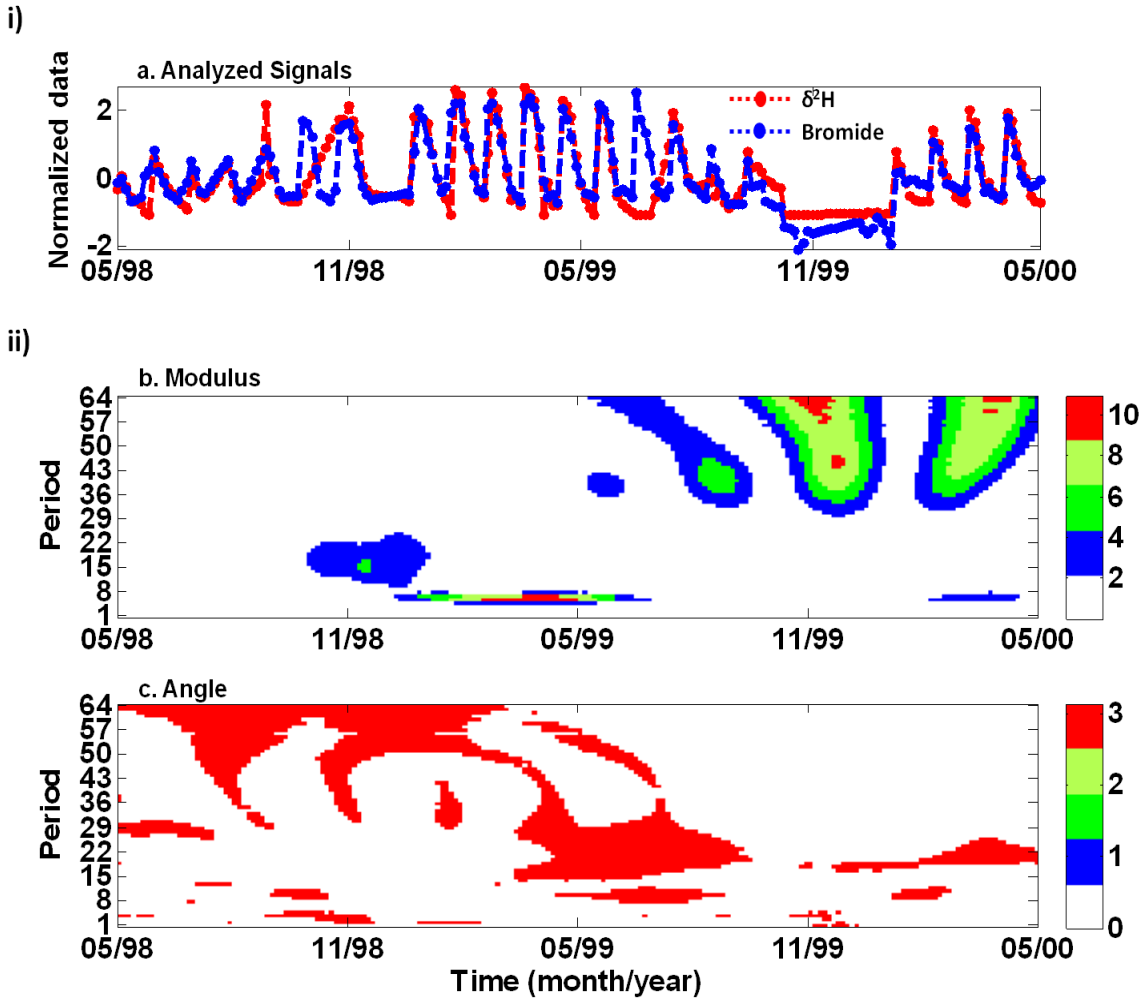

Figure B5: Cross wavelet analysis of bromide and δ^2H signals at the slough well from May 1998 to May 2000: i) time records of normalized bromide and δ^2H data, and ii) modulus and angle of the wavelet cross-spectrum.

VITA

Name: Bhavna Arora

Address: MS 2117, Rm. 235 Scoates Hall, Texas A&M University, College Station, TX 77843-2117

Email Address: bhavna2004@gmail.com

Education: B.Tech., Agricultural & Food Engineering, Indian Institute of Technology Kharagpur, India, 2006
M.Tech., Water Resources Development & Management, Indian Institute of Technology Kharagpur, India, 2006
Ph.D., Biological and Agricultural Engineering, Texas A&M University, 2012